

Printing a Stainless Steel Bridge

An exploration of structural properties of stainless steel additive manufactures for civil engineering purposes

Stijn Joosten

Faculty of Civil Engineering and Geosciences
Delft University of Technology



Printing a Stainless Steel Bridge

An exploration of structural properties of stainless steel additive manufactures for civil engineering purposes

by

Stijn Joosten

In partial fulfillment of the requirements for the degree of

Master of Science

in Civil Engineering

-

Faculty of Civil Engineering and Geosciences

Delft University of Technology

the Netherlands

4-13-2015

Thesis Committee

Prof. ir. F.S.K. Bijlaard	Delft University of Technology
Prof. dr. ir. I.M. Richardson	Delft University of Technology
Ir. P.A. de Vries	Delft University of Technology
Ir. D. Tuinstra	Arup

An electronic version of this thesis is available at

<http://repository.tudelft.nl>

*If I had asked people what they wanted,
they would have said faster horses.*

- Henry Ford

Abstract

The potential of additive manufacturing is great: highly complex and efficient structures can be manufactured with hardly any waste material. While high-tech industries such as aviation and medicine have already embraced additive manufacturing, civil engineering is lagging behind. Research on the structural properties of additive manufactures in civil constructions is necessary to build confidence with structural engineers.

The MX3D project aims to 3D print an 8 meter stainless steel bridge with gas metal arc welding based additive manufacturing. The basic elements - rods of 5 to 7 mm in diameter - are printed with 308LSi and 316LSi stainless steel. In this thesis, the structural properties of these elements are investigated by characterizing the geometry, performing structural tests, and studying the microstructure. Several batches were printed with varying process parameters. Every batch contained three types of rods, produced at different angles to the vertical: 0° , 30° , and 60° .

The rods were measured through photography and characterized by statistical distributions. Geater production angles led to larger geometrical inaccuracies. The critical geometrical parameters are the minimum and mean diameter. The variation around the mean was described using a normal distribution; the occurrence of small diameters using a Weibull distribution. This resulted in design graphs for the minimum diameter at increasing rod lengths.

Micrographs indicated an anisotropic austenitic microstructure of large columnar grains. The grains grew perpendicular to the weld pool, in the direction of the thermal gradient, across different deposition layers. For 0° rods, the grains grew in the main direction of the rod. At 30° and 60° , the weld pool was tilted, and the grain orientation deviated from the main direction, influencing structural behavior. Tensile tests on milled rods confirmed a reduction of the ultimate stress of 10 % for rods produced under an angle. Tensile tests further showed ultimate strength values averaging at 611 MPa. Because the 0,2 % proof strength was difficult to determine, it is proposed to use 50% of the ultimate strength as a value for the 0,2 % proof strength, ensuring that strength and ductility requirements are met. The observed Young's modulus showed great spread and was much lower than expected. This may be result of the anisotropic microstructure, but this is still unclear. Tests also revealed ductile material behaviour, meeting Eurocode requirements.

Buckling tests were performed for varying slendernesses. The results are not safely described by any of the existing Eurocode buckling curves. An alternative curve has been presented based on altered values for the imperfection factor and limiting non-dimensional slenderness. Fatigue tests have been performed on one type of element. Using the minimum diameter, a detail class of 81 was found.

Because of the large spreads in the properties and the risk of production errors, a quality control system based on ordinary welding is proposed. Conservative models give safe predictions of structural behaviour. Accurate structural models should take into account both geometrical and material variations.

This research gives confidence that stainless steel additive manufactures can be used in civil engineering structures and lays the basis for structural design rules.

Acknowledgements

Although this Master's thesis is a test of independence, it would not have come to fruition without the help and guidance of a number of people and institutions.

Firstly, I want to express my gratitude to the members of my committee: prof. ir. F.S.K. Bijlaard, prof. dr. ir. I.M. Richardson, ir. P.A. de Vries, and ir. D. Tuinstra. Their knowledge, guidance, and insightful comments challenged me to get the best out of myself.

My thanks go to ir. S. Galjaard for her enthusiasm and encouraging me to pursue additive manufacturing as a research topic. I would also like to say thanks to ir. M. Flint, my supervisor during the first few months of my thesis project. Many thanks to all my other colleagues at Arup for creating an energetic and inspirational environment to work on my thesis. The rounds of coffee and games of ping-pong were essential to keep a clear mind.

My sincere thanks also go to all the people at the Stevin II laboratory of the faculty of Civil Engineering for helping me set up and carry out my tests. Furthermore, I am very grateful to dr. ir. M. Amirthalingam for guiding me through the unfamiliar territory of microstructural research.

I am indebted to the generosity of Joris Laarman Lab and the MX3D project team, who supplied me with all the test pieces I needed. For his expert insight into the printing process, and all the time he invested, thanks to Filippo Gilardi.

Finally, I want to thank my housemates for making me feel at home, and my friends and family for their patience, kindness, and love.

Preface

As Additive Manufacturing (AM) methods are being developed further, 3D printers may become as common as 2D printers are today. The application of these methods on large scale components is a very exciting prospect. To a 3D printer, there is no difference between highly complicated and very simple geometry. The technique has the potential to create very efficient structures and reduce waste material. With AM, the engineer is no longer restricted to standard elements. In fact, virtually any shape can be designed and produced, which means our traditional construction types such as the beam-column structure and their joints can be completely reconsidered. The possibilities of additive manufacturing are many, but so are its challenges. A lot of research is still to be done for AM to be implemented in the construction industry. This thesis zooms in on a specific AM technique and investigates its structural applicability.

Understanding of the properties and structural behaviour of the material is essential for a safe application in engineering structures. By doing research and by designing and constructing pioneering projects, the way may be paved for a completely new kind of structures, possibly revolutionizing the construction industry. Engineers need to gain confidence in the material, and feel comfortable using it in their designs. This research aims to increase such confidence by looking into the application of a wire-based AM technique called MX3D, developed by Joris Laarman Lab. This technique is intended to be used to construct a bridge over a canal in Amsterdam. However, little is known about the material properties. Strength, stiffness, ductility, geometry and more need to be investigated and related to the production process in order to be able to make reliable predictions about the structural performance.

First, the problems and objectives will be identified. Then the research approach will be split into its main components and discussed accordingly. A literature research on additive manufacturing in general, specific materials and the effect of process parameters on microstructure and structural properties serves as a theoretical basis for the thesis. Different test and measuring methods to investigate structural properties are studied and the most relevant ones are selected. Specific testing procedures are then set up and executed. The results from these tests are analysed and compared to existing knowledge about stainless steel structural properties and design. The applicability of different analytical, numerical and FEM models to predict these test results is explored. Since the results show a lot of spread, the issue of consistency and quality control of the printing process is addressed. Finally, conclusions are drawn on the structural properties and the influence of the process, and recommendations are made on structural design and future research.

This thesis subject finds itself in a largely uncharted terrain for structural engineering. It serves as an exploration of wire-based AM in structural engineering, hopefully encouraging the application of AM in actual construction projects, and giving direction to future research.

Stijn Joosten
Amsterdam, 13 April 2015

Contents

Abstract	II
Acknowledgements	III
Preface	IV
Nomenclature	1
1 Introduction	3
1.1 Problem definition and objectives	3
1.1.1 Problem definition	3
1.1.2 The Technique	4
1.1.3 The Case	6
1.1.4 Research topic	6
1.2 Research Approach	7
2 Base material	8
2.1 Possible materials	8
2.2 Stainless Steel	9
2.2.1 Microstructure	10
2.2.2 Stress-strain	14
2.2.3 Recommended material	15
2.3 Summary	15
3 Process parameters and properties	16
3.1 Properties	16
3.1.1 Geometry	16
3.2 Parameters	18
3.2.1 General GMAW parameters	18
3.2.2 MX3D Parameters	18
3.2.3 Heat input and Cooling rate	19
3.3 Influence of process on properties	20
3.3.1 Overview of studies	20
3.3.2 Property Prediction	21
3.3.3 Direct process effects	22
3.4 Summary	23
4 Tests and measurements	24
4.1 Process measurements	24
4.2 Geometry	24
4.2.1 Manual measurements	24
4.2.2 Photogrammetry	25
4.2.3 Photographic method	27
4.2.4 Comparison	28
4.2.5 Summary	29

4.3	Mechanical Properties	29
4.3.1	Hardness test	29
4.3.2	Charpy impact test	30
4.3.3	Tensile test	30
4.3.4	Buckling test	31
4.3.5	Bending test	32
4.3.6	Fatigue test	32
4.4	Microstructure	33
4.4.1	Micrography	33
4.4.2	EBSD	33
4.5	Sample sizes	34
4.5.1	Fatigue testing	35
5	Test procedures	36
5.1	Static tensile testing	36
5.1.1	Specimen shape	36
5.1.2	Number of tests	37
5.1.3	Test description	37
5.2	Wire testing	38
5.2.1	Specimen shape	38
5.2.2	Number of tests	38
5.2.3	Test description	38
5.3	Buckling tests	38
5.3.1	Specimen shape	38
5.3.2	Number of tests	39
5.3.3	Test description	39
5.4	Fatigue tensile testing	40
5.4.1	Specimen shape	41
5.4.2	Number of tests	41
5.4.3	Test description	41
5.5	Micrography	42
5.5.1	Specimen shape	43
5.5.2	Number of tests	43
5.5.3	Test description	43
5.6	Vickers Hardness	43
5.6.1	Test description	43
6	Test results	44
6.1	Batches	44
6.1.1	Straight test pieces	44
6.1.2	Milled test pieces	45
6.1.3	Fatigue test pieces	45
6.2	Geometry	46
6.2.1	Batch 1	46
6.2.2	Batch 2	46
6.2.3	Batch 3	46
6.2.4	Batch 4	46
6.2.5	Overview	47
6.2.6	Geometry control	47

6.2.7	Minimum diameter	47
6.3	Microstructure	49
6.3.1	Batch 1	49
6.3.2	Batch 2	51
6.3.3	Batch 3	52
6.3.4	Batch 4	52
6.3.5	Overview	53
6.4	Vickers hardness	54
6.4.1	Batch 1	55
6.5	Tensile tests	55
6.5.1	Welding wire	55
6.5.2	Batch 1	56
6.5.3	Batch 2	57
6.5.4	Batch 3	58
6.5.5	Batch 4	60
6.5.6	Milled specimens	61
6.5.7	Overview	62
6.6	Fatigue tests	66
6.6.1	Overview	66
6.7	Buckling tests	67
6.7.1	Clamped tests	68
6.7.2	Hinged tests	68
6.7.3	Overview	68
7	Test modelling	70
7.1	Tensile tests	70
7.1.1	Failure load	70
7.1.2	Numerical model	70
7.1.3	FEM model	72
7.2	Buckling tests	72
7.2.1	Analytical model	72
7.2.2	FEM model	72
8	Quality control	74
8.1	Types of defects	74
8.2	Repairs	75
8.3	Inspection	76
8.4	Process control	76
8.5	Environment control	77
8.6	Test samples	77
9	Conclusion	79
9.1	Conclusions and recommendations	79
9.1.1	Geometry	79
9.1.2	Strength	81
9.1.3	Stiffness	83
9.1.4	Ductility	84
9.1.5	Stability	84
9.1.6	Fatigue	86

9.1.7	Microstructure	87
9.1.8	Quality control	88
9.1.9	Modelling structural behaviour	90
9.2	Printing a bridge	91
A	General	92
A.1	People	92
A.2	Timetable	95
B	Procedures and set-ups	96
B.1	Workflow photogrammetry	96
B.1.1	Photos	96
B.1.2	VisualSFM	96
B.1.3	Meshlab	97
B.1.4	Rhino	97
B.2	Photographic analysis	99
B.3	Tests setup	100
B.3.1	Tensile tests	100
B.3.2	Buckling tests	101
C	Results	103
C.1	Overview	103
C.2	Batch 1	106
C.2.1	Parameters	106
C.2.2	Geometry	107
C.2.3	F-u curves	113
C.2.4	Stress-strain curves	116
C.2.5	Welding wire	119
C.2.6	Correlations	120
C.2.7	Microstructure	123
C.2.8	Microhardness	127
C.3	Batch 2	129
C.3.1	Parameters	129
C.3.2	Geometry	130
C.3.3	F-u curves	135
C.3.4	Stress-strain curves	138
C.3.5	Correlations	141
C.3.6	Microstructure	144
C.4	Batch 3	146
C.4.1	Parameters	146
C.4.2	Geometry	147
C.4.3	F-u curves	151
C.4.4	Stress-strain curves	154
C.4.5	Correlations	157
C.5	Batch 4	160
C.5.1	Parameters	160
C.5.2	Geometry	161
C.5.3	F-u curves	165
C.5.4	Stress-strain curves	169

C.5.5	Correlations	173
C.5.6	Microstructure	176
C.6	Milled specimens	177
C.6.1	F-u curves	177
C.6.2	Stress-strain curves	182
C.6.3	Correlations	187
C.6.4	Microstructure	189
C.7	Fatigue	190
C.7.1	Parameters	190
C.7.2	Geometry	191
C.7.3	S-N	192
C.8	Buckling	193
C.8.1	Geometry	194
C.9	Geometry design graphs	195
	References	202

Nomenclature

Abbreviations

AM	Additive Manufacturing
bcc	Body-centered cubic
DMLS	Direct Metal Laser Sintering
EBS	Electronic BackScatter Diffraction
fcc	Face-centered cubic
FEM	Finite Element Method
GMAW	Gas Metal Arc Welding
hcp	Hexagonal close-packed
PPQR	Printing Procedure Qualification Record
PPS	Printing Procedure Specification
PQTR	Printer Qualification Test Record
SLM	Selective Laser Melting
SLS	Servicability Limit State
ULS	Ultimate Limit State
WAAM	Wire+Arc Additive Manufacture
WPQR	Welding Procedure Qualification Record
WPS	Welding Procedure Specification
WQTR	Welder Qualification Test Record

Subscripts

μ	Average
0.05	5 percentile
0.2	0.2 %
buc	Buckling
D	Design
M	Material

R	Resistance
u	Ultimate
y	Yield

Symbols

α	Generalized imperfection factor	
$\bar{\lambda}_0$	Limiting non-dimensional slenderness	
$\bar{\lambda}$	Non-dimensional slenderness	
\bar{R}	Lankford coefficient	
χ	Reduction factor buckling	
$\epsilon_{0.2}$	Strain at $\sigma_{0.2}$	
ϵ_u	Ultimate strain	
γ	Partial factor	
ρ	Pearson product-moment correlation coefficient	
$\sigma_{0.2}$	0.2% proof stress	$[N/mm^2]$
σ_u	Ultimate stress	$[N/mm^2]$
A	Rod cross-sectional area	$[mm^2]$
d	Rod diameter	$[mm]$
E_0	Initial Young's modulus	$[N/mm^2]$
F_{buc}	Buckling load	$[kN]$
f_u	Ultimate strength	$[N/mm^2]$
f_y	Yield strength	$[N/mm^2]$
I	Moment of inertia	$[mm^4]$
l_{buc}	Buckling length	$[mm]$

Specimen format: b-dd-\$

\$	Test piece designation	
b	Batch designation	
dd	Production angle	$[^\circ]$

Chapter 1

Introduction

1.1 Problem definition and objectives

In this section, the problem statement and objectives will be discussed.

1.1.1 Problem definition

As early as 1926, Baker patented “the use of an electric arc as a heat source to generate 3D objects depositing molten metal in superimposed layers”.¹ Not until the advent of

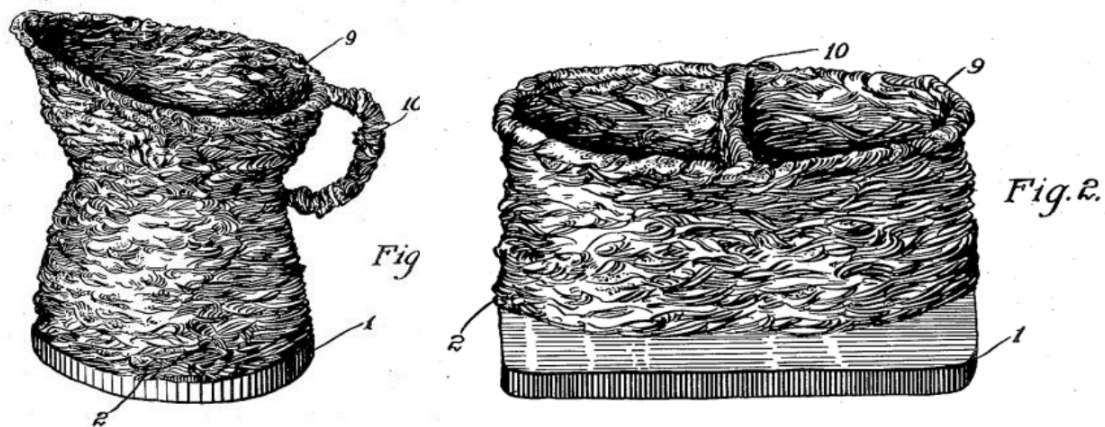


Figure 1.1: Baker's AM patent, 1926,²

computer-aided design (CAD) and the integration with robotics could this technique really take flight. Since these developments, however, additive manufacturing has mainly been the domain of high-tech industries and artists. At the moment, civil engineering structures are hardly considered as potential candidates for the application of AM. Considering the development of AM techniques, the decrease of costs, increase of production rates and part size, this is now changing. In order to support this development, research specific to the construction industry has to be carried out and actual structures have to set examples.

Aim

The aim of this thesis is to aid in the development of AM in civil engineering by studying a specific manufacturing technique, namely MX3D and investigating its structural applicability in the case of a footbridge.

¹Colegrove and Williams 2014, p.4.

1.1.2 The Technique

There are many different manufacturing techniques³, and many different manufacturers. Studying all of these within a seven month period is simply not attainable. Therefore, one such technique and manufacturer is selected for this thesis research. This choice should be made on the basis of two main factors. The first concerns the technique and includes relevance and potential for the civil engineering sector. This means relatively high deposition rates, low costs and robust production techniques are preferred when selecting a technique. The second is availability and feasibility. Laboratory experiments are expected to be an important part of the research, so it should be possible to easily produce test specimens. To address these factors the available techniques to directly produce metal objects can be split into two categories: powder bed processes and material deposition processes⁴.

Powder bed

In this process, the object is built up layer by layer from thin layers of metallic powder. When a layer of powder is deposited, the metal particles are fused together using lasers or an electron beam, producing a small slice of the final object. Another layer of powder is then laid on top and fused together. This is repeated until the entire object is constructed and the excess powder is removed. The entire process takes place inside an oven in which the environment is controlled and the temperature kept very close to the melting point of the powder in order to minimize the required energy input from the laser.

Material deposition

The second category, material deposition processes, works by feeding material through some kind of nozzle onto previous layers, building up the 3-dimensional object. The base material can be in the form of powder or wire and is molten using lasers, electron beams, an electric arc or a combination of methods.

Comparison

Typically, powder bed methods are associated with high accuracy, but low deposition rates when compared to wire-based AM⁵. They can be used for very detailed structures, such as implants or highly complex parts of structures. The steel node shown in 1.2a is made using direct metal laser sintering (DMLS), a technique in which metal powder is fused together by means of laser sintering. On the element level, it shows a lot of complexity. A closer look, however, reveals that the structure is not completely dense. Selective laser melting (SLM) is a different powder based technique that fuses the powder together by actually melting it instead of sintering it. This technique can yield structures of higher density, but still the surface will remain rough⁶. This is an important aspect of powder based AM. Wire-based AM on the other hand, cannot deal with very intricate geometries, but it does create fully dense structures. Cranfield University has made such structures using their Wire+Arc Additive Manufacture (WAAM), see 1.2b. For large scale and low cost application in civil engineering, wire-based material deposition techniques are preferred to powder bed techniques.

³Cruise and Gardner 2008.

⁴Centre for Additive Layer Manufacturing 2014.

⁵Mehnen et al. 2011.

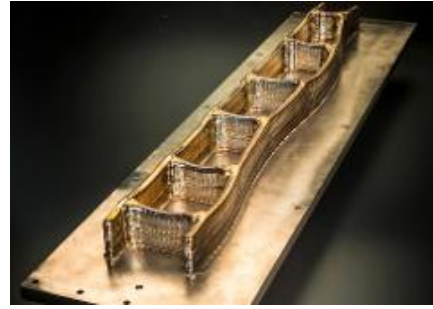
⁶Kruth et al. 2004, p.1.

⁷Niehe 2014.

⁸Cranfield 2013.



(a) DMLS node, prototype⁷ ©David de Jong



(b) WAAM part⁸

Figure 1.2: Metal AM techniques

MX3D

MX3D metal is an example of a wire-based technique and its developer, Joris Laarman Lab is based in Amsterdam. Furthermore, they are planning to print a bridge and willing to cooperate with this research and produce specimens to be tested. For these reasons, MX3D will be studied in this thesis.



(a) Welding machine and robotic arm



(b) Different rods

Figure 1.3: MX3D Metal Printing ©Joris Laarman Lab

MX3D makes use of a gas metal arc welding (GMAW) machine attached to a robotic arm. By welding small parts of material at a time along a path generated from CAD data, self-supporting metal lines can be manufactured. When producing a multitude of connected lines a 3-dimensional grid is created that can be used to construct a stiff structural system, see 1.3. This production of different types of rods and different geometries requires different process parameters. A vertical rod, an inclined rod, and a horizontal rod are all produced differently. Even if welding parameters such as arc voltage, wire feed speed, welding speed etcetera were to be kept constant, the orientation of the rod, the nozzle and the direction of the gravitational force will result in different rod properties. The geometry of the rods themselves -determined by process parameters- influences stiffness, weight and deformation capacity. Besides that, the material properties are greatly influenced by the microstructure, which is also highly dependent on the additive manufacturing process. Currently, the process parameters are determined by trial and error. Its results are judged only visually. Structural application requires a far greater understanding of the material properties of the material and control of the process.

1.1.3 The Case

Joris Laarman Lab and Arup are planning to design a footbridge that is to be printed on site using the MX3D technology. Conceptually, the project is meant to show the possibilities of additive manufacturing and give an idea of what future construction projects might look like. Functionally, it should increase the east-west connectivity of the city center. The bridge will span the Oudezijds Achterburgwal in Amsterdam, but the exact location is to be determined. It will span about 7 meters and is expected to be 3 to 4 meters wide. When designing such a bridge, many challenges arise. Of course, the final overall design plays an important role, but temporary situations and printing strategy should also be considered. Safety, aesthetics, environment etcetera should also be addressed. One of many other aspects is the control of the manufacturing process and the structural properties of the material.



(a) Dragon bench, MX3D structure
©Joris Laarman Lab



(b) Possible location

Figure 1.4: AM bridge case

The current largest MX3D structure is the dragon bench, a piece of furniture made up of interconnected curved stainless steel lines, see figure 1.4a. As such, its 3-dimensional grid is the most likely structure to form a bridge at this moment. The basic element in this structure is the rod, which can be seen in 1.3b

Although this Master's thesis is closely involved with the AM bridge project, it is not led by it. The results of the research of the thesis may support the bridge design, but the actual realisation of the bridge is not a direct goal.

1.1.4 Research topic

The following research question is at core of the research:

What basic structural properties should be considered when designing AM structures for civil engineering purposes?

This question is investigated in the context of the MX3D bridge case. Research will be done into the structural properties and how they are influenced by the printing process. By doing so, insight is gained into the limits of the manufacturing process and the possibilities for structural application. The MX3D technique and the intended application in a bridge determine some of the boundary conditions: the kind of material and the types of structures investigated, the kind of tests performed and the properties studied.

Secondary objectives

The objectives mentioned below will partially be addressed by the main research topic. The extent to which they will be further investigated may change over the course of

the thesis project. The subjects are at least expected to be an important part of the recommendations.

- Characterize geometry, set up measuring procedures.
- Identify and describe important structural phenomena through tests.
- Study influence of metallurgical changes due to process on structural properties.
- Investigate FEM, numerical and analytical methods to model structural behaviour.
- Give advice on design and manufacturing guidelines

1.2 Research Approach

The approach to this research can be split into four parts. The first part is a study phase, leaning heavily on literature research. This phase serves to get acquainted with additive manufacturing in general, learn about past research, study the manufacturing process and material properties and investigate models to link process and properties. Secondly, this acquired knowledge will be put to use in the test phase, which starts with the development of testing procedures and appropriate specimens. Subsequently, these specimens will be accurately measured and submitted to different tests. When all test data is acquired, the analysis phase starts. The data will be analysed, extracting structural properties, and compared to analytical and FEM models. Finally, recommendations are made and the final report is written.

Chapter 2

Base material

In theory, the MX3D process may use any wire that can be fed through the nozzle of the welding machine and act as a consumable electrode. Realistically, these materials cannot be studied in-depth within this thesis. Therefore, a choice for a specific material will be made at an early stage based on some simple assumptions.

2.1 Possible materials

In this section, some different groups of materials are named, and the chosen material is described in more detail in the following sections. The materials are judged on the following criteria:

- Durability
The bridge will be out in the open and because it is expected to be very complex, the need for post-treatment and maintenance should be kept to a minimum.
- Weldability
The welded steel should possess strength and toughness as required in service. Different types of cracking and microstructural changes should be considered.
- Strength
The material should have yield, tensile and fatigue strengths competitive with ordinary construction materials
- Stiffness
The stiffness, the stress-strain behaviour of the material is an important aspect of the structural behaviour, influencing load distribution and determining deformations.
- Ductility
In order to construct safely, ductility of the material should prevent brittle failure.
- Cost
At the moment production costs are high compared to material costs, so the prices of raw materials are not a very important factor yet. However, AM production costs are likely to go down as they are further developed, while raw material prices can be expected to stay at the same level or go up due to scarcity. In the future, material costs will become more important.
- Experience
An important practical consideration is how much experience one has printing a certain material. A certain material may be very promising on paper, but if the production process still has to be developed it is not a realistic choice.
- Availability
In the end, the material should be available in order to produce test specimens.

The considered material groups are:

- Carbon steels
Relatively the cheapest solution¹, but possible problems with weldability, control of weld pool and durability.
- Weathering steel
Better durability and higher strength than ordinary carbon steels, but possibly higher CEV². The weathered look may also be an architectural point of consideration.
- **Stainless steels**
Currently used at Joris Laarman Lab. More expensive than ordinary structural steels or weathering steels, but may provide superior corrosion protection, weld control and aesthetics.
- Aluminium alloys
Aluminium alloys are light, durable and can be made as strong as steel. Their stiffness, however, is one third of steel. Furthermore, aluminium alloys have no fatigue cutoff limit³. Lastly, their weldability greatly depends on the type of alloy⁴
- Titanium alloys
Widely applied in wire-based additive manufacturing. Very smooth surface, great control of weld shape. Good mechanical properties. However, these are very expensive.

Taking into account the different criteria mentioned above and the experience of the Joris Laarman Lab, a stainless steel might be a very good option. As far as the corrosion resistance of these materials goes, the surface finishing or lack thereof may play an important role. The durability of a material is inevitably linked to its surface and detail geometry.

2.2 Stainless Steel

Stainless steels differ in a number of ways from ordinary carbon steels. Of course, their improved corrosion resistant properties due to the minimum addition of 11% chromium is an important distinction⁵. Furthermore, microstructural composition and stress-strain behaviour are clearly different. It is important to keep in mind these distinctions when applying stainless steel in structures and design accordingly⁶. These aspects will be discussed in the following sections.

The main types of stainless steel are ferritic, austenitic and martensitic stainless steels. Additionally, duplex stainless steels and precipitation hardened stainless steels can be distinguished. Duplex and Austenitic stainless steels have the best corrosion resistance. Duplex has higher strength than austenitic steels, but lesser toughness and ductility. Another important property of austenitic stainless steels is that their mechanical properties are largely unaffected by welding, they cannot be hardened by temperature⁷, making them especially suited for use in AM. These differences between the groups have been summarized in table 2.1. Although duplex and precipitation hardening steels possess superior mechanical properties, they are very sensitive to the welding process. With regard to weld based additive manufacturing, they are not as robust a choice as austenitic stainless steels.

¹Beardmore 2014a.

²EFW 2009.

³Beardmore 2014b.

⁴TWI 2015a.

⁵ESDEP 2014a.

⁶SCI 2006.

⁷Mathers 2014.

⁸ESDEP 2014a.

Type	Corrosion	Ductility	Strength	Weldability	Magnetism
Austenitic	+	++	0	Good	Depends
Martensitic	0	-	++	Precautions	Yes
Ferritic	+	-	+	Precautions	Yes
Duplex	++	+	++	Precautions	Yes
Precipitation hardening	++	++	+++	Precautions	Depends

Table 2.1: Stainless steel groups, based on⁸. +, 0 and - are assigned relatively

2.2.1 Microstructure

Even within the different stainless steel groups, there are many different stainless steel alloys, each with different constitutive elements and their own specific properties. A subdivision into different types can be made based on their crystal structures and microstructural constituents. These constituents strongly affect the material properties. Furthermore, the grain size is of great importance to engineering properties. The the temperature is of great influence on the composition of the microstructure and thus it should be taken into account. Crystal structures make up the grains; the grains together form the metal structure and determine the type and properties of the stainless steel.

Crystal shape

Although there are seven basic crystal systems, and each of these systems can be arranged in 14 different lattice structures, the crystalline patterns of almost all structural metals are limited to three forms: face-centered cubic (fcc), hexagonal close-packed (hcp), and body-centered cubic (bcc) crystal lattices, see figure 2.1⁹. In steels, the most important

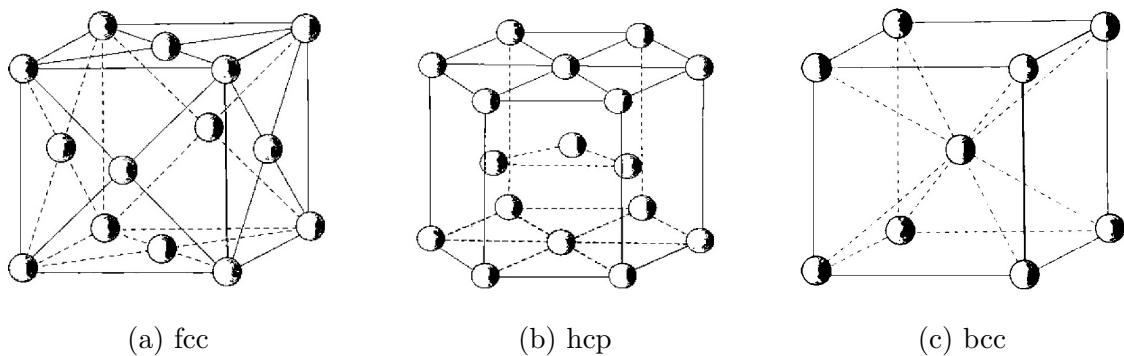


Figure 2.1: Crystal lattice structures bcc, hcp and fcc.¹⁰

lattice structures are bcc lattices, called ferrite or α , and fcc lattices, called austenite or γ . These are the building blocks of a steel and are of influence to various properties. In the fcc system, the atoms are in the most closely packed arrangement. It is characterized by high ductility, even at low temperatures, compared to the bcc system. This is because slip deformation occurs preferably along close-packed planes. In a bcc system, the structure is not close-packed, and slip deformation occurs along nearly close-packed planes, giving it more possible slip planes than an fcc system. The operability of these slip systems, however, depends on temperature and chemical composition. Hence they are not always

⁹Reardon 2011, p.20.

¹⁰Reardon 2011, p.21-22.

active, resulting in a more brittle structure¹¹. The relative proportions of ferrite and austenite in a certain steel therefore say a lot about its mechanical properties.

Grains

Grains are formed from uniformly oriented lattice structures. The grain boundaries are zones in which grains of different lattice structure orientation meet and a misfit between neighbouring atoms occurs. These boundaries can both strengthen and weaken a material¹², so control of the formation of these boundaries is essential to acquire desired material properties.

The grain size affects the mechanical properties of steel¹³. Smaller grain sizes do not only result in higher yield strength, but also increase the ductility and toughness of the material. The grain size can be influenced by controlling the temperature of the steel and by rolling the steel¹⁴. Since rolling is not an option, temperature control is the pre-eminent instrument to influence grain size in MX3D structures. The temperature can be controlled by the process parameters, which is described in more detail in chapter 3. Research at Cranfield has shown that grain growth in Ti64 alloys can be manipulated by changing one such parameter, namely the wire speed¹⁵.

Anisotropy

For grain formation to occur, different solidification nuclei are necessary. As they grow in different directions and meet, grain boundaries are formed. When these grains grow in the same direction, a columnar grain structure is observed. In some cases the material may even consist of one single grain, having one crystalline orientation. This type of microstructure is the result of directional solidification. In multipass welds, dendrites tend to grow in the direction of the temperature gradient¹⁶. This can lead to columnar grain structures. Since GMAW AM structures can in fact be considered multipass welds, their solidification is expected to be similar. Columnar grains are generally considered unfavourable, because they lead to anisotropy of mechanical properties¹⁷. In some cases, however, the properties associated with this microstructure may be desired. For the production of turbine blades for example, the material is forced to solidify into one single crystal, minimizing the effects of creep¹⁸.

Shaeffler diagram

The amount of austenite, ferrite and martensite in a stainless steel microstructure can be predicted using a Shaeffler diagram, see figure 2.2. This prediction is based on the Chromium and Nickel equivalents of the material.

The different coloured parts of the Shaeffler diagram are associated with specific welding problems encountered. Additionally, some commonly used types of welding wires are added into the diagram. A couple of these materials fall within a sort of sweet spot, a triangular patch in between the yellow and blue zones. They are mostly austenitic, but a small

¹¹Reardon 2011, p.28.

¹²Ibid., p.26.

¹³ESDEP 2014b.

¹⁴Ibid.

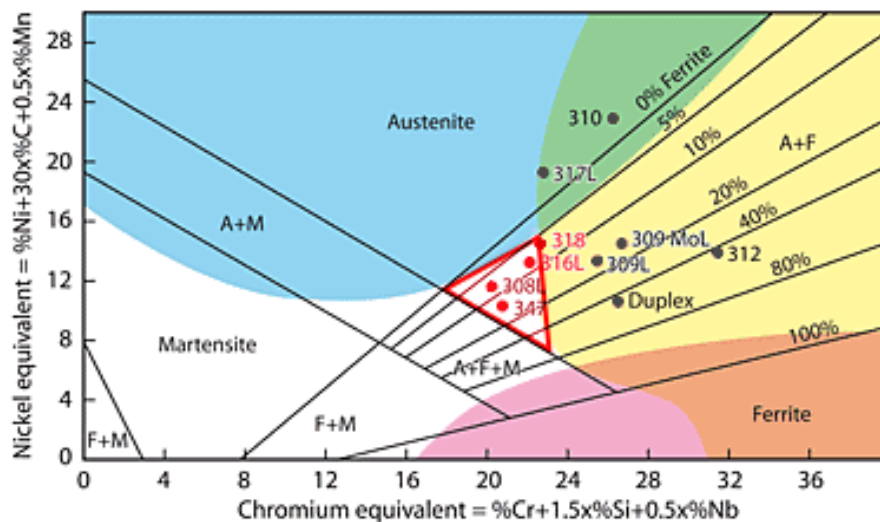
¹⁵Colegrove and Williams 2014.

¹⁶Moysan et al. 2003, p.80-81.

¹⁷Lampman et al. 1997.

¹⁸Smallman and Ngan 2013, p.105.

¹⁹Mathers 2014.

Figure 2.2: Shaeffler diagram¹⁹

(A=Austenite; M=Martensite; F=Ferrite) (Blue=Sensitive to hot cracking; Green=Extra sensitive to hot cracking; Pink=Grain growth and embrittlement; Yellow=Embrittlement in elevated temperature service or due to stress relief; Brown=Yellow and Pink)

amount of δ -ferrite gives them increased resistance against hot cracking²⁰. This sweet spot and the materials falling within it are marked red in figure 2.2.

Influence of temperature

When steel is heated to a certain temperature, its crystal structure begins to change; bcc crystal lattices can turn into fcc crystal lattices and vice versa. In the case of pure iron the change from bcc to fcc occurs at 910°C; below this temperature no metallurgical changes occur in the material²¹. By alloying the iron, stable fcc systems can be formed at lower temperatures. In the case of austenitic stainless steels for example, the primary crystal structure is fcc, even at room temperature. At the weld pool, the material is molten, but farther away, the temperature drops. The place at which the temperature gets below the point at which the microstructure is changed, demarcates the so called heat affected zone. This means that with every newly deposited metal layer a certain zone around the weld pool is changed metallurgically. These changes can be viewed and analysed through a microscope.

Research has shown that the cooling rate can have a large influence on steels that are not fully austenitic, suggesting the addition of a third dimension to the Shaeffler diagram²². Initially, faster cooling rates result in higher ferrite content, but as the cooling rate is increased further, a lower ferrite content is observed²³. This last trend, however, is usually only observed with very fast cooling rates associated with laser welding instead of GMAW. Cooling rate ranges for different processes are shown in table 2.2. The cooling rate during crystallisation for arc welding is indeed relatively low, but the range is big and the actual value depends greatly on the specific arc welding conditions. During the solidification process, segregation of alloying elements may take place, resulting in an inhomogeneous microstructure with different amounts of austenite and ferrite²⁵ and

²⁰Mathers 2014.

²¹ESDEP 2014b.

²²Vitek, Dasgupta, and David 1983; David et al. 1987; Elmer, Allen, and Eagar 1989.

²³David et al. 1987, p.22-24.

²⁴Elmer, Allen, and Eagar 1989.

²⁵Olson 1985; Howe 1991, p.291, p.2.

Process	Cooling rate [K/s]
Casting	$10^0 - 10^2$
Arc welding	$10^1 - 10^3$
Electron beam welding	$10^2 - 10^4$
Laser beam welding	$10^2 - 10^6$
Rapid solidification processing	$10^3 - 10^7$

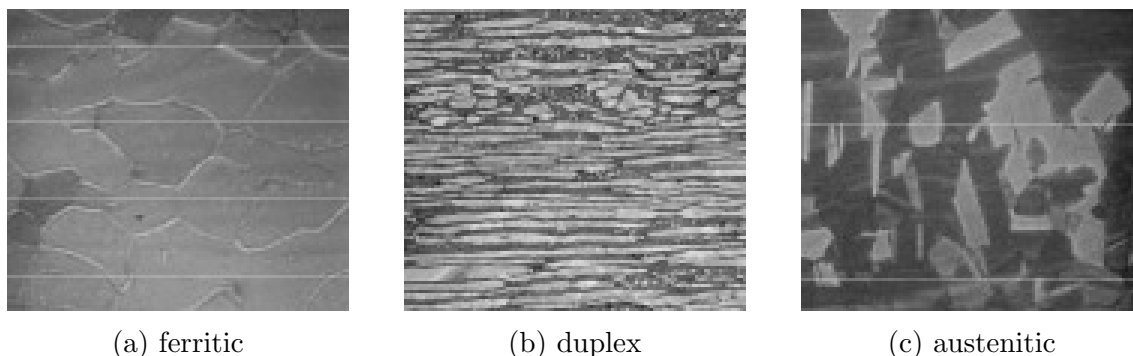
Table 2.2: Cooling rate ranges for different solidification processes²⁴

possible migration of chromium locally reducing corrosion resistance. Microstructural investigation can show the balance between austenite and ferrite and the distribution of alloying constituents in a certain material.

Furthermore, micrographs can show differences in cooling rate over a cross section. The direction, shape and spacing of dendrites provide information about the way the material has solidified, and how it may behave structurally²⁶

Examples

Figure 2.3 shows example micrographs of stainless steel microstructures. The change in microstructure from left to right, from ferrite to austenite via duplex, can be associated with an increasing nickel equivalent, which is also observed in the Shaeffler diagram, see figure 2.2. Note that the appearance of such micrographs is greatly dependent on the microstructure and the specific etchant used.



(a) ferritic

(b) duplex

(c) austenitic

Figure 2.3: Ferritic, duplex and austenitic microstructure²⁷

In figure 2.4, the ferrite, austenite and intermetallic content in ferritic-austenitic stainless steels are shown. The intermetallic content in such steels can be formed as a result of the welding process, and may reduce the corrosion resistance and toughness of the material²⁸. In case the chosen material contains only a small amount of ferrite, these intermetallic phases are not expected to pose much of a problem. Nevertheless, microstructural investigation will have to be done to verify this.

²⁶Elmer, Allen, and Eagar 1989, p.2119-2120.

²⁷IMO 2014.

²⁸TWI 2014a.

²⁹TWI 2014a.

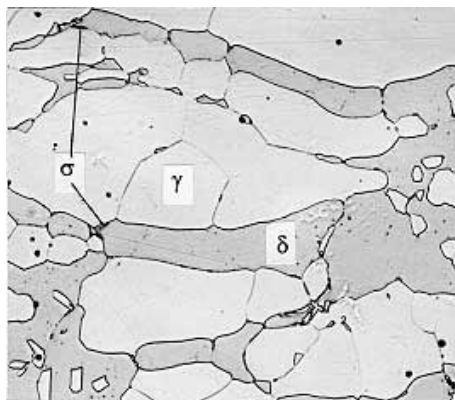


Figure 2.4: Ferrite (δ), austenite (γ) and intermetallic content (σ) in ferritic-austenitic stainless steels²⁹

2.2.2 Stress-strain

The stress-strain relationship of stainless steels is different from that of common carbon steels S235 and S355. While these carbon steels show a clear yield point, yield plateau and strain-hardening region, stainless steels exhibit different behaviour³⁰. Their yield point is not so clearly marked, which is why the 0.2% proof strength, $\sigma_{0.2}$, is used. Furthermore, there is no clear yield plateau; the stress strain diagram follows a smooth, gradual curve. This can be seen in 2.5. Carbon steel stress-strain relationships are often modeled bi-

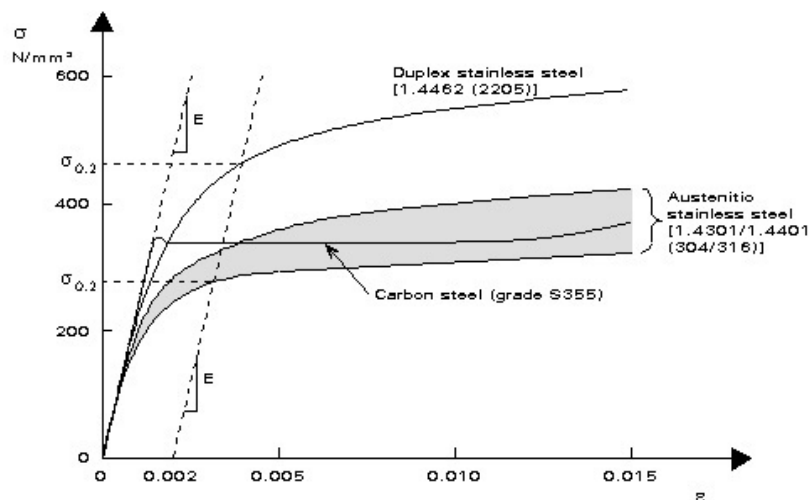


Figure 2.5: Comparison of stress-strain curves of stainless steel and ordinary carbon steel³¹

linearly, i.e. the first part up to the yield stress is formed by a linear line at an angle $E_0 = \frac{\sigma}{\epsilon}$ and from there a straight horizontal line approximates the yield plateau. Stainless steel stress-strain curves are often based on the Ramberg-Osgood expression. This expression gives a good fit to actual stress-strain data from testing up to the 0.2% proof stress. From this point onwards, however, large inaccuracies are observed. Therefore, Rasmussen has modified the Ramberg-Osgood expression in order to describe full-range stress-strain

³⁰Baddoo 2008.

³¹BSSA 2014.

curves for stainless steel alloys³².

$$\epsilon = \begin{cases} \frac{\sigma}{E_0} + 0.002 \left(\frac{\sigma}{\sigma_{0.2}} \right)^n & \text{for } \sigma \leq \sigma_{0.2} \\ \frac{\sigma - \sigma_{0.2}}{E_{0.2}} + \epsilon_u \left(\frac{\sigma - \sigma_{0.2}}{\sigma_u - \sigma_{0.2}} \right)^m + \epsilon_{0.2} & \text{for } \sigma > \sigma_{0.2} \end{cases} \quad (2.1)$$

The first part of this equation is actually the unaltered Ramberg-Osgood equation, the second part is the expression derived to describe the stress-strain curve for stresses above the 0.2 % proof stress. The parameters corresponding to a certain material can be determined from experimental data. Using the data acquired by Rasmussen, the stress-strain curve for stainless steel 316L can be composed³³. This curve can be implemented in FEM, numerical and analytical models.

2.2.3 Recommended material

From the different types of stainless steels that are shown in figure 2.2, 316L is recommended. Because it is a high chromium and low carbon austenitic stainless steel, it can be used in aggressive corrosive environments³⁴. Its carbon content is low and it falls within a sweet spot that is associated with good weldability. Although it is an austenitic stainless steel, which is less strong than other types of stainless steel, its strength is comparable to widely used S355 structural carbon steel, see figure 2.5. Its austenitic microstructure, however, also makes it ductile compared to other types of welding wires. Because of the higher alloying content required for increased durability, though, 316L is more expensive than for example 304, another common stainless steel.

In the end, the most important consideration is purely practical: JLL needs to have experience with the material and the material should be available to them. They have conducted some experiments with 316L, but they have the most experience using 308L. Stainless steel 308 is inbetween 304 and 316 as far as the addition of alloying constituents and associated corrosion behaviour and the position in the Shaeffler diagram go. The exact types of stainless welding wire that are used by JLL are 1 mm solid wires conforming to ER 308L and ER 316LSi called ‘Inertfil 308LSi and ‘Inertfil 316LSi’ by Oerlikon. Compared to ordinary 308L and 316L, the Si versions contain extra silicon, improving the wetting behavior of the weld metal, making it easier to clean and finish. According to the product sheet, both 308LSi and 316LSi possess a yield strength $f_y \geq 350N/mm^2$ and tensile strength $f_t \geq 510N/mm^2$. The ultimate strain is $\epsilon_u \geq 30\%$ for 316LSi and $\epsilon_u \geq 35\%$ for 308L³⁵. These values will be verified if possible by performing tensile tests, which are described in section 6.5.1.

2.3 Summary

The base materials that will be used are stainless steel types 308LSi and 316LSi. The stress-strain curve of stainless steel is different from ordinary carbon steel: it does not have a clear yield point. A modified version of the Ramberg-Osgood expression can be used to describe the behaviour. The exact structural properties are determined by the alloying elements and the microstructure. Optical microscopy can be used to investigate the microstructure and indicate the different metallic contents, and the size and shape of individual grains. This investigation can give insight into how the process influences the microstructure and thus the structural properties of the material.

³²Rasmussen 2003.

³³Ibid., p. 52.

³⁴Mathers 2014.

³⁵Oerlikon 2015a; Oerlikon 2015b.

Chapter 3

Process parameters and properties

In this chapter, different process parameters will be mentioned and their possible influences discussed based on literature research. The most relevant parameters in general GMAW will be identified and compared to parameters that are related to AM and MX3D in specific. Firstly, a description will be given of properties which are affected by these parameters.

3.1 Properties

The mechanical properties of the base material, which are described in chapter 2, are influenced by the welding process. Besides the properties of the material itself, the geometry of the produced rods is of great influence on the structural behaviour. From a structural engineering point of view and considering the case study, the most important structural properties that are being investigated are the following:

- Strength
 - Yield
 - Tensile
 - Fatigue
- Ductility
- Geometry
- Stiffness

In order to understand how the base material is altered by the process, and how this affects the material properties, the material is also studied at a smaller scale. To this end, the following additional aspects are addressed:

- Hardness
- Microstructure

3.1.1 Geometry

With any manufacturing technique, certain geometrical tolerances have to be taken into account. These deviations can be on a global level, e.g. a rod is curved instead of straight, or on a local level, e.g. the thickness is different than prescribed. The first is related to the accuracy of the robotic arm, and is dependent on the overall structure, so it should be taken into account when making a specific structural design. The latter, the local level, depends on process parameters and is apparent in all structures. This level of geometry will be subject of study in this thesis.

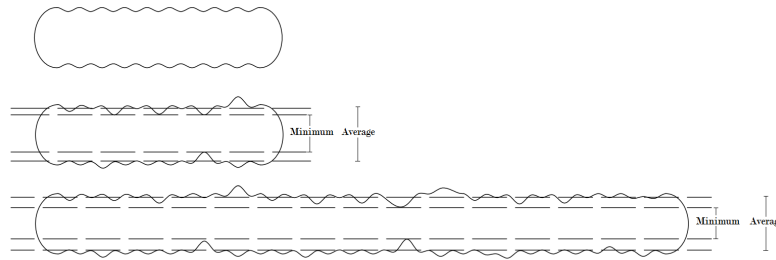


Figure 3.1: Geometric size effect

The following figures were made to illustrate the effects of the manufacturing process on the local geometry and subsequently structural properties. 3.1 shows that the longer rods are made, the larger the chance of a small diameter or other geometrical defect becomes. Statistical insight into the geometry is therefore necessary to make a safe structure.

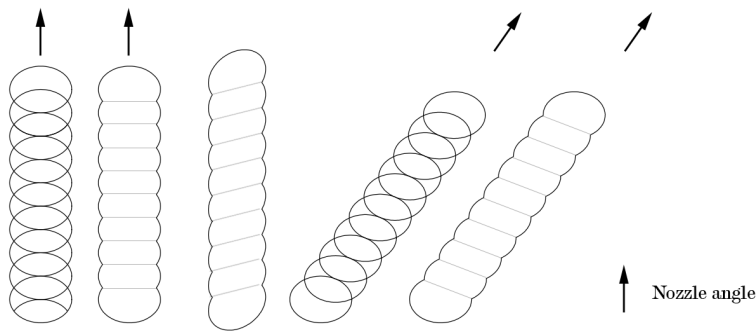


Figure 3.2: Influence of rod angle on geometry

Figure 3.2 is a schematic drawing of a metal rod. As the angle of the nozzle changes with respect to the rod and the direction of gravity, a different rod shape and anisotropy of the structure is to be expected.

Additionally, a simplified model of the structural behaviour of the rod under tension has been made to study the effect of a changing diameter on the deformation capacity, see figure 3.3b. In this calculation, the profile of the rod has been modelled as a sinusoid, see figure 3.3a. This model predicts half the deformation at failure for an irregular rod (black line) in comparison with straight rods (green and blue lines).

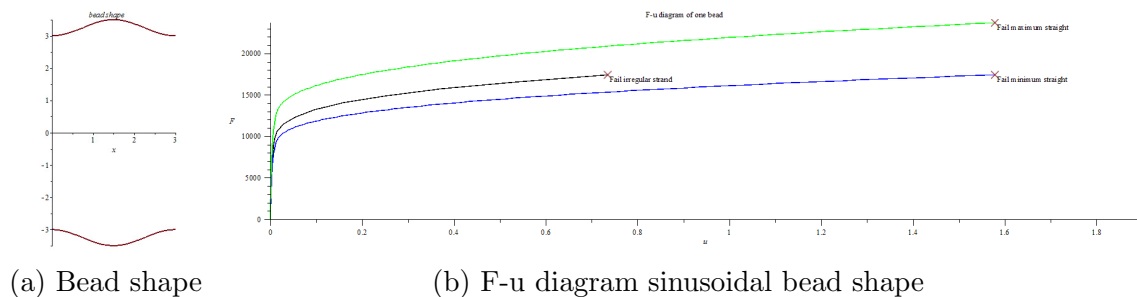


Figure 3.3: Influence of geometry on deformation capacity

Finally, one should be aware of notch effects. These effects may reduce the static and fatigue strengths of the rods.

3.2 Parameters

3.2.1 General GMAW parameters

Assuming the use of fixed material and shielding gas, the following GMAW parameters can be distinguished:

- Current
- Voltage
- Welding speed
- Wire diameter
- Wire feed rate
- Nozzle-to-bead distance
- Preheat temperature
- Gas flow rate

In practice, it is hardly possible to change one parameter while keeping the others constant. In the welding process, all these parameters are linked to each other. Current (I), voltage (V) and the other parameters are all linked through Ohm's law $I = \frac{V}{R}$ and the power (W) required for the welding process $W = I \cdot V$. Furthermore, in many welding machines, including the MX3D digi@wave280, the above parameters are not set directly, but limited to maximum or minimum values or controlled by output oriented settings such as arc length.

Quality control

In ordinary welding, a certain level of quality is guaranteed by controlling the process through welding procedure specifications (WPS). Such a specification contains all the information required for a qualified welder to perform a weld; it provides an allowable range of welding parameters that might be used. Each WPS is backed up by a welding procedure qualification record (WPQR). The WPQR concerns a record of an actual weld, and comprises qualification tests and precise welding parameters. To determine the range of WPSs to which a WPQR can be applied, a range of qualification is specified¹. Within this range, the WPQR serves as a proof that a weld produced according to a certain WPS will be of a certain quality.

These documents may serve as a starting point for future quality control of additive manufactures.

3.2.2 MX3D Parameters

In this section, a description is given of parameters that come into play in additive manufacturing in general and in MX3D in specific. In addition to the general parameters, the MX3D operator mentioned the following parameters to be of importance to the printing process:

- Cooling time
Set only as a minimum waiting time; will increase automatically in case multiple lines are printed at the same time

¹BCSA 2010.

- Welding pulse time
- Layer height

The cooling time indicates the time between subsequent metal deposits in the same spot, thus it indicates the preheat temperature of the previous layer. The welding pulse time is the period the machine prints or welds at a single spot and can be related to the welding speed parameter in ordinary GMAW processes. The layer height parameter is controlled through the 3D computer model. An MX3D model is built up of 3D lines, which are then subdivided into layers of certain layer height along the length of the line. Each of these layers is a point at which the MX3D machine deposits weld material. Hence, the layer height is of great influence on the structural properties and appearance of the rods.

The following parameters were not mentioned by the MX3D operator, but are also expected to play an important role (see also figure 3.2):

- Nozzle angle
- Rod angle

These parameters may change the properties of the rods, because the direction of the gravitational force is at an angle to the main rod direction and will have an influence on the weld pool. In practice, the nozzle is almost always in line with the rod angle, so in fact these two parameters may be joined into one angle parameter.

3.2.3 Heat input and Cooling rate

Heat input and cooling rate are a direct result of the welding parameters. They are very closely related and both influence the weld output to a great extent. They can be described as follows:

- Cooling rate²

$$R \propto \frac{1}{T_0 H}$$

where

$$R = \text{Cooling Rate } (^\circ\text{C}/\text{sec}) \quad (3.1)$$

$$T_0 = \text{Preheat Temperature } (^\circ\text{C})$$

$$H = \text{Heat Input (kJ/mm)}$$

- Heat input³

$$H = \frac{60 EI}{1000 S}$$

where

$$H = \text{Heat Input (kJ/mm)} \quad (3.2)$$

$$E = \text{Arc Voltage (Volts)}$$

$$I = \text{Current (Amps)}$$

$$S = \text{Travel speed (mm/min)}$$

²Funderburk 1999.

³Ibid.

The cooling rate can have a great influence on the microstructure of stainless steel alloys⁴. Because the microstructure greatly determines the structural properties of the material, it is important to get insight into the cooling rate. As equation 3.1 shows, the cooling rate depends on the heat input and preheat temperature. Consequently, in the MX3D printing process, the cooling rate is determined by the welding parameters, the time inbetween subsequent depositions of weld metal and the geometry and properties of the underlying material. Additionally, the environmental conditions and controlled cooling methods will influence the cooling rate.

3.3 Influence of process on properties

In this section, firstly an overview will be given of different studies relating process parameters to weld properties. This will give insight into the parameters that are being observed in relation to certain structural properties. Secondly, some of these researches will be selected and investigated to study the influence of input parameters on output properties. General trends or the lack thereof will be described.

3.3.1 Overview of studies

Benyounis and Olabi have presented a reference guide with regard to the “optimization of different welding processes using statistical and numerical approaches”⁵. As such, it is a great starting point to compare researches and choose the most relevant input parameters with regard to the studied output. Generally, the following output features of a weld can be distinguished according to Benyounis and Olabi, p.483:

- Weld bead geometry
- Mechanical properties
- Distortion

All of the outputs shown in table 3.1 can be assigned to one of these groups. It should be noted however that these groups are interdependent. The weld bead geometry for example is of influence the mechanical properties, according to Connor⁶.

Table 3.1 gives an overview of the GMAW prediction models mentioned by Benyounis and Olabi and their input and output. The ‘workpiece’ parameter is introduced as a collective term for inputs that describe the base material that is being welded on, e.g. the thickness of the base plate or the kind of edge preparation.

It is interesting to note that in none of these researches, cooling rate or preheat temperature have been addressed directly; no direct measures were taken to influence these parameters. Some other parameters seem to be present in nearly all of these models: voltage and welding speed. Others, such as material thickness and gap width are introduced depending on the type of workpiece that is being studied. In all cases, one or more of the following other parameters is used as input: current, wire feed speed and contact

⁴Elmer, Allen, and Eagar 1989.

⁵Benyounis and Olabi 2008.

⁶Ibid., p.484.

⁷Benyounis and Olabi 2008.

Research	1	2	3	4	5	6	7	8	9	10	11	12	13
Input													
Voltage	x	x	x	x	x	x	x	x	x	x	x		
Welding Speed	x	x	x	x	x	x	x		x	x	x	x	
Current		x		x			x	x	x				
Wire feed speed	x		x		x	x	x	x		x	x	x	
Nozzle distance	x					x	x	x					
Pulse frequency							x						
Gas flow rate							x						
Workpiece				x	x	x			x	x			
Number of runs										x		x	
Output													
Bead width	x	x	x	x	x			x	x		x		x
Bead height	x	x	x	x	x			x	x	x	x		x
Penetration	x	x	x	x			x	x			x		
Deposition efficiency											x		
Dilution	x			x									
Bag Length				x									
Tensile strength							x						
Shear strength							x						
Distortion											x	x	

Table 3.1: GMAW process parameters⁷

¹=Murugan and Parmar; ²=Kim et al.; ³=Kim et al.; ⁴=Chan et al.; ⁵=Christensen et al.; ⁶=Allen et al.; ⁷=Koganti et al.; ⁸=Nagesh and Datta; ⁹=Lee and Um; ¹⁰=Kim et al.; ¹¹=Correia et al.; ¹²=Murugan and Gunaraj; ¹³=Casalino et al.

tip-to-workpiece distance. Often in GMAW processes, the current is not directly controlled by the welder, but indirectly by the wire feed speed and contact tip-to-workpiece distance⁸. The selection of parameters is up to the researcher and should be based on the relationships he wants to describe.

Other researches have been described to predict mechanical properties such as yield and tensile strength and percentage elongation. These researches do not deal with GMAW specifically, but with different welding techniques. However, they do prove such models can be made.

Xiong, Zhang, Hu, et al. used RSM and ANN to predict weld bead geometry in GMAW-based additive manufacturing⁹. The input parameters were wire feed speed, welding speed, voltage and nozzle-to-plate distance, while the output consisted of bead width and height. This seems to be in good correspondence with the overview given in 3.1.

3.3.2 Property Prediction

Various methods are available to predict the non-linear effects of welding parameters. These methods are often used to optimize the welding processes, but have also been implemented to give direct feedback to a welding machine, improving control over the weld features¹⁰. Additionally, they could be applied in a parametric design, in which printing strategy and structural properties, as well as structural and architectural considerations are incorporated.

⁸TWI 2014b.

⁹Xiong, Zhang, Hu, et al. 2014.

¹⁰Ibid.

Benyounis and Olabi and Xiong, Zhang, Hu, et al. mention factorial design, linear regression, response surface methodology, artificial neural networks, the Taguchi method and genetic algorithms. Each of these methods has their own specific strengths and challenges. Response surface methodology is a very good option, because it requires only short computational time, is easy to understand, has a very high optimization accuracy level and software is readily available. This method performs better than other techniques when a large number of experiments are not affordable¹¹. Artificial neural networks may ultimately be better at predicting properties¹², but because of the use of hidden layers, little insight is gained into the effects of changing a certain parameter on the properties. Moreover, they require more computational time, making them less suited to application in a parametrized design process in which computationally heavy models are used.

Not only can these methods be used to optimize the process, but also to provide adaptive control during fabrication. The latter is essential in order to provide a controlled level of quality and to make the AM technique accessible to a layman. The development of such a method is not part of this thesis, but should definitely be considered for future research. Standardization of these methods may ultimately lead to a sort of quality control system comparable to the WPSs and WPQRs in ordinary welding.

3.3.3 Direct process effects

Many different studies have underlined the non-linear influence of process parameters on the weld properties and the difficulties in creating prediction models¹³. Direct effects can only be studied when other parameters are kept constant. These indoor experimental settings do not represent the welding process in practice, in which often the environment and the process inputs cannot be accurately controlled. Statements with regard the influence of a certain input parameter on output properties should therefore be approached with care. However, they do provide some insight and can act as guidance to improve the welding process, so an attempt is made to describe them in this section.

Murugan and Parmar have created different curves illustrating the influence of parameters on the weld bead geometry of stainless steel surfacing, describing both direct and interaction effects. The direct effects of higher voltage are: greater penetration, lower reinforcement, greater width, and greater dilution. Higher feed rate results in: increase in penetration and reinforcement, increasing dilution to an optimum and then decreasing, while width is unaffected. Increase in speed results in: decrease of penetration, reinforcement and width, while dilution is pretty much unaffected. Nozzle to plate distance increase results in: decrease of penetration, width and dilution; increase of reinforcement¹⁴. These correlations make sense when they are related to the heat input, as described in equation 3.2, and its influences on geometrical properties. The higher the heat input, the more material is molten, increasing the penetration and dilution. Additionally, because of higher heat input, the cooling rate will be lower, which means the weld material solidifies more slowly, giving it time to flow outwards, increasing width and decreasing reinforcement height. This is in agreement with the findings from Murugan and Parmar.

Since the cooling rate is affected by a change in heat input, the microstructure and thus the mechanical properties of the weld material will change. Quenching, the rapid cooling of a workpiece is meant to harden the workpiece and increase its strength. Slower cooling, associated with higher heat inputs, is expected to have the opposite effect. Indeed,

¹¹Benyounis and Olabi 2008, p.493.

¹²Xiong, Zhang, Hu, et al. 2014.

¹³Benyounis and Olabi 2008; Suryakumar et al. 2011; Xiong, Zhang, Hu, et al. 2014; Nagesh and Datta 2002; Xiong, Zhang, Gao, et al. 2013; Murugan and Parmar 1994.

¹⁴Murugan and Parmar 1994.

for a certain heat input range in the SMAW process, Funderburk describes the effects of an increased heat input (leading to a decrease in cooling rate) on material properties accordingly: decrease in yield strength, tensile strength and hardness, and increase of percent elongation.

Casagrande, Cammarota, and Micele have successfully related Vickers hardness and defect areas to fatigue strength of steels. The Vickers hardness appears to be proportional to the fatigue limit¹⁵. However, defects or crack initiation sites greatly influence the fatigue strength, and are expected to be of main importance to MX3D rods. Nevertheless, the direct influence of process parameters on hardness and thus fatigue strength has been included in table 3.2.

	Geometry		Microstructure			Strength			Ductility
	W	R	P	Di	H	Y	T	F	Du
Voltage	↑	↓	↑	↑	↓	↓	↓	↓	↑
Current	↑	↓	↑	↑	↓	↓	↓	↓	↑
Wire speed	—	↑	↑	↑↓	↓	↓	↓	↓	↑
Welding pulse time	↑	↑	↑	—	↓	↓	↓	↓	↑
Cooling time	↓	↑	↓	↓	↑	↑	↑	↑	↓
Nozzle distance	↓	↑	↓	↓	↑	↑	↑	↑	↓
Layer height	↓	↑	Perhaps similar to nozzle distance						
Rod angle	Possibly anisotropic effects								

Table 3.2: Direct process effects

W=width;R=Reinforcement; P=Penetration; Di=Dilution; Y=Yield strength; T=Tensile Strength; H=Hardness; Du=Ductility

These expected general trends have been summarized in table 3.2 for the MX3D process. Note that gas flow rate has been excluded from this table. This parameter will affect the weld pool, but no description of direct effects has been found in the literature. Furthermore, in the MX3D process it will be kept constant. The effects of layer height and rod angle, properties specific to the technique which are not described in literature, on the properties are based on observations of the MX3D process.

3.4 Summary

The most important structural properties have been identified, and the possible direct influences of process parameters have been described and summarized in table 3.2. However, the description of the actual relationship between process parameters and properties requires non-linear models, complicating the optimization of the AM process. In this thesis, a qualitative judgement is made about the way the process parameters affect the structural properties. This judgement may be the basis for quality control of MX3D produced structural parts, analogous to a WPS and ordinary welding. Further research and non-linear modelling may set further guidelines to control the process.

¹⁵Casagrande, Cammarota, and Micele 2011.

Chapter 4

Tests and measurements

4.1 Process measurements

The welding parameters and robotic parameters can simply be recorded during the process. Derivatives of these parameters, such as the cooling rate, have to be measured using special equipment. Thermocouples or infrared temperature sensors can record the thermal history during manufacture. If these direct measurements are lacking, the cooling rate could be deduced as a function of heat input, preheat temperature, material thickness, specific heat, density, and thermal conductivity¹, possibly supported by finite element modelling of subsequent material deposits. However, there are many unknown factors in such models. These factors, such as radiation, convection, environment temperature, moisture, air composition etcetera can never be controlled in practice.

Detailed on-line measurements of the thermal history are essential in order to understand how the material is formed and to find out how to improve the production process. Since the focus of this thesis is on structural properties rather than improvement of the production process, these measurements will not be performed within this research. However, it is highly recommended to perform such measurements in future research.

4.2 Geometry

To get a good idea of the shape of a rod, measuring methods have to be selected or developed. The length of a rod can be determined relatively easy. An average cross-section may be deduced from its density, weight and length. This manual measurement is discussed first. In this case, however, the variation of the cross section along its length is not taken into account. Secondly, two more detailed measuring methods are addressed that are based on photography.

4.2.1 Manual measurements

Archimedes

Assuming that the density of the produced specimens is known, their average cross section can be determined from their length, mass and density as follows:

$$A_{\mu} = \frac{\rho \cdot l}{m} \quad (4.1)$$

Sandmeyer steel provides a density of 7,90 g/cm^3 for steels 316 and 316L². 316LSi may be slightly different because of its different alloying constituents. In order to find out the actual density, Archimedes' principle can be applied. By submerging a rod into fluid, its volume can be measured by measuring the volume that is being displaced. If the mass is measured using an accurate scale, and divided by this volume, the actual density is found.

¹Funderburk 1999, p.2-3.

²Sandmeyer 2015.

Vernier caliper

The outer diameter of a rod at a specific location can be measured using a vernier caliper. Although this measurement itself is quite accurate, it is one-dimensional, while the geometry of the rod is in fact three-dimensional. Therefore, this measurement can only give a rough estimate of the cross section; when multiple measurements are done it can give a general idea of the variation in cross section.

The accuracy of the vernier caliper depends on the type of instrument used. When the diameter is read visually, the measurement is accurate to 0,05 mm. With a digital vernier caliper, the accuracy can be increased to 0,01 mm.

4.2.2 Photogrammetry

Using photogrammetry or structure from motion, 3D models can be built from photos. This is an exciting technique that can be an accessible and low-cost alternative to high-tech laser scanning. By analysing strategically taken photographs, computer software can build a 3D model of an object. It is based on a principle called parallax, the apparent shift of an object when it is viewed from different angles. This effect, which is used by our brain to perceive depth, can be easily observed by alternately closing one eye while looking at a nearby object. In the same way, the software interprets depth by comparing photos, identifying identical points and registering the parallax, locating the point in 3D space. When sufficiently many photos are taken from different angles, a point cloud can be generated from which the object may be reconstructed as a 3D model.

Many different photogrammetric software packages are available, some of which are available for free. Since there is no budget for such applications and the results of this study should be easily replicable, only free or commonly available applications will be used. Hence, commercial alternatives such as Photomodeler, Agisoft and acute3d will not be considered. In the following sections two photogrammetric methods will be discussed and compared: Autodesk's 123D Catch and a combination of Visual SFM and Meshlab.

Photogrammetric methods

123D Catch is a free tool provided by Autodesk that automatically generates 3D, textured models from a set of photos. This tool is very easy to use and even has a smartphone application. It is cloud-based, meaning that all images are hosted and analysed on-line. Therefore, this technique requires no computational power from the user's workstation. However, this tool does have its downsides. Because all computations take place in the cloud, there is no user control over the way the photos are analysed and the level of detail of the model that is generated. In fact, the photos are being downsized, limiting the detail of the 3D mesh. Furthermore, the number of photos cannot exceed 70³. The level of detail and reproducibility of 123D Catch models have to be studied in order to find out if 123D Catch is a suitable tool. Smart3DCapture Free edition is a different application based on the same technology, for which the same problems hold.

To find out the capabilities of this software package, a total of 35 photos has been taken of a sample rod from different angles. These photos were then uploaded to the Autodesk server and a model was generated. A visual comparison between the model and actual sample can be seen in figure 4.1. An examination of both outlines reveals quite a good match and level of detail. Many of the irregular features of the actual rod are also observed in the 3D model. Some details are not registered, though. The small piece of welding wire that is marked by the small red circle is absent in the 3D model. This does not seem to be just a result of its small size, since similarly sized features can be

³Spielman 2013.

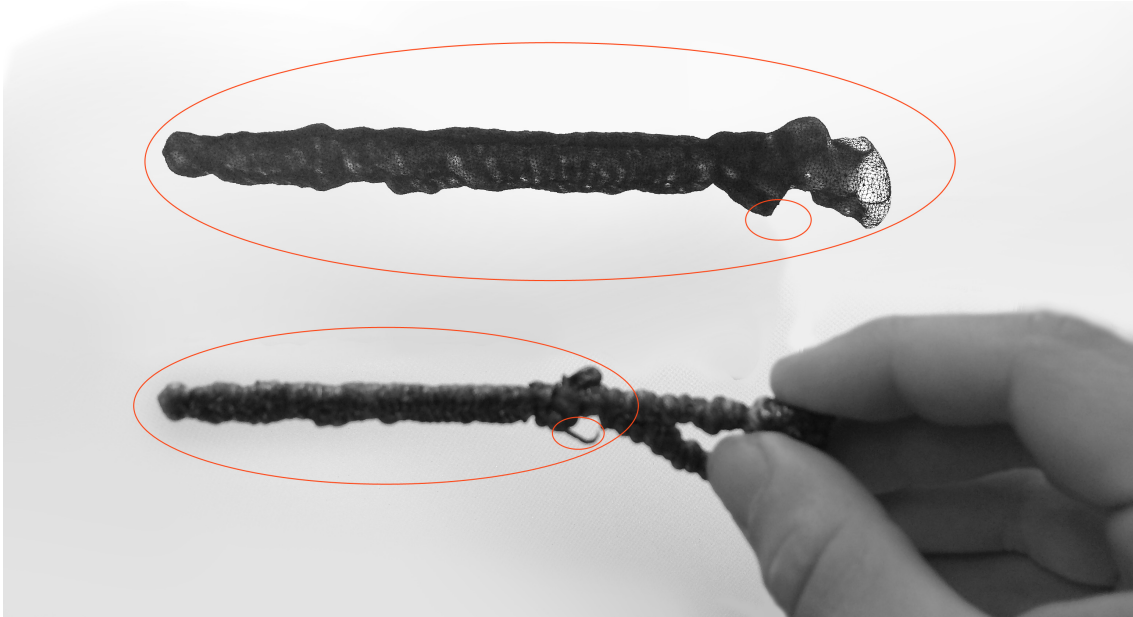


Figure 4.1: Visual comparison of photogrammetrical 123d catch model and actual rod

distinguished on the rest of the rod. Perhaps the photography strategy was not suitable to register this feature; maybe insufficient data points were acquired to build it in 3D. Here, the downsides of 123D catch become apparent: there is no control over and insight in the way the model is produced.

An alternative that allows for a lot of control and removes the black box nature of 123D catch can be found in a combination of softwares Visual SFM and Meshlab. These programs allow for the composition of highly detailed 3D photogrammetrical models. To test this method and compare it to 123D Catch, the same 35 photos were used. Three of these photos were not used to assemble the model because of blurriness. The results of this method turn out to be more detailed, registering more of the small irregular features of the rod. The model, after import into Rhinoceros, is shown in figure 4.2a. This model

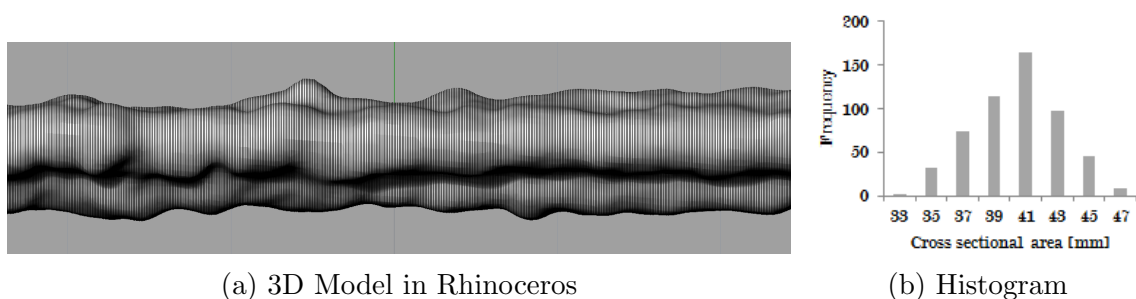


Figure 4.2: Visual SFM + Meshlab model in Rhinoceros and Excel analysis

can then be sliced into any wanted number of cross sections, indicated here by the black vertical lines. Using a script, these cross sections are created, their area measured and the data exported to an excel file. This data can be further analysed, extracting histograms and fitting distributions, see for example figure 4.2b. The workflow of the Visual SFM + Meshlab method is described in more detail in appendix B.1.

Accuracy

The accuracy of these photogrammetrical methods should be evaluated by comparing their results to manual measurements and possibly other calibrated photographic or 3D scanning methods. The more photos and the higher the resolution, the greater the accuracy of the method.

4.2.3 Photographic method

The manual measurement using a vernier caliper is accurate, but very time consuming if one wants to take many measurements in order to get an accurate description of the variation in cross section. What this instrument does in fact is measure the outline of a rod at a certain point. By taking a photo of the rod and analysing it on a computer, this outline can be measured much faster at many different points. Appendix B.2 shows this workflow. The result is two-dimensional. By rotating the test piece, taking more photos and combining the results, a more accurate description of the rod in three dimensions can be achieved. The different camera positions and an example of one such contour photo can be seen in figure 4.3.

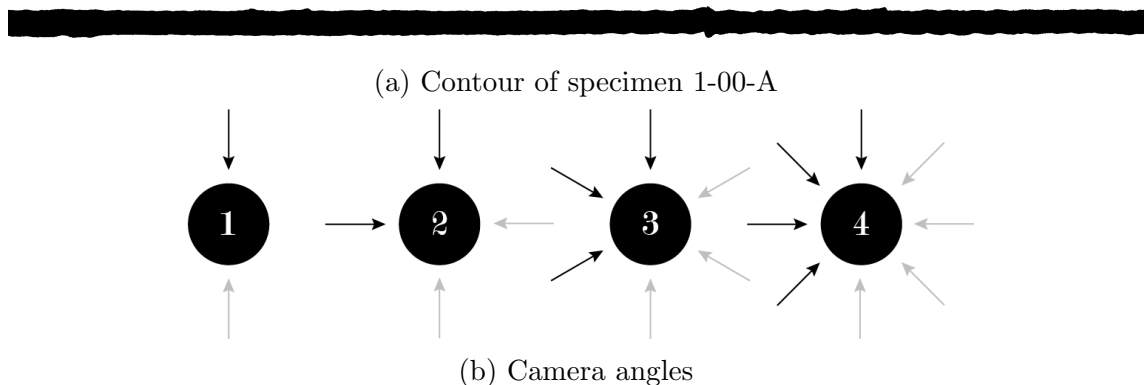


Figure 4.3: Contour photos

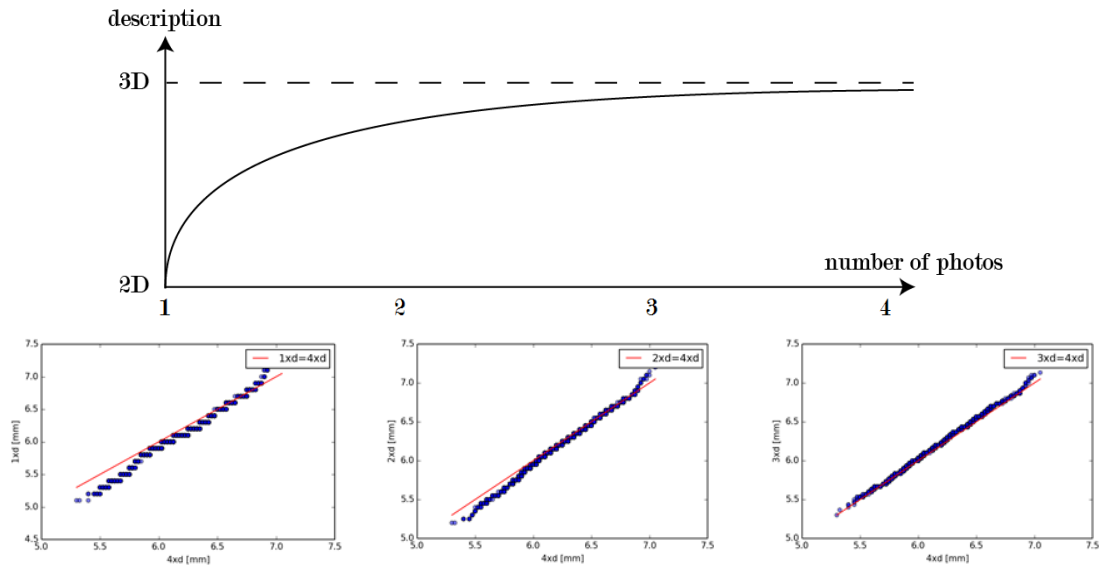
Number of photos and accuracy

For the second batch of test pieces, the diameter was described using one, two, three, and four photos. These descriptions were compared to each other using scatterplots to study the increasing accuracy. This comparison showed a marginal increase in accuracy when three or more photos were used, see figure 4.4. The red line indicates an exact match to four photos.

The accuracy of a single diameter measurement is limited by the number of pixels of the photo. The higher the resolution of the photo, the higher the accuracy of the measurement. Within this research, all photos were scaled down so that 1 pixel represented 0,1 mm.

Calibration

Comparison of measurements with this method to vernier caliper and photogrammetrical measurements, initially showed the need for calibration of the measurements, see appendix C.2.2. The photographic method underestimated the diameter by about 0.3 mm. At a later stage, however, it was discovered that this error was due to an oversensitivity of the Python script in combination with the file compression of the black and white images. The JPEG compression that was applied to the black and white contour images, resulted in images



(a) Scatterplots of 1, 2, and 3 photos compared to 4

Figure 4.4: Increasing accuracy of photographic method

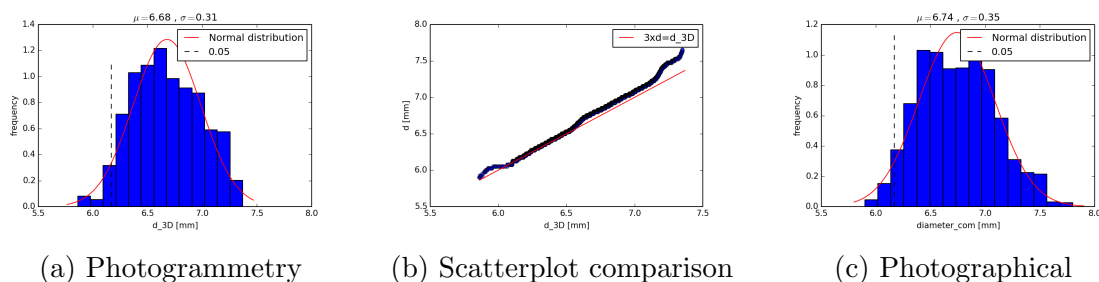
that were not completely black and white. Black pixels at the edge of a rod were actually turned into very dark grey pixels, and white pixels turned into light grey ones. Since the script was set to detect pixels that were exactly black, the grey pixels were left out, resulting in an underestimation of the diameter. By adjusting the threshold, this problem was eliminated, and diameter values corresponding to vernier caliper measurements were found.

Since the photographic measurements are dependent on the camera and the subsequent photo processing and analysis, it is recommended that these photographic methods are always verified by performing spot checks using a vernier caliper.

For the comparisons between different test pieces within one research, the calibration is not relevant. However, it should be taken into account when determining structural properties or when performing quality control.

4.2.4 Comparison

Previously, it was shown that from three contour photos, no significant increase in the description of the averaged diameter was found. This suggests an accurate description of the 3-dimensional geometry. In figure 4.5 the results from both methods are related through a scatter plot.



(a) Photogrammetry

(b) Scatterplot comparison

(c) Photographical

Figure 4.5: Comparison of photogrammetrical and photographic methods (2-60-C)

The red line in figure 4.5b represents a perfect fit between the methods. The data follows this line very nicely, indicating a good match, which means that the photographic method gives a good description of the cross-sectional area.

4.2.5 Summary

In this section a number of different measuring methods have been discussed. Photogrammetrical methods can give three-dimensional results, but are time consuming. These should only be used when a very accurate description of a test piece in three dimensions is required, e.g. as a comparison to simpler methods or for a benchmark FEM model. The photographic method is simpler and faster than photogrammetry, but is not truly three dimensional. Lastly, manual measurements cannot accurately describe the geometry of the test pieces, but are essential in verifying the rightness of the more complicated measurement forms.

4.3 Mechanical Properties

The results of the chosen test method need to contain the right information to study the selected structural properties: strength, stiffness, ductility and fatigue resistance. Some test methods are:

- Hardness test
- Charpy impact test
- Tensile test
- Buckling test
- Bending test
- Fatigue test

4.3.1 Hardness test

According to Smith et al., hardness tests are the most commonly executed type of mechanical tests, because they can be simply and rapidly performed at low costs while being nondestructive in nature⁴. The hardness of a material is a measure of its resistance to plastic deformation caused by an indenter pressed into its surface. Although the hardness of a material is related to properties such as yield or fatigue strength, this relationship can only be deduced experimentally, not analytically⁵. Hardness tests can be of great value to get quick insight into how different test pieces compare to each other, but additional testing has to take place to find out the actual strength, stiffness, ductility and fatigue properties, and to describe the correlation.

Over the years, different hardness tests have been developed. In order of time of invention, these are the Brinell, Rockwell, Vickers and Knoop hardness tests. Each of these tests has their own specific advantages and disadvantages related to the method. Out of these four, the Vickers hardness test is the most advanced method that is described in European standards. Moreover, the department of Materials Science and Engineering at Delft University of Technology has the equipment and experience to perform this test.

⁴Smith et al. 2006, p.302.

⁵Hirano, Sakane, and Hamada 2005; Takakuwa, Kawaragi, Soyama, et al. 2013.

Therefore, the Vickers method is the prime candidate for hardness testing both from a technological and a practical point of view.

With microhardness testing, different microstructures in a micrograph can be related to different structural properties.

4.3.2 Charpy impact test

To study whether a material will behave brittly or ductilely at a certain temperature, a Charpy impact test can be performed. A notched specimen is hit with a hammer swinging like a pendulum. The amount of energy that is absorbed in the impact is a measure for the resistance to fracture⁶. As described in section 4.3.3, ductility can also be investigated in a tensile test. However, some materials that behave ductilely in a tensile test, may behave brittly under impact testing. This is especially true for ferritic steels, which show a relatively high ductile-to-brittle-transition temperature (DBTT). At this temperature, the behaviour of the material changes from ductile for higher temperatures to brittle for lower temperatures⁷. For these kinds of materials, Charpy impact testing is a very valuable test method.

The materials considered in this research are known to be mainly austenitic and possess good notch toughness, see chapter 2. Furthermore, they will be applied in the moderate climate of the Netherlands, so they will not be exposed to extremely low temperatures. For these two reasons, the Charpy impact test is not expected to yield any more relevant results than a tensile test in the context of the AM bridge case.

4.3.3 Tensile test

A tensile test will cover the entire stress-strain diagram and will thus give great insight into yield strength, tensile strength, axial stiffness and ductility. When performing a tensile test, however, the specimens used are usually of a very particular shape. They are machined in such a way that they are wider at the ends, so that the specimen can be clamped at the ends and will fail in the middle. This would complicate the printing process and require very accurate machining. A possible way of producing such test specimens is shown in figure 4.6.

ISO describes different testing methods and types of test pieces. Interestingly, they mention the possibility to test specimens unmachined, if required⁸. Testing the specimens unmachined without transition radii and widened ends simplifies the rod production a great deal. However, because of the constant shape, it may be that some of the unmachined specimens will fail at one of the clamps, rendering the results of these test useless. The advantages of simpler production, however, greatly outweigh this downside. With ease, some extra specimens can be produced and tested if required.

⁶TWI 2015b.

⁷Smith et al. 2006, p.343-344.

⁸ISO 2009, p.43.

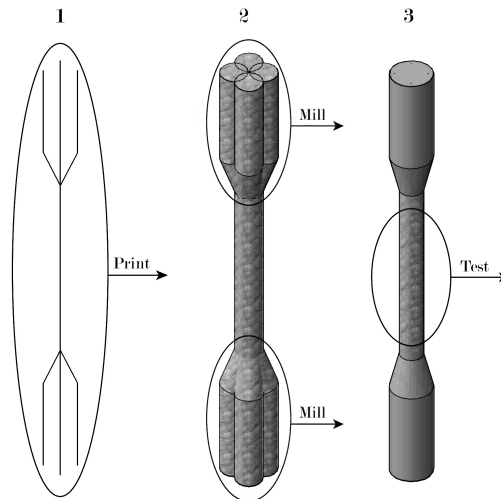


Figure 4.6: Proposal for test specimen build up (1=line model, 2=printed specimen, 3=printed and milled test specimen)

4.3.4 Buckling test

Buckling is a form of instability that can occur in members that are under compression. By reversing the tensile test setup, compressive forces can be applied on a test piece. By slowly increasing the force on the test piece, the moment at which it becomes unstable and buckles can be studied. The buckling load found in this test may then be compared to the one that is derived theoretically. This may result in a sort of buckling curve or general reduction factor to take into account the irregular test piece geometry.

The curves that are used to determine buckling capacity in the Eurocode and in the Design Manual For Structural Stainless Steel⁹ are based on the Ayrton-Perry formula. The ESDEP lectures explain how the Ayrton-Perry formula is derived and how the European buckling curves are constructed from this derivation¹⁰.

Equation 4.2 is the expression for the design buckling load $N_{b,Rd}$ in Eurocode 3.

$$N_{b,Rd} = \chi A f_y / \gamma_{M1} \quad (4.2)$$

γ_{M1} is a partial factor that is used in Eurocode 3 and the Design Manual for Structural stainless steel to achieve an accepted level of safety. For members checked for instability $\gamma_{M1} = 1,1$ ¹¹. In order to guarantee the same level of safety for the material investigated in this thesis, a different value may have to be used. This requires extensive statistical research that is not part of the scope of this thesis. Therefore, for now $\gamma_{M1} = 1,1$ is used.

f_y is the yield strength of the material, defined as $\sigma_{0,2}$ for stainless steels. A is the area of the cross section. χ is a reduction factor that is based on the Ayrton-Perry derivation, see equation 4.3.

$$\chi = \frac{1}{\phi + (\phi^2 - \bar{\lambda}^2)^{0,5}} \leq 1 \quad (4.3)$$

in which:

$$\phi = 0,5 (1 + \alpha (\bar{\lambda} - \bar{\lambda}_0) + \bar{\lambda}^2) \quad (4.4)$$

⁹SCI 2006.

¹⁰ESDEP 2015.

¹¹SCI 2006, p.6.

$$\bar{\lambda} = \sqrt{\frac{Af_y}{N_{cr}}} \quad (4.5)$$

N_{cr} is the Euler buckling load $\frac{\pi^2 EI}{l_{buc}^2}$. The generalized imperfection factor α takes into account all relevant defects, including geometric imperfections, eccentricity of applied loads and residual stresses in one single value. Therefore, α values are specific to a certain type of construction element. The limiting non-dimensional slenderness $\bar{\lambda}^2$ limits the reduction factor χ to 1,0 for small slendernesses. Below this non-dimensional slenderness, defects do not reduce the buckling load. This value is also dependent on the type of element.

Buckling test results can be related to this Ayrton-Perry based formula and compared to existing buckling curves. If the existing buckling curves do not adequately describe the buckling behaviour of the tested specimens, a new buckling curve may be developed based on adjusted α and $\bar{\lambda}^2$ values.

By definition of buckling, the yield stress is reached in the outer fiber of the element, resulting in plastic deformation. In practice, however, plastic deformation can be prevented by stopping a buckling test when the buckling load is reached. Thus, buckling test pieces can be tested more or less non-destructively, especially in the case of high slendernesses. If required, the test pieces can subsequently be submitted to other types of tests. In the case of tensile tests, any plastic deformation will only be of influence on the shape of the stress-strain diagram of the material; the ultimate stress will be unaffected.

What is further important in this test is to set the right boundary conditions. A pin-ended set-up is the easiest to analyse and model theoretically, but harder to carry out in practice than a clamped set-up. The connections at the ends of test piece have to be made such, that the test piece is completely free to rotate, while horizontal displacement is prevented. Special equipment would be necessary to set this up. From a practical point of view, a set-up with fixed ends is preferable. The tensile test set-up described before makes use of clamps that completely fix the test piece. This connection is so much stiffer than the test piece itself that it is assumed to be completely fixed.

4.3.5 Bending test

A bending test will only show the first part of the stress-strain diagram, since the tensile strength is not expected to be reached. Important structural aspects such as yield strength, bending stiffness and deformation capacity can be investigated in a bending test, though, and they can be compared to results from the tensile tests. A four-point bending test can be carried out rather easily. Single rods can be used straight from the printer. They may only have to be prevented from rolling or moving sideways. In a four-point bending test, the part of the rod in between the applied forces can be studied under influence of a bending moment only.

4.3.6 Fatigue test

There are multiple handbooks, standards and codes that describe how to perform a fatigue test¹². The fatigue tests will be performed using the same equipment that is used for the static tensile tests. In static tests, the rough surface of the specimens is not much of an issue. In fact, the rough surface will only increase the grip of the clamps. This surface roughness, however, will give rise to local high stress concentrations which may initiate a fatigue crack in the clamped zones, leading to premature failure of the specimen. This is a highly unwanted situation, because the results of such a test will have to be discarded

¹²ASTM 1963; ISO 2012.

and another long-lasting fatigue test will have to be performed, wasting time, money and material. Therefore, the specimens will have to be designed to prevent failure in the clamped zones. A dogbone shape could be one solution, see figure 4.6. As mentioned before, this would require complicated printing and machining procedures. Ideally, the printed shape would be designed so that extensive machining is not necessary. With a large clamped surface area, the stress concentrations may be reduced sufficiently to prevent crack initiation at the clamps. Simple grinding of the ends may further reduce stress concentrations. Nevertheless, the printing procedure would be complicated compared to a straight rod and the prevention of premature failure is uncertain. Another possibility is to produce a rod and fix it inside blocks on either end using a resin. This option is expected to minimize stress concentrations at the clamps and will allow for the printing process to remain simple. On the other hand, production of these blocks and the selection and application of resin pose their own challenges.

4.4 Microstructure

4.4.1 Micrography

One of the simplest ways to investigate microstructure is by making an optical micrograph. In this case, the microstructure is investigated through an optical microscope, and areas of interest are photographed. Before studying the sample under a microscope, however, it needs to undergo a series of processing steps.

Firstly, the area of interest has to be identified and cut from the base material. It is important that this cutting is done with a suitable abrasive, in order to prevent any microstructural changes to the sample. When cut, the sample is usually mounted in some sort of resin to ease the following processing and analysing steps.

Secondly, the sample is sanded and subsequently polished smooth. This is done in several steps, and with each step the coarseness of the abrasive is decreased. Thus, the medium particle size is gradually lowered from the order of 100-200 microns to about 1 micron. The required smoothness of the final polishing step depends on the material itself as well as the type of analysis that it will undergo.

When the surface is polished smooth, it can be chemically etched using a suitable etchant. This etchant reacts with the microstructure in the cross section. Depending on the orientation of the crystals and the composition of the alloy, the chemicals react differently with the microstructure, revealing or enhancing specific features that otherwise would not have been visible. The selection of an etchant should be based on the composition of the material and the microstructural features that are of interest.

Besides chemical etching, which is the most widely used etching technique, other techniques such as electrolytic etching can be applied¹³. In this case, however, chemical etching is expected to suffice.

4.4.2 EBSD

Through micrographs and etching, the grain orientation can be observed visually. Electron BackScatter Diffraction (EBSD) is a method to determine texture and orientation quantitatively. When an electron beam is fired at a point on the surface of a sample it is reflected back at a changed intensity depending on the orientation of the grain. By measuring this change in intensity of the reflected beam, the orientation of the grain can

¹³Zipperian 2011, p.140.

be described. Pole figures can be plotted to compare the orientations of multiple points to a reference coordinate system¹⁴.

4.5 Sample sizes

Choosing the right sample size is an important aspect when it comes to testing. A larger sample size will increase the accuracy and relevance of the results, but will also take more time to process. Assuming a normal distribution, the sample size can be determined for a certain desired confidence interval. Dekking describes how to do so using equation 4.6¹⁵.

$$n \geq \left(\frac{2z_{\alpha/2}\sigma}{w} \right)^2$$

where:

$$n = \text{size of sample} \tag{4.6}$$

$$z_{\alpha/2} = \text{z-test for desired confidence level } 1 - \alpha$$

$$\sigma = \text{standard deviation of measurements}$$

$$w = \text{width of confidence interval}$$

The apparent problem when using equation 4.6 to compute the number of required samples is the determination of the standard deviation. No prior tests have been performed on MX3D structures whatsoever, so there is no way to infer the order of magnitude of the standard deviation from previous results. All that can be done is to make an educated guess.

Often in literature a sample size of at least 30 is suggested, because from that size on, the Student's t-distribution matches the normal distribution very closely¹⁶. From a practical point of view, however, this is not feasible. Producing, testing and analysing 30 specimens per test would simply take too much time. Particularly fatigue testing is a big issue due to the many load cycles.

The minimum number of tests to determine any kind of statistical spread is two, but even slightly higher numbers will greatly increase the accuracy of the results. Figure 4.7 shows plots of the required number of samples related to confidence interval width for different values of σ . Indeed, the largest improvement in accuracy is observed in the lower range of sample sizes. The difference between sample sizes of 2 and 10 is much greater than the difference between sizes of 10 and 100, but it should be noted that this is greatly dependent on the standard deviation.

In order to acquire accurate statistical data, large sample sizes are required. This thesis aims to find out whether 3d printed metal, specifically stainless steel printed using MX3D, can be used in structural engineering and what challenges arise when this kind of material is used. Of course, it still holds that the more samples the more accurate the results, but smaller sample sizes will suffice within the scope of this thesis.

¹⁴Cambridge 2015.

¹⁵Dekking 2005, p.367-368.

¹⁶Lowry 2014.

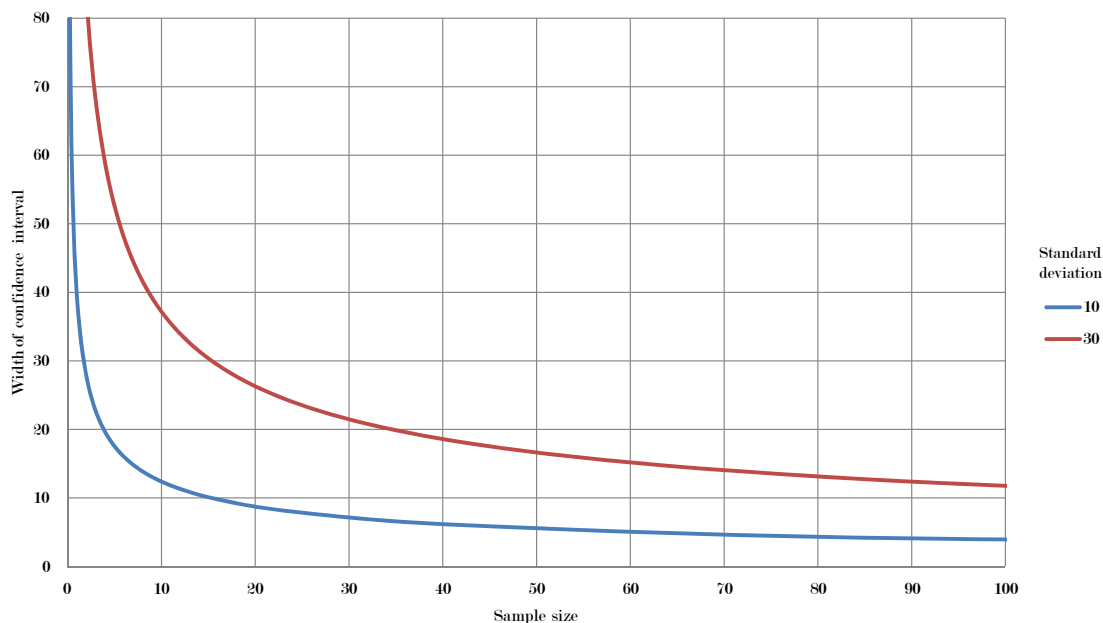


Figure 4.7: Sample size and 95% confidence interval for different standard deviations

4.5.1 Fatigue testing

Three methods of fatigue testing can be distinguished: standard tests, response tests and increasing amplitude tests. The former method is deemed the most suitable to determine an S-N curve, while the latter two methods are recommended to determine the long-life fatigue strength or the fatigue limit¹⁷. The constant amplitude standard tests can be further divided into two types: one in which a single specimen is tested at each stress level and one in which a group of specimens is tested at each stress level. Naturally, the type in which a group of specimens is tested at each stress level yields more accurate results and provides insight into statistical variability. The number of specimens necessary in this test can become very high, though. The ISO standard suggests a total of seven specimens per stress level for an exploratory experiment¹⁸. At four stress levels, this already amounts to 28 tests. When seven stress levels are investigated, each with ten or more specimens as recommended by ASTM, 70 tests will have to be performed. Such large numbers are not feasible within this Master's thesis study.

It is common practice to test 3 specimens per group at 3 different stress levels. Since no tests have been performed on MX3D rods before, a fourth stress level should be considered. This would mean that in total, $3 \cdot 4 = 12$ tests will be performed. Just to get a rough idea of how the material will behave, one specimen per stress level suffices. If desired, more tests can be performed to get more accurate data.

¹⁷ASTM 1963, p.9.

¹⁸ISO 2012, p.6.

Chapter 5

Test procedures

In the previous chapter, different test methods and their standard procedures have been described. The current chapter describes how these tests were set up specifically for this research.

In materials testing, it is common practice to machine or fabricate test pieces in such a way that failure occurs in a controlled area and geometrical inaccuracies are eliminated. Whilst in this case control over the failure area is desired, the elimination of geometrical inaccuracies is not. The geometrical deviations are an inherent property of the material and are a fact that needs to be dealt with in the structural design. Therefore, special attention is paid to the shapes of the test pieces.

Secondly, the number of specimens that is envisioned to be tested is discussed. This number is based on an assessment of accuracy and relevance of the results on the one hand, and on practicality on the other.

Lastly, the test itself is described, explaining the way of measurement, force introduction, boundary conditions etcetera.

5.1 Static tensile testing

Static tensile tests were performed on a number of different rods, produced with different parameters.

5.1.1 Specimen shape

The tensile tests were performed on unmachined test pieces. In order to make sure that the pieces will fail in the desired area, viz. outside the clamps, somewhere within the measuring range between the clamps, the printing of widened ends was considered. However, it turned out that for static tensile testing, this was not necessary; failure never occurred directly at the clamps.

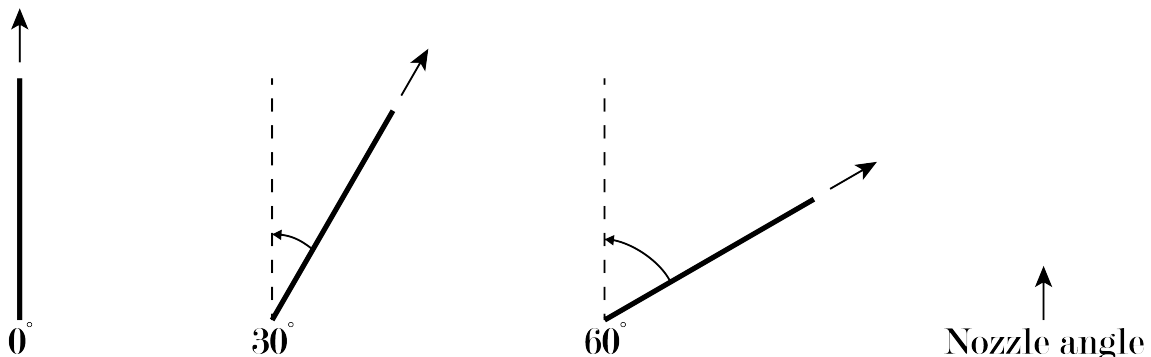


Figure 5.1: Test specimen production angles

The specimens are produced as straight printed lines at three different angles, see figure 5.1. Their length is 340 mm. When a small part is cut off for micrography, this

still leaves enough length to fit into the clamps in the existing tensile test setup, which are about 200 mm apart. Figure 5.2 is a photo of one such test piece.



Figure 5.2: Typical tensile test specimen

Additionally, some specimens will be milled and tested to find out what the effects of the geometry are. These specimens are produced by cutting an ordinary tensile test piece in half, and milling it down to a diameter of approximately 4 mm over a length of about 30 mm. One is shown in figure 5.3.

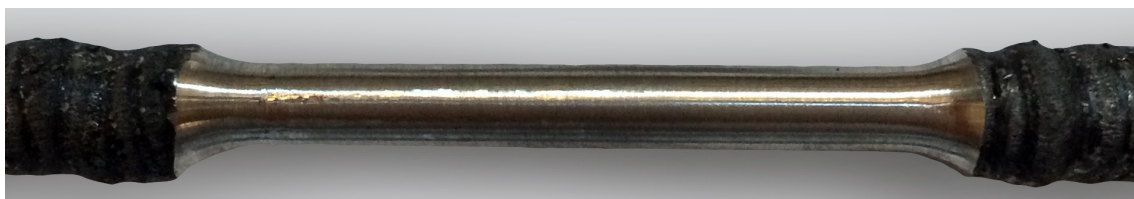


Figure 5.3: Milled tensile test specimen

5.1.2 Number of tests

At least three specimens are produced per set of parameters. In all of the batches, specimens are produced at three different angles. Therefore, each batch consists of nine specimens in total. If more accuracy is required, additional batches can be produced. For a more detailed description of these batches, see section 6.1.

The number of milled specimens is limited, because the milling requires expert technique, making the specimens costly. At least one at every angle should be produced, but two or more angle will give better insight in the spread of the results. This type is limited to one batch of specimens. By performing these tests, the geometrical variation is eliminated and the influence of the material itself on the structural properties can be studied. By comparing these tests to as printed specimens, the influence of the geometry on the structural properties can be investigated.

5.1.3 Test description

The static tensile tests were performed at the Stevin II Laboratory at the faculty of Civil Engineering of Delft University of Technology. A Dowty Rotel hydraulic tensile test machine was used. Image B.4 in appendix B.3 shows the test setup. At the top and bottom cylinders, hydraulic wedges are used to clamp the test specimen. The top cylinder stays fixed during the test, while the bottom cylinder is moved using hydraulic pressure, resulting in a certain force on the specimen. The test is displacement driven, i.e. the cylinder is being moved down at a certain prescribed speed in mm/s. The first part of the test, in which the material behaves more or less linear elastically, is carried out at a speed of 0.01 mm/s. When the material is in its plastic state, the speed is increased to 0.04 mm/s.

Measurements

This displacement cannot be used to accurately determine the elongation of the test specimen, because it is the displacement of the cylinder and thus includes deformations in the

entire setup, such as slip at the clamps. Therefore, extensometers measure the displacement over a certain range of the specimen in between the clamps. A special device is mounted to the test piece. This device consists of two fixings, clamped to the piece, that can move with the test piece as it elongates. This elongation is then registered by the extensometers, which can be used to calculate the mean strain over the measuring range.

5.2 Wire testing

5.2.1 Specimen shape

The wire that is tested is 1 mm in thickness and cut to about 300 mm in length to fit the tensile test setup. Because the wire is so thin, no machining can take place. Only part of the stress strain curve can be retrieved, because the wire will most likely fail at the clamps due to high stress concentrations.

5.2.2 Number of tests

Compared to the printed specimens, a wire test piece is very easily made. From a bigger roll, the test piece simply has to be cut to the required length. Analysis is also easier, because of its simple geometry. Therefore, the sample size can be increased. The first batch consists of six specimens. If the results give a reason to carry out more tests, the number of test pieces can be increased.

5.2.3 Test description

The test is performed in the same way as the tests on the printed specimens, see section 5.1.

5.3 Buckling tests

Basically, the buckling tests are performed by reversing the tensile test procedure, introducing a compressive force instead of a tensile one. Two rounds of testing with different test set-ups have been completed. The first round had a clamped set-up, investigating rods of different diameters at the same buckling length. The aim was to perform these tests non-destructively, so that the specimens could be used for both buckling and static tensile tests. In the second round of testing, a hinged set-up was used. The test specimens were fabricated at different lengths and used exclusively for buckling tests.

5.3.1 Specimen shape

The specimens used for the clamped tests are the same as the ones used for the tensile tests. The tested length L between the clamps, see fig 5.5a, is equal to 240 mm. The hinged specimens were produced at varying lengths, so that the effect of the slenderness could be investigated. The tested length of these specimens ranged from 109 mm to 237 mm. Either end of these specimens was grinded manually into a pointy tip, see figure 5.4. These tips fit into a small cavity on larger steel rods, which served as the hinge, see figure 5.6.



Figure 5.4: Hinged buckling test specimen

5.3.2 Number of tests

The first batch of specimens was only used for tensile testing. On batch 2 and 3 tensile test specimens, clamped buckling tests were performed, totalling 20 specimens. In batch 4, rods were produced solely for buckling tests. Eight 0° specimens were produced, four were produced at 30° and another four were produced at 60° .

5.3.3 Test description

Clamped set-up

The testing equipment is the same as for the static tensile tests. For this buckling test, however, no extensometers are attached to the test piece. The extensometers may increase the bending stiffness of the test piece, influencing the test results. Furthermore, they are not necessary to determine the buckling load. The point at which the test piece buckles can be judged from the force - cylinder displacement diagram and from visual observations.

The test piece is clamped at either end. Because the clamps and the test setup are much stiffer than the test piece, these connections are assumed to be fully fixed, which results in a buckling length of half the distance between the clamps. This is rendered schematically in figure 5.5a.

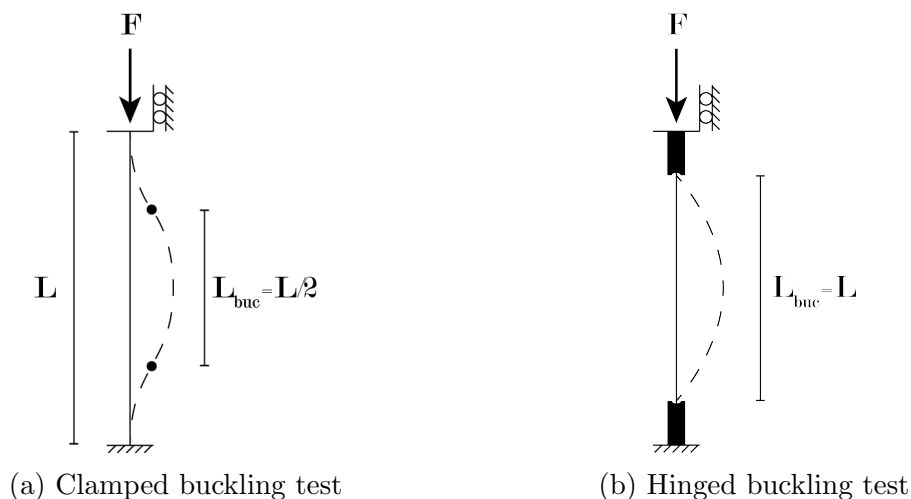


Figure 5.5: Types of buckling tests

By prescribing a small negative displacement of the cylinder, an increasing force will be exerted onto the test piece. Once this force reaches the buckling load, it will cease to increase, while at the same time the displacement keeps increasing. When this upper limit of the force is reached, the test is stopped in order to minimize permanent deformation and work hardening of the test piece, so that the test piece may subsequently be subjected to tensile testing. By definition, yielding occurs in the outer fiber of the rod when the buckling load is reached, but by stopping the test as soon as the buckling load is reached, plastic deformation is kept to a minimum. The cylinder displacement was set to 0.005mm/s . A load protection was set to minimize the force introduced as a result of the clamping.

Hinged set-up

The difference between the clamped and hinged set-up lies in the boundary conditions. In the hinged set-up, the rod is free to rotate at either end, which is schematized in figure 5.5b, while the actual test set-up is shown in figure 5.6. The buckling length is equal to the system length.



Figure 5.6: Hinged buckling test set-up

The procedure is identical to the clamped set-up. Again, the cylinder displacement was set to 0.005mm/s and the test was stopped as soon as the buckling load was reached.

5.4 Fatigue tensile testing

The ISO codes describes three different methods of fatigue testing, each aimed at obtaining certain data: testing to obtain fatigue life data, testing to obtain fatigue strength data and testing to construct an S-N curve¹. The first two test set ups are useful to verify whether a specific structure can cope with a certain applied fatigue load. They can provide accurate information about one stress level or fatigue life more easily than an S-N curve. The S-N curve, however, gives insight into the behaviour of a material over a greater range of stresses and fatigue lives. Therefore, the S-N curve test setup is most suited within the context of this thesis. If, for example, a certain detail of the actual design of the AM bridge case were to be evaluated, the first two methods would be a good choice.

According to the code, the most common fatigue response curves are either linear, or curvilinear². Commonly, S-N curves for stainless steel are described linearly, cut off at certain stress level, indicating the fatigue limit³. If this type of curve does not fit the plot well enough, a quadratic model can be considered. In this case, a general linear test should be used to evaluate the applicability of this quadratic model, as described in the ISO standard⁴.

¹ISO 2012, p.6-9.

²Ibid., p.9.

³Huang et al. 2006.

⁴ISO 2012, p.20.

In order to construct this curve, tests are performed at different stress levels. Because no prior research is available, the first stress level that will be investigated has to be an educated guess. Preferably, it should be a level somewhere in the middle of the SN curve, giving a good starting point to determine additional stress levels. A level that is too low will result in a great number of cycles to failure. A very high stress level on the other hand will result in premature failure. Neither of them gives a good indication of the other stress levels that should be investigated.

Based on the results from the first stress level, the next stress level is chosen as a proportion of this first level. Because the spread in fatigue lives is expected to be rather large due to the irregularity of the test pieces and because of the limited number of test pieces, this next level should not be chosen too close to the first stress level. If the results of the first two tests turn out to lie too far apart, an intermediate level can be chosen next. The stress levels chosen are based on the minimum diameters of the test pieces, because these levels are expected to be most indicative of the number of cycles to failure.

5.4.1 Specimen shape

Figure 5.7 is a photo of a typical fatigue test specimen. Fatigue cracks will form in areas of large stress concentrations and from existing defects. In order to minimize the stress concentrations and maximize the fatigue life time of the specimen at the clamps, the fatigue test piece were printed wider at both ends. This particular shape is conceived to force the test piece to fail somewhere in the middle.



Figure 5.7: Fatigue test specimen

5.4.2 Number of tests

Because high-cycle fatigue tests inherently take a long time, the number and type of specimens that can be tested is limited. Therefore, the fatigue specimens that are tested are made with only one set of parameters, under one angle, and using one type of material. In section 4.5.1, some considerations with regard to the fatigue testing sample size were mentioned. First, one fatigue test is carried out to test the setup and specimen shape. Next, four specimens are tested at different stress levels. Depending on the results, this test is then expanded with additional specimens.

5.4.3 Test description

For this test, the same equipment is used as in static tensile test. The difference lies in the way the computer controls the hydraulic cylinder and the measurement equipment. A

fatigue test is performed at a certain stress level, based on the minimum cross-sectional area of the test piece.

Measurements

The force is directly retrieved from the testing machine. An LVDT is magnetically fixed to one clamp and measures the displacement relative to the opposing cylinder, see figure B.5 in appendix B.3.2. The sinusoidal signals of force and displacement are then simplified before storing them to a file to limit the data and file size; the values at the peaks and valleys are stored, values inbetween are left out. The number of load reversals is counted and stored as well.

Because of the irregular shape and surface of the material, it is not possible to attach strain gauges to the test pieces. Furthermore, the extensometers that were used in the static tensile test cannot register the small and quickly alternating displacements occurring in a fatigue test. Therefore, the only instrument that can measure the deformation in the test piece is the attached LVDT. It should be noted that this LVDT registers displacement between the clamps, and thus includes deformations of the wide ends and slip in the clamps. However, since these parts are much stiffer than the actual tested part, they will hardly contribute to the measured displacement. Furthermore, the actual displacements and strains in the material are not as important as the general trend of increasing strains and displacements that occurs as the material is developing a fatigue crack. Through this trend, crack development can be observed, and the computer can be programmed to stop the test when displacements are getting too large.

5.5 Micrography

Different batches are analysed to find out their microstructural composition. The solidification type will be investigated and the grain structure examined. Special attention will be paid to the interface of subsequent weld deposits. Both longitudinal and transverse sections are analysed. Since the former cuts through different weld passes in the printing direction, it will provide most information about the manner of solidification and grain orientations.

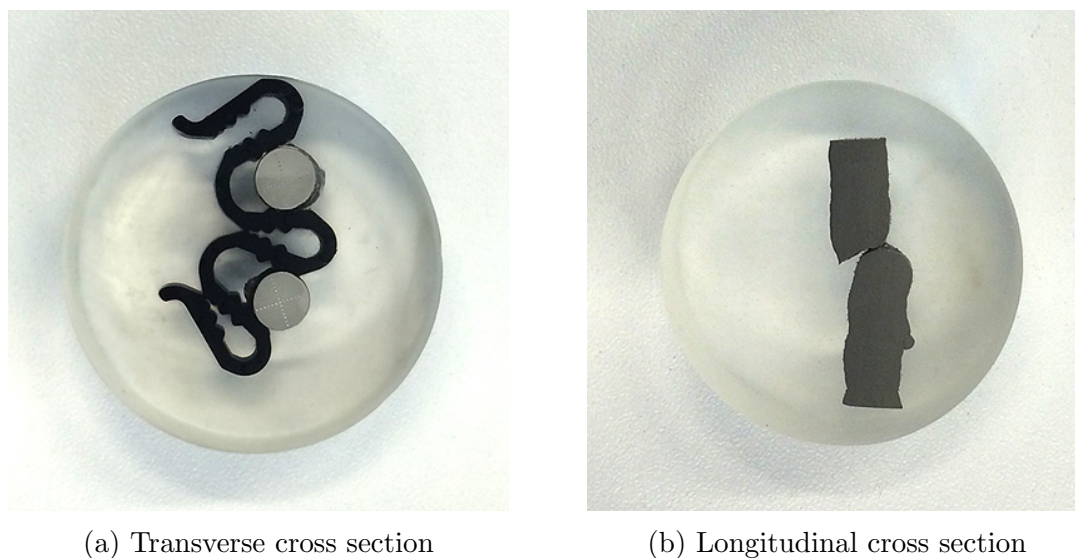


Figure 5.8: Types of microstructure specimens

5.5.1 Specimen shape

Two different types of shapes or cross sections will be analysed: longitudinal and transverse sections. The longitudinal cross sections can show how the specimen is built up; deposition layers will be visible. The transverse cross-sections can be used to investigate differences between central and outer areas of the specimen. The specimens are mounted inside a clear resin. The two types can be seen in figure 5.8

5.5.2 Number of tests

For the first batch, two transverse cross sections are taken per production angle, one close to the heat sink and another at the top of the test piece. In subsequent batches two and four, only longitudinal sections were analysed, because these gave the most valuable information. In batch 2 and 4, one longitudinal section was taken for each production angle, which resulted in 6 sections in total.

5.5.3 Test description

First, the specimen is prepared for micrography by sanding and polishing it. The final polishing step requires a diamond polishing liquid of 1 μ . After polishing, it is etched with a suitable etchant. Many different etchants can be used, and they all give different results. Kalling no.2, V2A, and a specially produced etchant have been applied. The latter etchant has proved to give the best results. This etchant was made by mixing 10 ml water, 30 ml hydrochloric acid (27%) and 1,5 ml hydrogen peroxide (30%). The specimen was immersed for four seconds.

The cross section is then studied through an optical microscope at different magnifications, and areas of interest are photographed. Composite images are made by combining multiple overlapping photographs and processed for further analysis.

5.6 Vickers Hardness

The Vickers Hardness testing can be performed on all of the specimens that were prepared for micrography. Any areas of interest observed in micrographs can subsequently be submitted to hardness testing.

5.6.1 Test description

The tests are performed using a Buehler Wilson VH3100 automatic microhardness tester. The indentations are made in a cross-shaped arrangement, and they are spaced at an appropriate distance dependent on the length of their diagonal. The ASTM recommends a minimum spacing of at least 2.5 times the diagonal⁵. By controlling this spacing, the individual measurements will not influence on another.

A load is applied of 2kgf, corresponding to a HV2 hardness scale. After setting the indentation locations, the machine will automatically indent the specimen, measure the diagonals and output the hardness values. These can then be analysed and related to visual observations of the microstructure.

⁵Vander Voort and Lucas 2015.

Chapter 6

Test results

In this chapter, the results from the different tests are discussed.

6.1 Batches

For this research, different batches of strands were produced and tested. The parameters and material from the first tensile test specimen batch serve as a reference point for the other tests. The subsequent batches were each produced with a variation of either the material or the process parameters. The degree of variation is limited by the MX3D operator experience. Practical issues such as testing time and availability at the laboratory and the MX3D workshop restrict the number of batches and amount of test pieces per batch.

Each of the test specimens have been given a name based on their batch and the way they were produced. This is done in the following format **b-dd-\$**. **b** indicates the batch. In the description of the batches below, the value for b is given in parentheses. **dd** stands for the angle at which it was produced in case there were different angles in this batch. **\$** is a letter, designating a specific test piece in the group. Specimen 3-60-B for example is part of batch 3, produced at 60°, and is named B, being preceded by specimen 3-60-A.

6.1.1 Straight test pieces

Welding wire (WW)

Six pieces of welding wire 308L were cut to the same length as the ordinary tensile test specimens and tested.

Batch 1 (1)

The first batch - printed with 308LSi was a relatively small one, which was aimed at finding out the best test methods, get some idea of the material properties and to give direction to further research. The first goal was to get acquainted with the testing and measuring equipment and to set up the testing procedures. Because no procedures or specimen shapes were specified for this material, new ones had to be developed and tried out. Secondly, (micro)structural properties were investigated in order to get an idea of the material behaviour and the way it was influenced by the additive manufacturing process.

Because there were visual clues that the angle at which a strand was produced would have an influence on the properties, specimens were printed at three different angles: 0°, 30° and 60° from the vertical position. Per angle three specimens were produced, totaling nine specimens. Their geometry was measured, and subsequently they were tested to failure in a static tensile test. Of some of these specimens, samples were taken to investigate the microstructure and the hardness.

The process parameters can be found in appendix C.2.1.

Batch 2 (2)

Since the angle appeared to play a significant role in the first batch, the second batch was produced with same number of test pieces, at the same angles. In this case, however, 316LSi welding wire was used. The process parameters were also kept constant, see appendix C.3.1.

This batch was used for both tensile and buckling tests. Specimen 2-00-A was lost due to a wrong set-up of a buckling test.

Batch 3 (3)

For the third batch of specimens, the process parameters were changed to increase the diameter of the test pieces, see appendix C.4.1. This leads to greater heat input and other process adjustments that will be of influence on the microstructure and structural properties. These test pieces are again produced with 308LSi. Both tensile and buckling tests were performed on this batch. Four test pieces were produced per production angle.

Batch 4 (4)

Batch 4 was meant to be produced with the same material and parameters as batch 3 in order to study whether the large amount of defects and bad results from batch 3 were a structural issue in the production process, or a one-time production problem, possibly caused by improper gas shielding. However, the process parameters were changed, so no direct comparison can be made.

Because many specimens were produced in total, buckling tests did not have to be performed on pieces that were used as tensile test pieces as well. Four straight 0° test pieces were cut into 8 buckling test pieces at different lengths. At 30° and 60°, two straight test pieces per angle were cut to four buckling test pieces per angle, again at varying lengths. These specimens are given the prefix (4B).

Specimens from batch 4 were also used to make the milled test pieces.

6.1.2 Milled test pieces

In order to find out the effect of the geometry on the mechanical properties, some specimens have been produced and milled. Twelve test pieces, four for each angle, have been produced and submitted to static tensile tests.

Milled batch (4M)

Six straight test pieces from batch 4, two at each angles, were each cut in half and milled smooth over a certain length. In this process, one 60 °specimen was destroyed in the milling process. Another contained a severe notch.

6.1.3 Fatigue test pieces

All of these test pieces were produced with material 308LSi and printed vertically. Their process parameters can be seen in appendix C.7.1.

Fatigue batch 0: (0F)

As a first test, a single test piece was produced and tested.

Fatigue batch 1: (1F)

This first proper batch consisted of four specimens. One of these was destroyed when first setting up the test. Therefore, only three specimens have been tested

Fatigue batch 2: (2F)

Five more test pieces were produced in batch 2.

6.2 Geometry

As described in section 4.2, manual measurements can only give an indication of the distribution of the cross section, because the surface of the rods is so irregular. Therefore, other methods have been employed. The photographic method was used for all of the test pieces. At least three photos were analysed per test piece. Additionally, a small number of test pieces was scanned in 3D through photogrammetry. These 3D models were compared to the contour photo results, and imported into Abaqus for FEM analysis. Finally, to verify and calibrate these measurements, vernier caliper measurements were performed on the entire first batch and as spot checks on the other batches.

6.2.1 Batch 1

Appendix C.2.2 contains the results from the geometrical analysis of the different test pieces. Histograms have been created and normal distributions have been fitted to them.

The results for test pieces produced at 0 and 30 degrees are close together. The 60 degree pieces, however, show a much bigger spread in diameter, resulting in a large standard deviation and low 5 percentile value for the diameter. The wobble factor is also much higher than for the other two angles.

The standard deviation and wobble factor of the 0 degree pieces also appears to be slightly higher than the ones produced at 30 degrees. A possible explanation for this unexpected difference might lie in a production error. All test pieces were printed in a single run. The printing robot deposited metal per droplet, moving to a next test piece after deposition of one droplet. Something in this shift from one angle to the other caused the 0 degree test pieces to be more wobbly at the base, where it was being printed simultaneously with the 30 and 60 degree pieces. Evaluation of the process and improvement by means of adaptive feedback should lead to the elimination of this problem in future batches.

The normal distribution appears to give an accurate and safe representation of the small cross sections of a test piece. This is made visible in the scatter plots presented in appendix C.2.2.

6.2.2 Batch 2

See appendix C.3.2

6.2.3 Batch 3

See appendix C.4.2

6.2.4 Batch 4

See appendix C.5.2

6.2.5 Overview

A comparison of the the 4 batches shows that batch 3 (Red) had the largest diameter, but at the same time the largest spread, resulting in a relatively low minimum diameter. Batches 1 (blue), 2 (green) and 4 (yellow) show lower spread. While in batch 1 and 4 the diameter decreased with increasing production angle, the diameter stayed the same or increased slightly with increasing production angle in batch 2. Perhaps, this is a result of a difference in viscosity of the molten weld metal of 316LSi and 308LSi. It might also have to do with a difference in process parameters. In order to investigate this, new test prints with the same process parameters would have to be made for both materials.

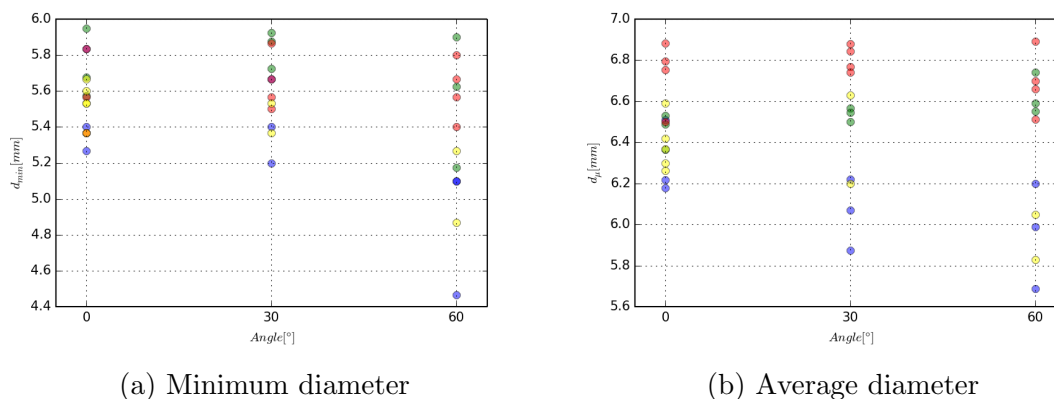


Figure 6.1: Geometry overview

6.2.6 Geometry control

The different batches have shown that different process parameters and base materials used lead to different geometrical properties. To some extent, the average diameter can be influenced by altering specific parameters such as the layer height. At a production angle of 0 degrees, the range is the smallest, showing an average diameter of 5.96 mm for batch 1, 6.08 mm for batch 2, 6.32 mm for batch 3. At an angle of 60 degrees, the largest spread is observed, ranging from 5.64 for batch 1 and 6.23 for batch 2 to 6.32 mm for batch 3. The standard deviation, however, also changes when the diameter changes. This leads to the fact that for batch 3, which contains the largest average diameters, the smallest diameters - the weakest links in a rod - are much closer to batch 1 and batch 2.

At the moment, it is not possible for an engineer to dictate certain geometrical characteristics and have elements produced accordingly. Rather, he should make use of a sort of catalogue, a collection of parameter sets and associated geometrical characteristics. These sets of parameters and characteristics should be provided by the printer operator based on testing and measurements. The engineer may then pick these sets as standard building elements, and use them to make his structural design.

6.2.7 Minimum diameter

The normal distribution can be used to describe the total geometry of a rod. For elements loaded in tension, however, the minimum diameter will be governing. Therefore, it is more important to give an accurate and safe description of these extreme values, which are often modelled using Gumbel, Frechet or Weibull distributions, rather than normal distributions.

Again, Python was used to locate and extract these minimum values. The photographic measurements gave a diameter profile of the rods along their length. Using a python script, the valleys in this profile were detected. The minimum distance between these peaks was set to 7 pixels, or 0.7 mm. This was done in order to prevent double counting of the same valleys due to small variations. This minimum distance was chosen smaller than 1 mm, since this was the minimum layer height that was set in the process parameters. A new valley might occur every new layer. If the minimum distance was set higher than 1 mm, the resolution would be too low, possibly missing some valleys. Figure 6.2 is an example of such a valley detection profile. Note that the values are plotted negatively, because the script works with peaks instead of valleys.

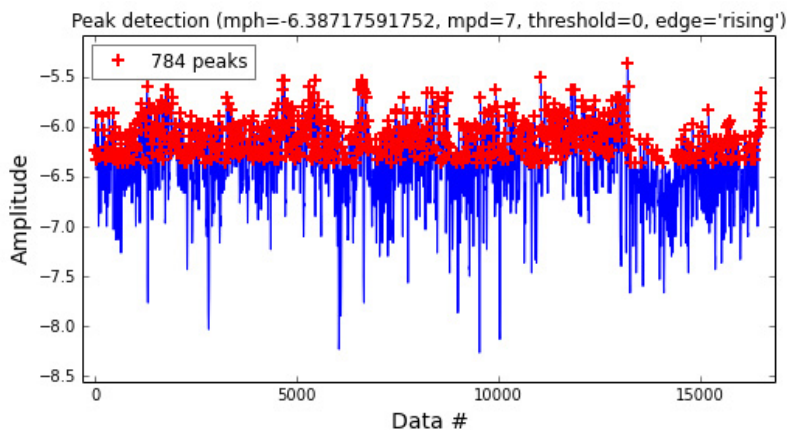


Figure 6.2: Valley detection profile of specimens 4-00

Now, the distance of these minima to the mean diameter is computed and represented in a histogram. The three extreme value distributions mentioned before are compared and the best fit is chosen. It turns out the values are best described by a Weibull distribution, see figure 6.3, which shows the probability density function of one minimum, occurring approximately once every 2 mm. Using Matlab, the shape parameters were fitted using MLE and 95% confidence intervals for these shape parameters were computed.

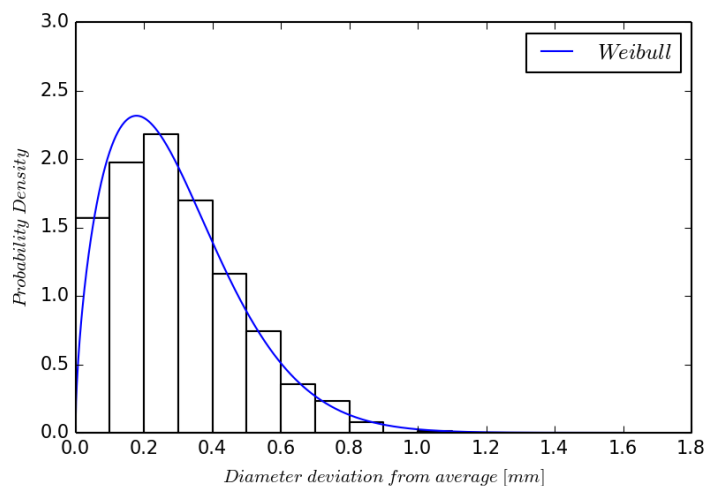


Figure 6.3: Weibull fit to extreme deviations from mean value

When designing a structure, an engineer needs to know what minimum diameter he should take into account to achieve a certain level of safety. Say this engineer wants to

know what minimum diameter will only be exceeded by 5% of all rods of this type and length. This minimum diameter is dependent on the number of minima inside the rod. If there is only one minimum, which would be for a rod of length $L_0 = 2$ mm, he can use the 95 percentile value of the distribution plotted above. For a 10 mm rod, he would need the $0.95^{2/10} = 0.99$ percentile value. In formula:

$$\text{Percentile} = 0.95^{\frac{L_0}{L}} \quad (6.1)$$

Now, for a certain length of rod, the required percentile value in the probability density function is found. Taking into account the confidence intervals of the shape parameters of the Weibull distribution, the corresponding diameter can be computed. Thus, for every type of rod, a design graph can be made, which plots the minimum diameter against the rod length. This is shown for one type of rod in figure 6.4. The width of the confidence intervals of the shape parameters depends on the number of minima analysed and the fit of the distribution to the data. Better fits and more data result in more accurate results and narrower intervals.

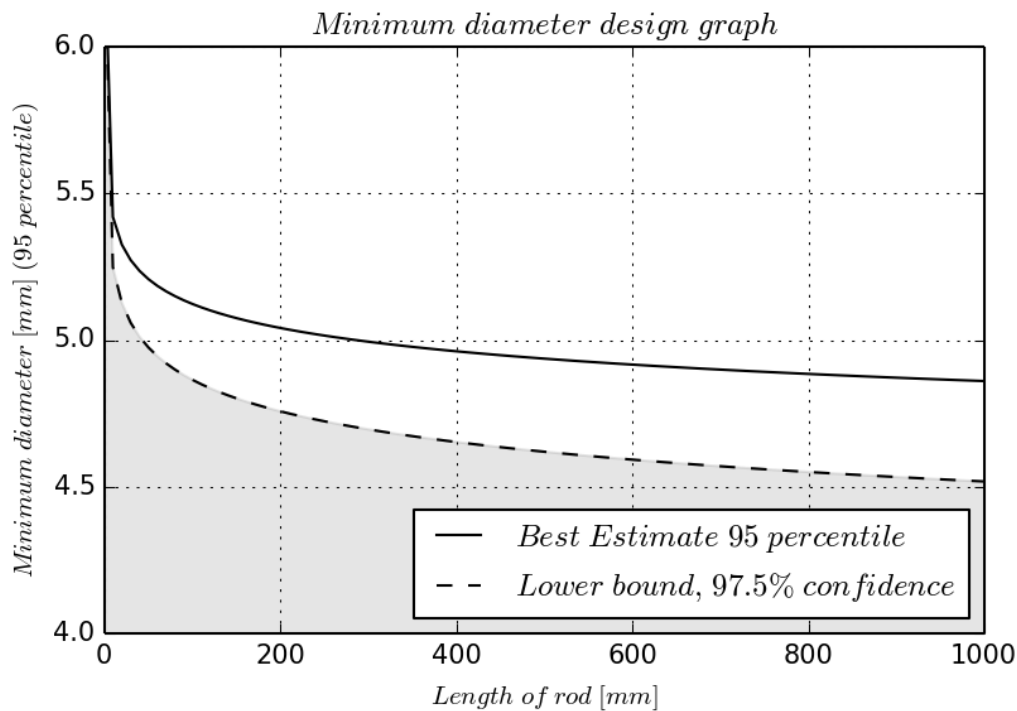


Figure 6.4: Design graph for 4-30 with $d_{average} = 6,42$

Design graphs for all other types of rods can be viewed in appendix C.9.

6.3 Microstructure

6.3.1 Batch 1

All specimens that were observed show an oriented dendritic microstructure and type FA solidification. Columnar grain formation occurs, solidification takes place in one preferential direction. Figure 6.5 shows a longitudinal cross section, taken from specimen 1-00-C after tensile testing and failure. Clearly, the dendrites and grains are all arranged in the same direction, even across different layers. This microstructure is typical for austenitic

stainless steel weldments. Multiple photographs were stitched together to form this composite image.

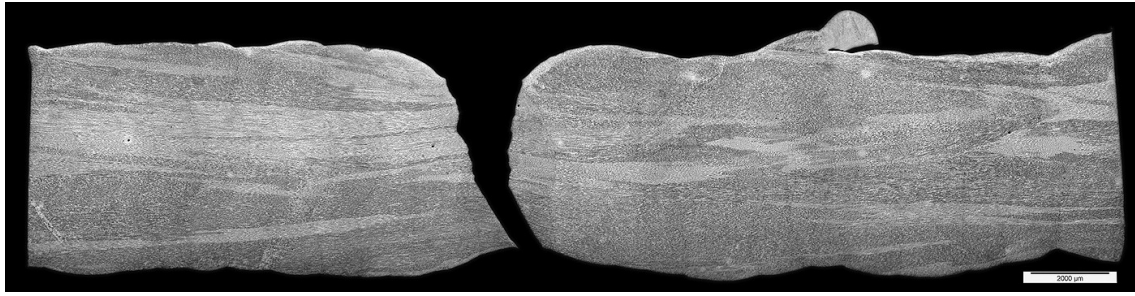


Figure 6.5: Longitudinal cross section of 1-00-C, after tensile failure

Figure 6.6 shows a cross section of strand 1-00-B, a vertically produced strand. The cross section was taken at the top of the strand, i.e. at the free end that was not directly connected to the base plate acting as a heat sink. Three areas, 6.6b, 6.6c, 6.6d, with different solidification patterns can be distinguished. The increasing dendrite size and spacing in areas 1, 2 and 3 indicates decreasing cooling time.

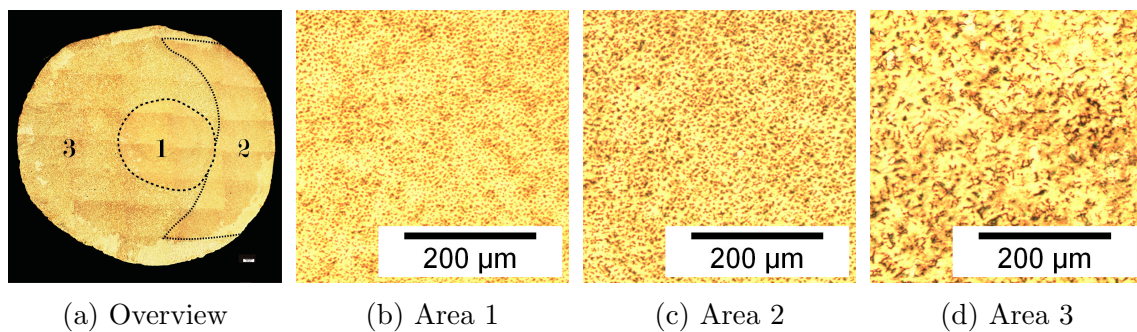


Figure 6.6: Microstructure of cross section of the top of specimen 1-00-B

Apparently, area 1 has cooled down the fastest, since it has the smallest dendrite size and spacing. This could be related to the position of the cross section. Consider figure 6.7. The cross section cuts through different deposition layers, which have different thermal histories and associated dendritic structures. The second image shows what happens when another droplet is deposited. In reality, these droplets are of irregular shape and size. Therefore, asymmetrical effects can be observed, such as the ones seen in 6.6. A test using thermocouples can be performed to measure the actual thermal history inside a strand.

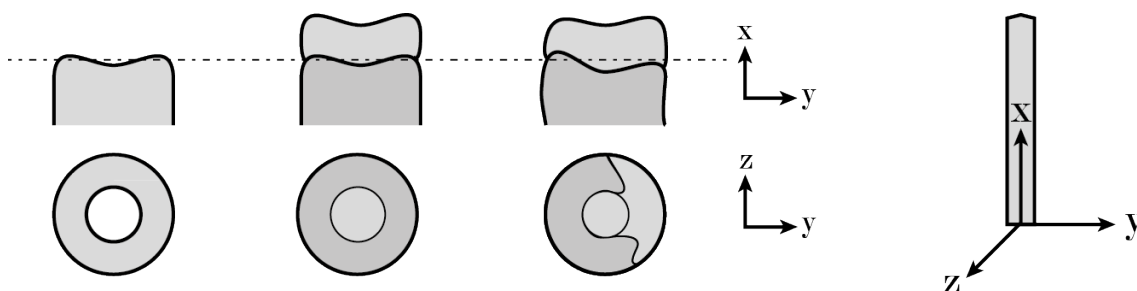


Figure 6.7: Schematic drawing of deposition, resulting in different dendritic structures

Areas with different dendritic microstructures will have different properties and exhibit different structural behaviour. Therefore, internal stress concentrations might occur at the boundaries between these areas, resulting in preferential failure planes. When the observed areas indeed have different structural properties, their hardness should also be noticeably different. With microhardness testing, this can be verified. This is further discussed in 6.4

6.3.2 Batch 2

In batch 2, one longitudinal section was made per production angle. These are shown side by side in figure 6.8. Subsequent weld passes and a pronounced directional grain structure are visible. The dendritic solidification is of type A.

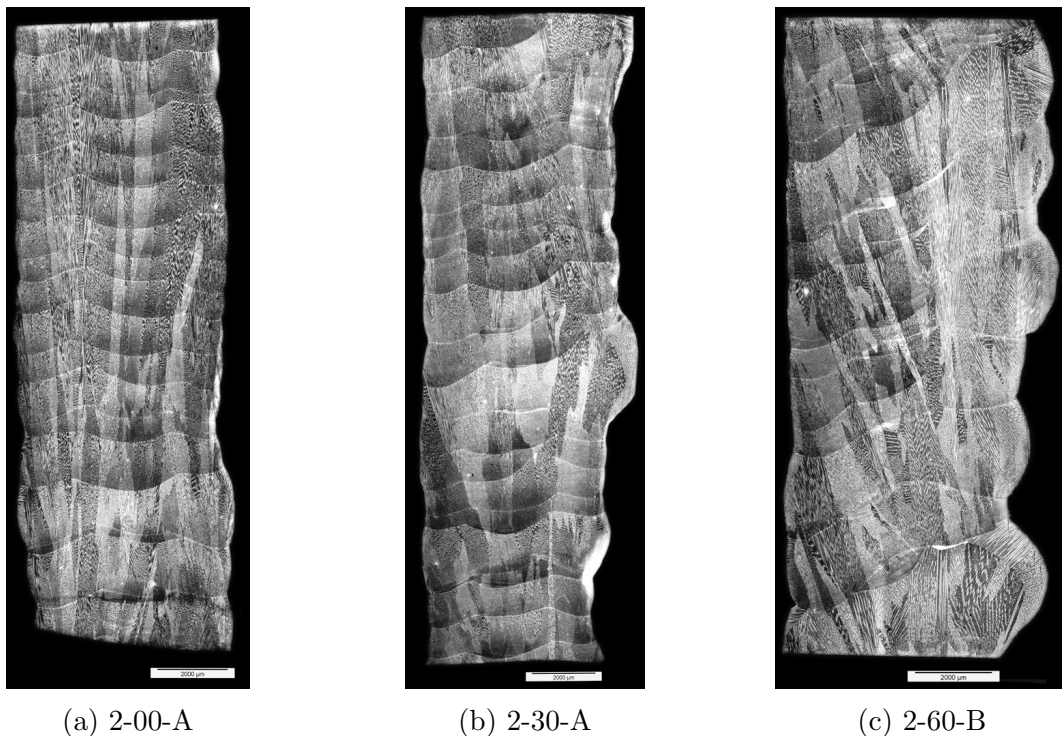


Figure 6.8: Longitudinal cross sections in Batch 2

Grain growth

The grain structure seems to grow perpendicular to the layers of deposition, which coincides with the direction of the thermal gradient. For the 30° and 60° specimens this means that the grains form at an angle with respect to the main orientation of the specimen itself. This can be seen in figure 6.9. In the areas where weld metal is dripping, grain orientation is more random. Solidification starts from different nuclei. This is observed on the right side of the micrograph in figure 6.8c.

Additionally, the deposition angle has been measured from the photos and plotted against the production angle in figure 6.10

Furthermore, the grains in the test pieces appear to grow through different deposition layers. When a new layer of weld metal is deposited, the new microstructure tends to grow from the crystals in the previous layer, taking the same orientation. This might occur when the previous layer is in a semi-solid stage.

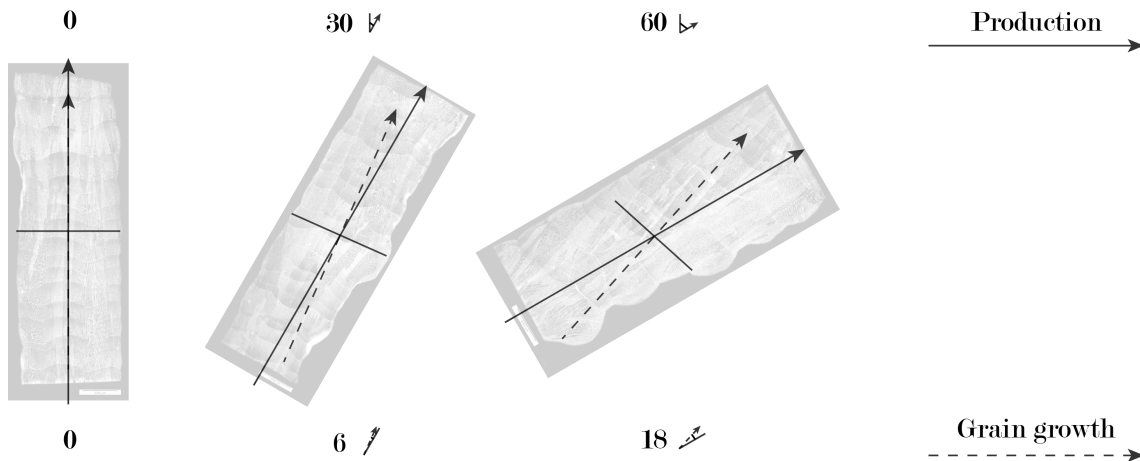


Figure 6.9: Production angle and grain growth direction

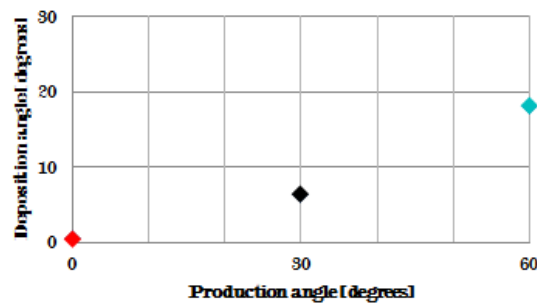


Figure 6.10: Production angle versus deposition angle

Anisotropy

Because of the different grain orientations, these specimens are expected to behave differently under structural testing along their main axis. This will be verified through tensile tests, see section 6.5.3. This kind of anisotropy also occurs in rolled sheet metal, in which it is of importance to cold-forming. For rolled sheet metal, this can be expressed with the Lankford-coefficient, \bar{R} see equation 6.2.

$$\bar{R} = \frac{R_0 + R_{90} - 2 \cdot R_{45}}{4} \quad (6.2)$$

For comparison between different types of additive manufactures and their grain structures, it may be useful to express the structural behaviour of additive manufactures with such a coefficient.

6.3.3 Batch 3

No microstructural analysis was performed on batch 3, because it was badly produced.

6.3.4 Batch 4

To verify the directional, columnar grain growth for 308LSi test specimens, another three longitudinal sections were taken, which are presented in figure 6.11.

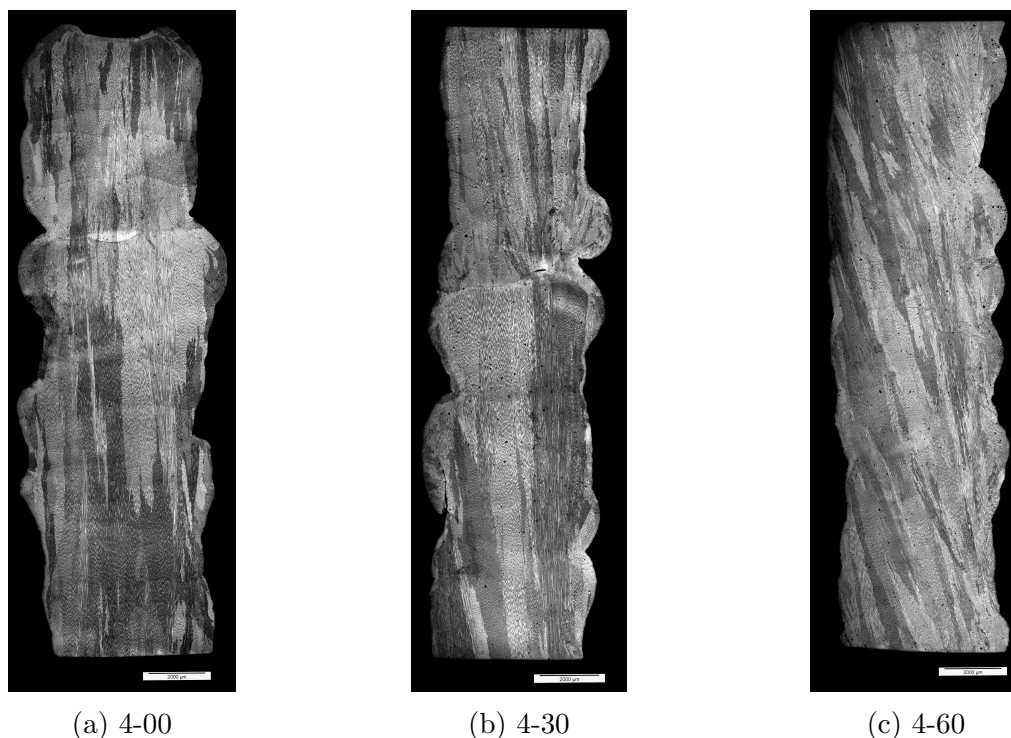


Figure 6.11: Longitudinal cross sections in Batch 4

Grain growth

These micrographs again show large columnar grains. The weld passes are more difficult to make out in these images, because the material seems to react differently to the etchant. However, the grains again grow across different deposition layers. The much longer waiting time between different depositions that was applied in this batch in comparison to batch 2 did not hinder this continued growth.

Once again, it is observed that grains grow at angle with respect to the main rod axis of rods produced at an angle. Because the deposition layers are not clearly visible, no accurate measurements of the deposition angles could be made this batch. However, some of the main grain orientations were measured from the micrographs. For the specimens of type 4-30, the grain orientation of the large angled grains was about 7° - 8° ; for specimens of type 4-60, the grain orientations ranged from 15° to 20° . This is in line with the results from batch 2, see figure 6.10.

Anisotropy

Because of the large columnar grains, the microstructure of this material is anisotropic. The direction of these columnar grains depends on the production angle. The structural performance is therefore expected to be dependent on both the production and the testing angle. This is verified in tensile tests in section 6.5.6.

6.3.5 Overview

Grain growth

Longitudinal micrographs have shown directional growth of columnar grains. The grains tend to grow perpendicular to the weld pool, taking the orientation of the grains in previously deposited weld metal. This leads to grains that grow across different deposition

layers. Because the weld pool is tilted for test pieces produced at 30° or 60°, the grains are also formed at an angle with respect to the main orientation.

Anisotropy

The anisotropic grain structure is expected to result in anisotropic structural behaviour. Tensile tests on milled specimens have clearly shown a connection between production angle and ultimate strength, which is in support of this claim. This is described in more detail in section 6.5.6. Besides ultimate strength, it is expected to influence the entire stress-strain diagram. Since plastic deformation occurs along grain boundaries, ductility is expected to be reduced for columnar grains. This is also expected to affect the 0,2% proof strength. The actual effect of the microstructure on the structural properties should be investigated through structural testing. Milled specimens are ideal, because any geometrical influences are eliminated.

Corrosion resistance

One of the main reasons to choose a stainless steel as the base material are its corrosion resistant properties. Normally, this is ensured by careful surface preparation and minimization of segregation of alloying elements. Neither of these aspects is guaranteed in the additive manufactures studied here. When the surface is left untreated, the material may not form a protective oxide layer, leaving the material susceptible to corrosion. Moreover, due to segregation of alloying constituents, particularly chromium, the material may not have the right composition to provide sufficient corrosion resistance.

Stress corrosion cracking can be a problem in austenitic stainless steels. This corrosion and subsequent cracking occurs along grain boundaries. Due to the columnar grain structure, very large grain boundaries extend deep inside the material. A printed structure can fail if cracking occurs along such a boundary. In test piece produced at an angle, the grain boundaries along the columnar grains are even exposed at the surface, possibly further increasing the risk of stress corrosion cracking.

Measurements of the type of elements present in and along grain boundaries and at the surface need to be carried out in order to identify possible problems with regards to corrosion. Manufactures should also be tested in corrosive environments in future research.

EBSD

The qualitative observation of anisotropy and grain growth can be verified by doing an EBSD measurement, which will give exact information about the orientation of the grains. This is not part of the scope of this thesis, but an EBSD measurement can give valuable information in future research.

6.4 Vickers hardness

After the microstructural analysis and associated polishing, Vickers microhardness tests were performed. Two samples have been investigated, 1-60-B and 1-60-C, both produced at a 60 degree angle. Because it was expected that more hardness testing would not yield any additional insight relevant within the scope of this thesis, no further testing was performed.

6.4.1 Batch 1

Appendix C.2.8 contains combined microscopical imagery and hardness plots of the different cross sections that were analysed. One might expect to measure higher hardness values for the finer dendritic structures, but in fact the tests that were performed do not indicate such a relationship very clearly; fluctuations in hardness appear not to relate to the different dendritic structures. In some cases, a small drop in hardness is observed in the area around the boundary between different structures. These drops, however, also occur in areas where no microstructural boundaries are apparent. The variations are too small to be considered significant.

These findings do confirm the statement that austenitic stainless steels cannot be hardened by heat treatment and are largely unaffected by welding, see section 2.2.

The analysis of longitudinal sections and the comparison of hardness values between different grain orientations may be an area of future research. By measuring hardness of columnar grains at different angles, further insight might be gained into the anisotropic properties of the material.

6.5 Tensile tests

In this section the results from the static tensile tests are discussed. An overview of the test results can be seen in table C.2 in appendix C.1.

6.5.1 Welding wire

The results have been included in appendix C.2.5. The test results B, C, and D are pretty consistent. Results E and F are clearly different. The values for the Young's modulus and 0.2% proof strength are markedly lower. Note also the wobbliness of the curves of test E and F compared to the three other results. This gives reason to believe that something went wrong in the test set up. Additional tests should be performed to find out whether this is the case.

Interestingly, the welding wire shows lower values for the Young's modulus than expected, while the 0.2% proof strength values are much higher than what is guaranteed by the manufacturer for welded structures. The latter is not very surprising, considering that welded structures contain many more imperfections than pure, smooth, welding wire. One would expect to see Young's modulus values in the range of 190 to 210 MPa, though. Perhaps this is due to the nature of the testing method. This tensile test setup might simply not be suited to find out the Young's modulus for such small test pieces. Misalignments of the welding wire in the testing machine might also have led to a reduced measure of the Young's modulus. Moreover, since the diameter of the welding wire is relatively small, the accuracy of the measurements of the diameter becomes especially important. The supplier specifies a welding wire diameter of 1,0 mm. With the manual vernier caliper that was used, the measurements are only accurate to about 0.05 mm, which is 5 percent of the expected diameter of 1,0 mm. Since cross-sectional areas are being considered, this error is squared.

All in all, more accurate testing and measuring methods should be applied to study the welding wire structural behaviour in detail. The current tensile tests, however, were only performed to get an idea of the influence of the process on the base material. It is clear that these drawn filler metals have greatly different properties than the printed product, so no extra tests are performed.

6.5.2 Batch 1

Nine tensile tests were performed in total for this batch. Appendix C.2.3 contains all the unprocessed F-u diagrams from the tests. Appendices C.2.4 and C.2.6 contain respectively the stress-strain diagrams and plots of the correlation between different parameters.

0.2 % proof strength

Values for $\sigma_{0.2}$ range from 270 MPa to a little over 330 MPa. The value seems to increase for 60°specimens. $\sigma_{0.2}$ is difficult to determine, however, since it is dependent on E_0 and the shape of the stress-strain diagram. Because the geometry of 60 °specimens has a greater spread, the material appears stiffer when stiffness is related to the minimum diameter. This will result in higher measured values of $\sigma_{0.2}$.

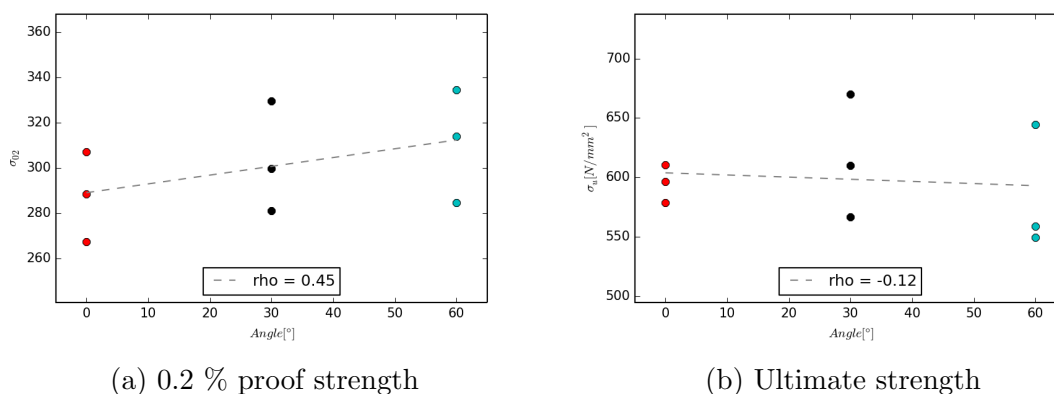


Figure 6.12: Strength batch 1

Ultimate strength

σ_u ranges from 550 MPa to 670 MPa, and is about two times bigger than $\sigma_{0.2}$. These values are plotted in figure 6.12b. This plot does not show a clear connection between strength and production angle. The spread in strength is slightly bigger for the specimens produced at an angle than that of vertically produced specimens, though.

Young's modulus

Surprisingly, the Young's modulus is smaller than expected and it also shows a great spread, see figure 6.13a. From these first results, no significant correlation between the Young's modulus and other properties, e.g. the production angle, diameter standard deviation and wobble-effect, can be found, see figure C.23e.

Ductility

The test pieces all have an ultimate strain in the range of 10 to 22 % . In general, $\sigma_{0.2}$ is about half of σ_u . This means the test pieces have deformation capacity and warn before failing by showing clear deformations. Moreover, this will not happen suddenly, the material has only used half its capacity when it has reached its 0.2% proof strength.

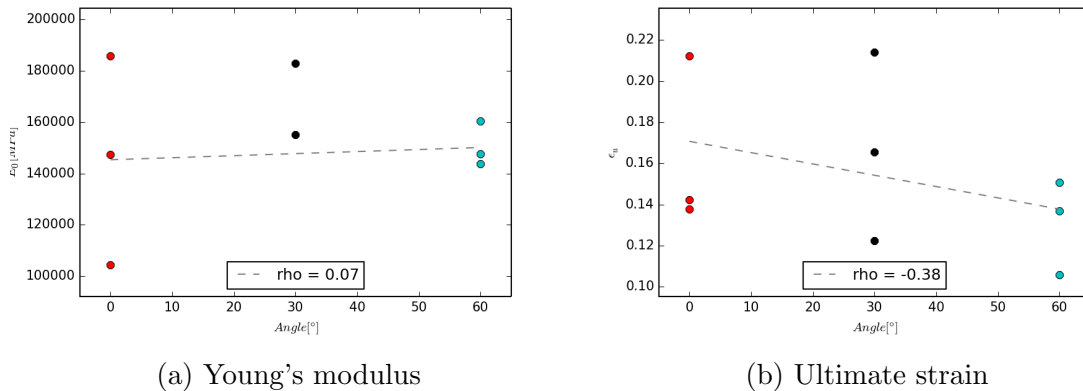


Figure 6.13: Stiffness and ductility batch 1

6.5.3 Batch 2

Appendices C.3.3, C.3.4, C.3.5 contain respectively the raw F-u diagrams, engineering stress-strain diagrams, and correlations between geometrical properties and test data.

0.2 % proof strength

$\sigma_{0.2}$ is again higher for 60° specimens. In this case, the specimens produced at a 30° have the lowest value for $\sigma_{0.2}$. This can be explained from the fact that these specimens showed relatively small deviations from the average diameter; the stresses in the cross sections of the rod are close together.

Ranging from 290 MPa to 350 MPa with an extreme value of 390 MPa, the values are slightly higher than those found in batch 1, but they show a similar spread.

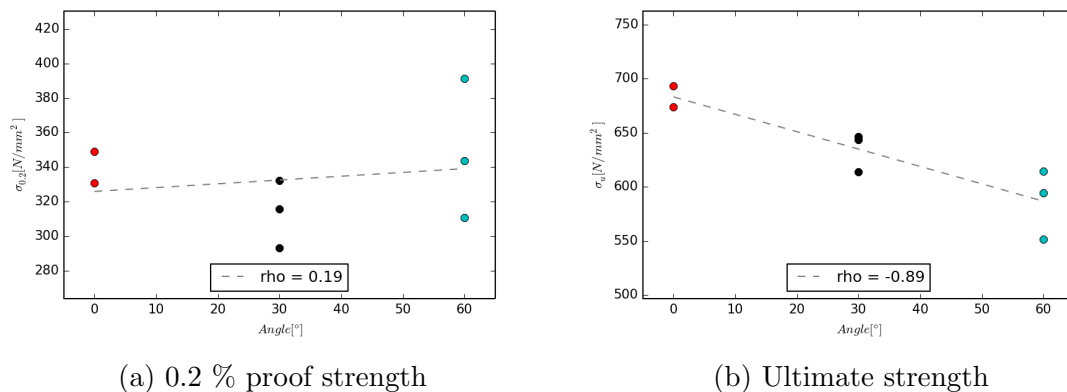


Figure 6.14: Strength batch 2

Ultimate strength

The range in σ_u , 560 MPa to 690 MPa, is only marginally higher than in batch 1. Again, σ_u is about 2 times as big as $\sigma_{0.2}$. These values are plotted in figure 6.14b.

The results seem to indicate a correlation between production angle and σ_u . Since the geometrical deviations in this batch are rather low, this correlation might be a result of the mechanical properties of the material itself. Tests on milled specimens should be performed to further investigate this theory.

Young's modulus

With the exception of one extreme value of about 275 GPa, figure 6.15a gives the same picture of the Young's modulus as the results from batch 1. The extreme value was found due to a measuring error. The extensometers were stuck in the very beginning of the test, so zero displacement was measured, leading to a high value of E_0 .

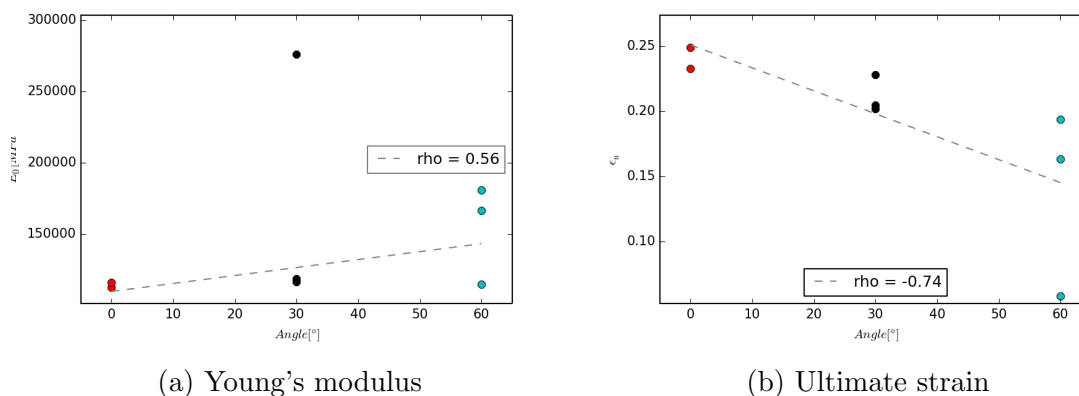


Figure 6.15: Stiffness and ductility batch 2

Ductility

Figure 6.15b shows greater ductility for batch 2 specimens than in batch 1. This might be a result of smaller geometrical deviations rather than actually improved material properties. Comparison of milled specimens may verify this.

One very low value of ϵ_u below 10% was observed. This was caused by a geometrical defect in the specimen.

6.5.4 Batch 3

Again, all the results from this batch have been supplied in the appendix, particularly sections C.4.3, C.4.4, C.4.5.

This batch showed relatively low strength values and ductility. In the fracture areas, large pores were visible, see figure 6.16. On paper, only small changes were made to the



Figure 6.16: Porosity in batch 3

production process in order to increase the diameter of the test pieces, but the decrease in performance is drastic due to the large number of defects. The observed porosity could

have been caused by moisture or rust, but this is not very probably as the workshop environment had not been changed between the batches. A more likely explanation lies in improper gas shielding. In between the second and third batch, the nozzle was fixed provisionally after breaking down. Possibly, this fix was not comprehensive, resulting in poor gas distribution and subsequently great porosity. An additional batch will have to be produced to confirm this was only a one-time production error that can be eliminated. This batch of specimens is not suited for structural application.

0.2 % proof strength

$\sigma_{0.2}$ values do not show a significant reduction due to the material defects. The stiffening effect and increase of $\sigma_{0.2}$ for specimens produced at angle is not observed in this batch, possibly because all of the specimens are very irregularly shaped.

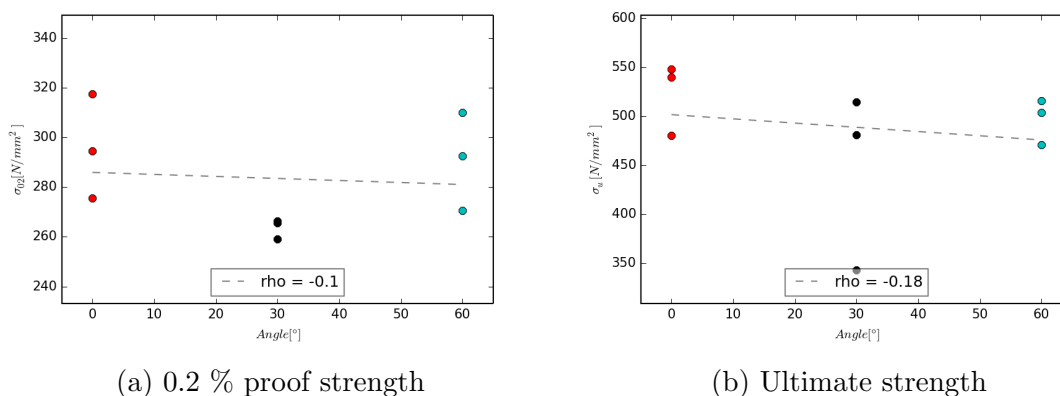


Figure 6.17: Strength batch 3

Ultimate strength

σ_u values are markedly lower than in previous batches. The highest value is only 550 MPa, which was the lowest value observed in batches 1 and 2. Moreover, an extremely low value of 350 MPa was found for one specimen.

Young's modulus

Some very high Young's moduli are observed in this batch. This is because the extensometers did not register any displacement at the beginning of the test. Some friction in the measuring equipment prevented them from moving initially. Once this friction had been overcome, however, the measurements proceeded correctly. Readings for strength and ultimate strain values are unaffected.

The observed spread in the results is large once again. However, the average stiffness values for the correctly measured specimens is higher than before. This is probably a result of a greater stiffening effect because the geometrical deviations are greater.

Ductility

While some specimens still exhibited quite some toughness, most specimens had low values of ϵ_u due to material defects. One specimen even had an ϵ_u of about 3%. This lowered ductility can be a great problem for the safe design of structures.

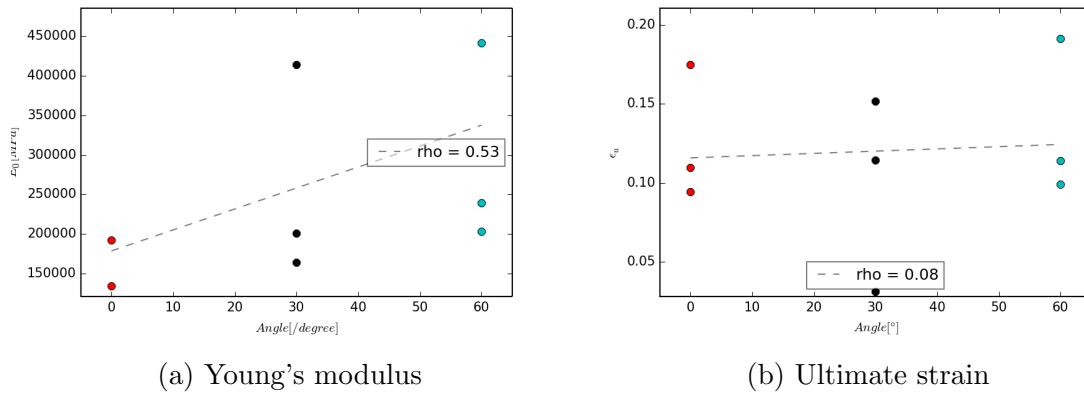


Figure 6.18: Stiffness and ductility batch 3

6.5.5 Batch 4

This batch gave results that were comparable to the first two batches and did not contain material defects like batch 3. However, because the parameters were changed with respect to batch 3, the broken nozzle cannot be singled out as the reason for the material defects in batch 3. Appendices C.5.3, C.5.4, C.5.5 hold all the results from this batch.

0.2 % proof strength

Values for $\sigma_{0.2}$ are in a slightly lower range than in batches 1 and 2. $\sigma_{0.2}$ ranges from about 245 MPa to approximately 280 MPa. The spread in results is smaller than in previous batches, and there does not seem to be a clear connection between the production angle and $\sigma_{0.2}$. However, it should be noted that only two specimens were tested for the 30° and 60° production angles.

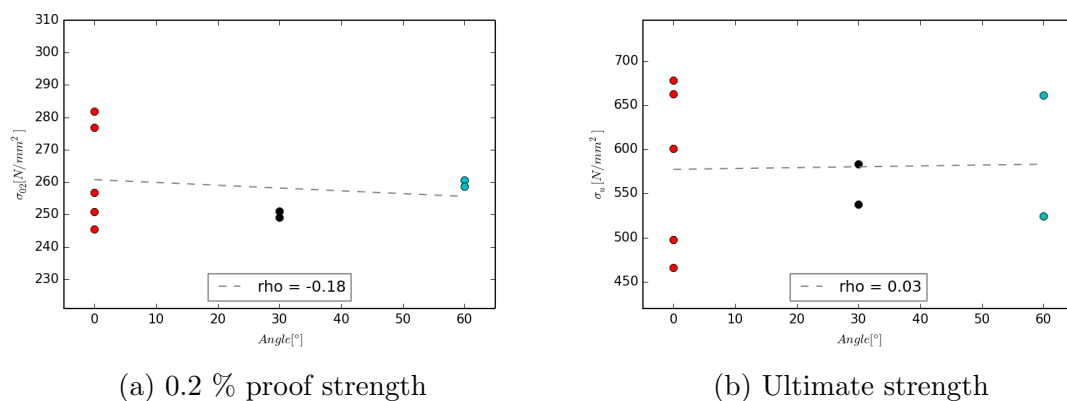


Figure 6.19: Strength batch 4

Ultimate strength

σ_u ranges from 460 MPa to 680 MPa. The two lowest values of σ_u at 0°, and the lowest value of σ_u at 60° were a result of geometrical defects that were identified before testing commenced. Without these defective test pieces, σ_u is in the range of 530-680 MPa, which is very similar to batch 1. The results are plotted in figure 6.19b. Again, σ_u is found to be about 2 times as big as $\sigma_{0.2}$.

Young's modulus

In batch 4, the perceived Young's modulus is low as well, and also shows quite some spread.

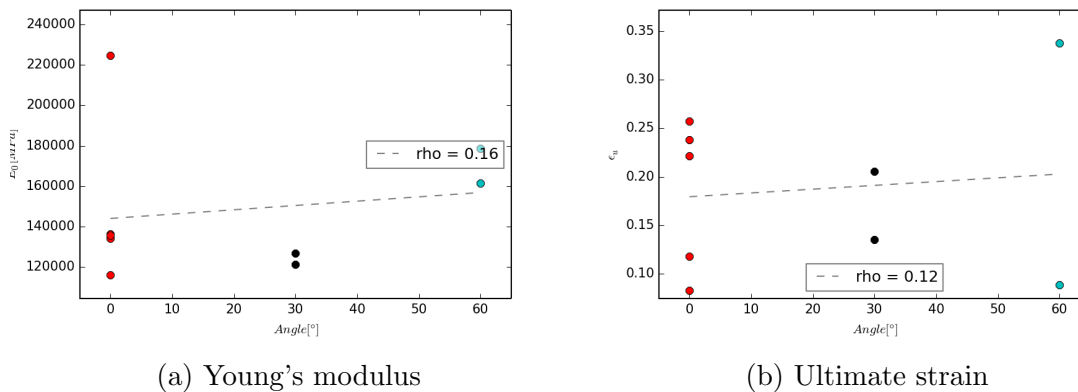


Figure 6.20: Stiffness and ductility batch 4

Ductility

The specimens that show the lowest ϵ_u correspond to the specimens with lowered σ_u that contained a geometrical defect.

6.5.6 Milled specimens

Please see appendices C.6.1, C.6.2, C.6.3 for any results not included here. As expected, the milled specimens gave much more consistent results than the rough specimens. The spread in structural properties was much smaller thanks to the elimination of geometrical variations. Moreover, the properties of the material itself could be studied.

These results should be compared to batch 4 in particular, because these milled specimens come from the same batch.

One result is excluded from the comparison below. Due to a mistake in the milling process, specimen S-60-B was notched, leading to premature failure. In the appendix, the result is included for reference.

0.2 % proof strength

$\sigma_{0.2}$ again shows quite some spread. Since the Young's modulus could not be measured accurately, the calculation of $\sigma_{0.2}$ is also inaccurate. In general, though, $\sigma_{0.2}$ is lower than in the batches of ordinary specimens. Because the diameter is the same over the entire milled area, the stiffening effect that was observed and described in the other batches does not occur. This results in a lower, more accurate value of the actual 0.2 % proof strength.

Ultimate strength

Like in batch 3, the ultimate strength is negatively correlated with the production angle, see figure 6.19b. Since all geometrical influences are eliminated by milling the specimen, this correlation must be a result of a difference in material properties between the different production angles. Also here, σ_u is about two times $\sigma_{0.2}$.

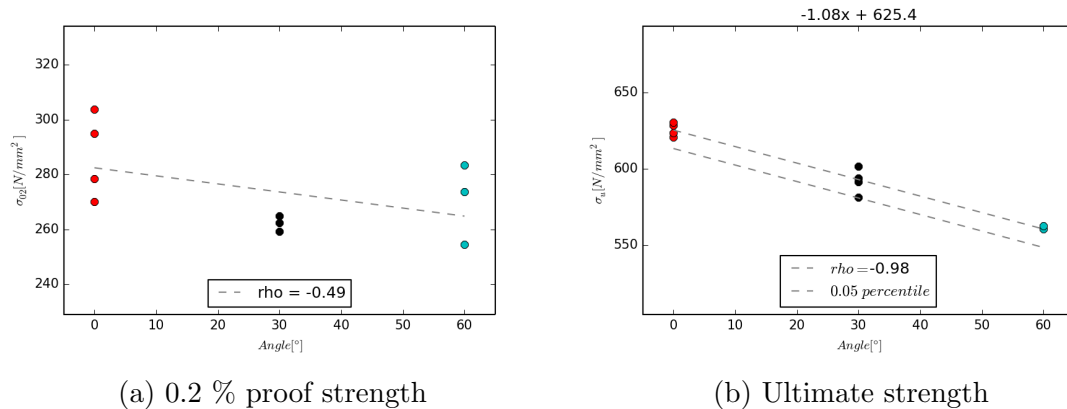


Figure 6.21: Strength batch 4, milled

Young's modulus

The current test set-up did not allow for a direct measurement of the Young's modulus, because the milled area was too small to attach the extensometers that were used in the other tests.

Ductility

As expected, the ductility of these milled specimens is much higher than for the ordinary batches. However, ϵ_u is lower than the theoretical values supplied by Rasmussen, 0.51 %. Apparently, the printed microstructure is different, leading to different structural behaviour.

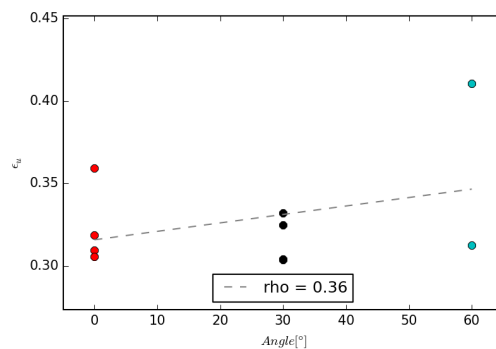
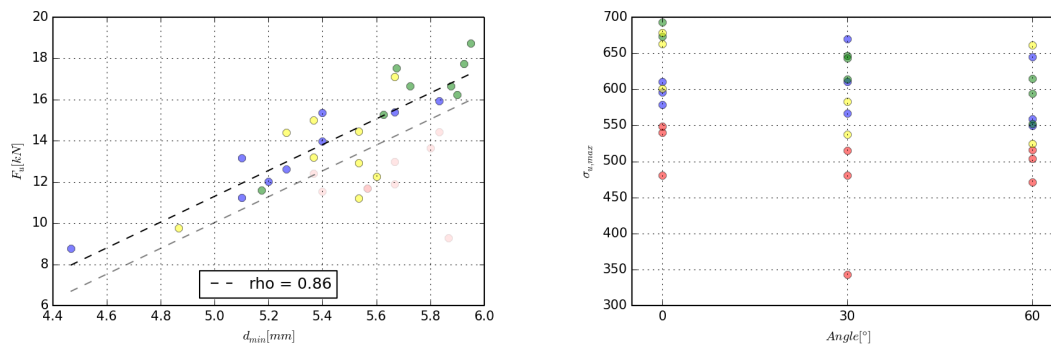


Figure 6.22: Ultimate strain in milled specimens

6.5.7 Overview

In the following overview, the different batches are compared and plotted together. To distinguish between these batches, they have been given different colours. Batch 1 = blue; batch 2 = green; batch 3 = red; batch 4 = yellow.

Batch 1, 2 and 4 performed similarly. Their failure load could be predicted from their geometry fairly well, see figure 6.23a. In the case of batch 3 this was hardly possible; defects inside the material determined the failure load. This leads to greatly reduced ultimate stresses, which can be seen in figure 6.23b. The defects are most likely caused by a broken nozzle, but this has to be verified by printing another batch with the same parameters.



(a) Minimum diameter versus failure load (b) Production angle versus ultimate stress

Figure 6.23: Overview of tensile test results
(batch 1 = blue; batch 2 = green; batch 3 = red; batch 4 = yellow)

Material

Two types of stainless steels, 316LSi and 308LSi, have been investigated. The test results show similar structural properties for both materials. On average, the strength of 316LSi, $\sigma_u = 629 \text{ MPa}$ is higher than that of 308LSi, $\sigma_u = 603 \text{ MPa}$. However, this difference is marginal, considering the large spread of the results.

The differences between these two materials can be further investigated through comparison of both materials through tests on milled specimens.

Production angle

Tensile tests on untreated specimens indicated a connection between production angle and σ_u irrespective of geometrical influences. This effect is confirmed by tensile test on milled specimens. A strong negative correlation between production angle and σ_u was found. This dependency was shown in figure 6.19b.

The influence of the production angle on $\sigma_{0.2}$ and the ductility is less clear. The spread in $\sigma_{0.2}$ and ϵ_u is large compared to the spread in σ_u , which is due to several reasons. First, $\sigma_{0.2}$ is based on the Young's modulus which is difficult to determine from a tensile test. Secondly, strain-hardening plays an important role. Because stainless steel does not have a clear yield plateau, geometrical deviations influence the stiffness of the rod and alter the shape of the stress-strain diagram.

Process sensitivity

The variations in process parameters did not result in significant changes in strength values. This is in line with the findings from the literature research; the structural properties of these types of steels are relatively insensitive to the welding process.

Batch 3, however, saw markedly reduced strength values, with σ_u reaching values as low as 343 MPa. This was caused by material defects due to a production error.

The variations in process parameters in this research were only small. Further research is necessary to see if greater variations will result in greater differences between batches.

0,2% proof strength

$\sigma_{0.2}$ averages at 299 MPa for correctly printed test specimens, but again, large spreads are observed. On average, $\sigma_{0.2}$ is 280 MPa in milled specimens. The difference between these values is likely caused by strain-hardening in the as printed test specimens, causing extra stiffness and leading to a higher value for $\sigma_{0.2}$.

Ultimate strength

Ultimate strengths of correctly printed test specimens range from 550 to 700 MPa, averaging at around 611 MPa. Milled specimens show less spread than as printed specimens, but also average at about 600 MPa, ranging from 565 MPa for 60°specimens to 625 MPa for 0°specimens. This value is very close to 616 MPa, which was reported for 316LSi steels by Rasmussen¹. The welding wire manufacturer reported a σ_u of at least 520 MPa. Indeed, this value is exceeded for all correctly produced specimens.

Young's modulus

The spread in Young's modulus is an important aspect to consider when designing a structure. When a certain part of a construction is less stiff than expected, alternative load paths may be engaged, leading to overloading of stiffer structures. However, it seems unlikely that there would truly exist such a big spread in a property that is usually considered an accurate and constant material property in structural engineering. A lower or higher calculated Young's modulus can be caused by wrongly calibrated measurements of the diameter. This would not explain the spread though. It may be that the extensometers are not accurate at small displacements, or because the tensile test is simply not a good way of determining the Young's modulus.

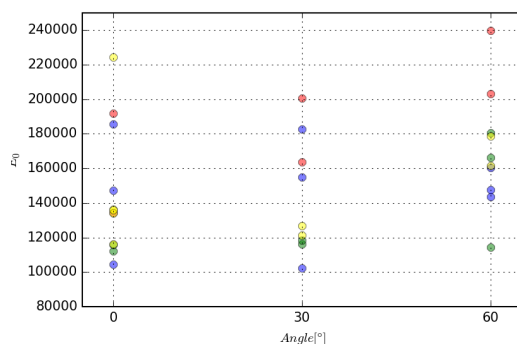


Figure 6.24: Young's moduli for all batches

The geometrical deviations do influence the perceived stiffness of a rod. Depending on what value of the diameter is taken for the calculation of stress, the perceived stiffness can be higher or lower than the actual value of the material. All the stress-strain data in this thesis is based on the minimum diameter unless noted otherwise. In this case, the fact that the rest of the rod is of greater diameter, means that the perceived Young's modulus should be higher. The measurements, however, show lower values. According to the numerical models that were made of the rods, see section 7.1.2, the perceived Young's modulus of for example test specimen 4-00-A would be 244.000 MPa. If the average diameter were used, the perceived Young's modulus would be slightly lowered in comparison to the actual value of 190.000 MPa, to a value of about 188.000 MPa.

Residual stresses are known to lower the apparent stiffness of a material. However, the rods are hardly restrained as they are produced, so it is not very likely that residual stress play an important role. Finite element modelling and neutron imaging can give insight in any residual stresses that might be present in the material.

Alternative test methods should be considered to determine the Young's modulus. The milled specimens that were investigated in this thesis, were milled over only a very small

¹Rasmussen 2003.

area. This area was too small to attach the extensometers that were used in the other tests. Tensile tests on milled specimens with proper equipment to measure the extension of the milled area can exclude any effects of geometry on the stiffness. Bending tests can be performed to determine bending stiffness. From these results, the Young's modulus can also be calculated. Other alternatives include resonant frequency and wave propagation methods.

Ductility

It was suspected that the production angle of a test piece would have a profound influence on the ultimate strain, because the irregularity of the geometry increases as the production angle increases. Large deviations in the rod diameter lead to lowered deformation capacity. While figure 6.25 shows a slight decrease of ϵ_u as the production angle increases, the effect is small. The ultimate strain is mostly determined by the occurrence of extreme values of the diameter. These areas of small cross-sectional area are determining for ϵ_u . Such defects can occur at any production angle, affirming the need for quality control. The

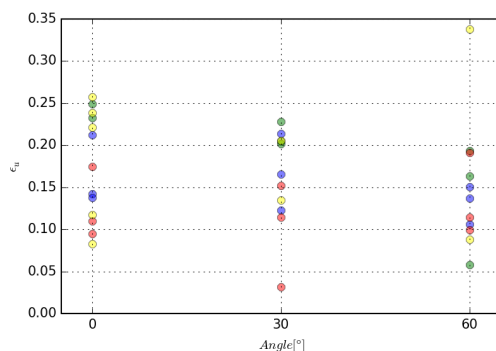


Figure 6.25: Diameter standard deviation versus ultimate strain

specimens that did not contain a geometrical or material defect, exhibited tough material behaviour. The eurocode² describes the ductility requirements as seen in equation 6.3.

$$\begin{aligned}
 f_u/f_y &\geq 1.10 \\
 \text{Elongation at fracture} &> 15\% \\
 \epsilon_u &\geq 15\epsilon_y \text{ with } \epsilon_y = 0.2\%
 \end{aligned}
 \tag{6.3}$$

Only the second requirement is not met for all correctly printed specimens. The actual lowest value of ϵ_u for these specimens was 12 %. It should be investigated whether this is enough to design safe structures, or if the process needs to be further improved.

Design

In ordinary steel structures, the ultimate strength of the weld material is used to determine the capacity. The design philosophy is to make the weld so strong that plastic deformation can occur outside the weld area. The deformation capacity is thus provided by the surrounding material. Since printed structures are in fact one big weld, there is no surrounding material, and the ductility requirements have to be fulfilled by the printed material itself, see also section 9.1.4. When the ultimate strength is used to design these structures, large plastic deformations may occur and deformation capacity is not guaranteed. Therefore, a lower value must be taken into account. In traditional stainless steel

²NEN 2011a, p. 30.

structures, the 0.2% proof strength is used. However, this value has proven to be difficult to determine from tests. The 0.2% proof strength should be chosen such, that safe structures can be designed while minimizing the amount of material used. The value must be safe, but not too conservative.

Because σ_u is clearly defined, and the ratios between $\sigma_{0.2}$ and $\epsilon_{0.2}$ and σ_u and ϵ_u determine the deformation capacity and safety of the structure, it is suggested to choose $\sigma_{0.2}$ as a percentage of σ_u . When $\sigma_{0.2}$ is taken as 50% or lower of σ_u of milled specimens, all Eurocode ductility requirements with regards to strength are met. Furthermore, when this value is used in combination with a lower bound value for the minimum diameter, the occurring stress is expected to be below the actual $\sigma_{0.2}$ and the larger diameters lead to added stiffness. This ensures the material is still in the elastic region, preventing plastic deformation and providing sufficient stiffness, which is important for SLS calculations.

In ULS, a higher value can be considered. Plastic deformation may occur, as long as sufficient deformation capacity and safety is guaranteed. Nevertheless, the choice for an increased strength value in ULS should be supported by further research and thorough statistical analyses of safe design values.

6.6 Fatigue tests

The fatigue batches were produced with the same parameters and are discussed together. Table C.1 in appendix C.1 summarizes the results.

6.6.1 Overview

In figure 6.26, the fatigue lifetimes have been plotted in an S-N diagram. The logarithmic fit to the data excludes the first specimen, which was produced as a test and greatly outperformed the other specimens.

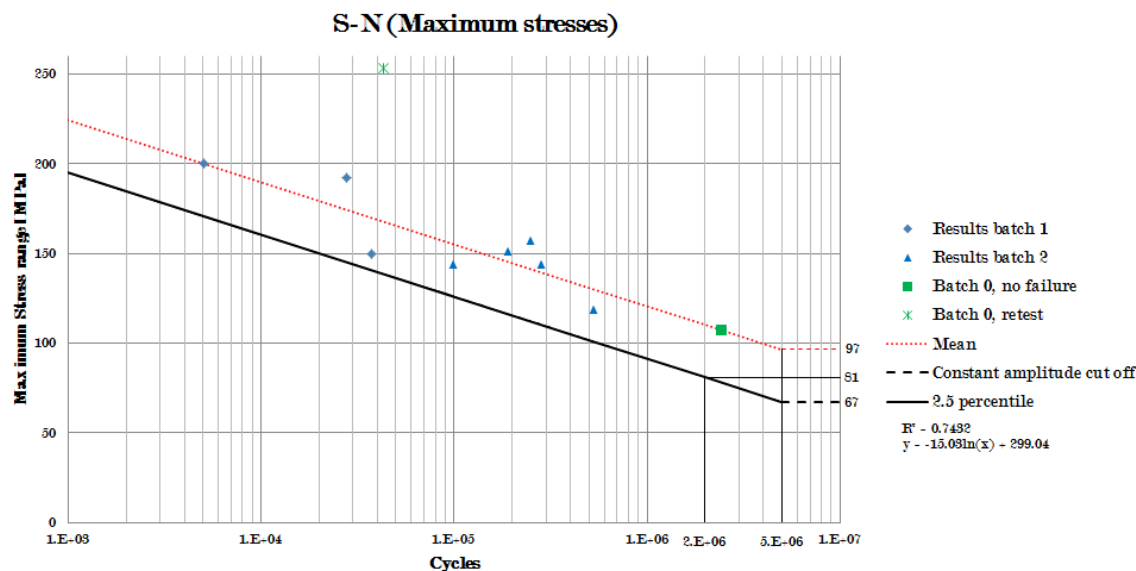
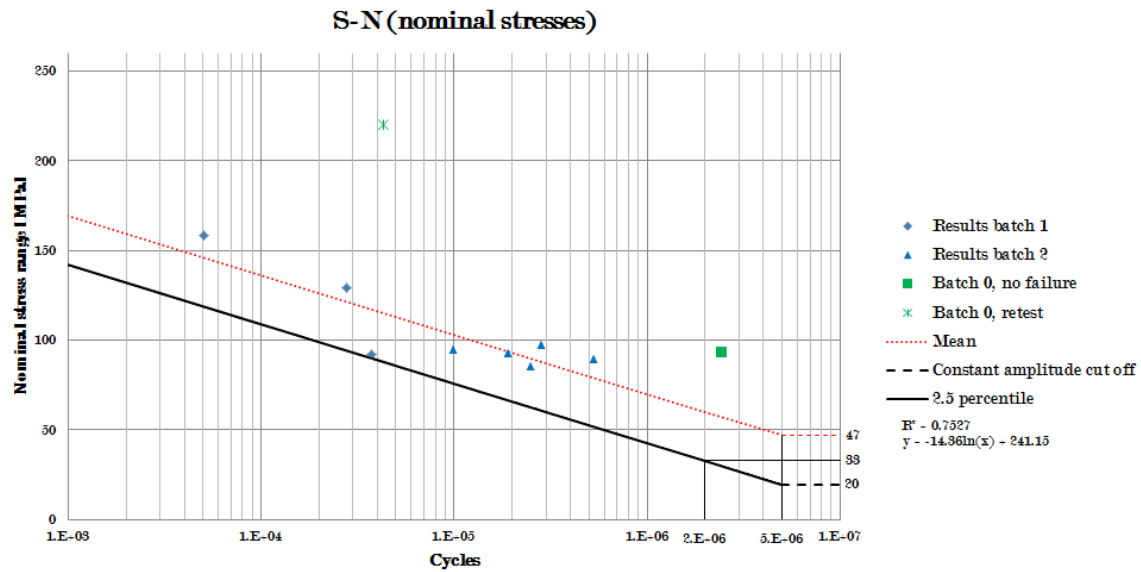


Figure 6.26: S-N data

The very first fatigue specimen, coloured green and indicated 'batch 0' was first test at a stress level of about $100N/mm^2$. After two and a half million cycles, and more than two weeks of testing at 2 herz, the test was stopped. Because no significant change in displacement amplitude had been registered, it was assumed that hardly any damage was



done so far. (See appendix C.7.3 for typical crack development in the test pieces) The piece was subsequently tested at a higher stress level, $250\text{N}/\text{mm}^2$ so that it would surely fail within an acceptable period of time. The following test pieces were tested at intermediate stress levels.

The Eurocode 3 provides guidance on the use of these test results to determine the fatigue strength of a certain detail. This determination should be based on at least 10 tests. The standard deviation, the dimensions of the test pieces and the effects of residual stresses should be taken into account³. In any case, if fatigue loading is expected to play an important role in a structure, more research needs to be done on the influence of the welding parameters and on specific constructional details or joints.

Nevertheless, the S-N diagrams include a mean fit to the data, as well as a 5 percentile design curve. As expected, the SN diagram indicates increasing fatigue lifetimes for decreasing stress levels. It is expected that this trend will go towards a cut-off limit, beyond which no failure will occur. With a greater number of tests, a more accurate fatigue strength class may be assigned to this type of structural element. This cut-off limit is usually set at 5 million cycles for constant amplitude loading. Figure 6.26 shows the S-N curve based on the minimum diameter of the test pieces, corresponding to a detail class of 81 MPa at 2 million cycles. Lower allowable stresses and a detail class of 33 MPa are found when the average diameter of the rod is used, see figure ???. Either curve may be used to assess fatigue damage in a rod. The minimum diameter curve, however, allows for better comparison to other types of rods which are produced differently. The average diameter curve can only be used for this type of rod, because it does not correct for any geometrical deviations.

6.7 Buckling tests

The test results from both type of buckling tests, clamped and hinged, are addressed in this section. See table C.3 in appendix C.1 for an overview of the results.

³NEN 2011b, p.26.

6.7.1 Clamped tests

Batch 2

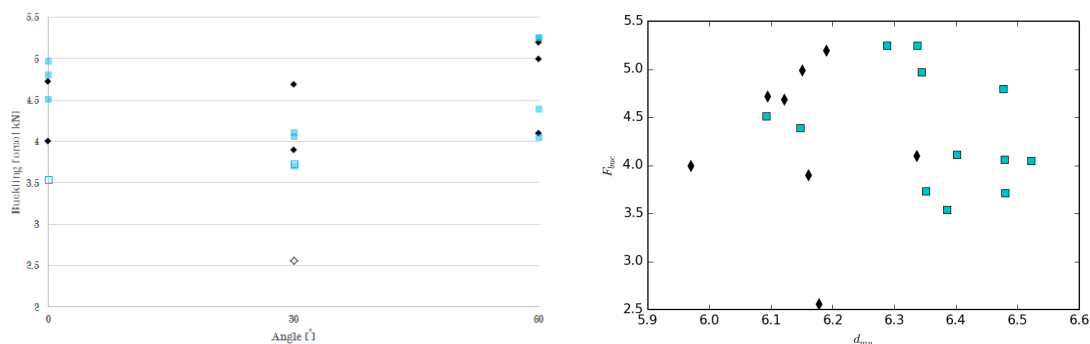
Since only tensile tests were performed on batch 1, batch 2 is the first batch that included buckling tests.

Batch 3

Buckling tests were performed on all of the test pieces in batch 3.

Overview

Figure 6.28a shows the results from the first set of buckling test per production angle. Unlike for the tensile test results, there is no clear indication of a correlation between the angle and the buckling load. Local geometrical characteristics are not of much influence either on the buckling load. In figure 6.28b the average diameter is plotted against the buckling load. The reason for the apparent lack in correlation lies in the fact that the



(a) Production angle versus buckling load (b) Production angle versus buckling load

Figure 6.28: Overview of buckling load results

Batch 1 = black; batch 2 = cyan

slenderness is only slightly altered. In the range investigated, the geometrical and material imperfections of the rod and the forces and displacements that are introduced as a result of the clamping are of far greater influence than the small change in diameter. To study the influence of the diameter of the rods and the influence of the buckling length, a test has to be set up with a larger range of slendernesses. Additionally, to eliminate any moments or initial imperfections that may be introduced by the clamping of the test piece, the test set-up should be changed. A set-up with two hinged connections at different system length is proposed for further study.

6.7.2 Hinged tests

Batch 4

With specimens from batch 4, hinged buckling tests were performed on a range of slendernesses. The results will be discussed in the next section

6.7.3 Overview

The results of both clamped and hinged tests have been combined in figure 6.29. The relative slendernesses are plotted against the ratio between the buckling load and the

plastic compressive resistance. This figure is based on a theoretical value of the Young's modulus, namely $E = 190.000N/mm^2$, and an average value of the yield strength of $280N/mm^2$. These values were chosen, because the actual properties proved to be difficult to determine from the tests. The average diameter was used to determine N_{pl} and a partial factor $\gamma_{M1} = 1.1$ was applied.

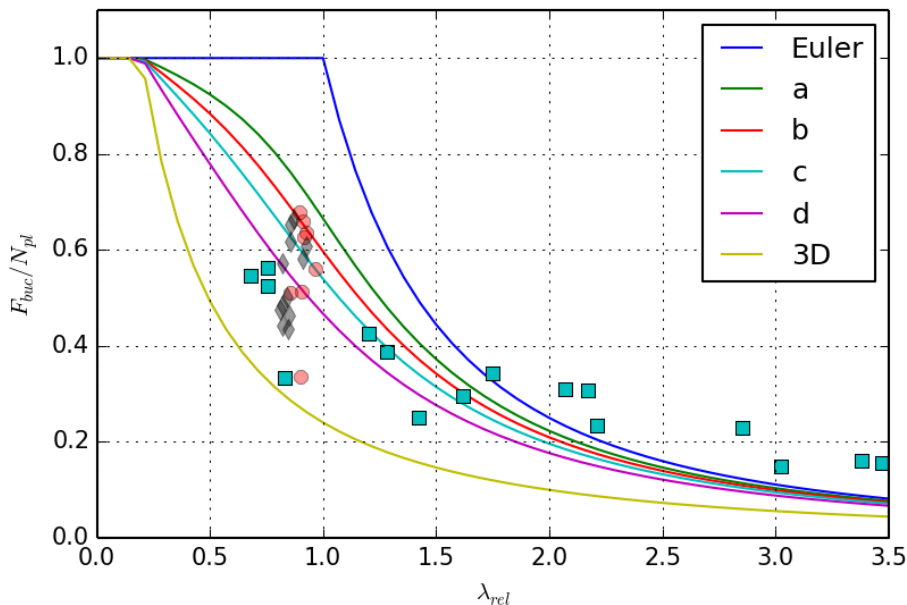


Figure 6.29: Buckling curves and test results

The results do not correspond to any of the buckling curves that are currently given in the code. Therefore, a buckling curve specific to this production method and material is proposed, which is indicated in the diagram as curve '3D'. A value for the limiting non-dimensional slenderness of 0.1 has been used to take into account the high local deviations of the geometry. Additionally, to account for global inaccuracies, the imperfection factor was set to 3 so that all test result fall within the buckling curve. This proposed buckling curve can be seen in figure 6.29.

Some results are above the Euler buckling load, which is likely caused by strain-hardening of the material⁴. Because stainless steel has no yield plateau, strain-hardening plays a larger role for the buckling behaviour than in ordinary construction steel.

Existing buckling curves overestimate the buckling load for smaller slendernesses. Therefore, the proposed buckling curve is more conservative than existing buckling curves for ordinary steel structures. The geometrical deviations in the printed rods are far greater than those in rolled, cold-formed or welded sections. This leads to greater eccentricities of the applied loads and greater internal moments, reducing the buckling resistance. It is practically impossible to determine the neutral line of a rod and, let alone apply a load centrally. Eccentric load introduction is inevitable.

The 3D buckling curve in figure 6.29 is determined visually by varying the imperfection factor α and the limiting non-dimensional slenderness $\bar{\lambda}_0$. α was set to 3, and $\bar{\lambda}_0$ to 0.1. Future research should address best fit methods to fit a buckling curve to the data. Through statistical analysis of this fit, confidence intervals of this curve can be created, and a certain level of safety can be guaranteed.

⁴ESDEP 2015.

Chapter 7

Test modelling

In this chapter, analytical, numerical and FEM models are presented and compared to actual test data. Depending on the complexity of these models, the amount of models is limited to a certain number of specimens.

7.1 Tensile tests

7.1.1 Failure load

The determining factors for the failure load are the minimum diameter and the ultimate strength. A model was made to predict the failure load based on the actual measured minimum diameter of a rod and the ultimate strengths found in the milled specimens tests. In figure 7.1, the predicted failure load is plotted against the actual failure load and linear regression has been applied to all test pieces that were produced correctly and did not contain an obvious defect. The linear regression is very close to an exact prediction,

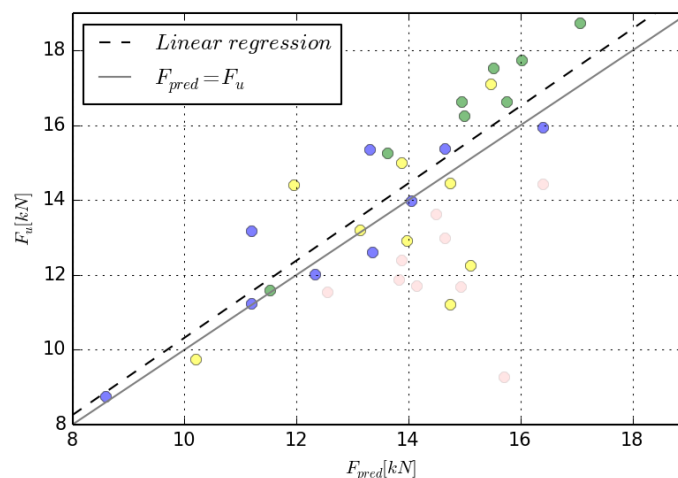


Figure 7.1: Predicted failure load versus actual failure load

it almost matches the purple line, which represents the line $F_u = F_{prediction}$. The test results show some spread around this line, though, which is to be expected considering the spread in strengths observed in the actual tensile tests.

If other materials are to be used for printed structures, a model like this may give an idea of the expected failure load. Ultimate strength data from milled specimens, combined with the expected minimum diameter can provide a good indication of the failure load.

7.1.2 Numerical model

The tensile test pieces were modeled as bars under axial loading. Their cross-sectional area varies along their main axis, based on the photographic data of the diameters (1). In the

numerical model, the force was increased stepwise. For each load step, the strains were obtained through the cross-sectional data and the Rasmussen stress-strain relationship (2). By integrating the strains over the length of the bar, the displacement at the end was obtained (3). This procedure is shown schematically in figure 7.2.

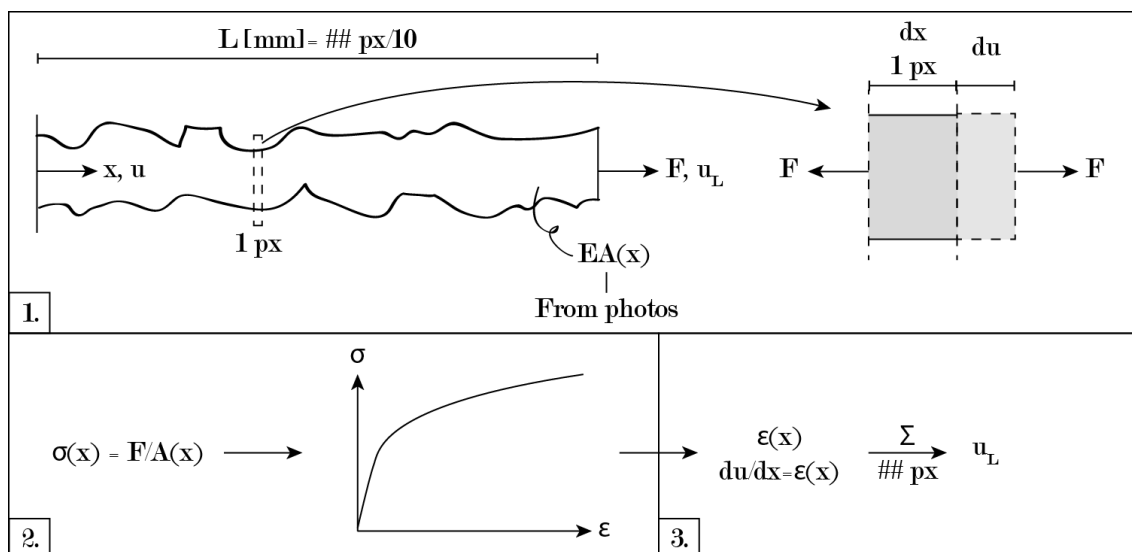


Figure 7.2: Numerical model

Comparison to test data

In all of the stress strain diagrams in the appendix, the numerical prediction has been plotted. It always underestimates the the ultimate stress and strain. The yield strength, however, is consistently overestimated. The plotted models are based on theoretical stress-strain data.

Stress-strain data from milled specimens improve the estimation of the ultimate stress, but do not improve the overall shape of the stress-strain diagram.

Interestingly, rods deform a lot more than predicted through the numerical model. It is not clear at this moment why this happens. Perhaps, the problem lies in the description of the material properties. While the geometry is modelled as varying over the length, the material properties are considered constant. As shown in the micrographs and determined through structural tests, the material is not isotropic. Grains are oriented at different angles and are of different size and shape. Furthermore, small defects inside the material might occur once in a while. In a milled specimen, failure will occur where the material is weakest. This weak spot may determine the deformation capacity. In a normal specimen, the structural behaviour is a function of both material and geometry. The chance that a weak spot inside the material coincides exactly with an extreme diameter is very small.

A model with both varying material properties and geometrical properties might perform better than the current model. At the moment, however, the model is conservative with regards to deformation capacity, which is preferable when the underlying mechanisms of structural behaviour are unknown.

Simplified models

This numerical model is not always practical. Firstly, the exact geometry is not always known. Catalogues of type of rods will only include average diameters, standard deviations and safe minimum diameters. For calculation purposes, a model based on these parameters

should be investigated and compared to the more complicated model. An example of such a model, using a sinusoid to describe the model geometry was described in section 3.1.1.

Secondly, even if the exact geometry is known, the model is not suited to quick calculations. A computer is required to perform the calculation. Quick hand calculations can be made if simplified models are created based on fictional structural properties, such as an effective modulus of elasticity and average strain data.

7.1.3 FEM model

The next step up in model complexity is a FEM model. By using actual geometrical and material properties of rods, the structural behaviour can be modelled very accurately. By performing structural tests as well, these models can be fine-tuned to match real world data. With these kind of models, costly and time-consuming laboratory experiments may be replaced. They may also be used to check the structural capacity of structures that are already printed. By making a 3D scan of the printed structure and turning it into a finite element model, the capacity of existing structures may be assessed. It can play a role in on site inspection.

By using 3D models obtained through photogrammetry, some FEM analysis was performed. Figure 7.3 for a test in Abaqus. These particular models are not meant to give an accurate representation of the structural behaviour; they contain many flaws. Rather, they should be treated as a proof of concept and give direction to future research. Photogrammetrical data can be used to construct a FEM model, and such a model may give valuable insight into structural behaviour, but in future research, this topic should be addressed in more detail.

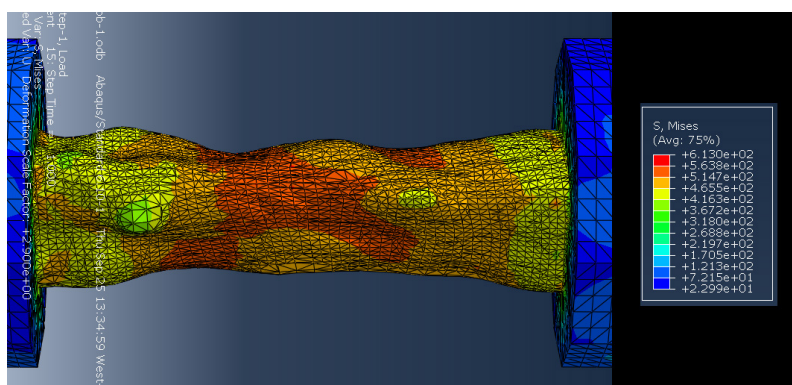


Figure 7.3: Example of modelling plastic rod behaviour in Abaqus

7.2 Buckling tests

7.2.1 Analytical model

Based on the Eurocode and the Ayrton-Perry formula for buckling strength, buckling loads can be predicted.

7.2.2 FEM model

Like the FEM models for the tensile test, these models were only made to show that photogrammetrical data can be implemented to model buckling behaviour in Abaqus.

A FEM model in which the non-linear buckling of the test pieces was analysed resulted in buckling loads that were in the same order of magnitude, about $0.5 \cdot F_{Euler}$, as the true buckling loads for the clamped specimens. However, these results are based on theoretical stress-strain data and do not take into account clamping moments. See figure 7.4 for an example of such a test in abaqus.

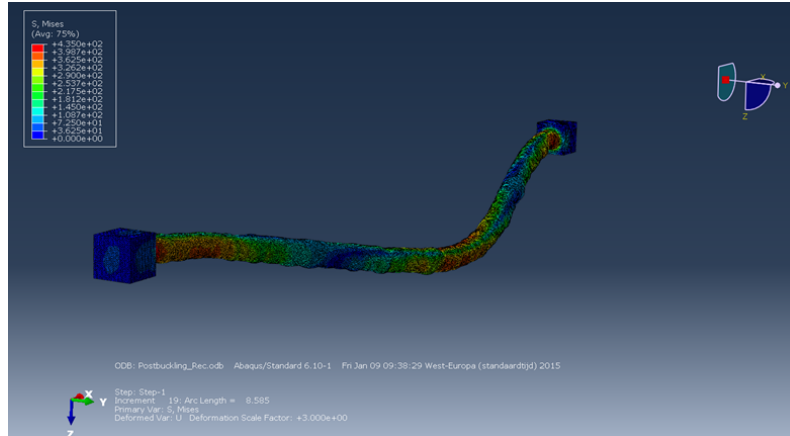


Figure 7.4: Example of modelling buckling in Abaqus

The model that was made for this research was based on a clamped test set-up. However, it is very difficult to model the boundary conditions in this set up. Plastic deformation and moments introduced due to the clamping were modelled. It is recommended that future models are based on a hinged set-up. In this set up, the load introduction is very clear and the boundary conditions are simple.

By calibrating the model and performing analyses, the effect of rod geometry on the imperfection factor and the limiting non-dimensional slenderness can be investigated without performing actual laboratory experiments. Moreover, these models can be also be used as a part of on site inspection. The effect of a certain misprint or geometrical defect in a structure that is printed on site can be studied without damaging the original structures. An assessment can then be made whether a repair is actually necessary.

Chapter 8

Quality control

The test results have indicated a great spread in structural properties. Due to a faulty production process, the structural properties of test specimens in batch 3 were greatly reduced. For some specimens in the other batches, low strength and ductility values were found as well because of defects in the material. These findings emphasize the need for quality control to be able to design economically and safely. This issue is addressed in this chapter.

8.1 Types of defects

The defects that have been found in test pieces can be divided into two main groups: material defects and geometrical defects. Material defects occur inside the material, while geometrical defects are given shape by the material.

Material defects

Batch 3 clearly showed degraded structural properties. This was most likely due to a broken nozzle, which led to poor gas shielding, possibly directing the gas into the weld pool instead of around it. This defect is shown in figure 8.1.



Figure 8.1: Material defect in batch 3

Other defects, such as cold and hot cracking or lack of fusion have not been observed. Slag inclusions are not an issue, because no flux coating is used. When other materials or welding processes are used, different weld defects may occur.

Geometrical defects

In all batches, geometrical defects appeared once in a while. Such a defect takes the form of a locally very small diameter or a misprint of material. The former might occur due to chance or because the welding torch is not at the right height. Since no on-line measurement and feedback of layer height was present, errors in the position of the robot with respect to the workpiece- for example due to shrinkage - can pile up and result in a defect. A misprint is caused by a misalignment of welding torch and workpiece.

Asymmetric shrinkage of the workpiece may play a role here, but also a shift of the workpiece or robotic arm because either of them is moved or shaken. The rods printed in this case were relatively small and stiff. In larger structures that are prone to vibrations, misprints or other geometrical defects might be likely to the relative movement welding torch and workpiece. Such effects should be considered when determining a printing strategy.

Figure 8.2 shows a misprint and a very small diameter.

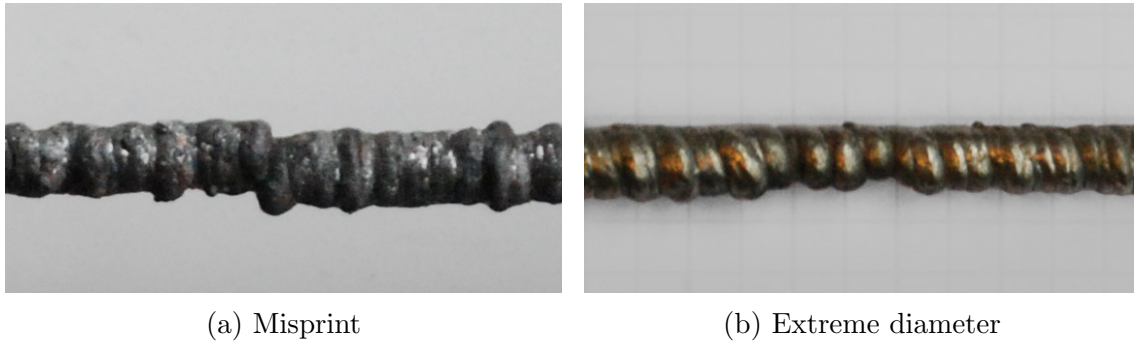


Figure 8.2: Geometrical defects

8.2 Repairs

Defects should either be repaired, or the safety concept of the structure should be such to allow for failure of individual elements. If sufficient redundancy is present, some elements can be allowed to fail. However, this is not very economical, and even in redundant designs, it might occur that a defect occurs in a critical area. In this section, some suggestions are made on when and how to repair a specific defect.

Defects greatly reduce the structural performance of rods loaded in tension. Repairs of such defects are therefore essential in tension elements. Compression elements are relatively insensitive to material defects, but they are sensitive to eccentricities as a result of misalignments. Reductions in stiffness due to small diameters only play a significant role if they are close to halfway the buckling length. At these points, the curvature is the greatest and a reduction in stiffness will lead to the greatest reduction in capacity. Defects in tension elements should always be repaired; defects in compression elements only require repair in specific cases.

Material defects are difficult to repair, if it is at all possible to locate them. The affected area has to be grinded away or cut out and then reprinted.

Geometrical defects can be repaired much more easily. The repair area should first be cleaned, to minimize the risk of contamination of the weld pool. In case of a small diameter, some extra weld material can simply be printed onto the structure to strengthen it. This will work for both tension and compression elements. In case of a misprint or misalignment, extra material can be printed in order to reduce stress concentrations and to make the transition from one side to the other more gradual. This will work well for tension elements. Thanks to the ductility of the material, the failure load of the tension element is likely not reduced. In the case of small misalignments in non-critical areas, this approach is also suited to compression elements. If the eccentricity due to the misprint is large and will critically lower the buckling load, another repair method is needed. In such a case, the element could be cut at the misalignment, repositioned, and then printed or welded together in the right position.

The types of repairs described above are based on engineering judgement and experience with ordinary repairs of welds. Their effectivity is not proven and should be demonstrated in laboratory experiments. Repairs in ordinary steel structures are known to weaken the base material. Due to the welding process, the microstructure is disrupted, alloying components are segregated and residual stresses are introduced. In a printed structure, however, the base material is welded itself. Any problems associated with the welding process are already inherently part of the structure. Some additional residual stresses may be introduced, and the existing columnar grain structure may be disrupted, but these effects will probably be marginal compared to the irregularities already presented in the material and the geometry.

In structures that are grinded or otherwise processed to reduce geometrical irregularities, the impairing effects of a repair will become more evident. Again, these statements will have to be backed up by tests in future research.

8.3 Inspection

If a defect is to be repaired, it has to be detected first. Hence, inspection of the structure after printing is essential. All printed structures should at least be visually inspected.

By visual inspection, geometrical defects can be detected quite easily. All batches of test specimens were examined before they were tested. Any defects, small diameters or misprints, were documented. All the test pieces - with exception of batch 3 - that failed prematurely, contained a visually detected defective area. Failure always occurred in this area. In only a few cases an area was marked as a defect while failure occurred elsewhere. If required, critical areas such as joints may undergo additional inspection. Photographic and photogrammetrical or other 3D scanning methods can give a good representation of the geometry. Nevertheless, a visual inspection proved to be sufficient for the test pieces in this research.

Defects inside the material are much harder to detect. Naturally, they cannot be observed visually. Ordinarily, such defects are detected by means of magnetic, ultrasonic or radiographic testing. Magnetic and ultrasonic testing, however, cannot be performed on small, irregular surfaces. Radiographic testing may be possible, but is by far the most cumbersome of the three. Moreover, since an image of the rod does not include any depth information, it will be difficult to distinguish between irregularities of the geometry and internal defects. The circular shape further complicates radiographic testing; because of the variation in thickness, the edges will likely be overexposed. Radiographic testing is only useful in very specific cases.

For material defects in particular, the focus should be on prevention rather than inspection and repair. Printed test samples can give an idea of the quality of the printed material without resorting to expensive and difficult non destructive testing. Additionally, 3D scanning of the structure and finite element modelling can help in the assessing whether a repair is necessary.

8.4 Process control

Since there are no practical ways of inspecting and repairing material defects, it is of great importance to control the process and minimize the chance of occurrence of such a defect. Through test prints, a consistent quality for a certain type of rod has to be proven. All process parameters for this type have to be documented exactly. The procedure describes the type of printer, the material, the shielding gas, robotic parameters and all other relevant process parameters. Structural tests and accurate measurements have to

be carried out on the test prints. By performing statistical analyses on the results, safe design values should be given for the geometry and the resulting strength. The specific parameters and properties from this thesis research have been supplied in the appendix.

As Additive Manufacturing techniques are further developed, the documents describing the printing procedures should be standardized. In ordinary welded structures, Welding Procedure Statements (WPS) and Welding Procedure Qualification Records (WPQR) fulfill this role. The printing equivalents would be a Printing Procedure Statement (PPS) and Printing Procedure Qualification Record (PPQR). A PPS should contain all the information that is needed for a printer operator to print a certain structure. An allowable range of welding and robotic parameters is supplied. The PPQR is a report of an actual printed structure, that includes structural test results and an accurate geometrical description. Depending on the application of the structure, specific qualification records may be required. In the case of this bridge, this record would include results from both static tensile tests and fatigue tests. The precise process parameters that were used to print this structure are also included.

The operator of the printer himself should also be qualified. A Printer Qualification Test Records (PQTR), analogous to a Welder Qualification Test Record (WQTR), is a document that describes which printing procedures the operator is certified to execute. Lastly, printing inspectors should also be certified professionals. They are certified to inspect and approve of printing operators, procedures and actual structures.

8.5 Environment control

All test specimens examined in this thesis were produced in a protected environment. The printing robot was inside a workshop, with no outside influence. Rain or wind did not hinder the production process. In an outside environment, when a structure is printed on site, this is not the case. If the structural elements studied in this thesis are to be used for outdoor application, the indoor printing environment has to be replicated. In ordinary welding, welding tents are used to protect the welding process from the environment. Wind, rain, and moist have to be kept away from the weld pool to control the process and prevent defects. Wind drafts can result in impaired gas shielding and poor weld pool shape. Moisture in weld areas can lead to rust, porosity and hydrogen cracking. The quality and consistency of the printing process in an outdoor environment, with or without welding tent is not guaranteed. Therefore, additional testing should take place in order to investigate what influence the environment might have on the geometrical and material properties.

8.6 Test samples

An essential part of the control over the process is the printing of test samples. Since the properties of printed material vary from batch to batch, test prints should be made whenever production starts or restarts. Parts of the printing robot may break down and result in material defects that cannot be detected visually. Test samples are indispensable for the detection of any material defects.

These test prints should be measured accurately, and compared to the required geometrical properties. The prints should also be kept for tensile testing to verify ductility and strength. Because it is not practical or economical to test them in a laboratory individually, they may be stored and tested together at a later stage. However, if there is reason to believe that material defects have occurred, tensile testing should be carried out as soon as possible. If the measurements or material properties differ significantly from

the design values, the printing process should be stopped, and the printing robot should be examined. Any structures already printed in this same batch should be inspected thoroughly. If necessary, repairs or replacements should be printed. If the structural properties are lowered, but still meet requirements with regards to ductility, recalculation of the structure is also an option.

Chapter 9

Conclusion

9.1 Conclusions and recommendations

9.1.1 Geometry

The geometry of the rods studied within this thesis is highly irregular. First, the level of control over the geometry during production is described. Secondly, the effect of the production angle on the geometry is explained. Then, the characterization of this geometry is discussed. Next, the correlation between the length of rod elements and the expected minimum diameters is stressed. Finally, on the basis of these conclusions, recommendations on the design are given.

Control

With the current printing procedure, only small adjustments can be made to the geometry. The average diameters produced ranged from 5.7 mm to 6.9 mm. With the current state of the control over the process, it is not possible to input certain desired geometrical properties and have the material printed accordingly. However, there is some trial and error experience with changing the parameters in order to influence the diameter. The exact effect of changing a certain parameter, however, is not known.

Therefore, a design should be based on types of rod elements of which the properties are known. Per type, the process and the resulting geometrical properties are described. The engineer can then pick the types of elements he wants and apply them in his design.

Response surface methodology has the potential to quantitatively predict certain geometrical properties and steer the process on-line. Setting up such a method lies outside the scope of this thesis, but is essential in the further development of additive manufacturing, increasing its range of applications, and making it more accessible to a wider range of users.

Production angle

As the production angle of a rod increases, so does the geometrical inaccuracy. Rods produced at 60° show greater spread than those produced vertically or at 30°. The average diameter is affected, as well as the spread in diameter and the minimum diameter. This leads to reduced ductility and strength values. An economical design should take into account the effect of the production angle on the geometry.

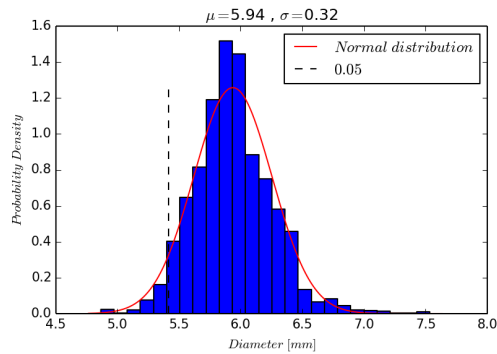
Characterization

The minimum diameter from actual measurements is a good predictor of tensile failure load. Since accurate measurements of the actual structure are not yet present in the design stage, safe values for the rod diameter should be provided by the supplier.

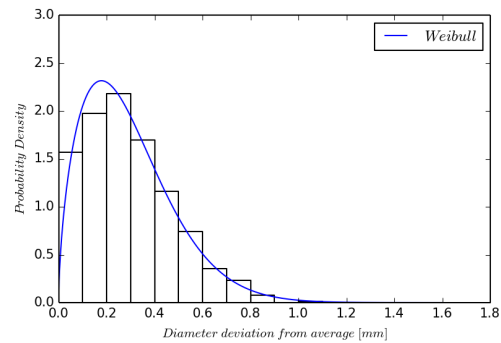
Statistical descriptions of the product based on actual measurements can be used to give such safe values. This research suggests the use of a normal distribution to describe the total geometry of a rod. Additionally, the minimum diameters of rods have been analyzed.

The Weibull distribution gives an accurate representation of these diameters. See figures 9.1a and 9.1b for examples of normal and Weibull fits to the data.

Depending on the level of safety required, a certain percentile value of these distributions may be used. The choice for this value should be based on the safety concept of the design. If redundancy is present in the design, a higher characteristic value for the diameter may be used.



(a) Distribution of total geometry



(b) Distribution of extreme minimum diameters

Length dependency

The 95 percentile value of the minimum diameter of a rod depends on the length of a rod. A minimum occurs approximately once every 2 mm. The distribution of these minima follows approximately a Weibull curve. The chance of occurrence of a small diameter increases as the rod length increases. Because of the shape of the distribution, the minimum diameter decreases more rapidly for smaller lengths. For larger lengths, the minimum diameter approaches an asymptote.

Design

In the previous paragraphs, it was pointed out that each of the following aspects has to be taken into account when designing for certain geometrical properties: the process parameters and specifically production angle, the length dependency, and the statistical description of the geometry.

This results in a design database for different rod types. For each type of rod the process parameters are described, the average diameter is given, and a minimum diameter design graph is given. The process parameters and geometrical descriptions are given in appendix C. Design graphs for all types of rods are given in appendix C.9. Figure 9.2 shows one such design graph for rod lengths of 0 to 1000 mm based on tests performed in this research.

This graph plots the 95 percentile value of the minimum diameter (y-axis) for the length of a rod (x-axis). The gray area represents safe choices of diameters based on 97.5 percent confidence of the Weibull parameters. For example, with a confidence level of 97.5%, 95% of the rods of length 200 mm will have a minimum diameter that is larger than 4.75 mm.

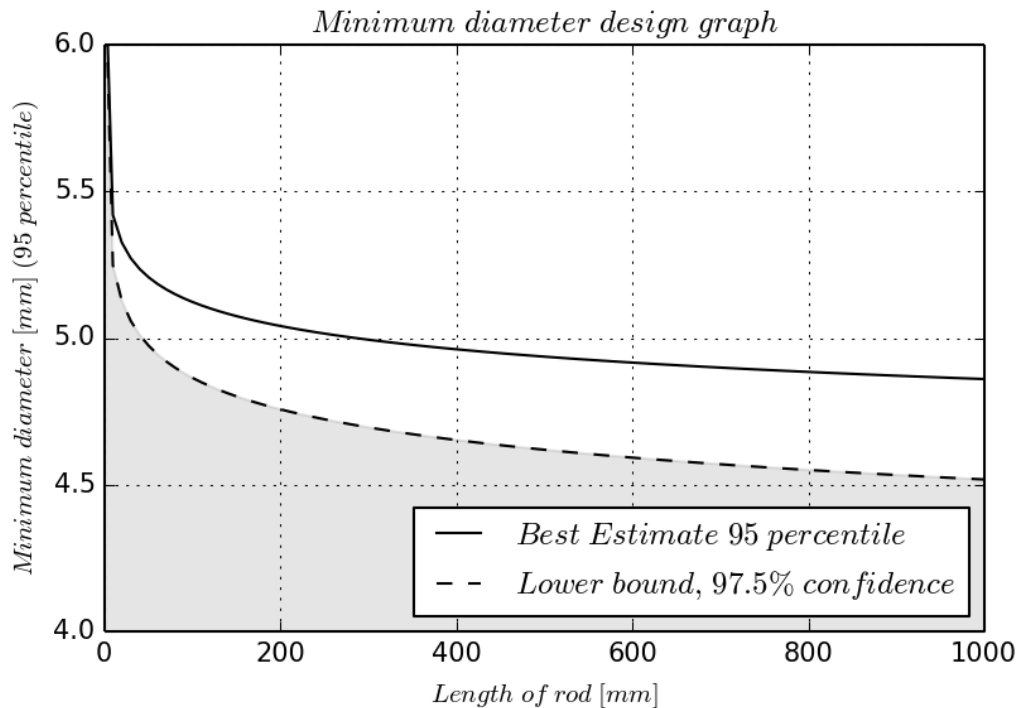


Figure 9.2: Design graph for 4-30 with $d_{average} = 6,42$

9.1.2 Strength

Tensile tests were performed on different batches of specimens. Each batch had their own set of process parameters. Two types of stainless steels, 316LSi and 308LSi, have been investigated. The basic element that was studied in this case was a rod, tested in tension along its main axis. The interpretation and application of the results of this study should be limited to this type of structural element, range of parameters and these two materials.

All stresses are based on the minimum diameter of the rod.

Material

Two types of stainless steels, 316LSi and 308LSi, have been investigated. The test results show similar structural properties for both materials. On average, the strength of 316LSi, $\sigma_u = 629 \text{ MPa}$ is higher than that of 308LSi, $\sigma_u = 603 \text{ MPa}$. However, this difference is marginal, considering the large spread of the results.

The differences between these two materials can be further investigated through comparison of both materials through tests on milled specimens.

Production angle

Tensile tests on untreated specimens indicated a connection between production angle and σ_u irrespective of geometrical influences. This effect is confirmed by tensile test on milled specimens. A strong negative correlation between production angle and σ_u was found. This dependency is shown in figure 9.3.

The influence of the production angle on $\sigma_{0.2}$ and the ductility is less clear. The spread in $\sigma_{0.2}$ and ϵ_u is large compared to the spread in σ_u , which is due to several reasons. First, $\sigma_{0.2}$ is based on the Young's modulus which is difficult to determine from a tensile test. Secondly, strain-hardening plays an important role. Because stainless steel does not have

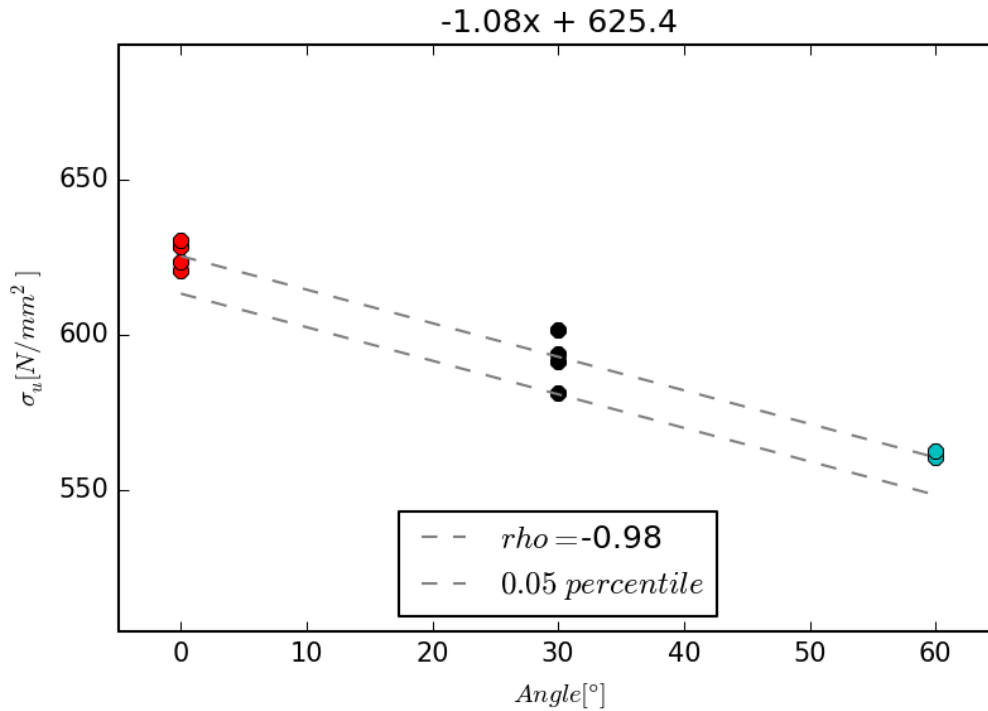


Figure 9.3: Ultimate stress versus production angle in milled specimens

a clear yield plateau, geometrical deviations influence the stiffness of the rod and alter the shape of the stress-strain diagram.

Process sensitivity

The variations in process parameters did not result in significant changes in strength values. This is in line with the findings from the literature research; the structural properties of these types of steels are relatively insensitive to the welding process.

Batch 3, however, saw markedly reduced strength values, with σ_u reaching values as low as 343 MPa. This was caused by material defects due to a production error.

The variations in process parameters in this research were only small. Further research is necessary to see if greater variations will result in greater differences between batches.

Ultimate strength

Ultimate strengths of correctly printed test specimens range from 550 to 700 MPa, averaging at around 611 MPa. Milled specimens show less spread than as printed specimens, but also average at about 600 MPa, ranging from 565 MPa for 60°specimens to 625 MPa for 0°specimens. This value is very close to 616 MPa, which was reported for 316LSi steels by Rasmussen¹. The welding wire manufacturer reported a σ_u of at least 520 MPa. Indeed, this value is exceeded for all correctly produced specimens.

The most accurate values have been found for milled specimens. These values and the dependency of the production angle that was described should be used to describe the ultimate strength, see figure ??

¹Rasmussen 2003.

0,2% proof strength

$\sigma_{0.2}$ averages at 299 MPa for correctly printed test specimens, but again, large spreads are observed. On average, $\sigma_{0.2}$ is 280 MPa in milled specimens. The difference between these values is caused by strain-hardening in the as printed test specimens, causing extra stiffness and leading to a higher value for $\sigma_{0.2}$.

Design

In ordinary welded structures, the capacity is determined based on the ultimate strength of the weld material. In those cases, deformation capacity is provided by the surrounding material. In printed structures, the ductility requirements have to be fulfilled by the printed material itself, see also section 9.1.4. Rather than using the ultimate strength in design calculations, the 0.2% proof strength must be used. However, this value is difficult to determine from tests. The 0.2% proof strength should be chosen such, that safe structures can be designed while minimizing the amount of material used. The value must be safe, but not too conservative.

Since $\sigma_{0.2}$ is clearly defined, and the ratios between $\sigma_{0.2}$ and $\epsilon_{0.2}$ and σ_u and ϵ_u determine the deformation capacity and safety of the structure, it makes sense to choose $\sigma_{0.2}$ as a percentage of σ_u . When $\sigma_{0.2}$ is taken as 50% of σ_u , all Eurocode ductility requirements with regards to strength are met. Moreover, this value is lower than the observed $\sigma_{0.2}$ in tests, ensuring sufficient stiffness for SLS calculations.

In ULS, a higher value can be considered, but this should be supported by further research and thorough statistical analyses of safe design values.

9.1.3 Stiffness

Stress-strain curves

Theoretical stress-strain curves do not match the milled specimen test results exactly. Although the found strength values are roughly the same, the stiffness and ductility differ from theoretical predictions. In general, the stress-strain curve from test data is shorter, the ultimate strain is lower. Since the strength values are in the same order of magnitude, strain hardening occurs at an increased rate.

Young's modulus

The Young's moduli determined through tests average at 172 GPa, which is lower than the expected 190 GPa. Moreover, they show a great spread at a standard deviation of 75 GPa.

It is not entirely clear why this is observed. In the elastic region, the irregularity of the geometry should not have an influence on the stress-strain diagram. One problem is the fact that a tensile test is generally not suited to find out the Young's modulus of a material.

Secondly, Residual stresses can influence the perceived Young's modulus, because they will lead to early yield in the material, subsequently lowering the stiffness of the material. It is not expected, however, that residual stresses play a big role in the rod elements in this research, because they are free to deform while they are being manufactured.

Design

If the Young's modulus truly varies from rod to rod, this can lead to unwanted load paths in statically indeterminate structures. Rods with a high Young's modulus will be loaded

more heavily than those with a low Young's modulus. It is considered more likely that the currently performed tests are inadequate to determine the Young's modulus, than that the modulus actually has a great spread and is much lower than observed. Further research is necessary to reject the theoretical value of the Young's modulus and use the calculated Young's moduli in calculations.

More tests have to be carried out to investigate the Young's modulus, and find out whether it truly has a lower value, and if the spread is due to chance and unsuited measuring methods or an actual material property. Milled specimen tests can be set up to specifically to determine the Young's modulus. In the current set up for milled specimens, it was not possible to accurately determine the stiffness. Bending tests should be performed as well to assess bending stiffness and deduce the Young's modulus. Other tests such as the resonant frequency method and wave propagation methods should also be considered.

9.1.4 Ductility

Requirements

The printed material exhibits tough, ductile behaviour. All correctly printed elements conform to the ductility requirements for ordinary steels described in the Eurocode². These requirements can be seen in equation 6.3.

Generally, the elements that do not perform sufficiently on these requirement are defective elements. They contain either a material or geometrical defect. Only a few correctly printed specimens did not fulfill the requirement of an elongation at fracture of at least 15 %. All correctly printed elements had ultimate strains of over 12 %. Further research is necessary to assess whether sufficient deformation capacity is guaranteed.

Spread

ϵ_u has a large spread because it is an average value over a certain length. As such, it depends highly on the geometrical deviations. Moreover, the place of failure plays a great role. In some cases, the fracture occurs outside the measuring range of the extensometers, leading to a lower observed ϵ_u .

Design

Since the material is ductile and the structural elements have deformation capacity, safe structural designs can be made. Loads will be redistributed and plasticity theory can be applied. Structures will warn and deform heavily before they fail. However, to guarantee sufficient deformation capacity, quality control and repair of defects is of the essence.

9.1.5 Stability

Geometrical influences

For tensile tests, the production process and the resulting geometrical deviations and grain structure play an important role for the structural behaviour. In buckling tests, however, the global geometry determines the buckling load. The average diameter and buckling length are the most important factors.

²NEN 2011a, p. 30.

Production angle

Test specimens of approximately equal slenderness have been compared to study the influence of the production angle on the buckling load. No negative effect of the production angle on the buckling behaviour has been found.

Process sensitivity

The process parameters do not affect the buckling behaviour of test specimens. Even material defects such as porosity, which were present in batch 3 and greatly reduced the tensile performance, did not influence the buckling load.

Buckling curves

A calculation of the stability may be based on the Ayrton-Perry formula³. The results found in this study do not conform to any of the existing buckling curves in the Eurocode. Therefore, appropriate values for the limiting non-dimensional slenderness $\bar{\lambda}_0$ and the imperfection factor α should be derived. This study suggests a lowered value of the non-dimensional slenderness to account for the high local deviations in geometry. Additionally, to account for global inaccuracies, the imperfection factor should be chosen such that a safe buckling curve is created. The test results and a proposed buckling curve can be seen in figure 9.4. This figure is based on a theoretical value of the Young's modulus, namely $E = 190.000N/mm^2$, and an average value of the yield strength of $280N/mm^2$. These values were chosen, because the actual properties proved to be difficult to determine from the tests. The average diameter was used to determine N_{pl} and a partial factor $\gamma_{M1} = 1.1$ was applied.

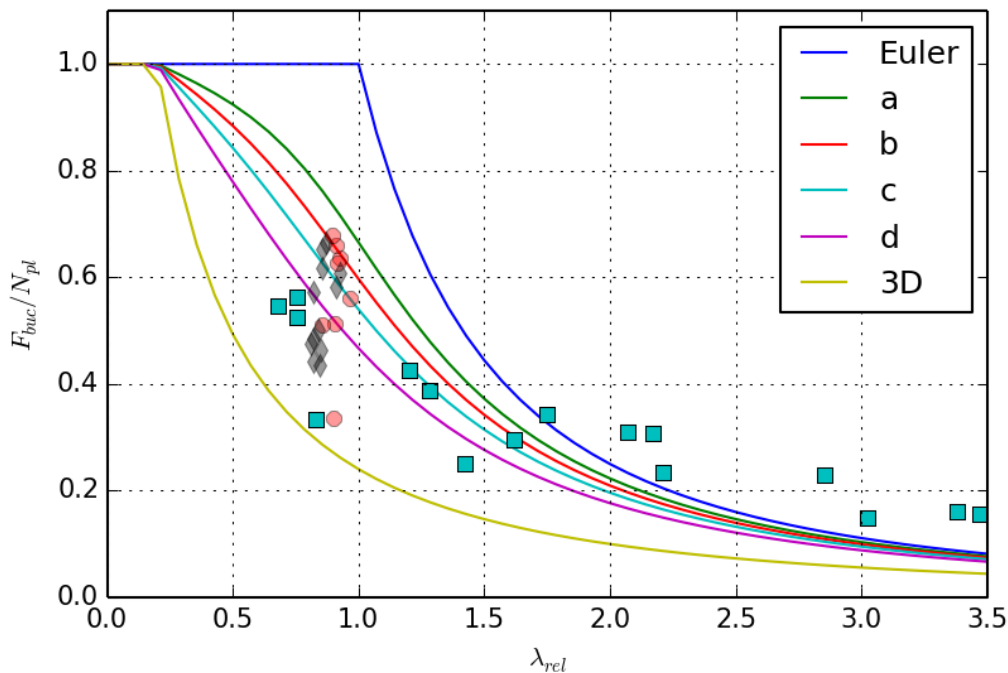


Figure 9.4: Buckling curves and test results

³ESDEP 2015.

The test results show higher values than the Euler buckling load for great slendernesses. This is caused by strain-hardening of the material and an absence of a yield plateau.

Existing buckling curves overestimate the buckling load for smaller slendernesses. Therefore, the proposed buckling curve is more conservative than existing buckling curves for ordinary steel structures. The geometrical deviations in the printed rods are far greater than those in rolled, cold-formed or welded sections. This leads to greater eccentricities of the applied loads and greater internal moments, reducing the buckling resistance. It is practically impossible to determine the neutral line of a rod and, let alone apply a load centrically. Eccentric load introduction is inevitable.

The 3D buckling curve in figure 9.4 is determined visually by varying the imperfection factor α and the limiting non-dimensional slenderness $\bar{\lambda}_0$. α was set to 3, and $\bar{\lambda}_0$ to 0.1. Future research should address best fit methods to fit a buckling curve to the data. Through statistical analysis of this fit, confidence intervals of this curve can be created, and a certain level of safety can be guaranteed. The partial factor γ_{M1} should be adjusted accordingly.

Design

A conservative buckling curve should be used for the design of compression elements. This research suggests the use of the '3D buckling curve' from figure 9.4. Because the buckling load is not influenced by the production angle, compression elements can be applied at any angle in a design. Since tensile elements are more sensitive to production angle, it makes sense to use vertical tensile elements and diagonal compression elements in a truss-like structure.

9.1.6 Fatigue

Production angle and process sensitivity

The tests in this study were limited to on one type of specimens. These specimens were produced with one set of parameters, and printed vertically. Additional testing needs to take place to investigate the influence of the production angle and other process parameters on the fatigue resistance. Moreover, material connections have to be tested in order to be able to design a structure for fatigue loading.

Spread

The results show great spread, so more specimens of this same type should be investigated to get a more accurate value for the detail class. The Eurocode suggests the use of at least 10 specimens per detail class.

Design

Fatigue tests have been performed in pure tension. Figure 9.5 shows an S-N curve based on the minimum diameter of the test pieces. A detail class of 81 MPa is found at 2 million cycles. An S-N curve using the average diameter of the rod, leads to lower allowable stresses and a detail class of 33 MPa.

In ordinary structures, the S-N diagrams are based on the nominal diameter. In this case, though, comparison of S-N diagrams on the basis of the average diameter is not possible, because the geometrical deviations - which vary per batch - are not taken into account. Therefore, the S-N diagram on the basis of the minimum diameter should be used as a comparison between batches. A design value of the minimum diameter should be used to determine the fatigue strength.

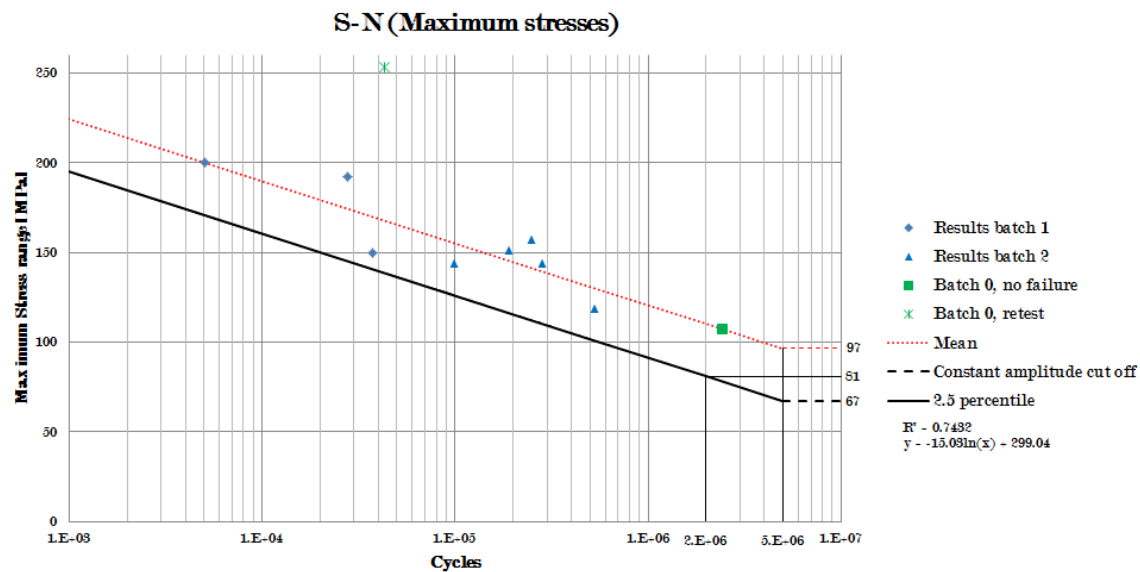


Figure 9.5: S-N Curve based on minimum diameter

Future research on milled specimens and comparison to as printed specimens can give insight into the effect of stress concentrations. Differences between the S-N curves of milled specimens and S-N curves of printed specimens on the basis of the minimum diameter may be expressed in a stress concentration factor. By determining such factors, it may be possible to calculate fatigue strengths for a wide range of geometries, without performing specific testing on each of them.

9.1.7 Microstructure

The microstructure of the material is mostly austenitic with a small amount of ferrite, as predicted through the Shaeffler diagram. 308LSi showed type FA solidification, while 316LSi was characterized by type A solidification.

Directional grain growth

Through micrography, it has been observed that the grain structure in the structural elements grows directionally. Large columnar grains are formed, which follow the direction of the thermal gradient of the weld pool. As the orientation of the weld pool changes due to a change in gravitational pull due to a changed production angle, so does the direction of the grains with respect to the main orientation of a rod.

Grain growth across weld passes

As grains are formed in a newly deposited layer of weld metal, they take the orientation of previous grains, apparently fusing together to form large columnar grains across different weld passes. In future research, EBSD can be used to verify and quantify this observation.

Anisotropic structural behaviour

Columnar grains limit the amount of plastic deformation in the material when they are loaded in their main direction. This explains the low values for ultimate strain found in the milled specimens tests when compared to theoretical values. These theoretical values are based on material with an isotropic grain structure.

Due to the directional grain structure, the material is expected to behave in an anisotropic manner. Indeed, structural testing confirms that rods produced under an angle have different structural properties: ultimate strength values are reduced, as shown in figure 9.3. This anisotropy becomes especially imported in joints or larger AM structures, when structures are loaded perpendicular to the grain orientation.

The anisotropy is also expected to influence ductility. There are too few test results for specimens produced at an angle, specifically 60 °to give a clear quantitative expression. Additional testing in which the grain structure is loaded perpendicular to its main orientation has to be carried out.

In the case of the structural elements studied here, the anisotropic behaviour as a result of the grain structure is largely overshadowed by the geometrical influences. Taking into account this anisotropic behaviour, however, leads to better predictions of failure load. Moreover, if the structure were to be processed, e.g. sanded, to reduce geometrical variability, the anisotropic behaviour will play a more important role.

Furthermore, since the microstructure varies throughout the rods, the material properties will also vary

Corrosion resistance

Since one of the main considerations for the choice of a stainless steel as the base material is corrosion resistance, it is advised to perform measurements and tests to investigate the actual corrosion resistance of printed material. Normally, a certain degree of corrosion resistance is achieved through surface preparation and control over the alloying constituents. If the surfaces of printed structures are not treated, it might be that no protective oxide layer is formed, leaving the material vulnerable to corrosion. Moreover, segregation of alloying constituents, in particular chromium, can lead to reduced corrosion resistance.

In austenitic stainless steel, stress corrosion cracking along grain boundaries can be a problem. Since the microstructure of the material studied is made up of long grains, with long grain boundaries, it may be extra sensitive to stress corrosion cracking. Especially in the case of the rods produced at an angle, this may be a problem. Columnar grains that have their boundaries exposed due to their misorientation with respect to the structural element, will be most vulnerable. Corrosion at the edges of the material may progress along these boundaries into the material and cause stress corrosion cracking.

In future research, this has to be further investigated by performing measurements on the composition and corrosive properties of the material along the grain boundaries.

9.1.8 Quality control

Since the results between batches are highly variable, and because of the sensitivity of the print quality to the process, thorough quality control is necessary. This control should encompass the following aspects: control of the process, characterization of the resulting material, inspection of printed structures, repair of defects.

Types of defects

Two distinct types of defects are observed in test pieces: material defects inside the material itself, and geometrical defects shaped by the material.

The first type of defect has occurred in batch 3, in which porosity led to reduced strength and ductility properties. This type is a result of a lack of control over the process. In this case, a broken nozzle led to poor gas shielding.

The second type of defect, a geometrical one, can be a result of specific printing parameters or it can occur by accident, for example when the robotic arm is accidentally

pushed from its position. This defect can take the shape of a misalignment of material or a locally very small diameter.

Repairs

Defects in tension elements should always be repaired; defects in compression elements only require repair in specific cases. Compression elements are insensitive to material defects, but sensitive to misprints. Small diameters are only an issue in compression elements if they are located near the points of greatest curvature. Tension elements are sensitive to all types of defects.

Material defects are relatively hard to locate and repair. The affected area has to be cut out and then reprinted. Geometrical defects, however, are relatively easy to repair. Whenever a misprint or small diameter is detected, extra material can simply be welded onto the existing structure. Note that this surface should be clean, to minimize the risk of material defects.

The effectivity of these repairs will have to be demonstrated through tests. It is expected that these repairs will be fairly effective, and that they will not have a significant negative influence on the base material. In traditional steel structures, welding repairs disrupt and damage the microstructure of the base material. In the case of a printed structure, the base material is already welded and its microstructure disrupted. Still, locally the grain structure will be affected, which will influence the material properties. Additionally, some residual stresses may be introduced. However, the impairing effects of the repair are expected to play only a minor role in comparison to the geometrical inaccuracies in the material. When larger structures are printed, and subsequently processed to eliminate geometrical inaccuracies, the degrading effects of a repair will become more evident.

Inspection

Geometrical defects can be easily detected by a visual inspection. All of the specimens in batches 1, 2 and 4 that showed strongly reduced ductility, were flagged in advance for having a defect. For critical areas, photographic or photogrammetrical measurements may be taken to see if the geometry is within tolerance.

Material defects such as slag inclusions or porosity cannot be detected visually. Due to the rough surface and complicated geometry, magnetic, ultrasonic and radiographic testing is very difficult on site. Therefore, it is essential to carefully control the process and minimize the risk of this type of defects.

Process control

The first type of defect, a material defect, should be controlled by a careful description and execution of the printing procedure. The adequacy of this procedure should be verified by printing and examining test batches.

The printing procedures and the resulting material have to be documented and analysed well. Small changes in the process can lead to drastically reduced structural properties. This procedure should describe the type of printer, the material, the shielding gas and all other relevant process parameters. In addition, resulting strength values, medium diameters and a description of safe minimum diameters should be supplied. The specific parameters and properties from this study have been supplied in the appendix.

In a later stage of development of printing machines, these procedures must be developed into Printing Procedure Statements and Printing Procedure Qualification Records.

Like the WPS and WPQR for welding, these documents are to be used to ensure the quality of the printed material.

The operator of the printer should also be qualified to do his job through a PQTR, the printing equivalent of a WQTR. He must show that he has proper understanding of a specific printing procedure and that he can consistently produce printed material at a certain level of quality. This person does not have to be a welder. Setting up and executing the printing process requires a very different set of skills than ordinary welding does.

Test samples

Whenever production restarts, test specimens should be produced to ensure that the printed material is of the desired properties. These test specimens should be accurately measured and inspected for any material defects. The measured properties may not deviate too much from the desired properties. When the quality of the material is at question, additional tensile tests should be performed to verify if the material has sufficient ductility and strength for its purpose.

9.1.9 Modelling structural behaviour

Analytical, numerical and FEM models have been made to model the rod structural behaviour. While it is possible to make safe predictions with these methods, it has proven difficult to precisely model the actual behaviour. This research showed that 3D photogrammetrical data of rod geometry can be used for a FEM model. Further calibration and verification of such models, however, has to take place in future research.

Tensile test

A numerical model of a rod, using stress-strain data of a milled specimen combined with the geometrical data of the rod, does not yield exact predictions of the structural behaviour of the rod in a tensile test. While failure load is predicted accurately, the ductility of actual test specimens is greater than predicted by the numerical model. When the yield stress of the model material is lowered, while the ultimate stress is kept the same, the predictive value improves. Perhaps stress concentrations or residual stresses in the outer layers of the material lead to a reduced yield strength of the material. Another possible flaw in the model lies in the assumption that the material properties are constant over the length. Improved models should include the fact that the material is not isotropic and varies along the length. With further improved FEM models, the effects of residual stresses, material defects and geometrical deviation in three dimensions can be studied.

Buckling test

The Ayrton-Perry formula can be used to make an analytical prediction of the buckling load. The imperfection factor α implies a great simplification of rod geometry by reducing it to a single value. Furthermore, this model does not take into account strain-hardening. Through statistical analysis, safe buckling curves can be created, but for an accurate prediction of buckling load, FEM models are more suited. The actual rod geometry and strain-hardening can be included. The current models yielded buckling loads that were in the same order of magnitude as the tested values, but further improvement is necessary. Future models should be based on hinged test set-ups rather than a clamped set-up, because the load introduction and boundary conditions are very clear for hinged set-ups. When the current inaccuracies are dealt with, and the models are calibrated to

test data, FEM analysis can be used to study buckling behaviour without performing tests and buckling curves can be constructed for a wide range of geometries.

9.2 Printing a bridge

Now that this report has come to its conclusion, one final question remains: is it possible for a structural engineer to safely design a printed bridge?

Naturally, this report on its own does not come close to the existing body of knowledge on traditional steel structures; Eurocodes on additive manufactures are still a long way off. However, the findings of this report give the confidence that a safe design with additive manufactures is possible. With sufficient control over the quality of the printed product, and a proper understanding of the structural behaviour, an engineer will be able to design a structure with a certain level of safety.

This thesis is focused on the basic element of a rod. The next step would be to study the structural behaviour of joints and larger printed structures. These structures can be designed using the findings from this thesis. By printing such structures and testing them, structural interaction and system effects can be studied.

A full-scale prototype of a printed bridge can prove its safety and give confidence to researchers and engineers to further develop additive manufacturing in structural engineering. If we had to wait to build ground-breaking structures until all design codes were fully developed, there would never have been pyramids, a pantheon, or the Eiffel tower. In fact, the codes would never have been developed without pioneering structures. At a certain point, you have to make do with the knowledge you have, trust your engineering judgement and take a chance. Only then can innovation take place.

Audentis Fortuna iuvat

- *Vergilius*

Appendix A

General

A.1 People

Committee

Prof. ir. F.S.K. Bijlaard

Chairman

Position: Professor Steel Structures
University: Delft University of Technology
Faculty: Civil Engineering and Geosciences
Department: Structural Engineering
Address: Stevinweg 1, room 2.53 Stevin II
2628 CN Delft
the Netherlands
Telephone: +31 15 27 84581
E-mail: F.S.K.Bijlaard@tudelft.nl

Prof. dr. I.M. Richardson

Materials Science and Engineering

Position: Professor of Joining Technology
University: Delft University of Technology
Faculty: Mechanical, Maritime and Materials Engineering
Department: Materials Science and Engineering
Address: Mekelweg 2, room H-1-260
2628 CD Delft
the Netherlands
Telephone: +31 15 27 85086
E-mail: I.M.Richardson@tudelft.nl

Ir. P.A de Vries*University Supervisor*

Position: Researcher Steel and Timber Structures
University: Delft University of Technology
Faculty: Civil Engineering and Geosciences
Department: Structural Engineering
Address: Stevinweg 1, room 2.56 Stevin II
2628 CN Delft
the Netherlands
Telephone: +31 15 27 84034
E-mail: P.A.deVries@tudelft.nl

Ir. D. Tuinstra*Company Supervisor, Senior Bridges Engineer*

Position: Senior Bridges Engineer
Company: Arup
Department: Infrastructure
Address: Naritaweg 118
1043 CA Amsterdam
the Netherlands
Telephone: +31 20 752 31 73
E-mail: dimitri.tuinstra@arup.com

Candidate**S.K. Joosten***Student Structural Engineering, Steel and Timber Structures*

Surname: Joosten
Given names: Stijn Koenraad
University: Delft University of Technology
Faculty: Civil Engineering and Geosciences
Address: Jacoba van Beierenlaan 19
2613 HV Delft
the Netherlands
Telephone: +31 6 25 40 7882
E-mail: skjoosten@hotmail.com
Date of birth: 15 November 1989
Nationality: Dutch

Others involved

Arup:

Ir. M.G. Flint

Former Company Supervisor, Bridge Engineer

Ir. S. Galjaard

Senior Designer, Additive Manufacturing Team Leader

MX3D:

Filippo Gilardi

MX3D Expert, Developer and Operator

TU Delft:

Dr. Ir. Murugaiyan Amirthalingam

Postdoctoral Researcher, Department of Materials Science and Engineering, Faculty of 3Me

A.2 Timetable

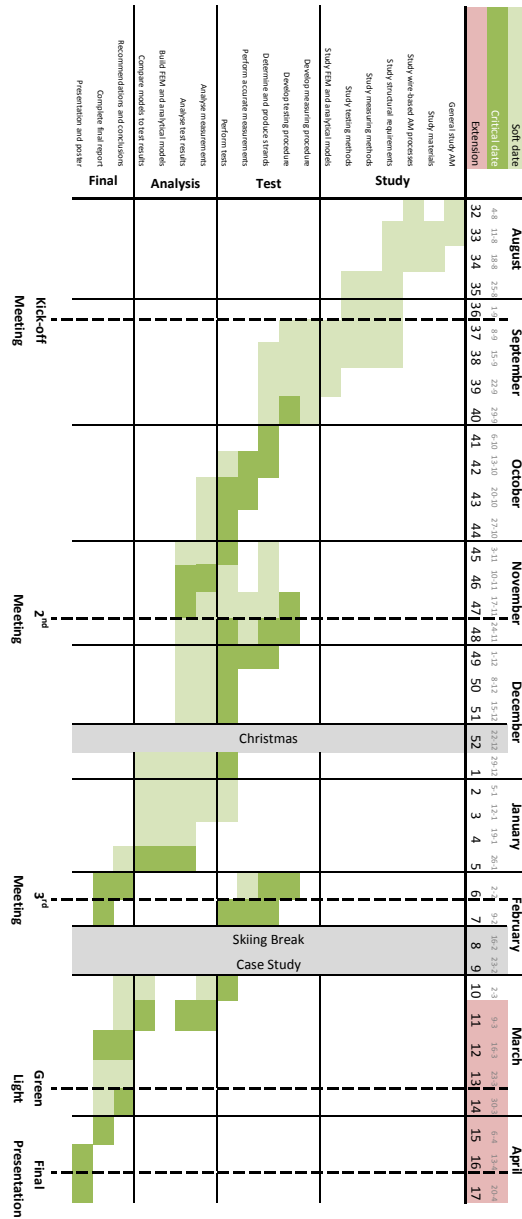


Figure A.1: Timetable of thesis project

Appendix B

Procedures and set-ups

B.1 Workflow photogrammetry

The photogrammetrical scanning workflow is explained in more detail in this sections. It can be subdivided into several steps: taking photos; importing photos into VisualSFM and generating a point cloud; cleaning up the point cloud and transforming it into a mesh in Meshlab; scaling and trimming the mesh in Rhino, exporting it for use in Abaqus or slicing it into equally spaced sections, and exporting the surface area data to Excel; analysing and comparing the data in Excel or Python. For a more general description of the first three steps, please see the tutorial by Spielman¹, which served as a basis for the workflow described here.

B.1.1 Photos

The accuracy of the model greatly depends on the number and quality of the photos that are used to generate a point cloud. For each model, at least 40 photos were taken of a strand. Photos in which the strand was not in focus were deleted. Good results were achieved when about 30 photos were taken all around the strand at two different angles, having the entire strand in focus, and the remaining photos were used to capture specific details.

Additionally, reflective surfaces create problems when generating the point cloud. To minimize reflections, the scanned strands were covered in a thin, non-reflective layer of paint. Ordinary white wall paint was used and eliminated any problems associated with reflective surfaces.

These photos were taken with a Nikon D60 camera, at a resolution of 3872x2592 pixels. The focal length was set to 55 mm, the aperture to 1/5.6.

B.1.2 VisualSFM

Before importing the photos into VisualSFM, they were first resized to a maximum width/height of 3200 pixels, because at larger resolutions the program is not able to create a point cloud. After import, unique features in the photos are identified and related to each other through the sift and match function. Subsequently, a sparse 3D reconstruction can be made, in which the camera positions are solved and a preliminary point cloud is created. In this step, the camera positions can be checked. Finally, a dense reconstruction is performed, producing a point cloud that will be used to generate a mesh in the next phase.

¹Spielman 2013.

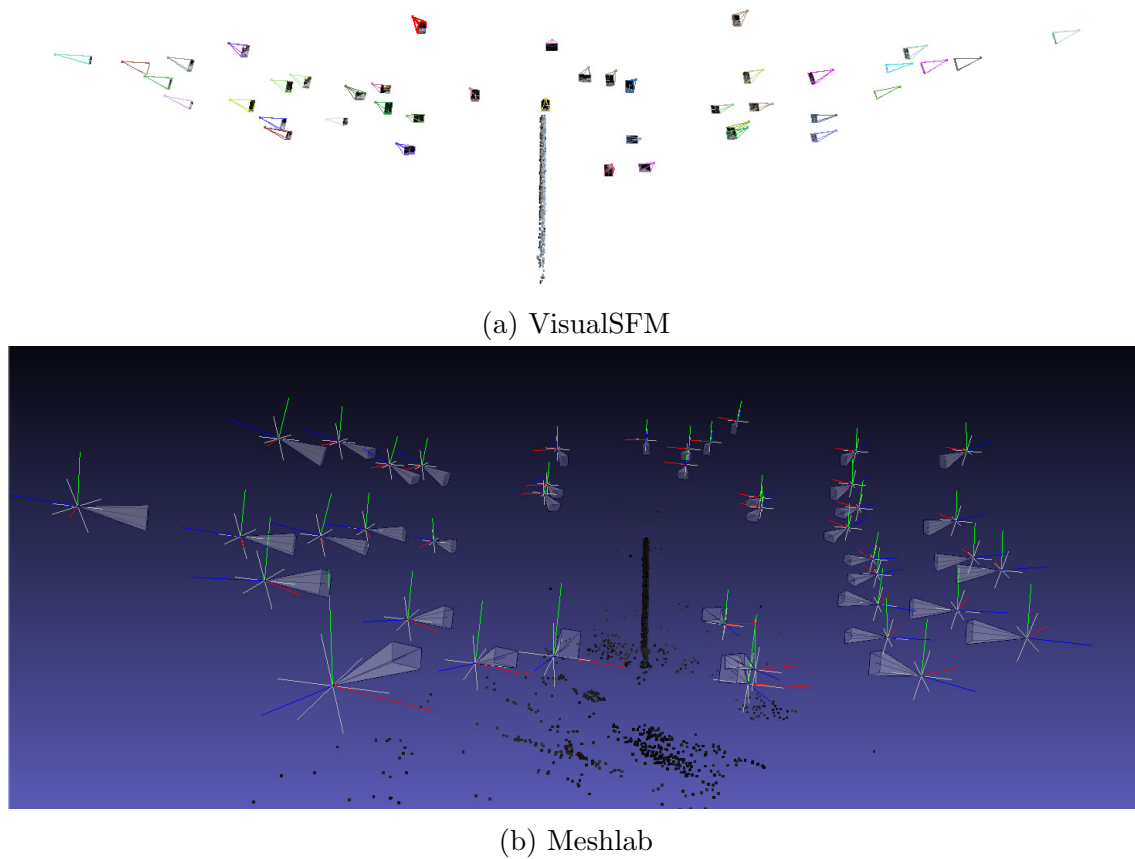


Figure B.1: Point cloud and camera positions

B.1.3 Meshlab

In Meshlab, the dense point cloud is imported. This point cloud, however, covers not only the strand, but also some of its surroundings. Before generating a mesh, these surrounding points are selected and removed. Now, a mesh is created using the poisson surface reconstruction with the following settings: octree depth 10, solver divide 6, samples per node 1, surface offsetting 1. The octree depth is of main influence to the level of detail of the mesh. The greater the depth, the greater the detail, but the more complicated the mesh. At a value of 10, the detail did not increase any further. Once the mesh is created, it is exported as a .stl file.

B.1.4 Rhino

The .stl mesh is imported into Rhino, along with a photo from the photographic analysis. This photo is used as a reference to scale the 3D model, see figure B.2.

Rhino:

- Import .stl
- Trim mesh
- Scale and position
- Repair mesh
- Convert to nurbs

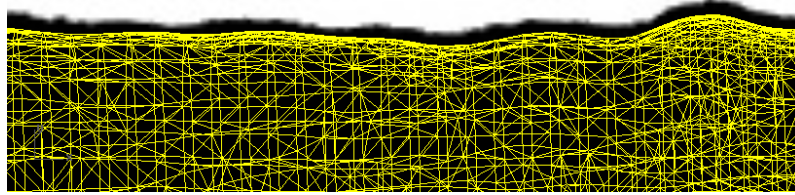


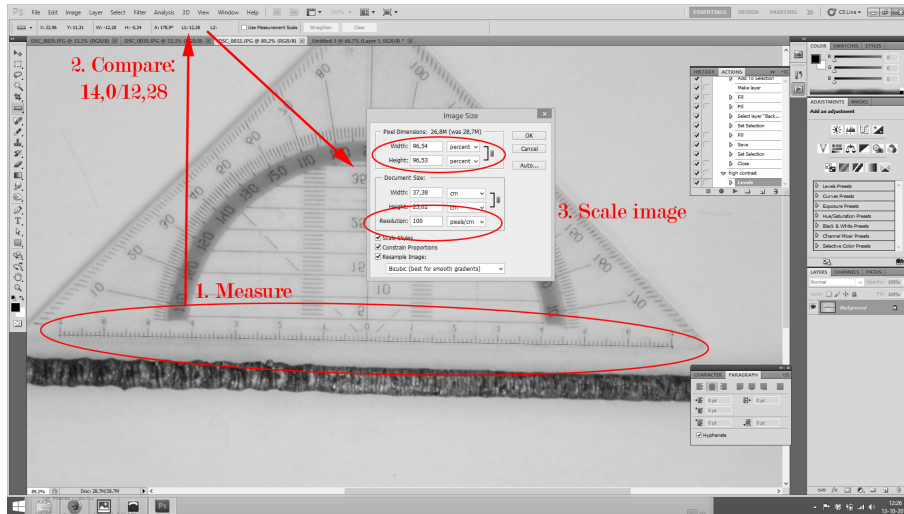
Figure B.2: Scaling 3D model (y) by matching features to photographic data (b&w)

- Export as .sat

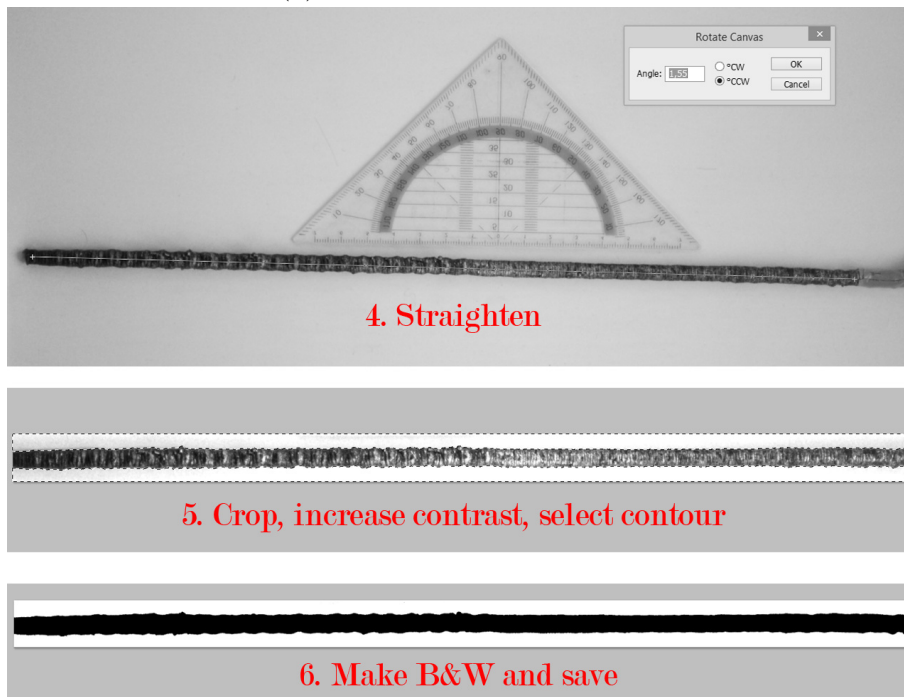
After scaling, the model is trimmed to only include the tested area and reflect the length of the images used in the photographic method. Then the mesh is converted to a NURBS polysurface. This model can be exported as .sat to be imported into Abaqus for a FEM analysis of the strand. It can also be sliced into equally spaced sections in order to analyse the variability of the cross-sectional area. Using a Rhino script, the 3D model is sliced into a number of sections equal to the number of pixels in horizontal direction of the photographic data. The surface area data is then exported to excel making use of another script. This numerical data may then be analysed and compared to the photographic data by means of, for example, a scatterplot.

B.2 Photographic analysis

The images below show the workflow for the analysis of the cross section. After preparing the images, they are analysed using a python script, counting black pixels.



(a) Measure and scale image



(b) Straighten and convert to black and white

Figure B.3: Photographic analysis

B.3 Tests setup

B.3.1 Tensile tests

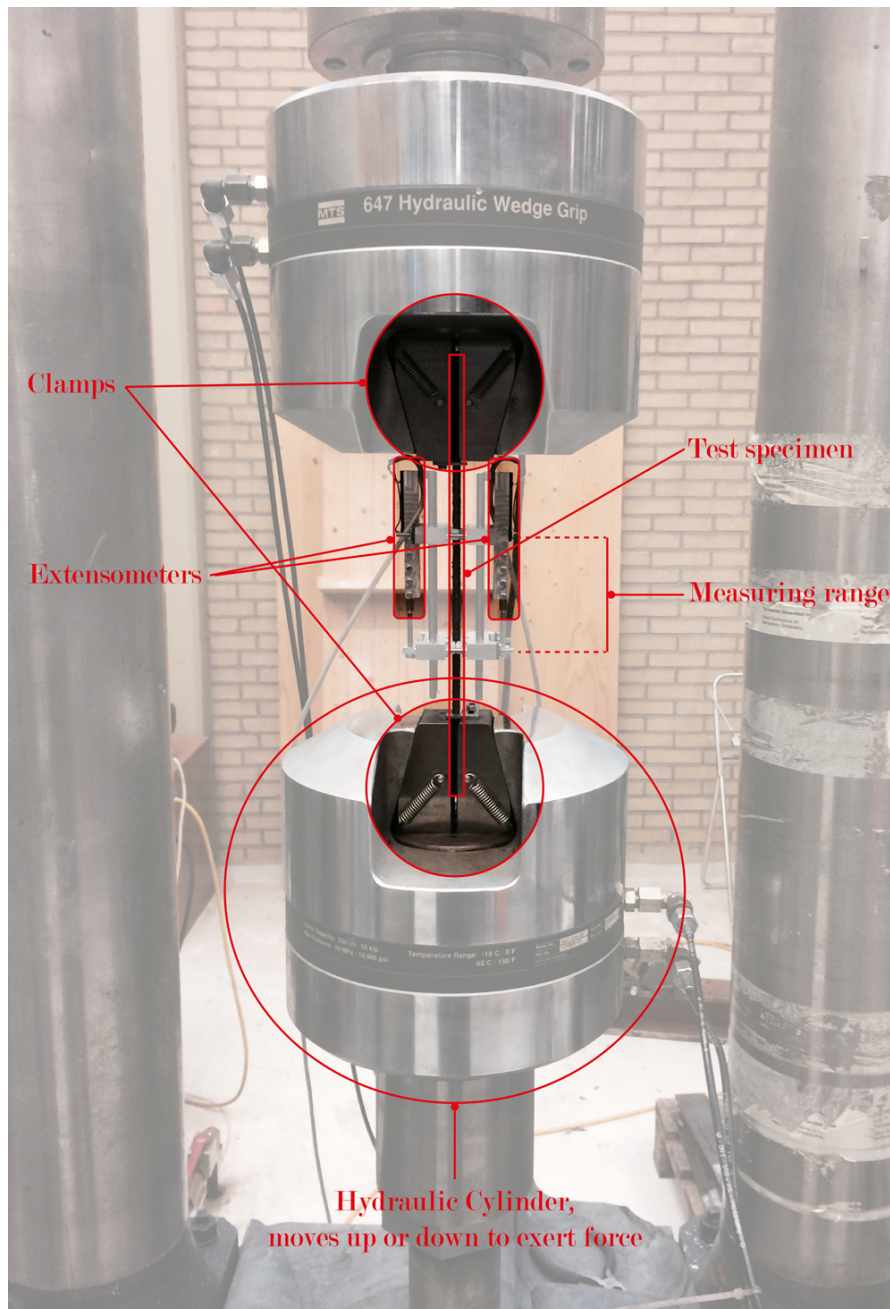


Figure B.4: Tensile test setup

B.3.2 Buckling tests

Clamped set-up

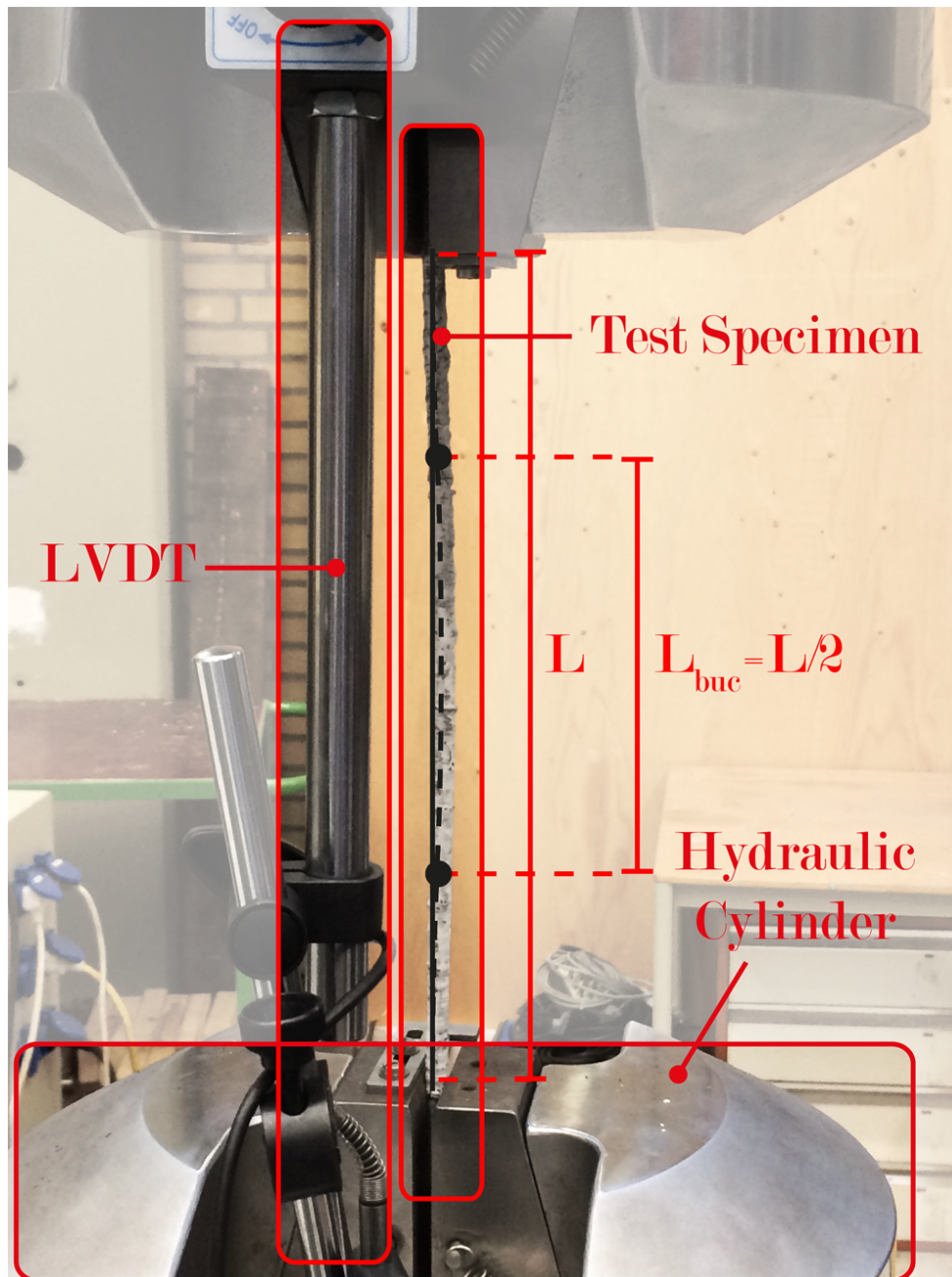


Figure B.5: Clamped buckling test set-up

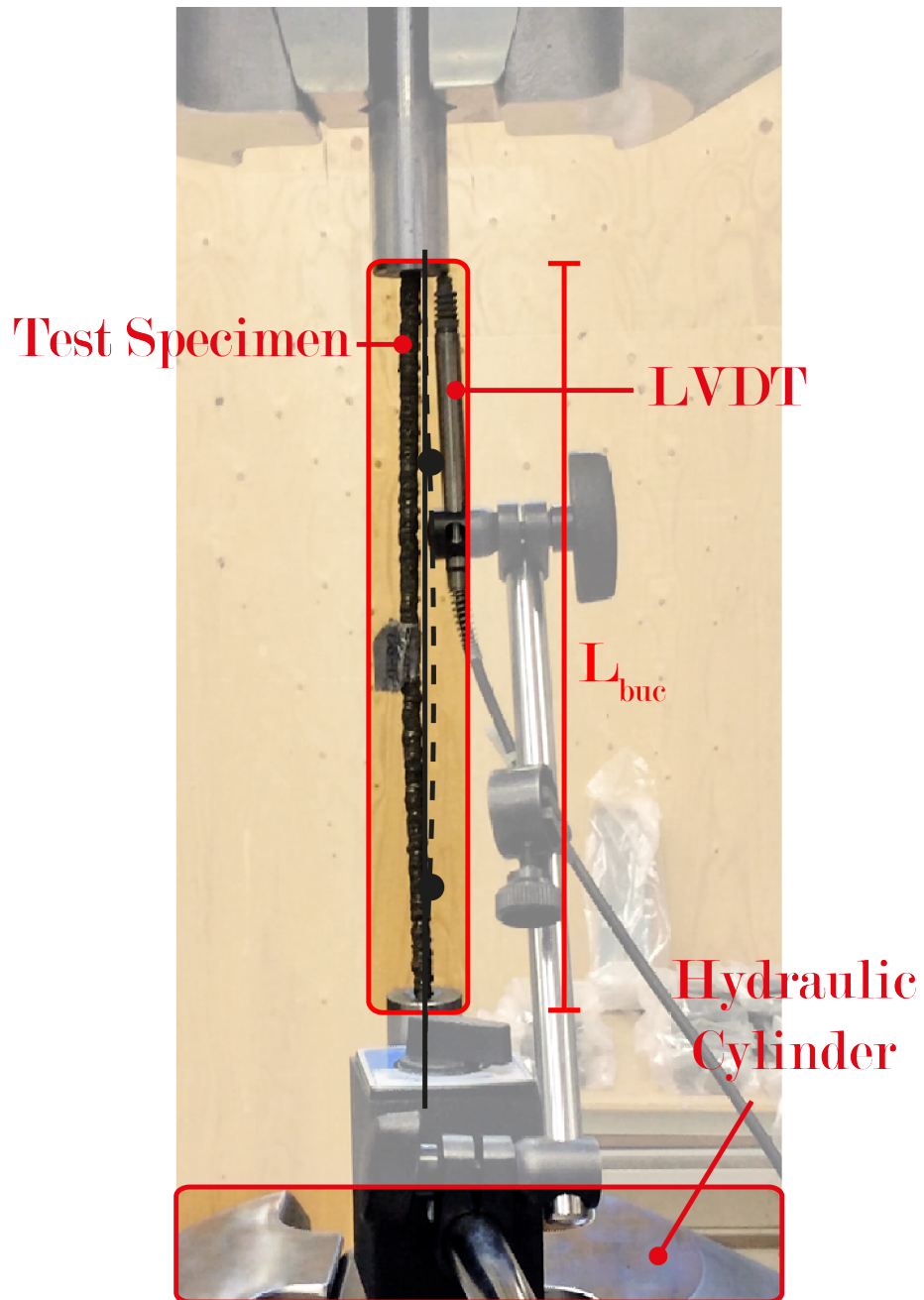
Hinged set-up

Figure B.6: Hinged buckling test set-up

Appendix C

Results

This appendix contains the results from the tests performed for this thesis. Please take note that the number of significant figures is limited by the accuracy of the measuring methods. In some of the graphs included in this appendix, numbers have not been rounded. A single diameter measurement using the photographic method is only significant to 0,1 mm, see section sec: photomethod.

C.1 Overview

First, an overview is given of all the test results in tabular form. In the following sections, more detailed results are presented per batch.

Batch	Angle [°]	Specimen	d_{mu} [mm]	d_{min} [mm]	F_{min} [kN]	F_{max} [kN]	ΔF [kN]	$\Delta\sigma_{max}$ [N/mm ²]	Cycles	h _z
1F	0	A1 (no fail)	6,36	5,93	0,3	3,26	2,96	107	2411538	2
		A2	6,36	5,93	0,3	7,3	7	253	43332	2
		B	6,27	5,13	0,28	4,26	3,98	193	27760	6
		C	6,33	5,63	0,245	5,235	4,99	200	5030	4
		D	6,44	5,05	0,23	3,23	3	150	37475	2
		E	6,66	5,6	NA	NA	NA	NA	NA	NA
2F	0	A	6,26	5,15	0,21	3,21	3	144	285055	6
		B	6,54	5,67	0,25	3,25	3	119	531890	4
		C	6,34	5,15	0,285	3,275	2,99	144	99952	6
		D	6,34	4,68	0,26	2,96	2,7	157	251716	6
		E	6,17	4,83	0,285	3,055	2,77	151	191478	6

Table C.1: Overview of fatigue test results

Batch	Angle [°]	Specimen	d_{mu} [mm]	d_{min} [mm]	$\sigma_{0,2}$ [N/mm ²]	σ_u [N/mm ²]	ϵ_u [%]	F_u [kN]	E_0 [GPa]	
1	0	A	6,22	5,27	289	579	14,2	12,6	104	
		B	6,51	5,83	267	596	21,2	15,9	186	
		C	6,18	5,40	307	611	13,8	14,0	147	
	30	A	6,07	5,67	281	610	21,4	15,4	102	
		B	5,87	5,20	300	567	12,2	12,0	183	
		C	6,22	5,40	329	670	16,6	15,4	155	
	60	A	6,20	5,10	334	645	15,1	13,2	160	
		B	5,99	5,10	285	550	13,7	11,2	144	
		C	5,69	4,47	314	559	10,6	8,76	148	
2	0	A	6,53	5,58	NA	NA	NA	NA	NA	
		B	6,49	5,95	331	674	24,9	18,7	112	
		C	6,36	5,68	349	693	23,3	17,5	116	
	30	A	6,57	5,88	293	614	20,5	16,6	276	
		B	6,50	5,73	332	647	20,2	16,6	116	
		C	6,55	5,93	316	643	22,8	17,7	118	
	60	A	6,55	5,18	391	552	5,8	11,6	181	
		B	6,59	5,63	344	615	16,3	15,3	114	
		C	6,74	5,90	311	594	19,4	16,2	166	
3	0	A	6,75	5,57	294	481	9,4	11,7	57994	
		B	6,88	5,83	276	540	17,5	14,4	134	
		C	6,79	5,37	317	549	11,0	12,4	192	
		D	6,50	5,37	NA	NA	NA	NA	NA	
	30	A	6,88	5,57	266	481	11,4	11,7	201	
		B	6,84	5,87	259	343	3,1	9,28	414	
		C	6,77	5,67	266	515	15,2	13,0	164	
		D	6,74	5,50	NA	NA	NA	NA	NA	
	60	A	6,89	5,80	271	516	19,1	13,6	203	
		B	6,51	5,40	310	504	9,9	11,5	441	
		C	6,66	5,67	292	471	11,4	11,9	240	
		D	6,70	5,57	NA	NA	NA	NA	NA	
4	0	A	6,37	5,60	245	498	11,8	12,3	136	
		B	6,30	5,53	257	601	22,2	14,4	116	
		C	6,42	5,53	251	466	8,3	11,2	225	
		D	6,26	5,37	277	663	23,8	15,0	134	
		E	6,59	5,67	282	678	25,7	17,1	136	
	30	A	6,63	5,53	251	538	13,5	12,9	121	
		B	6,20	5,37	249	583	20,6	13,2	127	
	60	A	5,83	4,87	261	525	8,8	9,76	162	
		B	6,05	5,27	259	661	33,8	14,4	179	
	4M	0	A	3,82	-	270	628	35,9	7,22	-
			B	3,88	-	304	621	31,0	7,36	-
			C	3,87	-	295	631	31,9	7,42	-
D			3,85	-	278	624	30,6	7,24	-	
30		A	3,83	-	331	591	30,4	6,83	-	
		B	3,91	-	262	594	30,4	7,12	-	
		C	3,89	-	265	602	32,5	7,16	-	
		D	3,89	-	259	581	33,2	6,90	-	
60		A	3,89	-	274	560	31,3	6,67	-	
		B	3,89	-	284	470	9	5,21	-	
		C	3,76	-	254	562	41,1	6,74	-	
		D	3,91	-	NA	NA	NA	NA	-	
WW	NA	A	1,0	NA	NA	NA	NA	NA	NA	
		B	1,0	-	1177	-	-	1,18	146	
		C	1,0	-	1175	-	-	1,18	144	
		D	1,0	-	1183	-	-	1,18	139	
		E	1,0	-	1238	-	-	1,24	72	
		F	1,0	-	588	-	-	0,59	69	

Table C.2: Overview of tensile test results

Batch	Angle [°]	Specimen	d_{mu} [mm]	F_{buc} [kN]	L_{buc} [mm]
2	0	A	6,53	NA	NA
		B	6,49	4,72	120
		C	6,36	4,00	120
	30	A	6,57	2,56	120
		B	6,50	4,69	120
		C	6,55	3,90	120
	60	A	6,55	4,99	120
		B	6,59	5,20	120
		C	6,74	4,10	120
3	0	A	6,75	4,97	120
		B	6,88	4,80	120
		C	6,79	3,54	120
		D	6,50	4,51	120
	30	A	6,88	3,71	120
		B	6,84	4,06	120
		C	6,77	4,11	120
		D	6,74	3,73	120
	60	A	6,89	4,05	120
		B	6,51	4,39	120
		C	6,66	5,25	120
		D	6,70	5,25	120
4B	0	A	6,48	1,93	223,8
		B	6,57	2,54	170,8
		C	6,23	2,67	168,5
		D	6,35	4,53	113,0
		E	6,57	3,66	147,2
		F	6,28	2,43	189,2
		G	6,48	4,59	109,5
		H	6,39	1,22	227,4
	30	A	6,38	3,16	147,9
		B	6,52	1,99	198,3
		C	6,13	3,94	108,8
		D	6,29	1,26	236,7
	60	A	6,05	1,14	230,5
		B	6,34	2,01	154,8
		C	6,53	2,65	192,1
		D	6,27	2,63	116,8

Table C.3: Overview of buckling test results

C.2 Batch 1

C.2.1 Parameters

The process parameters in table C.4 have been used in the production of the first batch of tensile test specimens.

Per request of MX3D, the process parameters have been excluded from this public version. Please contact MX3D at <http://www.MX3D.com> or gijs@MX3D.com.

Base material
CONFIDENTIAL
Robot
CONFIDENTIAL
Welding
CONFIDENTIAL

Table C.4: Process parameters tensile tests

C.2.2 Geometry

The histograms on the following pages show the distribution of the diameter of the different specimens. Per specimen, the data from three photos was taken and combined to get these results. Additionally, the data of these specimens has been combined to give a description of the distribution of the diameter per angle. Scatter plots have been made to analyse the goodness of fit to the normal distribution. Further analysis has to be carried out on the statistical description of the diameter.

Manual measurements have been carried out using a vernier caliper. In order to get a rough idea of the spread of the diameter of the strands, multiple measurements have been carried out per strand. Each strand was divided into three equal areas. In each area, the smallest, largest and what seemed like an intermediate diameter were visually selected and measured. This resulted in nine measurements per strand, see figure C.1. These measurements should be more or less in agreement with the histograms found using the photographic method. These manual measurements resemble the results from

Test piece	1-00-				1-30-				1-60-			
	A	B	C	Av	A	B	C	Av	A	B	C	Av
Average	5,9	6,4	6,6		6,2	5,8	6,5		6,1	6	5,9	
	6	6,3	6,1	6,2	6	6,1	6,5	6,1	6,5	5,9	5,6	5,93
	6,1	6,2	5,9		6,1	6	6,1		5,9	6	5,5	
Small	5,5	5,9	5,9		5,8	5,1	6		5,4	5,3	4,4	
	5	5,8	5,7	5	5,6	5,6	5,9	5,1	5,5	5,5	5	4,4
	5,8	6	5,7		5,6	5,4	5,3		5,3	5	5,2	
Large	6,4	7,1	7		6,5	6,3	6,9		6,6	7	7	
	6,3	6,6	6,4	7,1	6,3	7,1	6,9	7,1	6,7	6,6	6,5	7,9
	6,5	7	6,6		6,5	6,7	6,6		7	6,5	7,9	

Figure C.1: Manual vernier caliper measurements

the photographic method. The increasing spread and decreasing diameter with increasing production angle is observed in both methods. An important difference becomes apparent, though, when the average values from these manual measurements are compared to the combined geometrical histograms in appendix section C.2.2. The average values of the vernier caliper measurements are consequently larger than the values found through the photographic method. This may well be a result of bias in visually picking an average diameter, but may also be caused by an error in the photographic method, possibly created in the transformation from full colour photo to black and white image. A calibration of the photographic method based on the weight or by comparing measurements of distinct features has to be carried out.

0 degrees

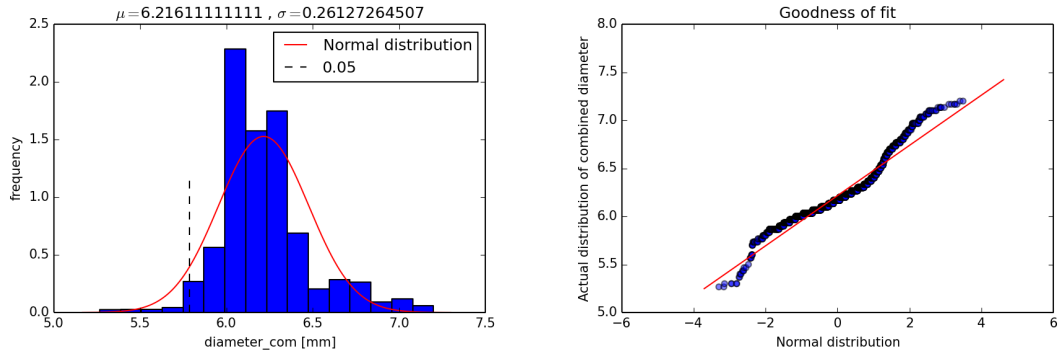


Figure C.2: 1-00-A geometry

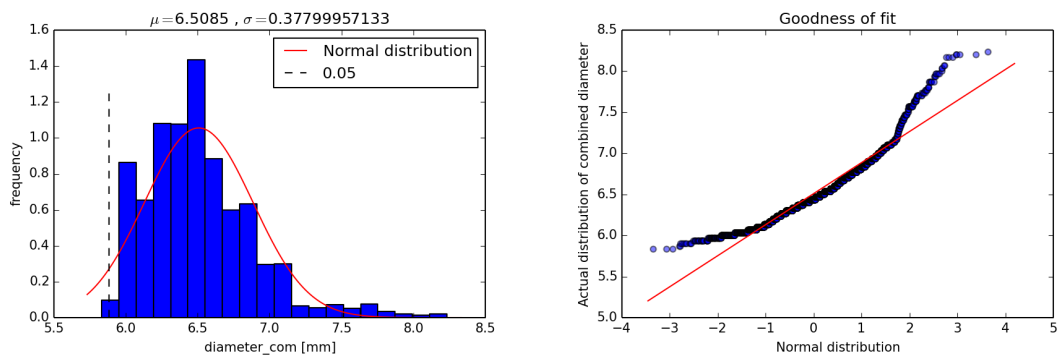


Figure C.3: 1-00-B geometry

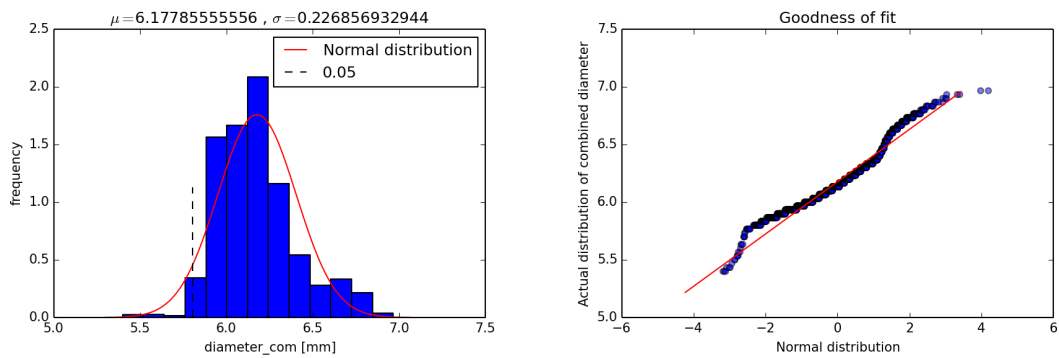


Figure C.4: 1-00-C geometry

30 degrees

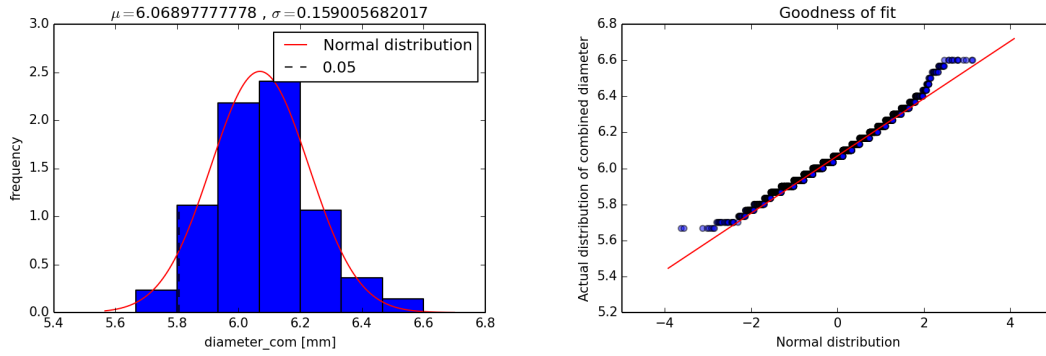


Figure C.5: 1-30-A geometry

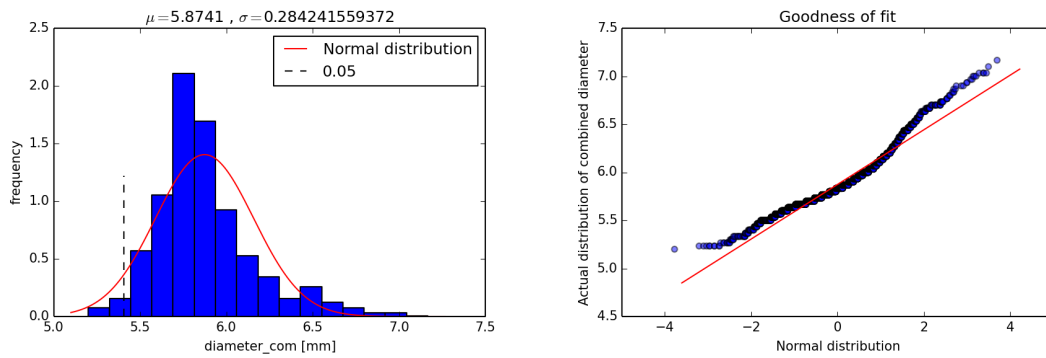


Figure C.6: 1-30-B geometry

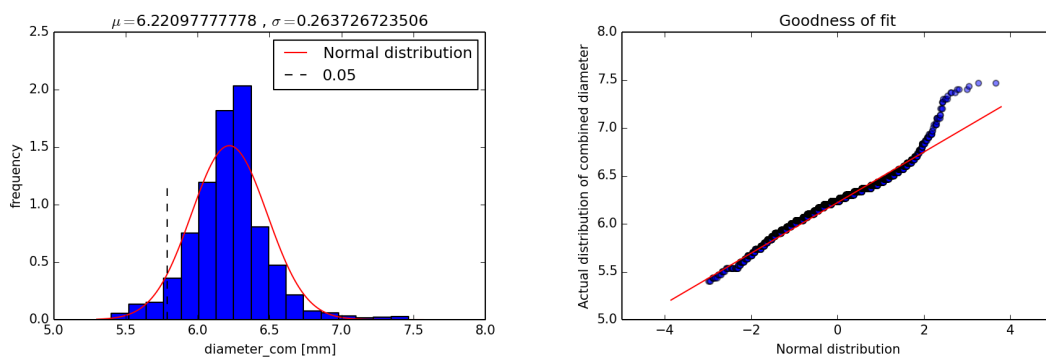


Figure C.7: 1-30-C geometry

60 degrees

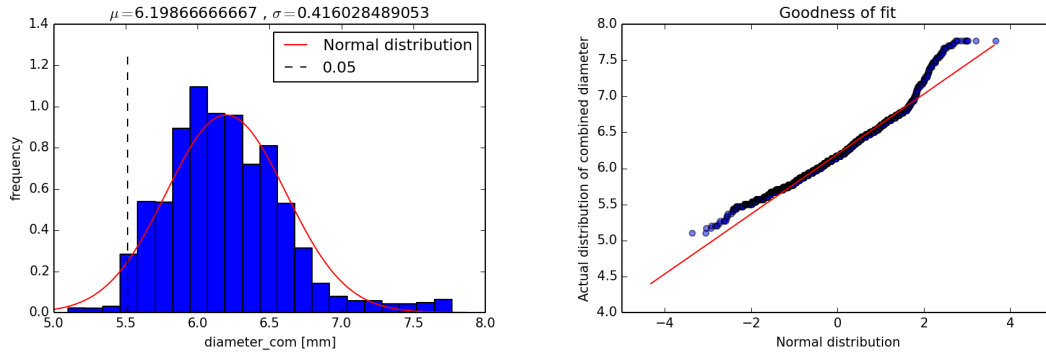


Figure C.8: 1-60-A geometry

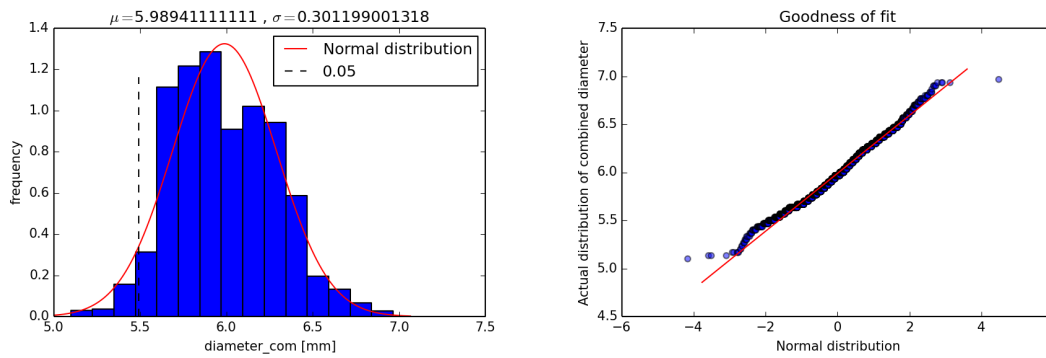


Figure C.9: 1-60-B geometry

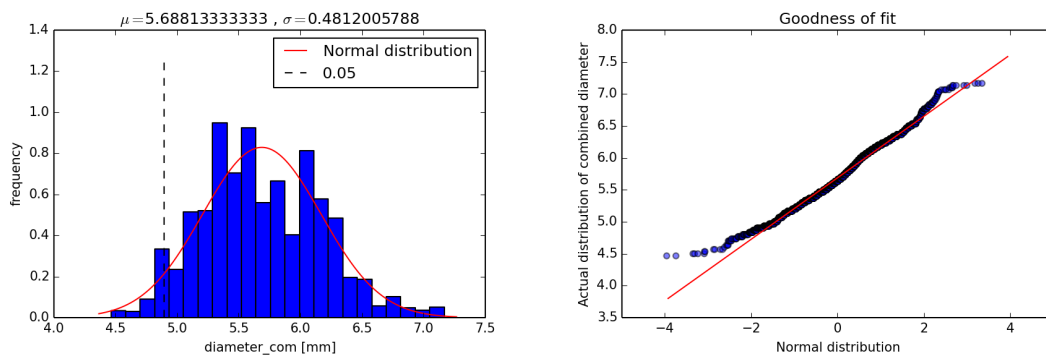
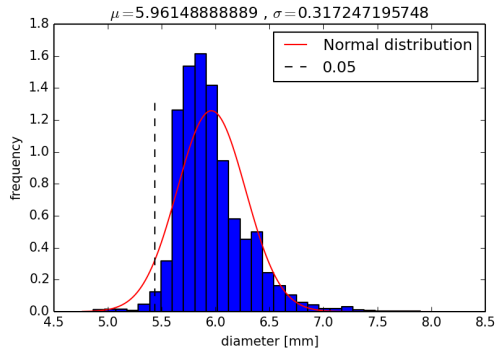


Figure C.10: 1-60-C geometry

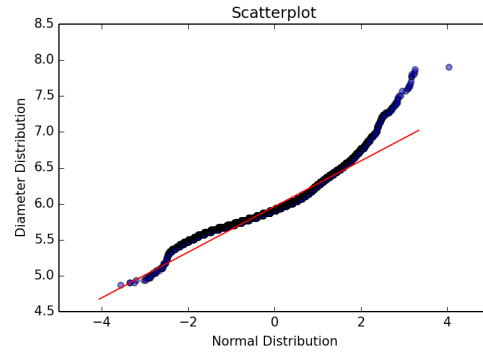
Combined distributions per angle

Here, the distributions of each specimen are combined per angle, because they are produced in the exact same way, and should therefore be part of the same, larger total distribution. Again, normal distributions have been fitted to these combined distributions. Scatter plots are provided to study the goodness of fit. If the distribution is truly normal, the points in these plots should all be on a straight line. The closer these points are to a straight line, the better the fit.

For all angles, the normal distribution gives an overestimation of the larger diameters of a strand. This, however, will not lead to any unsafe situations. The lower tail of the distribution is much more important for a safe structural design. Overestimation of the smallest diameter will lead to overestimation of the failure load; whereas an underestimation of the smallest diameter will lead to safe, but possibly also uneconomical design. Judging by the scatter plots, the normal distribution is generally a good fit. Only for the samples printed vertically, series 1-00, a slight underestimation of the smallest diameters is observed, but as mentioned before, this will only result in safe designs.

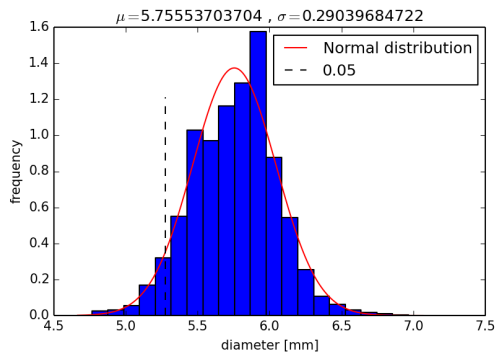


(a) Combined diameter distribution

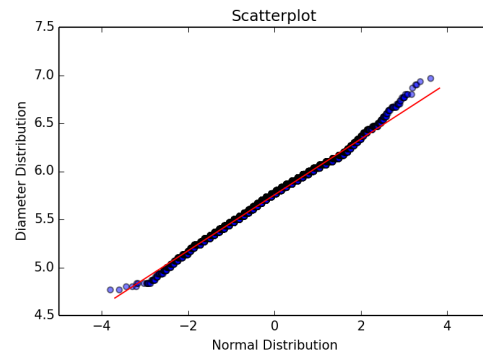


(b) Fit to normal distribution

Figure C.11: Combined geometry for specimen type 1-00

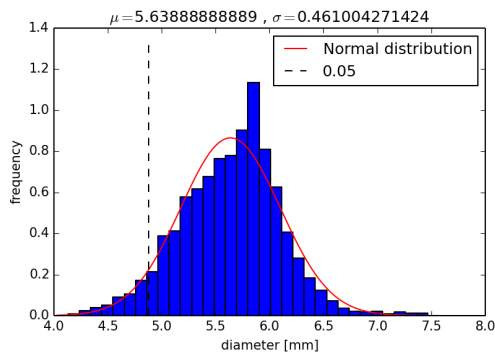


(a) Combined diameter distribution

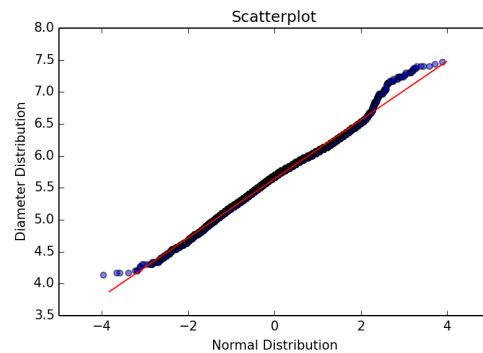


(b) Fit to normal distribution

Figure C.12: Combined geometry for specimen type 1-30



(a) Combined diameter distribution



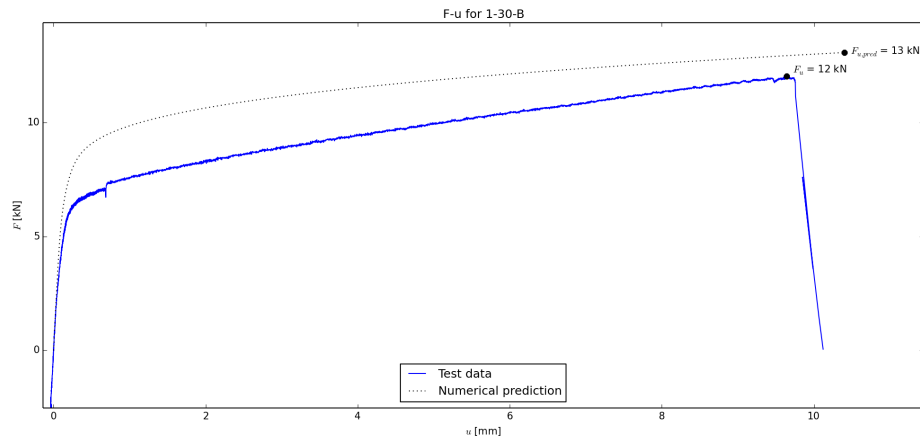
(b) Fit to normal distribution

Figure C.13: Combined geometry for specimen type 1-60

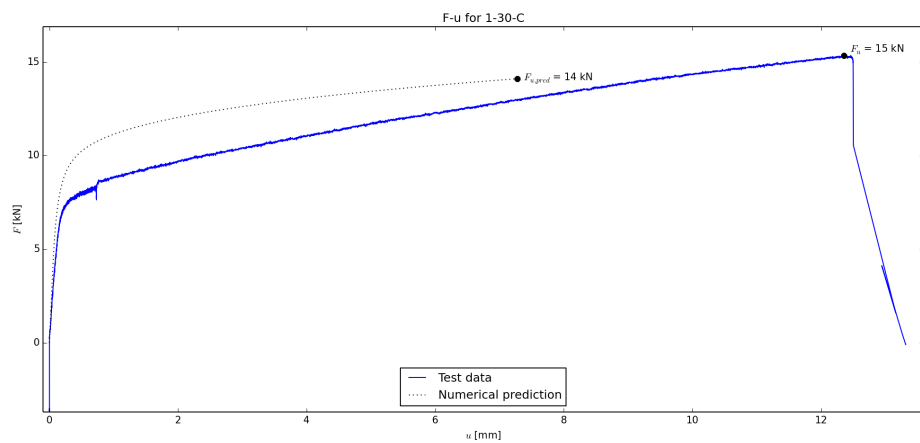
C.2.3 F-u curves

The following force-displacement curves show the raw results from the tensile tests that were performed.

0 degrees



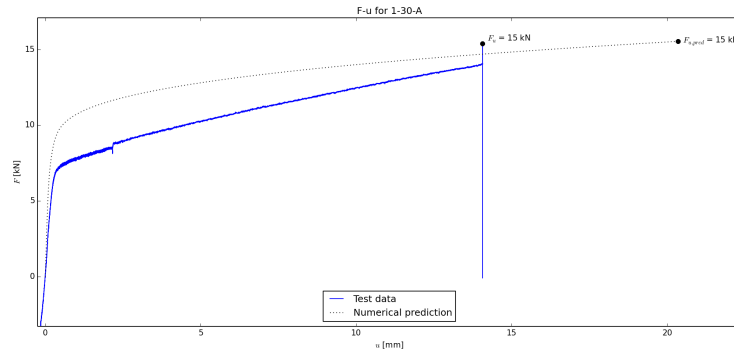
(a) 1-30-B



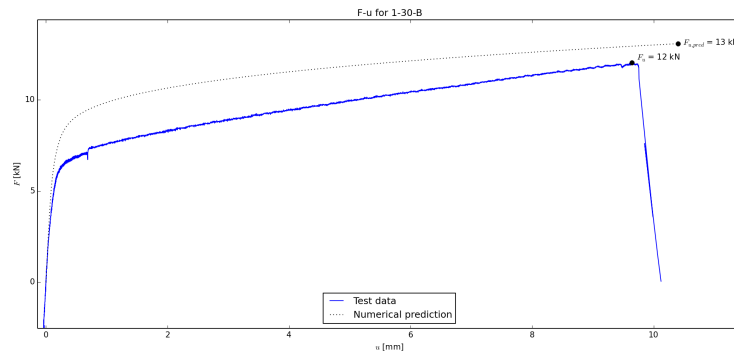
(b) 1-30-C

Figure C.14: F-u diagrams at 30 degrees

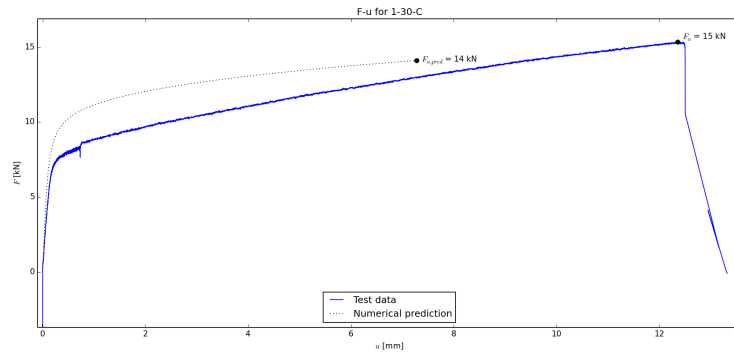
30 degrees



(a) 1-30-A



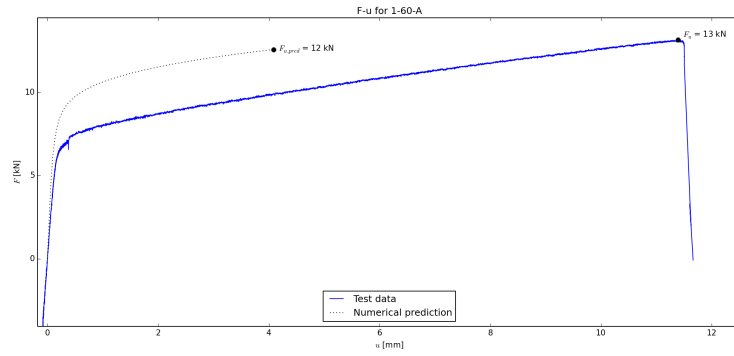
(b) 1-30-B



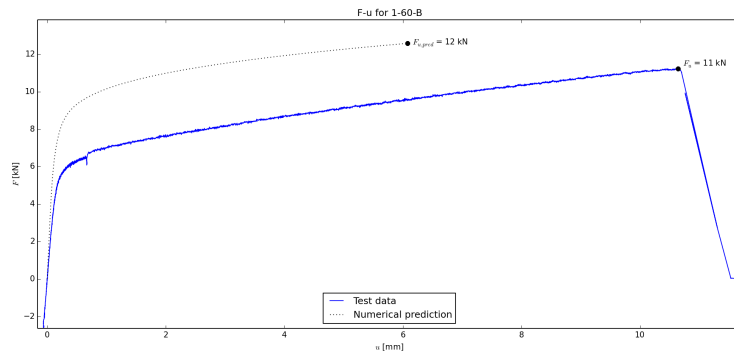
(c) 1-30-C

Figure C.15: F-u diagrams at 30 degrees

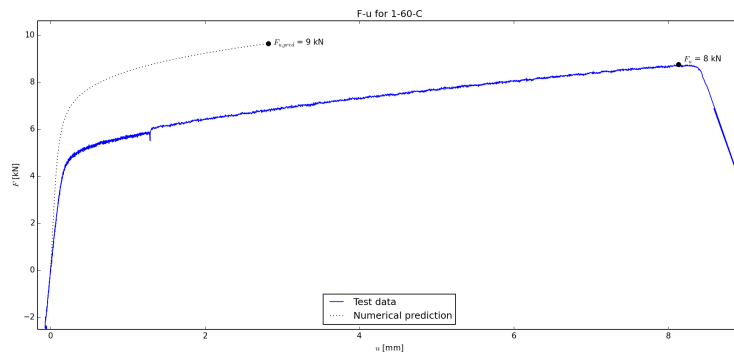
60 degrees



(a) 1-60-A



(b) 1-60-B



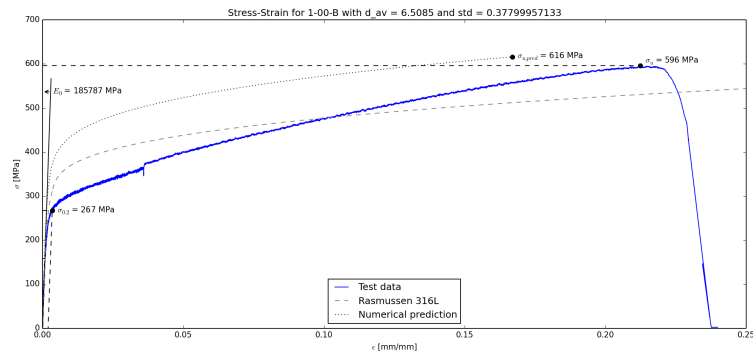
(c) 1-60-C

Figure C.16: F-u diagrams at 60 degrees

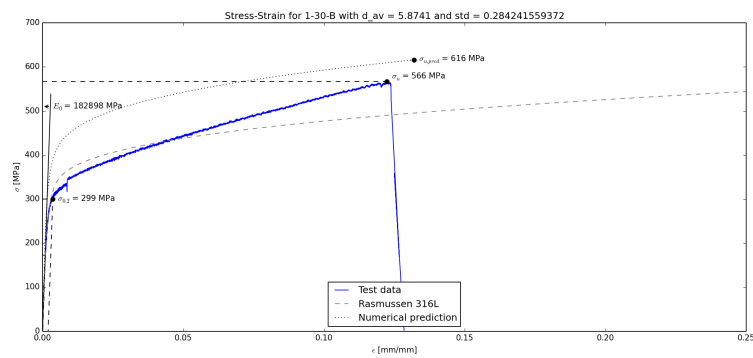
C.2.4 Stress-strain curves

The following stress-strain curves are based on the average diameters of the strands.

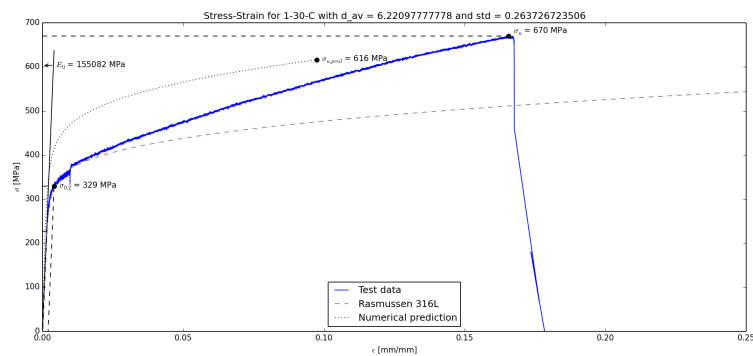
0 degrees



(a) 1-00-B



(b) 1-30-B

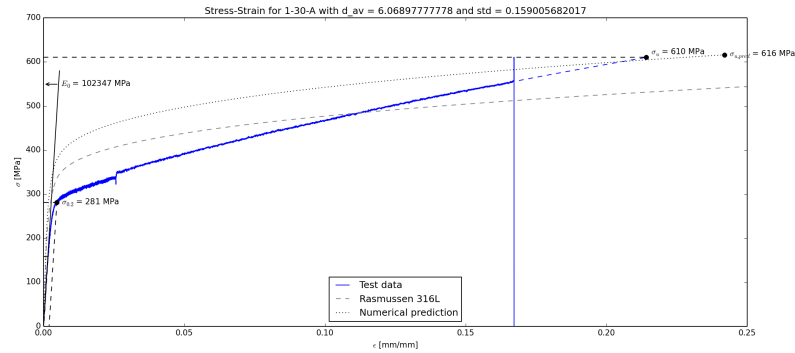


(c) 1-30-C

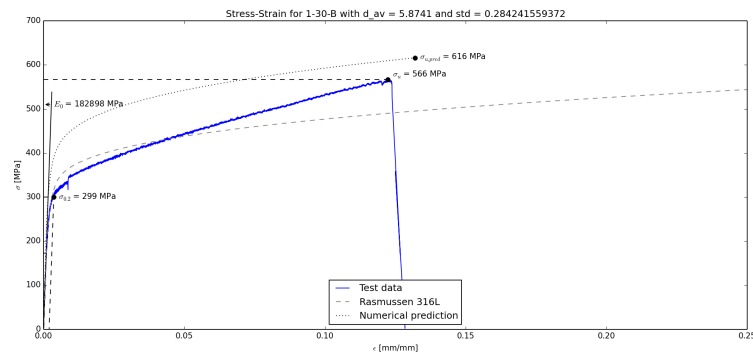
Figure C.17: Stress-strain diagrams at 30 degrees

30 degrees

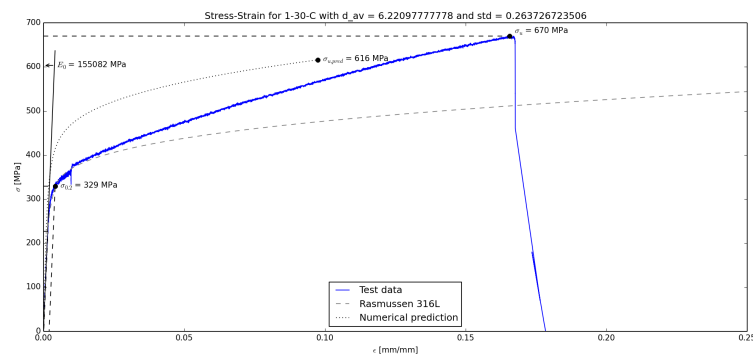
Note that the stress strain diagram C.18a was extrapolated to find the ultimate strain. The final displacement was outside the range of the extensometers. The dotted line represents the extrapolation that is based on a second order polynomial fit to the plastic region of the stress-strain diagram.



(a) 1-30-A



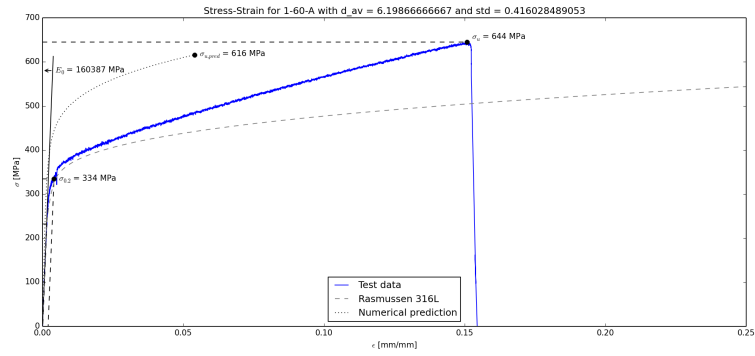
(b) 1-30-B



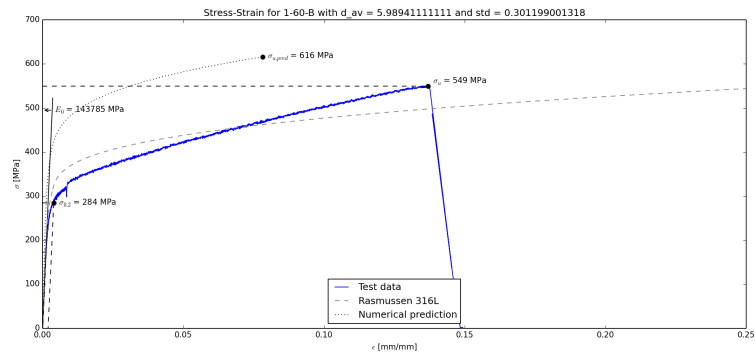
(c) 1-30-C

Figure C.18: Stress-strain diagrams at 30 degrees

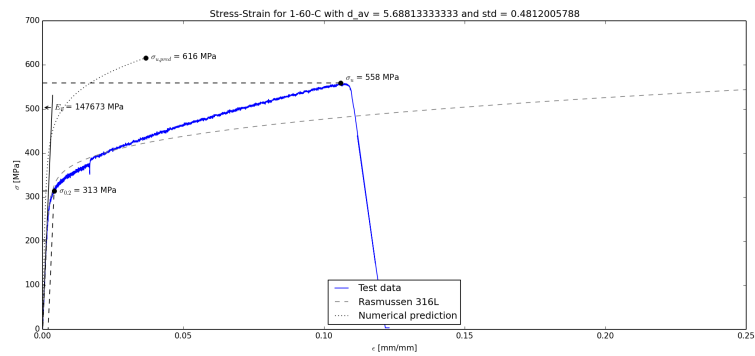
60 degrees



(a) 1-60-A



(b) 1-60-B

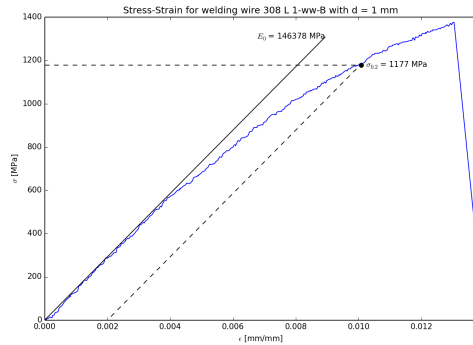


(c) 1-60-C

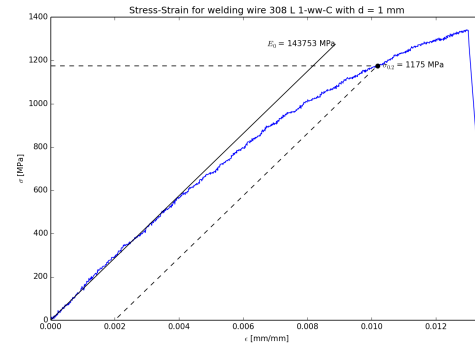
Figure C.19: Stress-strain diagrams at 60 degrees

C.2.5 Welding wire

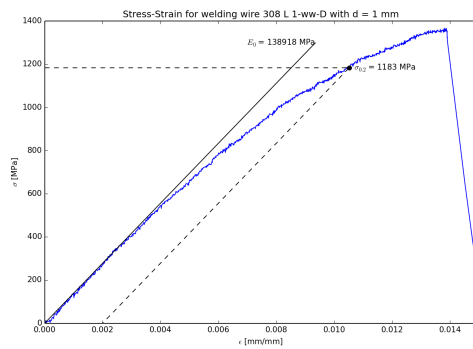
Six tests were performed, but only five of them are shown below. In the first test, the extensometers were not properly attached, so no accurate strain data could be retrieved. None of these tests give the entire stress-strain curve, because premature failure occurred in the clamped area. Young's moduli and the 0.2% proof strengths have been extracted from the raw data, though.



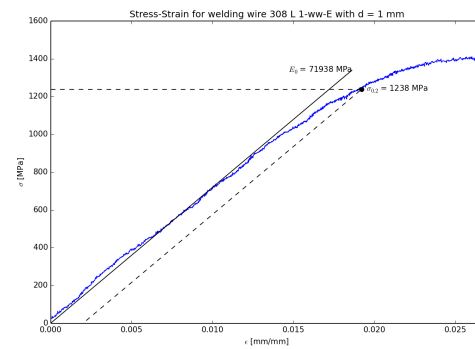
(a) B



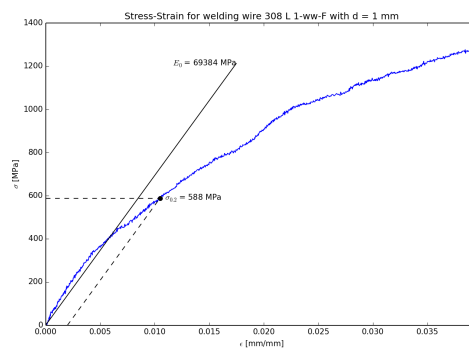
(b) C



(c) D



(d) E



(e) F

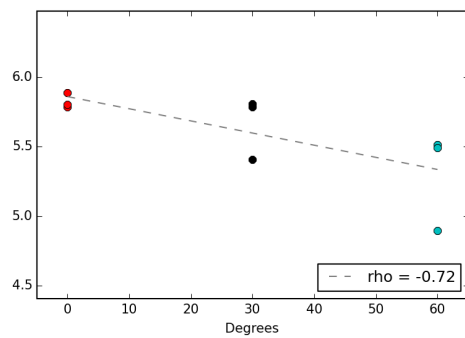
Figure C.20: Stress-strain diagrams of welding wire

C.2.6 Correlations

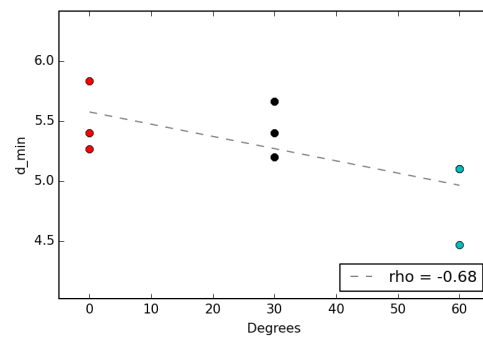
Different properties and parameters have been plotted against each other to investigate their relationships. For each plot, the Pearson product-moment correlation coefficient ρ has been presented. This value ranges from -1 to 1. The closer this value is to 1 or -1, the greater the correlation. Variables with a correlation coefficient that is (close to) 0 are not correlated.

Angle

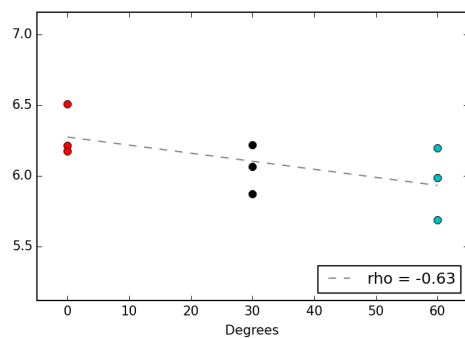
The plots in this subsection show how geometrical and mechanical properties vary with the angle at which the test pieces are produced.



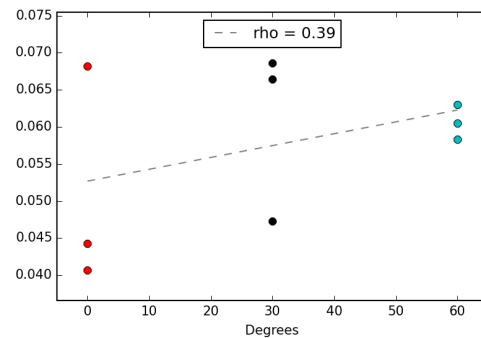
(a) Angle versus 5 percentile diameter



(b) Angle versus minimum diameter

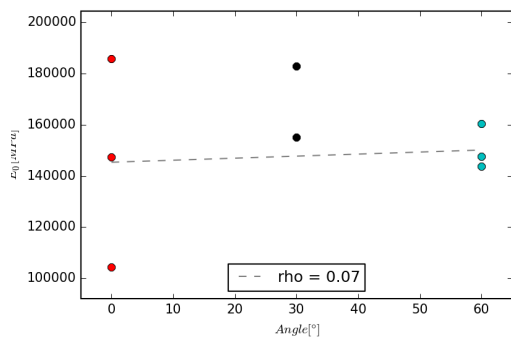


(c) Angle versus average diameter

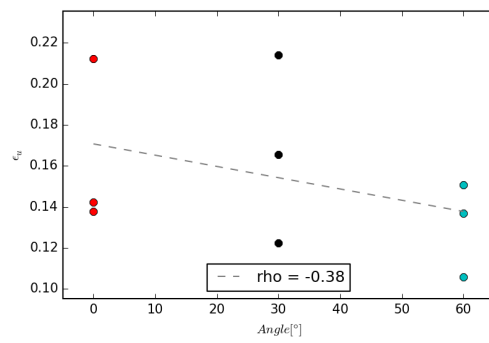


(d) Angle versus wobble factor

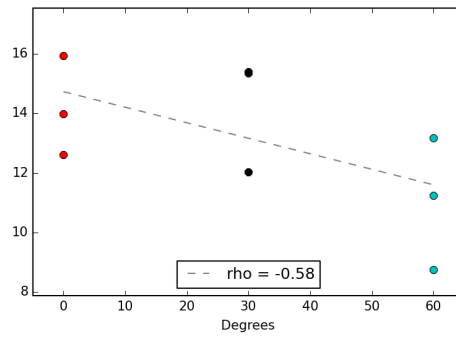
Figure C.21: Correlations between angle and geometry



(a) Angle versus Young's modulus



(b) Angle versus ultimate strain

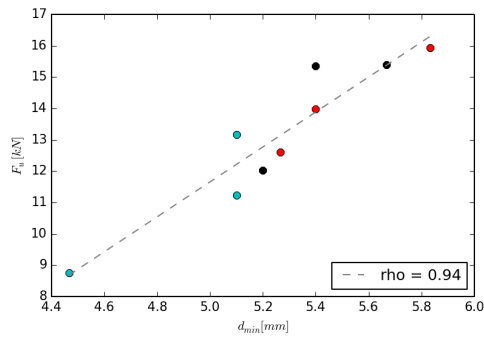


(c) Angle versus failure load

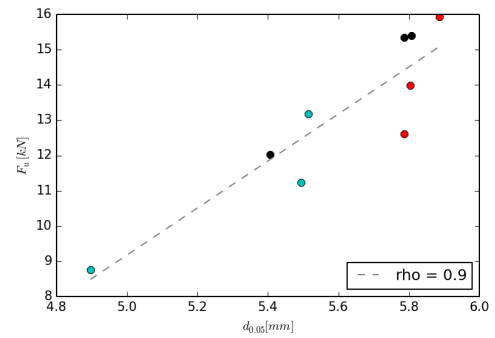
Figure C.22: Correlations between angle and mechanical properties

Geometry versus mechanical properties

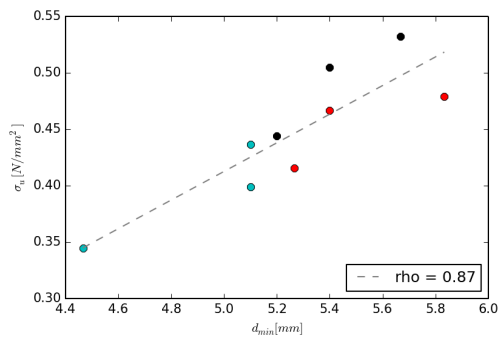
Here, geometrical and mechanical properties have been plotted against each other.



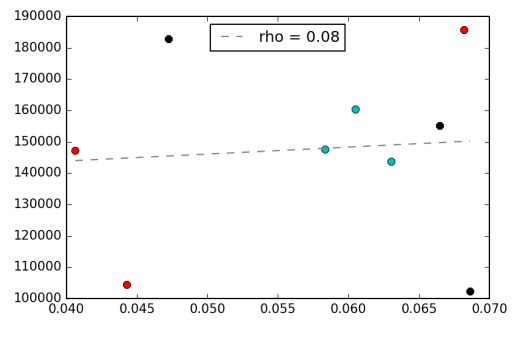
(a) Minimum diameter versus actual failure load



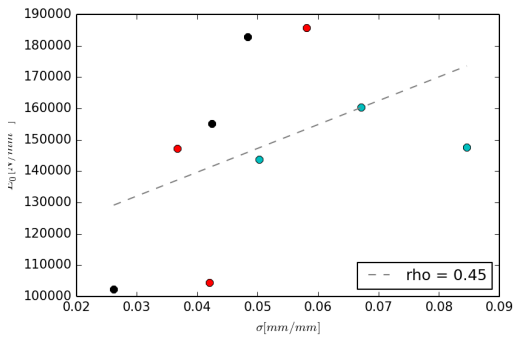
(b) 5 percentile diameter versus failure load



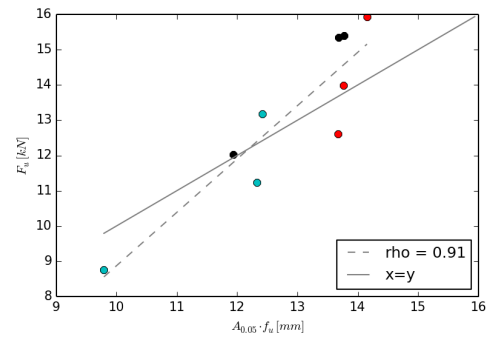
(c) Minimum diameter versus ultimate stress



(d) Wobble factor versus Young's modulus



(e) Diameter standard deviation divided by mean area versus Young's modulus



(f) Expected versus actual failure load
Based on 5 percentile diameter and ultimate stress as provided by filler metal provider

Figure C.23: Correlations between geometry and mechanical properties

C.2.7 Microstructure

This sections gives overview images of the microstructures of the different samples investigated using optical microscopy. Dendritic structures are clearly visible. Boundaries between clearly different structures have been marked.

1-00

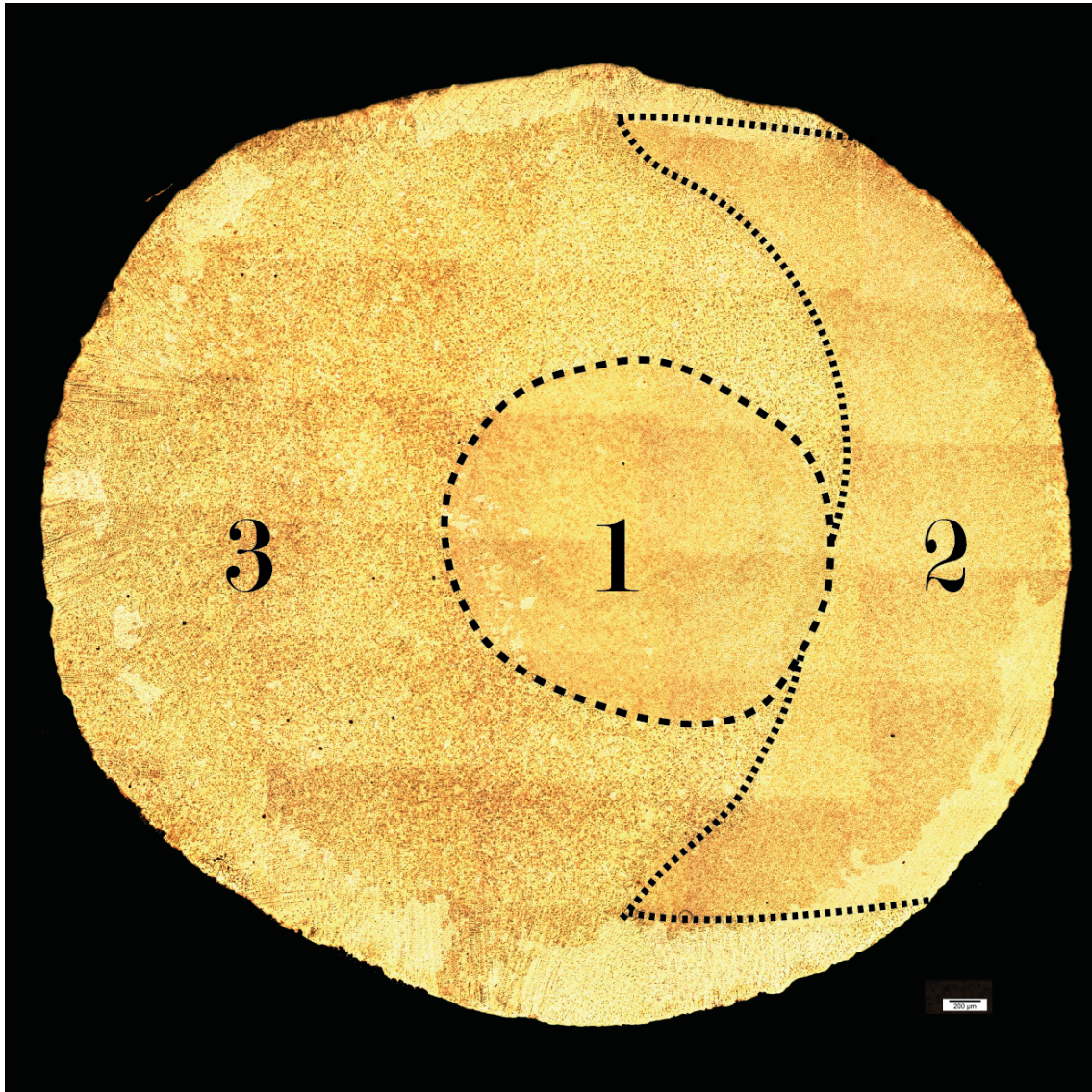


Figure C.24: Microstructure of 1-00-B, top of test piece, etched with 10 ml H₂O, 30 ml HCl (27%), 1.5 ml HO

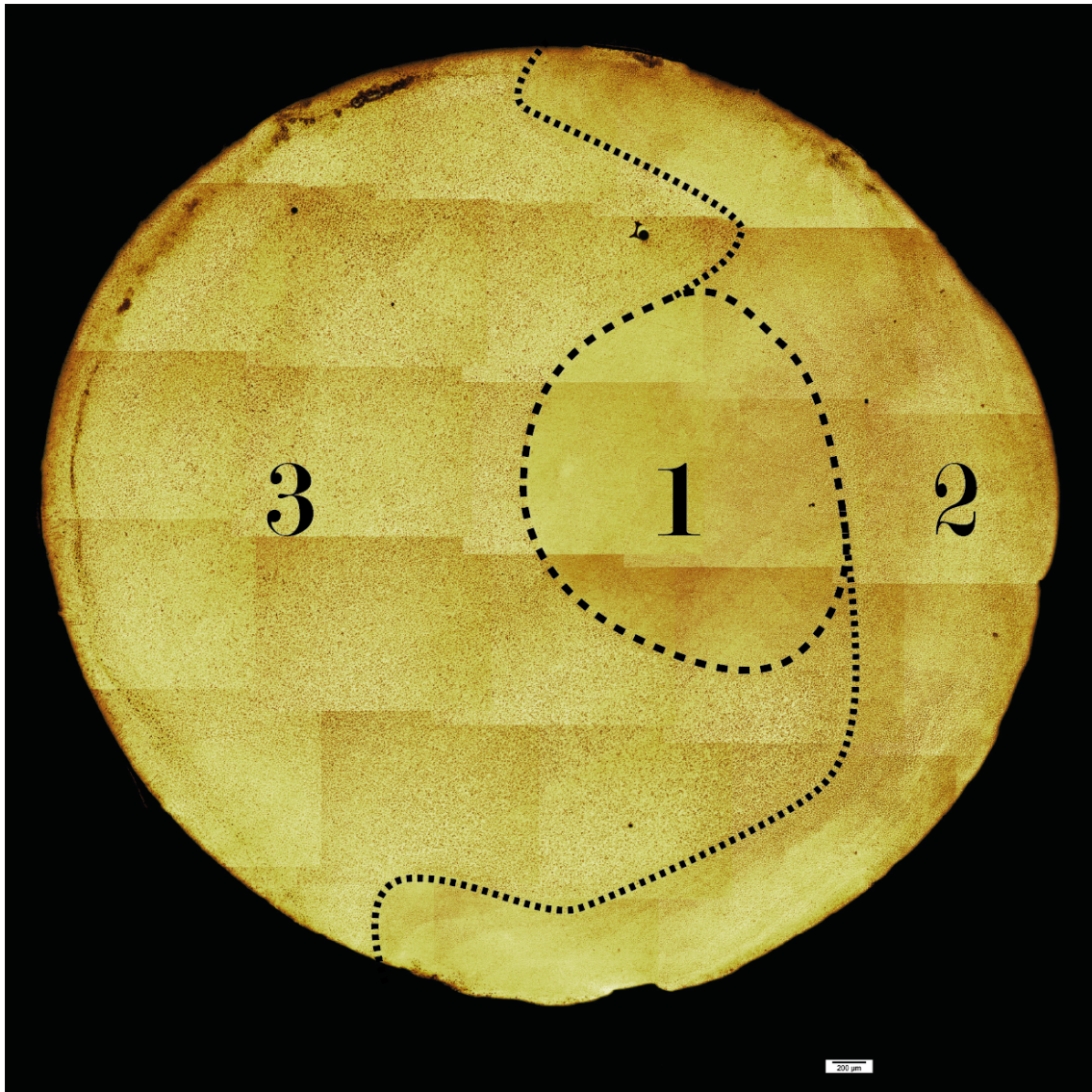


Figure C.25: Microstructure of 1-00-C, base of test piece, etched with Kallings no.2

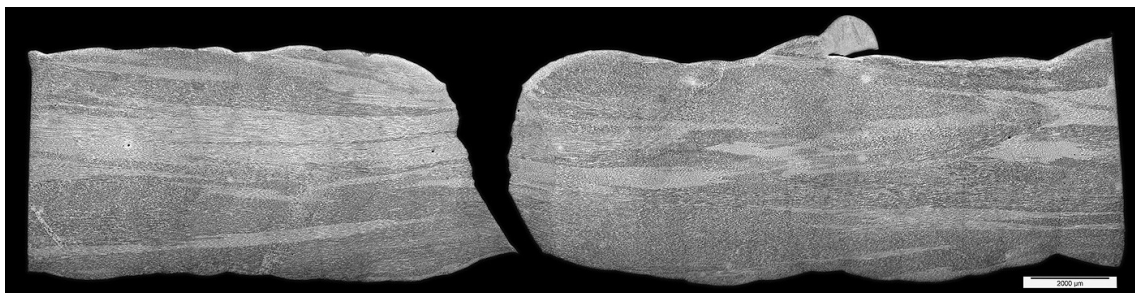


Figure C.26: Microstructure of 1-30-B, longitudinal section at failure location, etched with 10 ml H₂O, 30 ml HCl (27%), 1.5 ml HO

1-30

Only one sample was taken in this series. Individual dendrites can be made out, but the micrograph is not clear and some artefacts due to the etchant are visible. The use of a different etchant is advised to get better results.

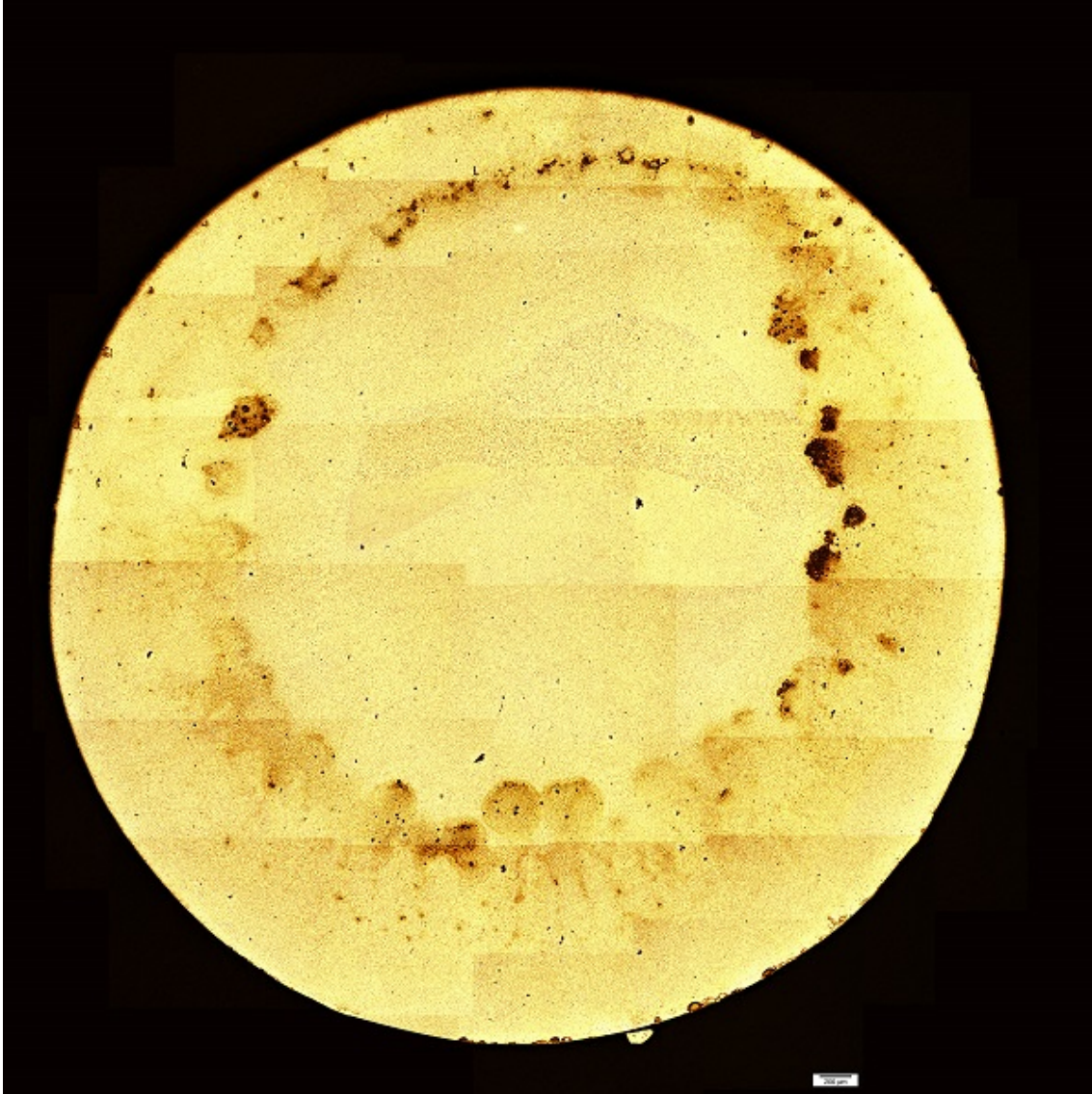


Figure C.27: Microstructure of 1-30-B, base of test piece, etched with Kalling's no.

2

1-60

1-60-B and 1-60-C were etched with V2A etchant. Please see appendix C.2.8 for these results in combination with the results from hardness testing.

Welding wire

Micrographs of the welding wire have been included here. The results are very unclear. Future samples should be etched with a different etchant.

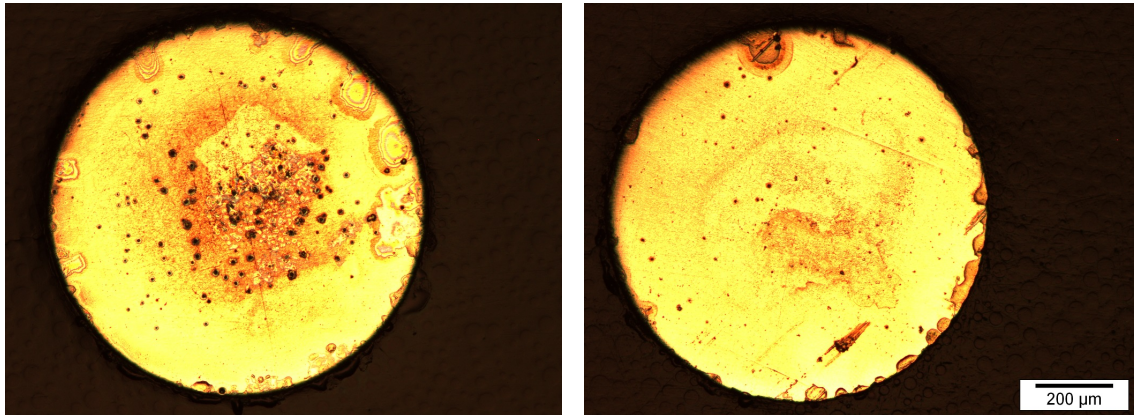


Figure C.28: Microstructure of welding wire, etched with Kalling's no. 2

C.2.8 Microhardness

The following images combine micrography of specimen cross sections and the corresponding plots of microhardness values. The diamond shapes indicate points of measurement. Different solidification area boundaries have been marked with dotted lines.

The average hardness of this cross section, taken at the top of specimen 1-60-B, is 169 HV.

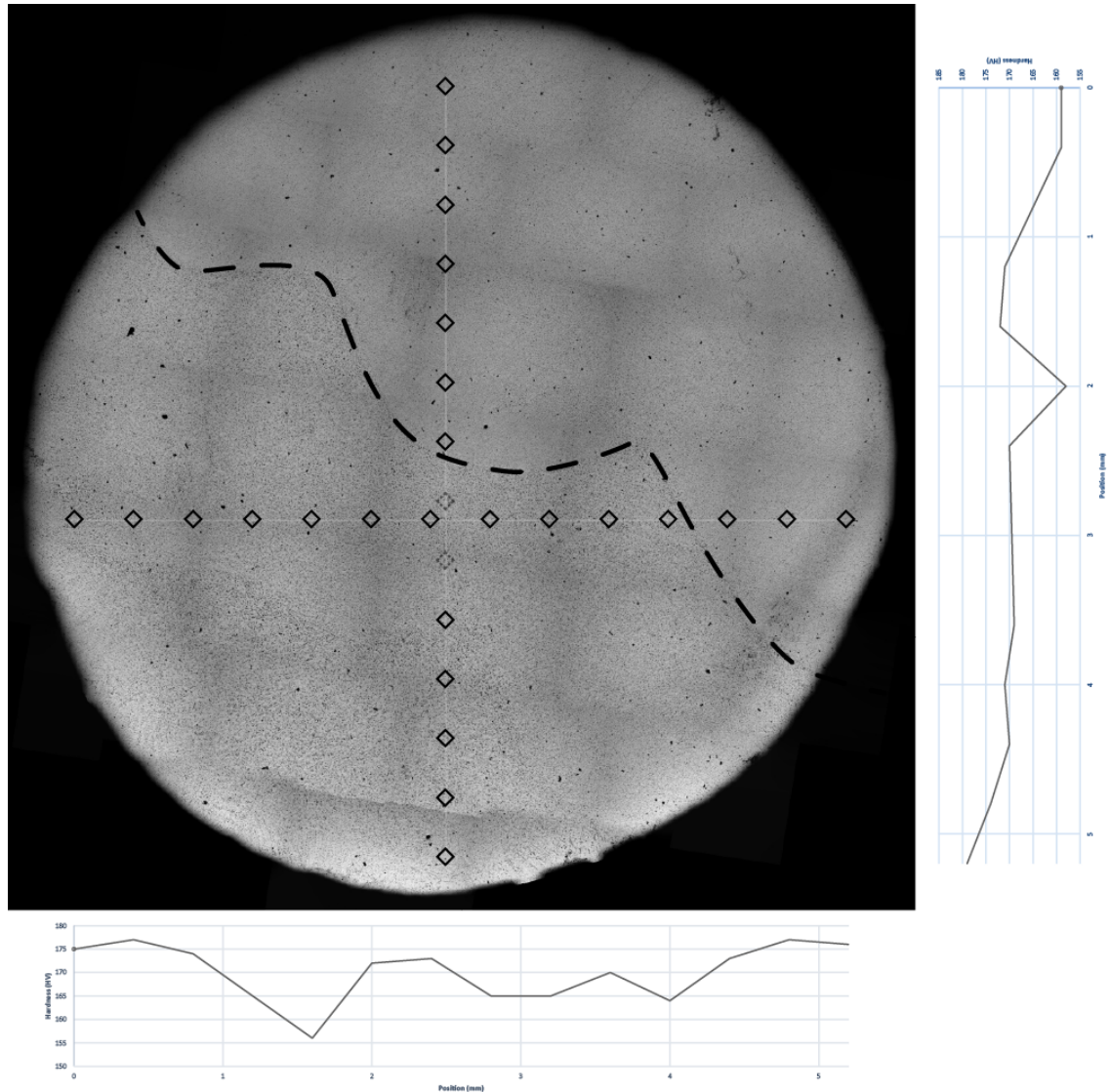


Figure C.29: Microstructure and Vickers hardness of 1-60-B

The average hardness of this cross section, taken at the heat sink of specimen 1-60-C, is 166 HV.

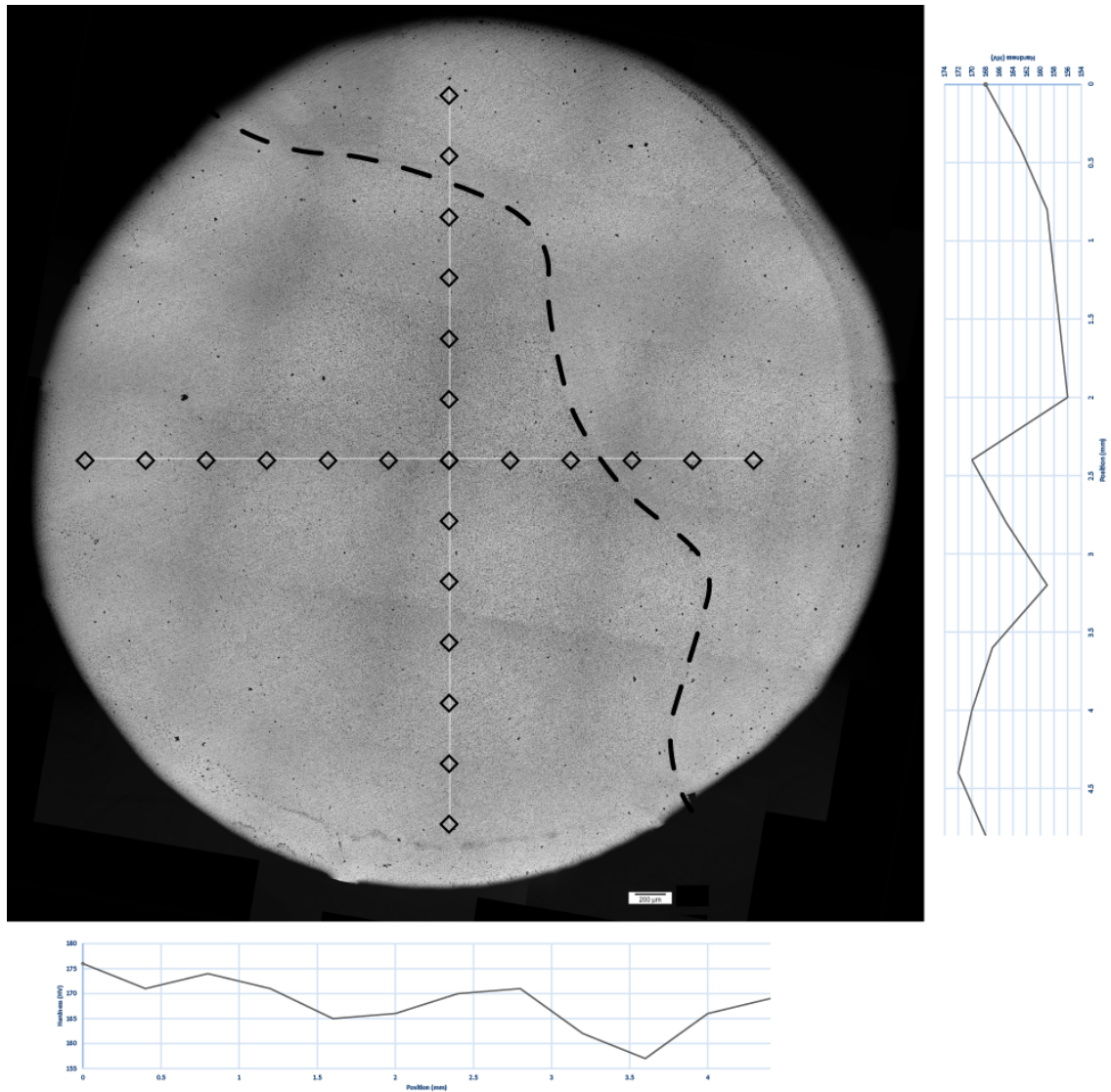


Figure C.30: Microstructure and Vickers hardness of 1-60-C

C.3 Batch 2

Unfortunately, specimen 2-00-A was destroyed when first setting up the buckling test. Therefore, no structural testing has been performed on this specimen. The geometrical data is included, though.

C.3.1 Parameters

The process parameters in table C.5 have been used in the production of the second batch of tensile test specimens.

Per request of MX3D, the process parameters have been excluded from this public version. Please contact them at <http://www.MX3D.com> or gijis@MX3D.com.

Base material

CONFIDENTIAL

Robot

CONFIDENTIAL

Welding

CONFIDENTIAL

Table C.5: Process parameters tensile tests

C.3.2 Geometry

The histograms on the following pages show the distribution of the diameter of the different specimens. Per specimen, the data from four photos was taken and combined to get these results. Additionally, the data of these specimens has been combined to give a description of the distribution of the diameter per angle. Scatter plots have been made to analyse the goodness of fit to the normal distribution. Scatter plots were also used to investigate the accuracy of different methods. The distributions for the cases in which 1, 2, 3, and 4 photos were used to describe the diameter have been compared to each other and to results from the photogrammetrical method.

0 degrees

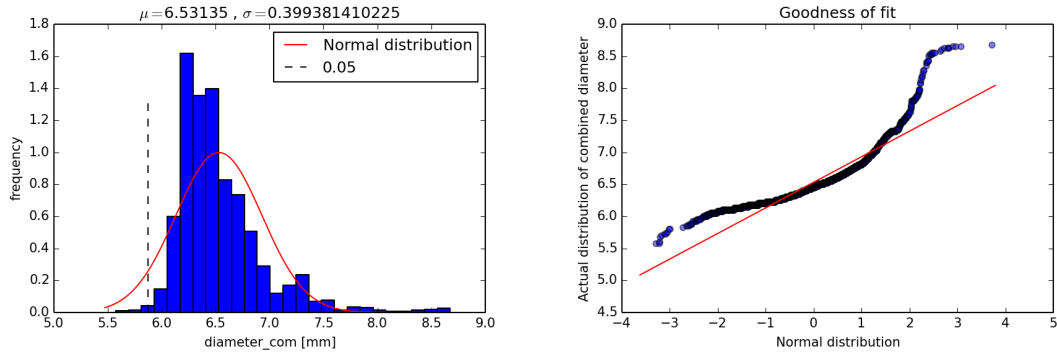


Figure C.31: 2-00-A geometry

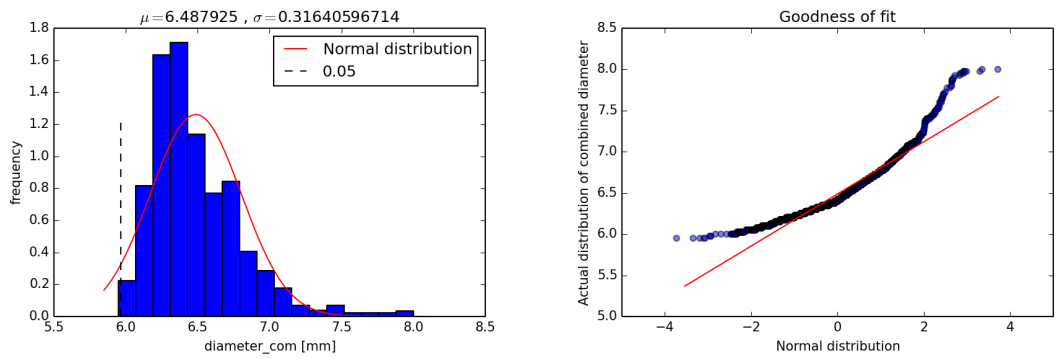


Figure C.32: 2-00-B geometry

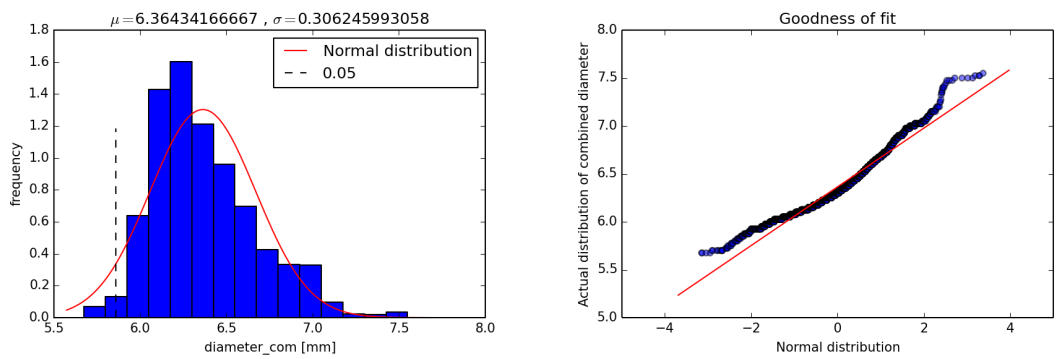


Figure C.33: 2-00-C geometry

30 degrees

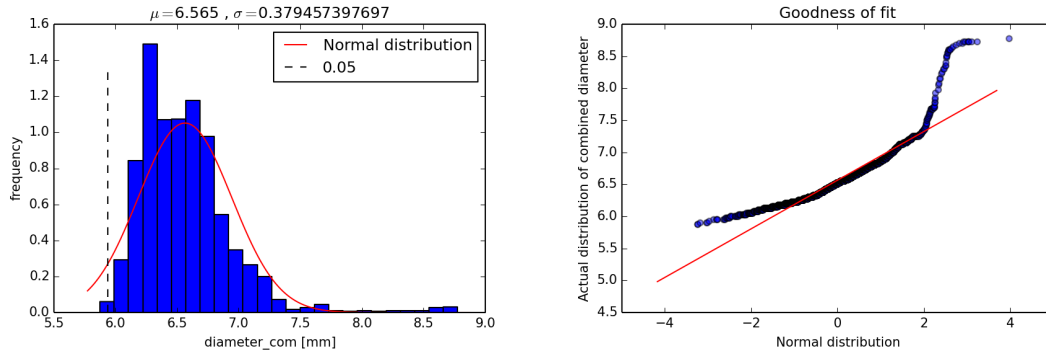


Figure C.34: 2-30-A geometry

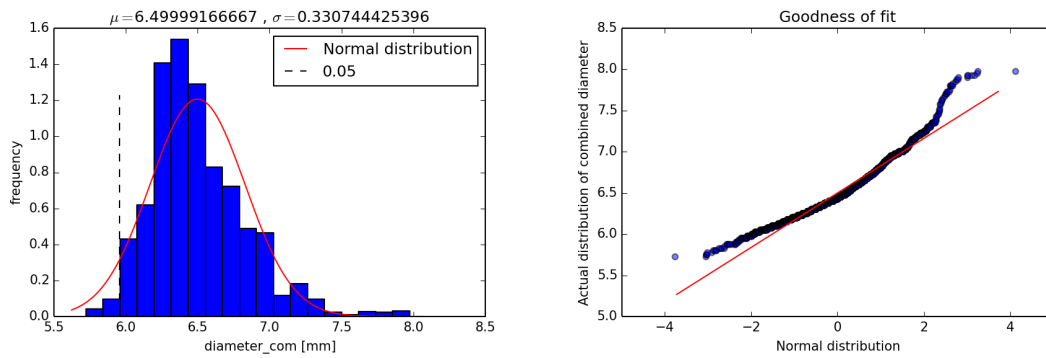


Figure C.35: 2-30-B geometry

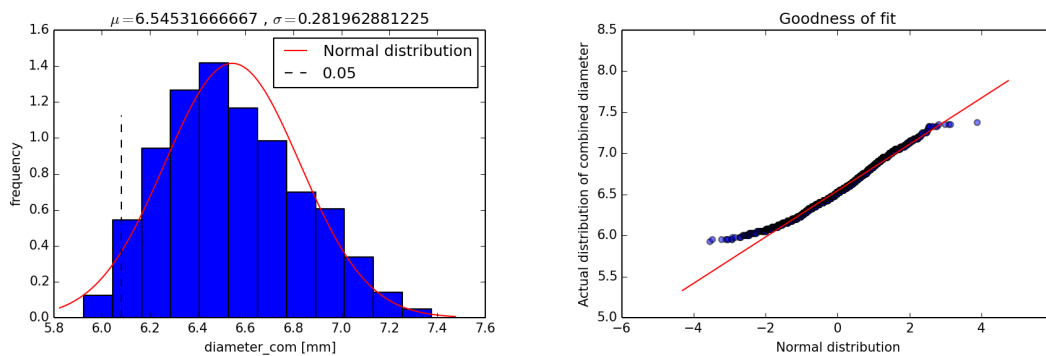


Figure C.36: 2-30-C geometry

60 degrees

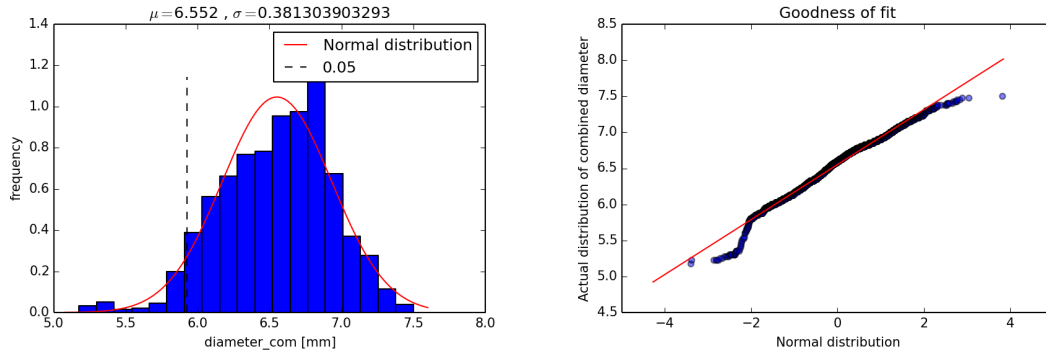


Figure C.37: 2-60-A geometry

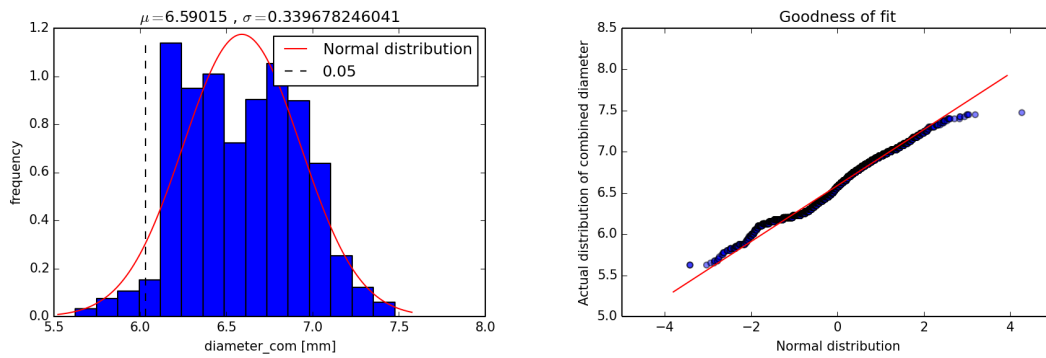


Figure C.38: 2-60-B geometry

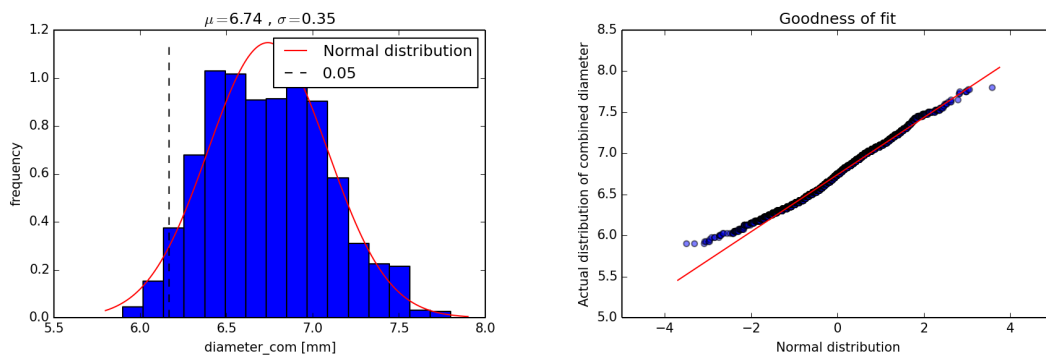
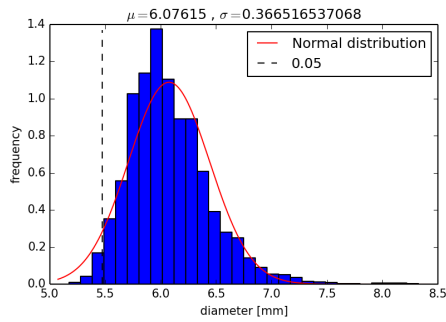


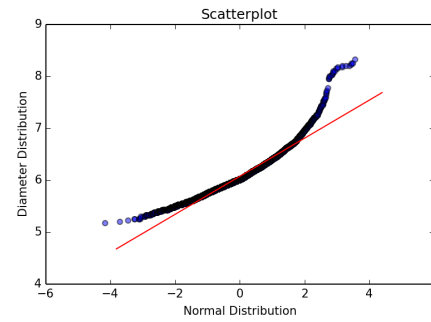
Figure C.39: 2-60-C geometry

Combined distributions per angle

Here, the distributions of each specimen are combined per angle, because they are produced in the exact same way, and should therefore be part of the same, larger total distribution. Again, normal distributions have been fitted to these combined distributions. Scatter plots are provided to study the goodness of fit. Figure C.41 is the only case in which the normal distribution gives an overestimation of the minimum diameter. This is caused by an obvious defect (see also figure ??), which should be repaired after quality control.

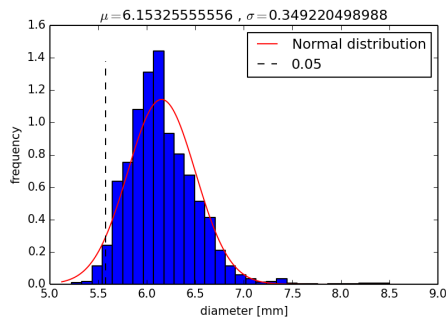


(a) Combined diameter distribution

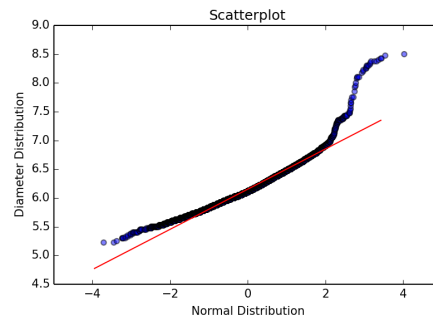


(b) Fit to normal distribution

Figure C.40: Combined geometry for specimen type 2-00

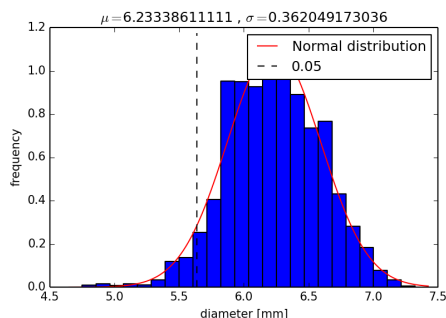


(a) Combined diameter distribution

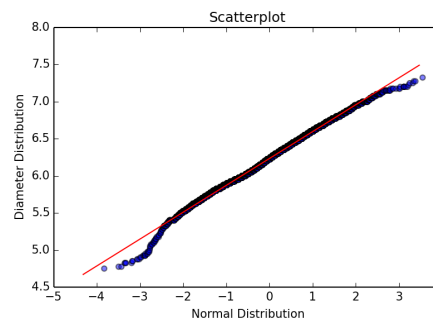


(b) Fit to normal distribution

Figure C.41: Combined geometry for specimen type 2-30



(a) Combined diameter distribution



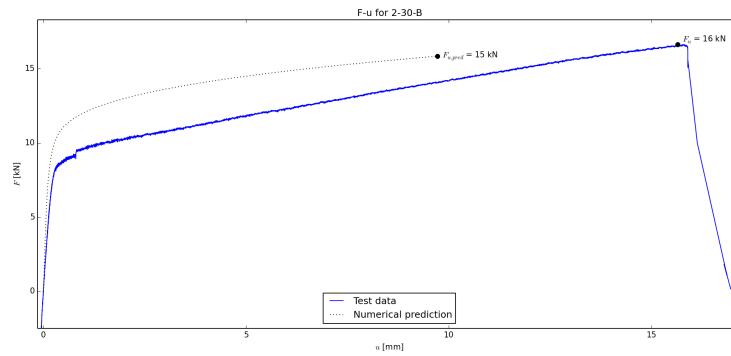
(b) Fit to normal distribution

Figure C.42: Combined geometry for specimen type 2-60

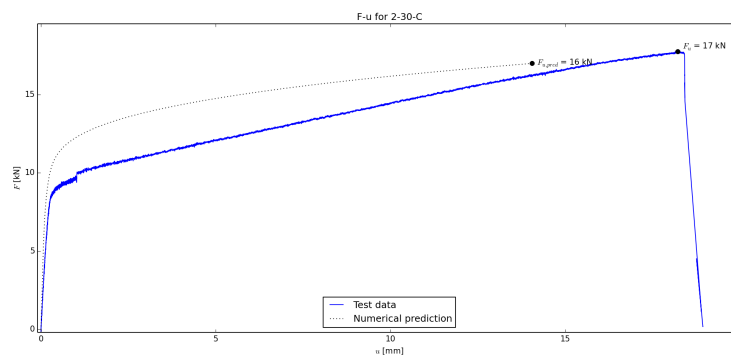
C.3.3 F-u curves

The following force-displacement curves show the raw results from the tensile tests that were performed.

0 degrees



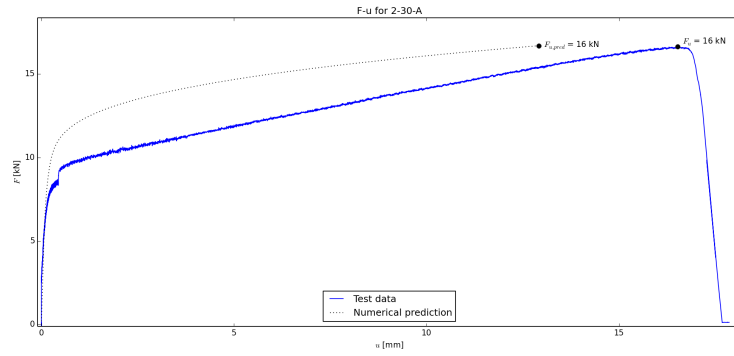
(a) 2-30-B



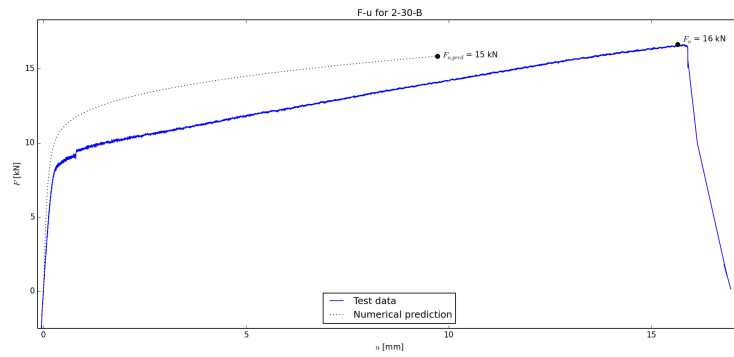
(b) 2-30-C

Figure C.43: F-u diagrams at 30 degrees

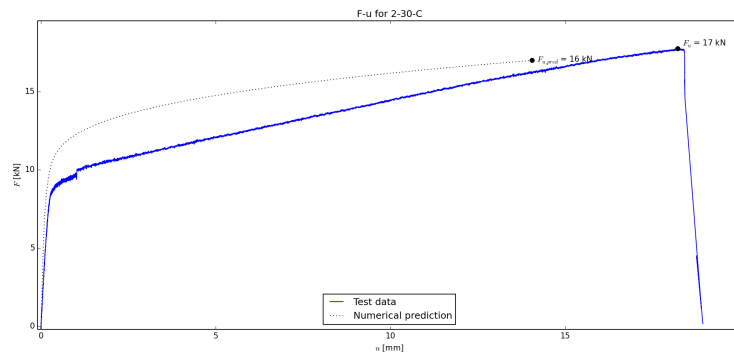
30 degrees



(a) 2-30-A



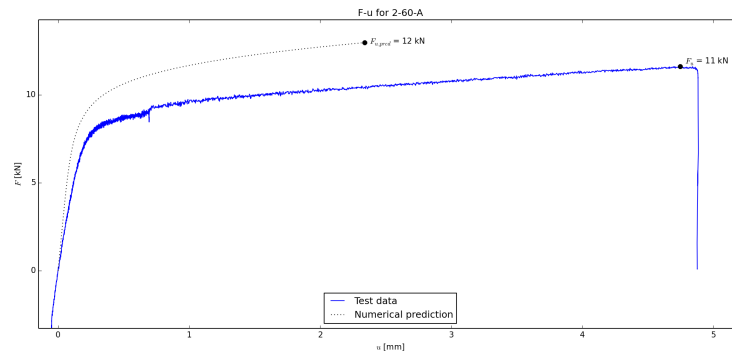
(b) 2-30-B



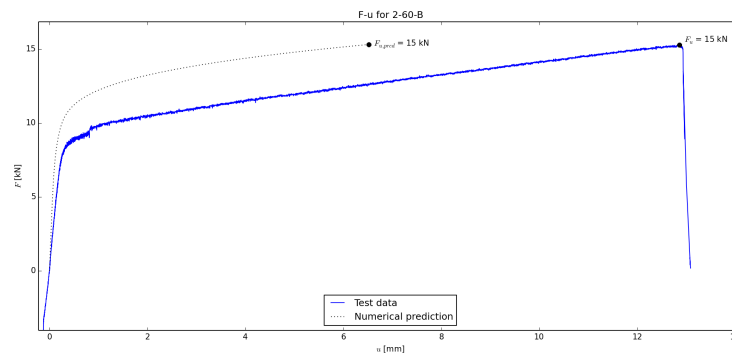
(c) 2-30-C

Figure C.44: F-u diagrams at 30 degrees

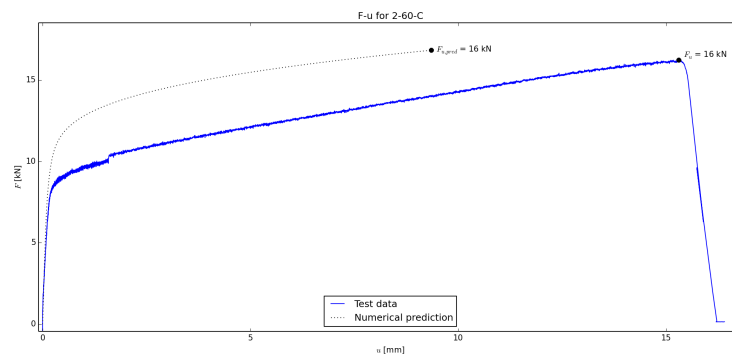
60 degrees



(a) 2-60-A



(b) 2-60-B



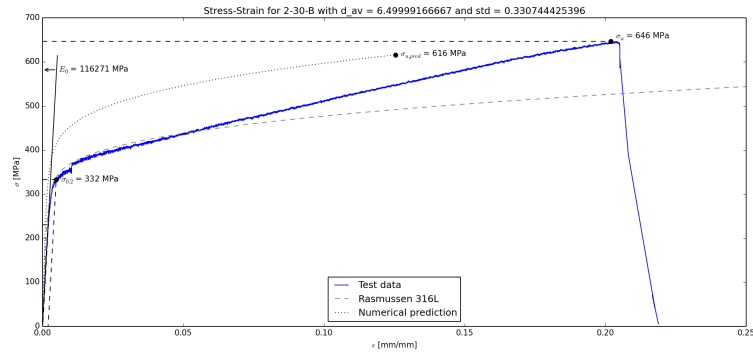
(c) 2-60-C

Figure C.45: F-u diagrams at 60 degrees

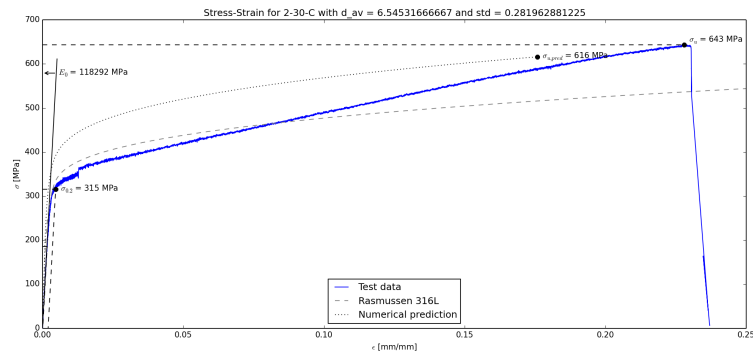
C.3.4 Stress-strain curves

The following stress-strain curves are based on the average diameters of the strands.

0 degrees



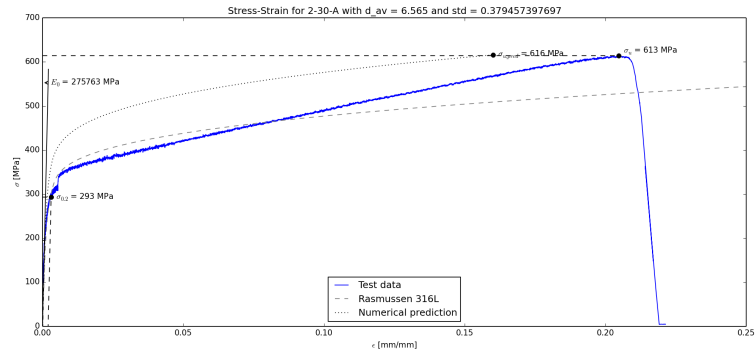
(a) 2-30-B



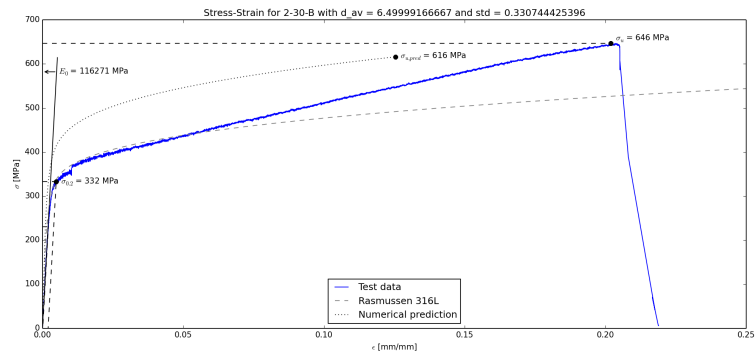
(b) 2-30-C

Figure C.46: Stress-strain diagrams at 30 degrees

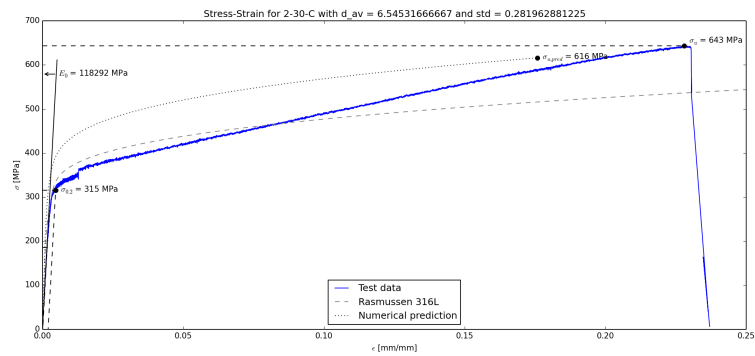
30 degrees



(a) 2-30-A



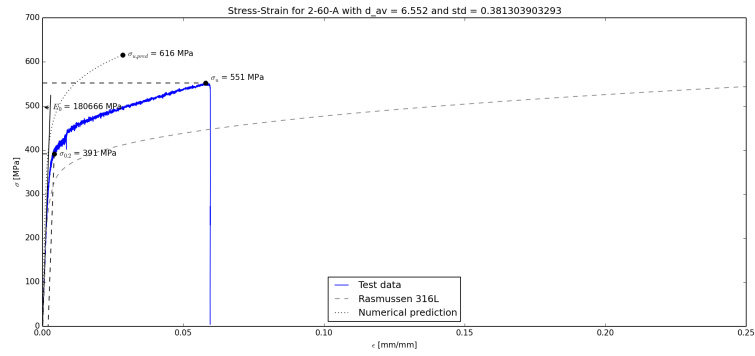
(b) 2-30-B



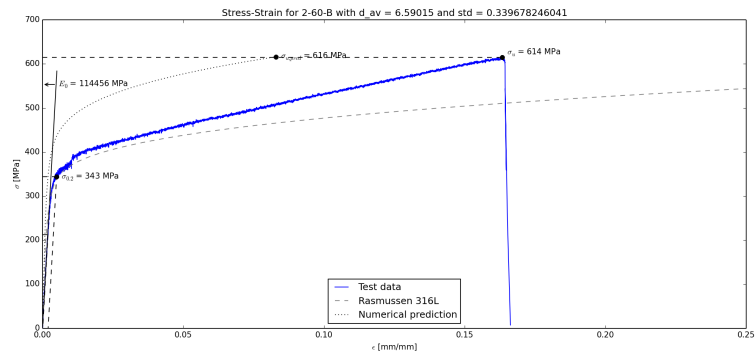
(c) 2-30-C

Figure C.47: Stress-strain diagrams at 30 degrees

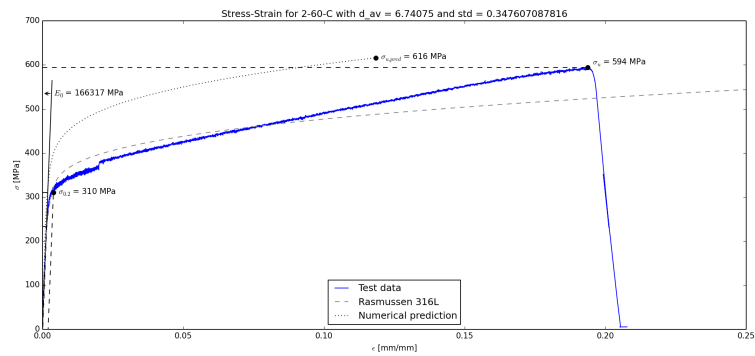
60 degrees



(a) 2-60-A



(b) 2-60-B



(c) 2-60-C

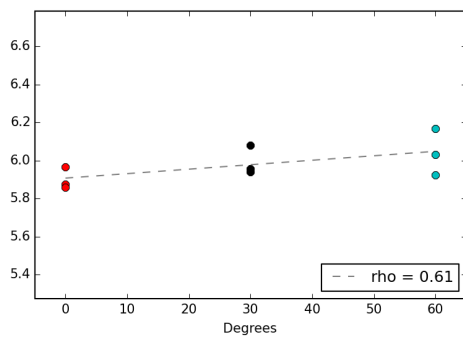
Figure C.48: Stress-strain diagrams at 60 degrees

C.3.5 Correlations

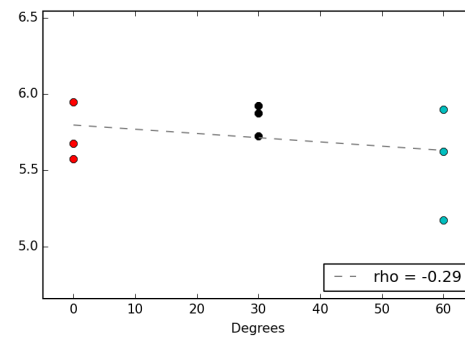
Different properties and parameters have been plotted against each other to investigate their relationships. For each plot, the Pearson product-moment correlation coefficient ρ has been presented. This value ranges from -1 to 1. The closer this value is to 1 or -1, the greater the correlation. Variables with a correlation coefficient that is (close to) 0 are not correlated.

Angle

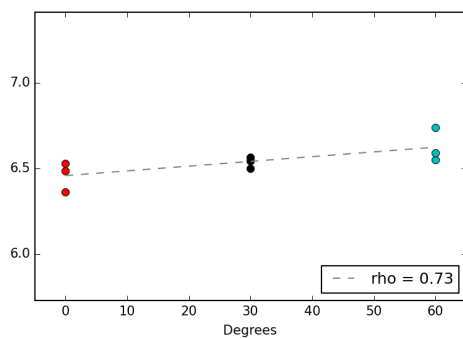
The plots in this subsection show how geometrical and mechanical properties vary with the angle at which the test pieces are produced.



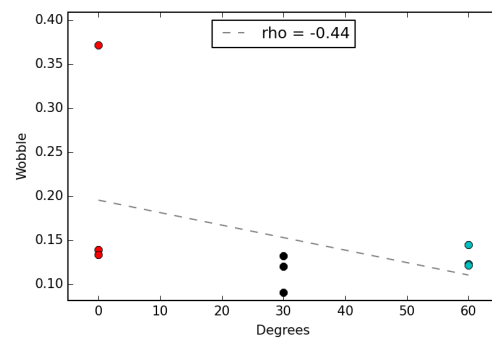
(a) Angle versus 5 percentile diameter



(b) Angle versus minimum diameter

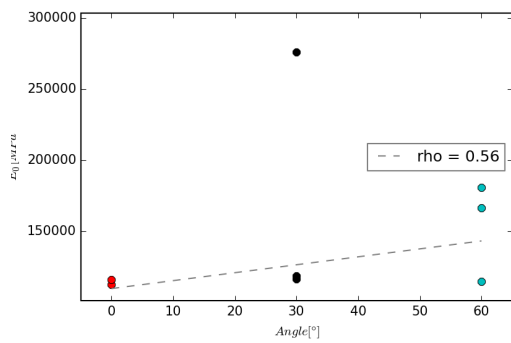


(c) Angle versus average diameter

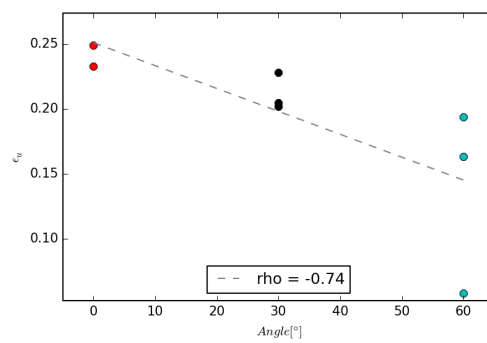


(d) Angle versus wobble factor

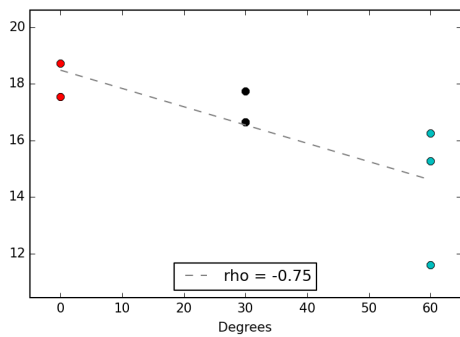
Figure C.49: Correlations between angle and geometry



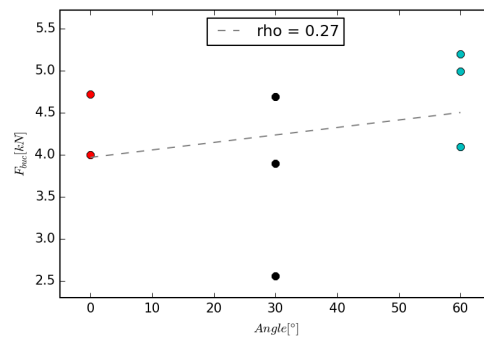
(a) Angle versus Young's modulus



(b) Angle versus ultimate strain



(c) Angle versus failure load

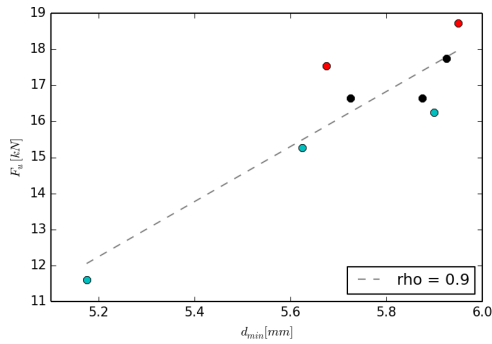


(d) Angle versus buckling load

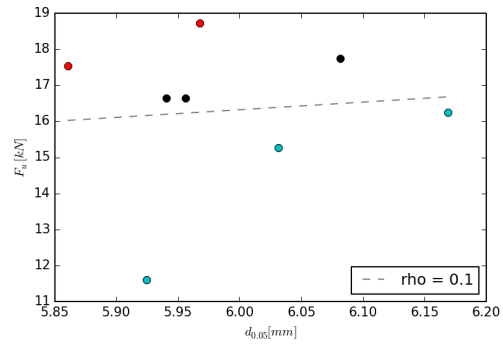
Figure C.50: Correlations between angle and mechanical properties

Geometry versus mechanical properties

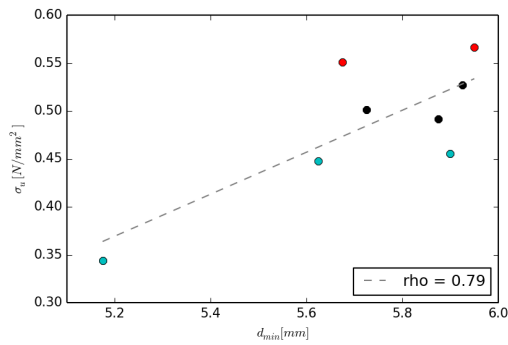
The plots in this subsection show correlations between geometrical and mechanical properties.



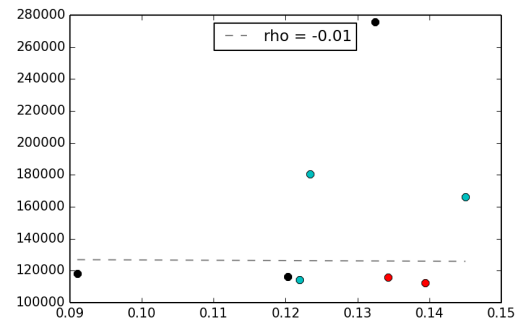
(a) Minimum diameter versus failure load



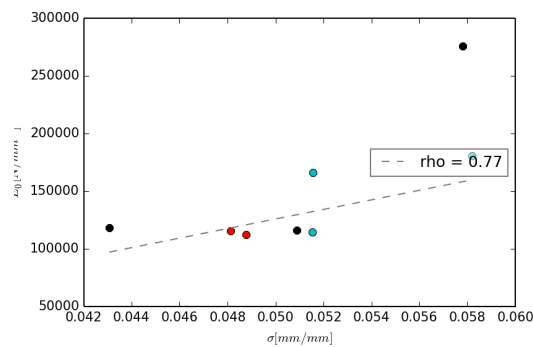
(b) 5 percentile diameter versus failure load



(c) Minimum diameter versus ultimate stress



(d) Wobble factor versus Young's modulus



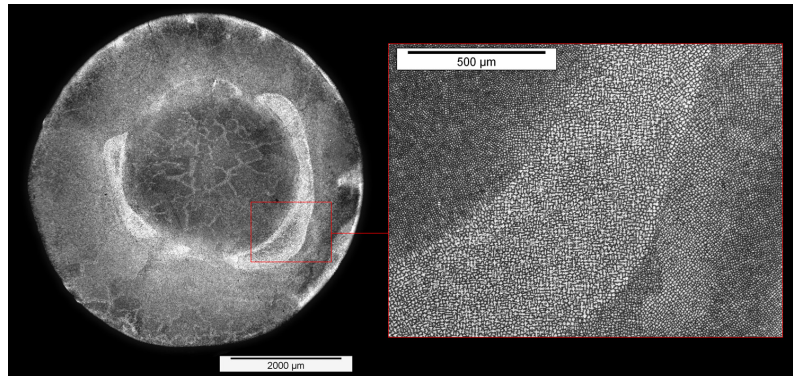
(e) Diameter standard deviation divided by mean area versus Young's modulus

Figure C.51: Correlations between geometry and mechanical properties

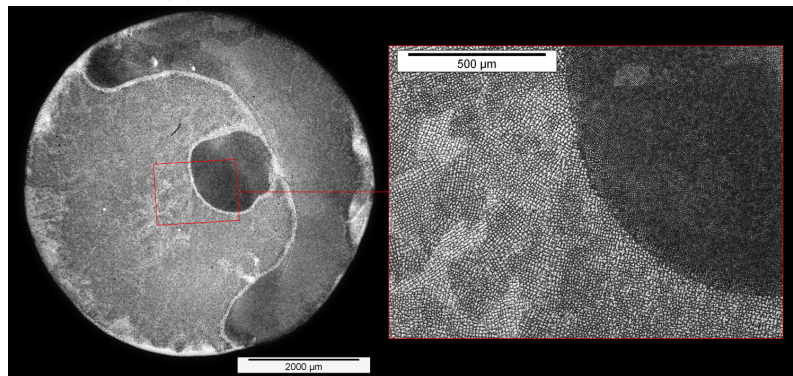
C.3.6 Microstructure

This sections gives overview images of the microstructures of the different samples investigated using optical microscopy. Weld passes and grain formation are clearly visible.

Cross sections



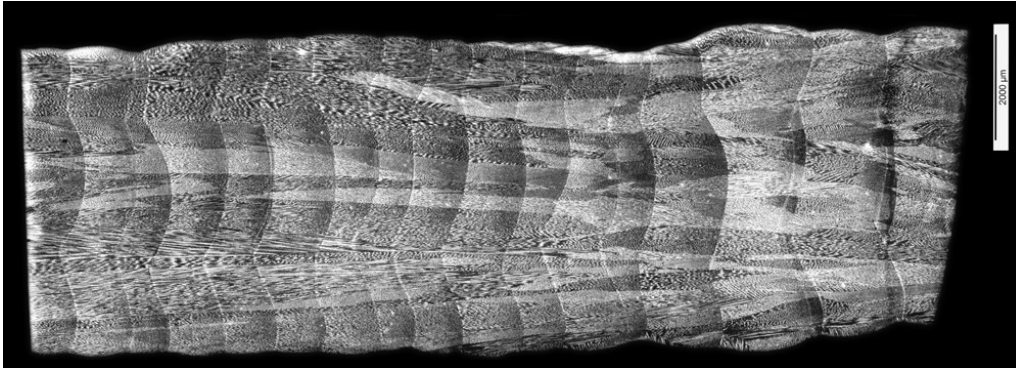
(a) Microstructure of specimen 2-00-A



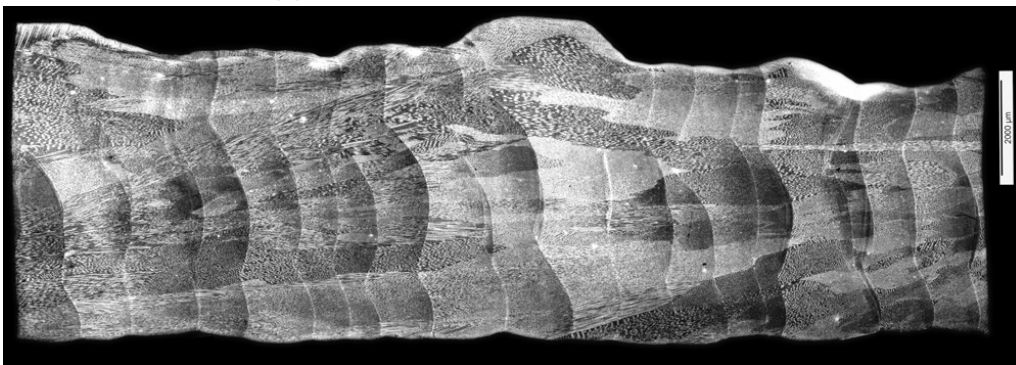
(b) Microstructure of specimen 2-30-A



(c) Microstructure of specimen 2-60-A

Longitudinal sections

(a) Microstructure of specimen 2-00-A



(b) Microstructure of specimen 2-30-A



(c) Microstructure of specimen 2-60-A

C.4 Batch 3

C.4.1 Parameters

The process parameters in table C.6 have been used in the production of the third batch of tensile test specimens. The parameters were changed to increase strand diameter. The welding time was increased, increasing the amount of material deposited per layer.

Per request of MX3D, the process parameters have been excluded from this public version. Please contact MX3D at <http://www.MX3D.com> or gijs@MX3D.com.

Base material
CONFIDENTIAL
Robot
CONFIDENTIAL
Welding
CONFIDENTIAL

Table C.6: Process parameters tensile tests

C.4.2 Geometry

The histograms on the following pages show the distribution of the diameter of the different specimens. Per specimen, the data from four photos was taken and combined to get these results.

0 degrees

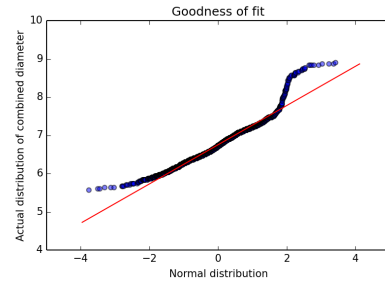
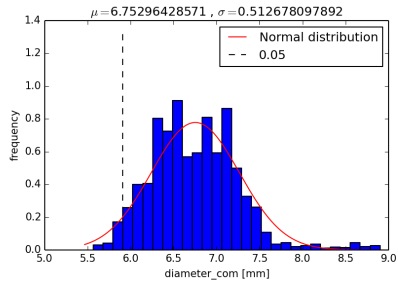


Figure C.54: 3-00-A geometry

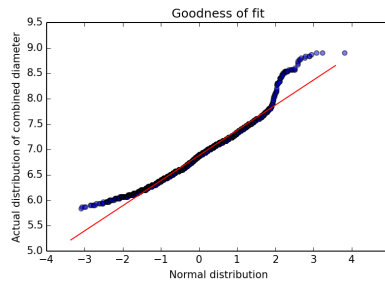
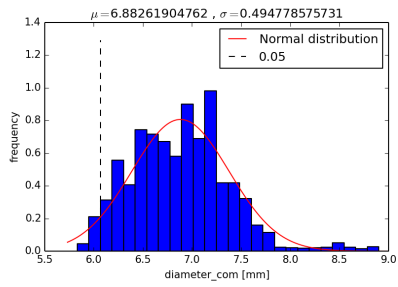


Figure C.55: 3-00-B geometry

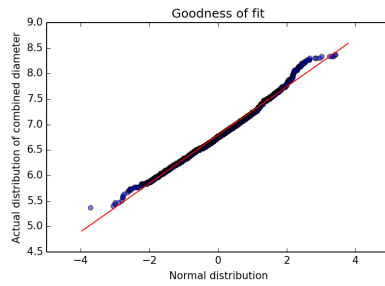
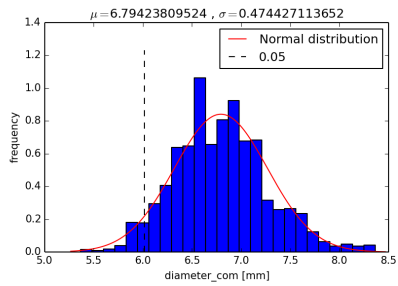


Figure C.56: 3-00-C geometry

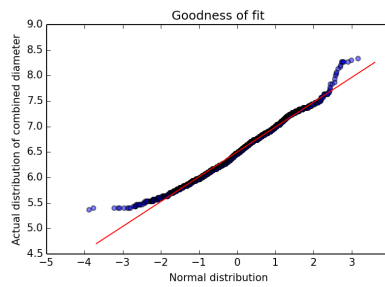
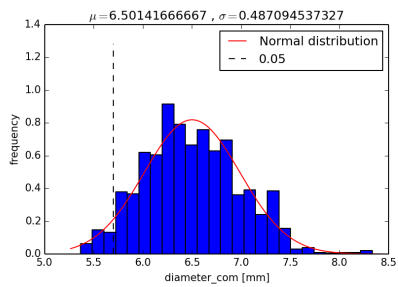


Figure C.57: 3-00-D geometry

30 degrees

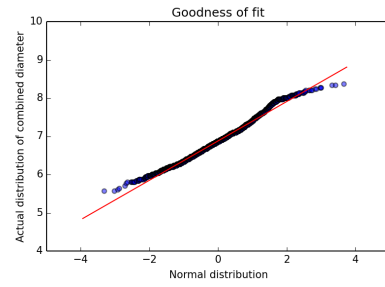
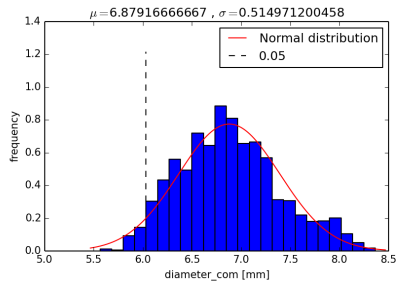


Figure C.58: 3-30-A geometry

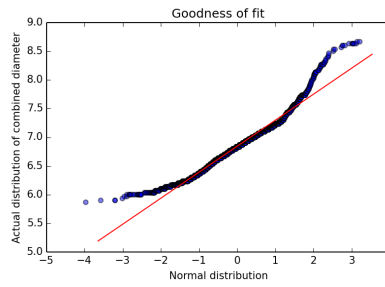
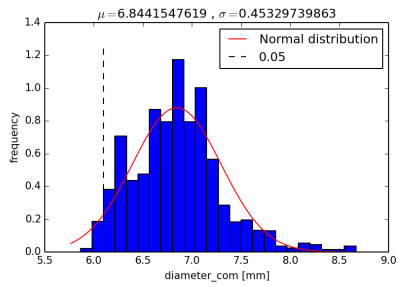


Figure C.59: 3-30-B geometry

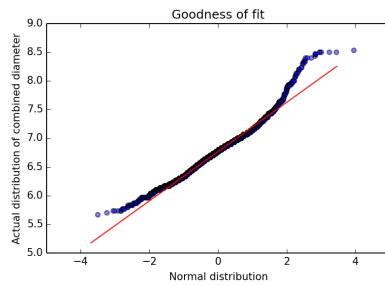
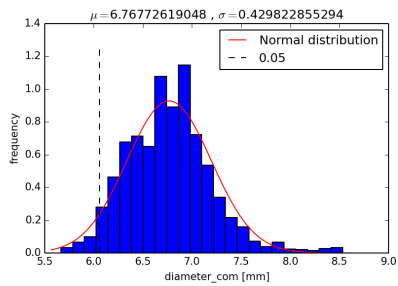


Figure C.60: 3-30-C geometry

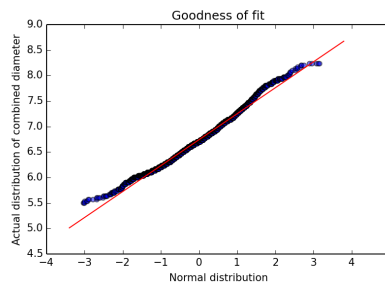
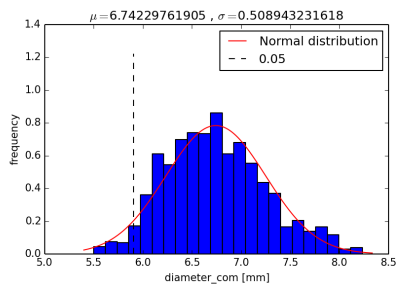


Figure C.61: 3-30-D geometry

60 degrees

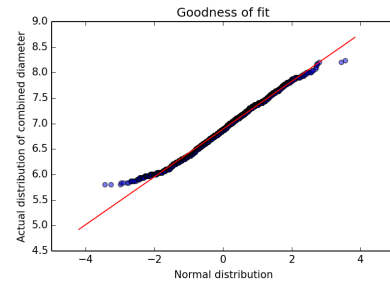
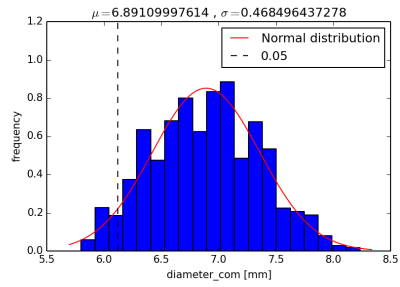


Figure C.62: 3-60-A geometry

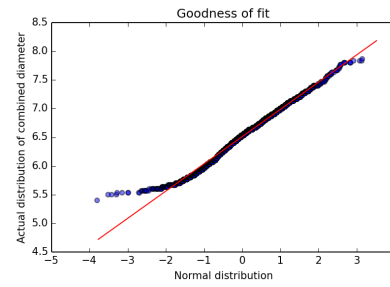
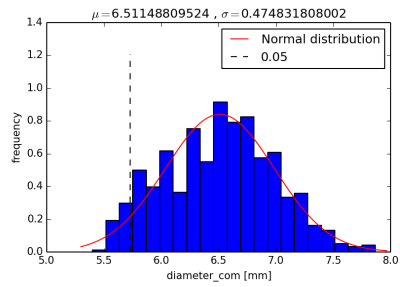


Figure C.63: 3-60-B geometry

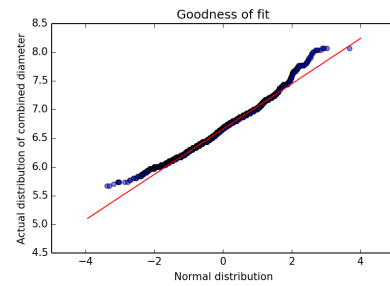
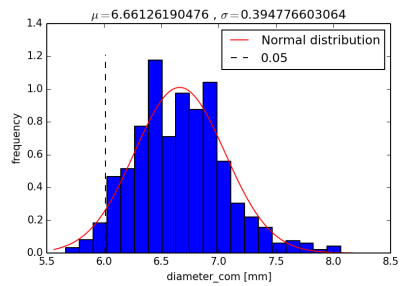


Figure C.64: 3-60-C geometry

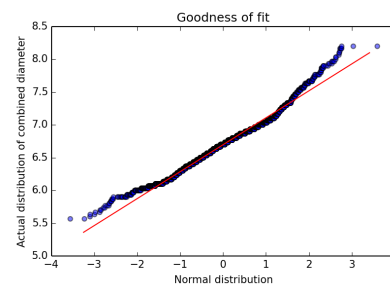
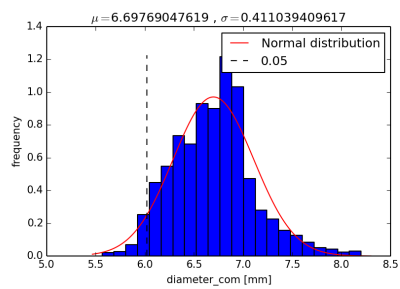
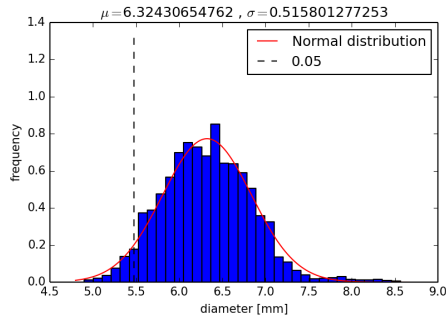


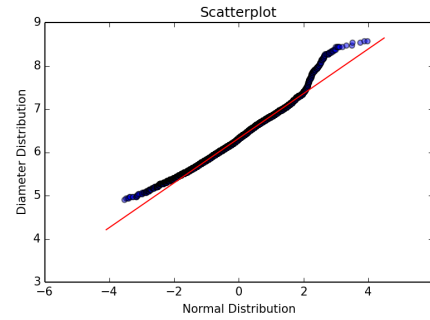
Figure C.65: 3-60-D geometry

Combined distributions per angle

Here, the distributions of each specimen are combined per angle, because they are produced in the exact same way, and should therefore be part of the same, larger total distribution. Again, normal distributions have been fitted to these combined distributions. Scatter plots are provided to study the goodness of fit.

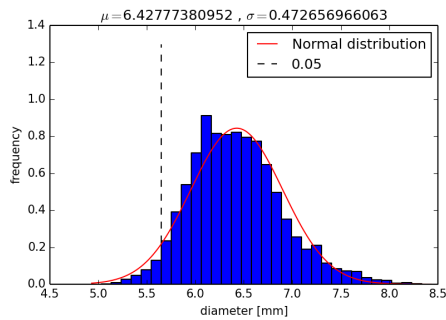


(a) Combined diameter distribution

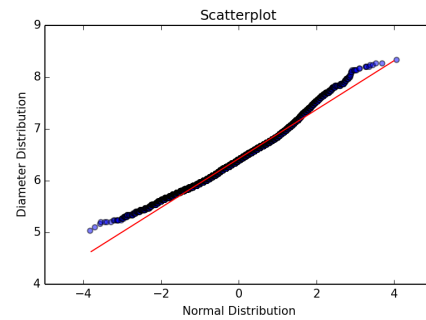


(b) Fit to normal distribution

Figure C.66: Combined geometry for specimen type 3-00

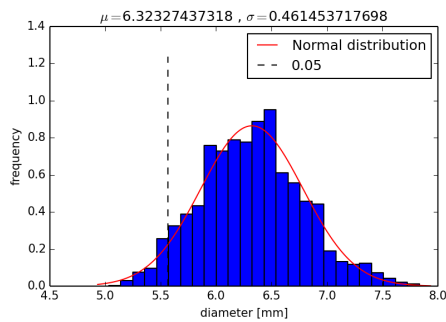


(a) Combined diameter distribution

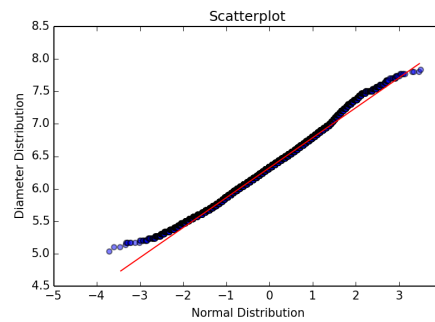


(b) Fit to normal distribution

Figure C.67: Combined geometry for specimen type 3-30



(a) Combined diameter distribution



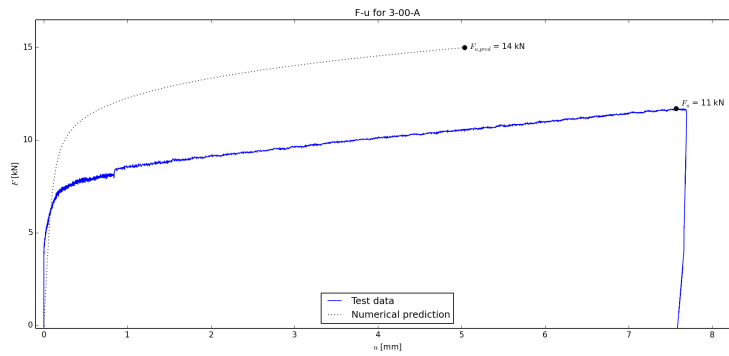
(b) Fit to normal distribution

Figure C.68: Combined geometry for specimen type 3-60

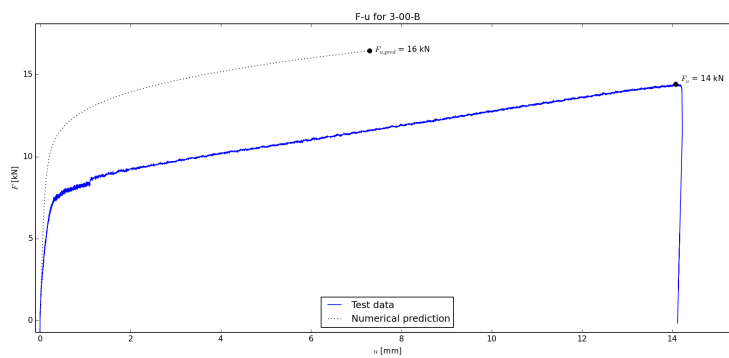
C.4.3 F-u curves

The following force-displacement curves show the raw results from the tensile tests that were performed.

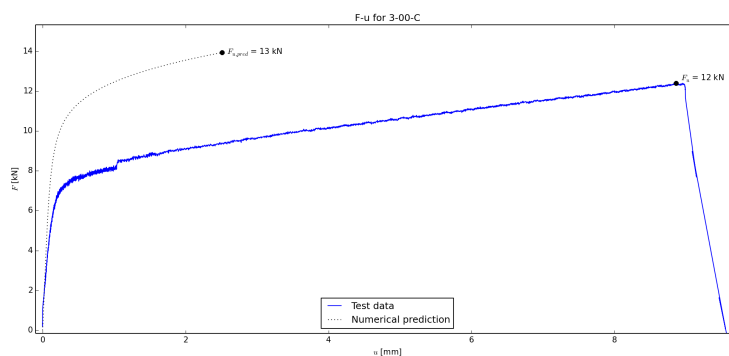
0 degrees



(a) 3-00-A



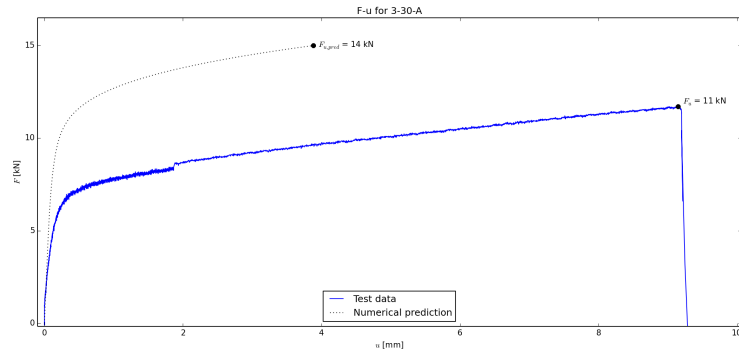
(b) 3-00-B



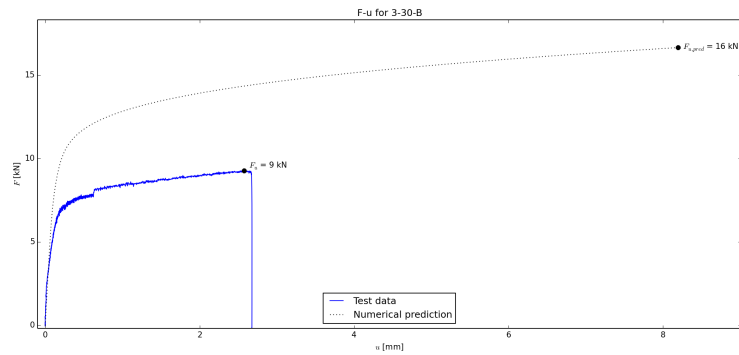
(c) 3-00-C

Figure C.69: F-u diagrams at 0 degrees

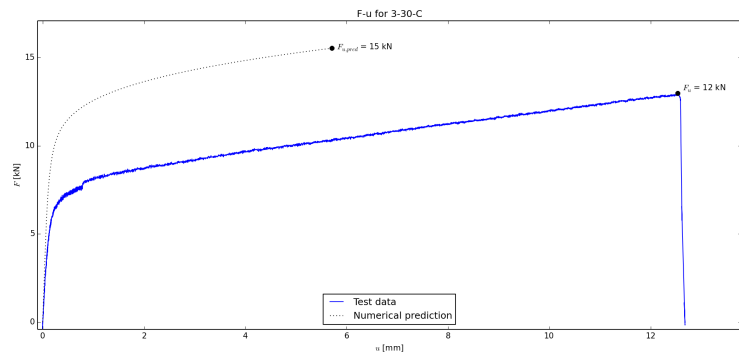
30 degrees



(a) 3-30-A



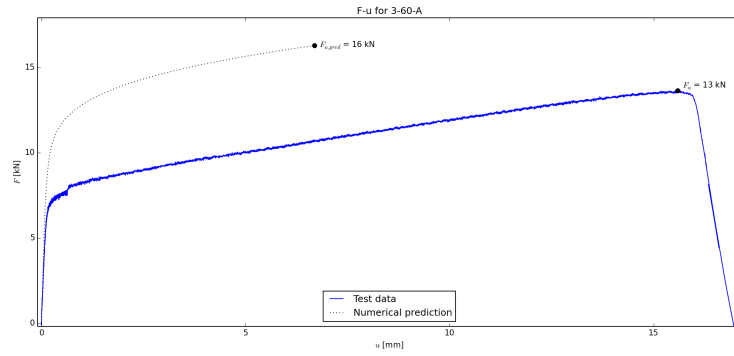
(b) 3-30-B



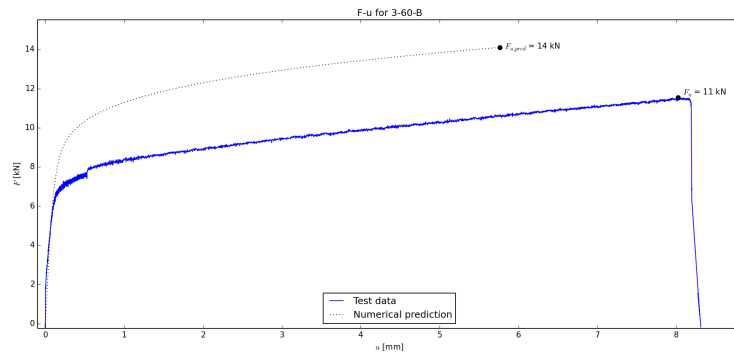
(c) 3-30-C

Figure C.70: F-u diagrams at 30 degrees

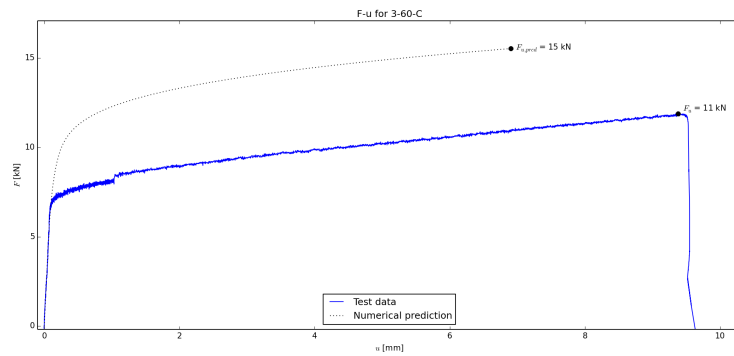
60 degrees



(a) 3-60-A



(b) 3-60-B



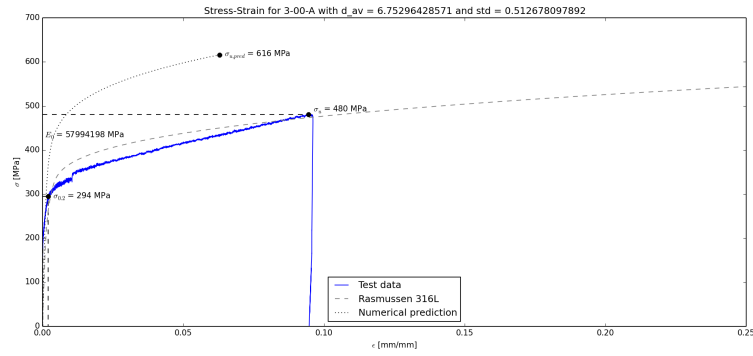
(c) 3-60-C

Figure C.71: F-u diagrams at 60 degrees

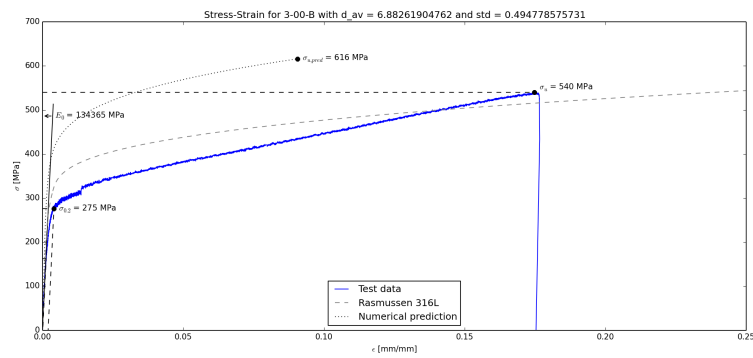
C.4.4 Stress-strain curves

The following stress-strain curves are based on the average diameters of the strands.

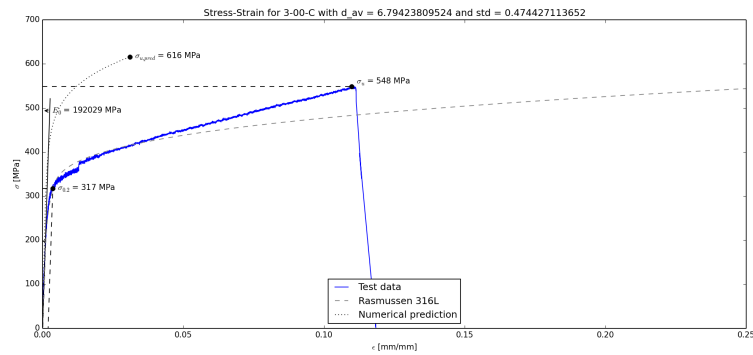
0 degrees



(a) 3-00-A



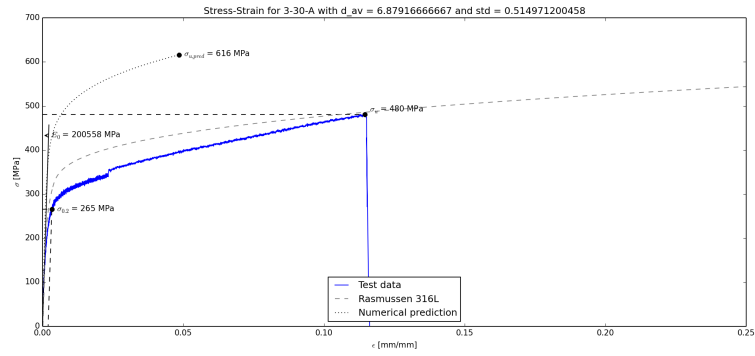
(b) 3-00-B



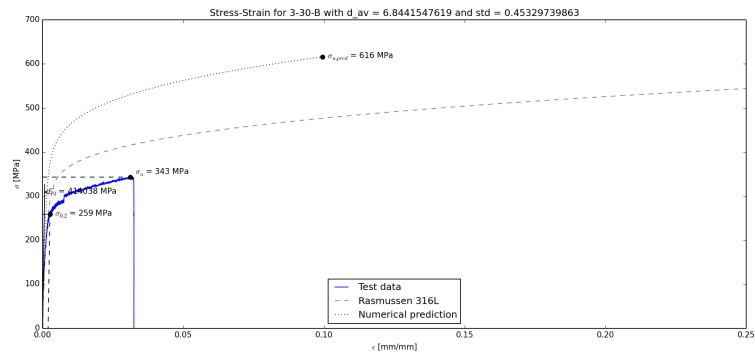
(c) 3-00-C

Figure C.72: Stress-strain diagrams at 0 degrees

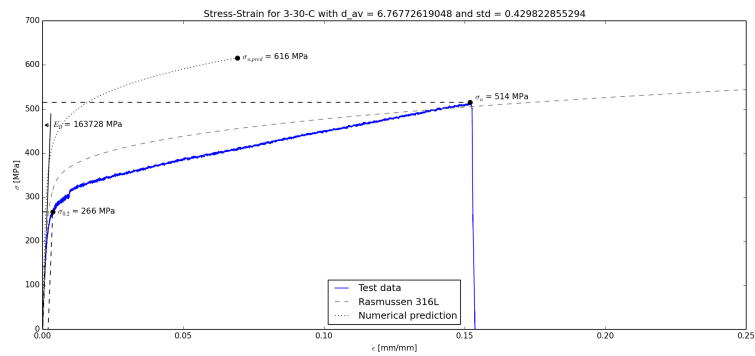
30 degrees



(a) 3-30-A



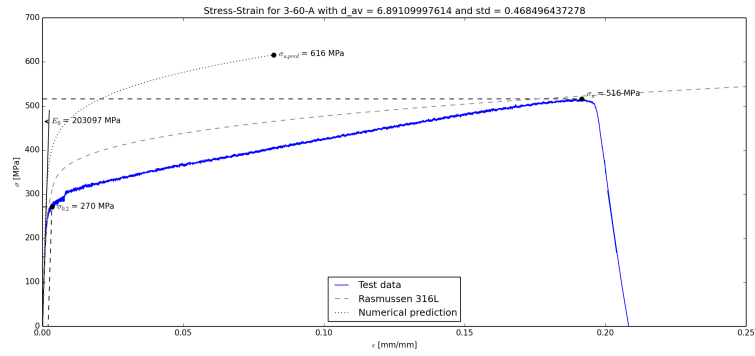
(b) 3-30-B



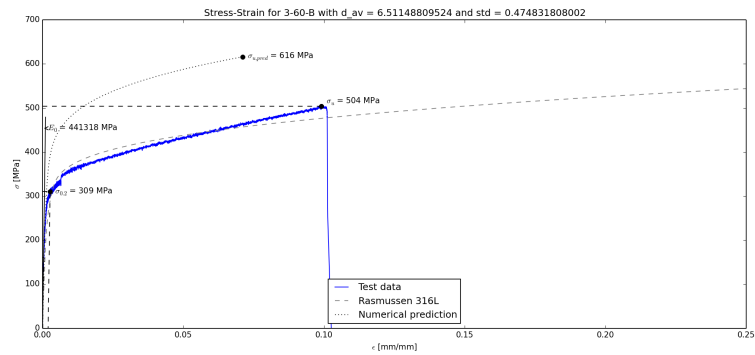
(c) 3-30-C

Figure C.73: Stress-strain diagrams at 30 degrees

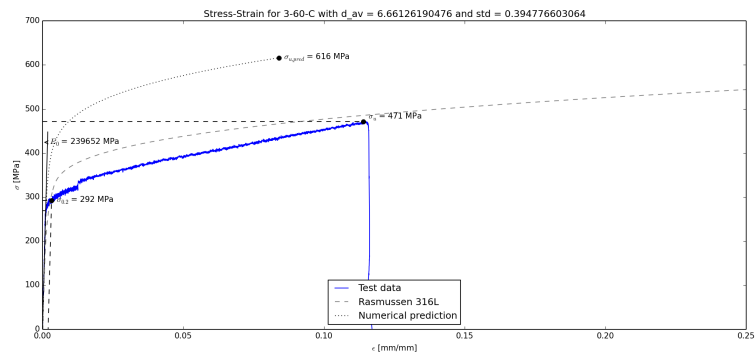
60 degrees



(a) 3-60-A



(b) 3-60-B



(c) 3-60-C

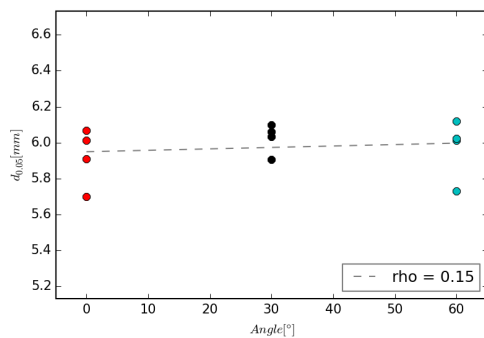
Figure C.74: Stress-strain diagrams at 60 degrees

C.4.5 Correlations

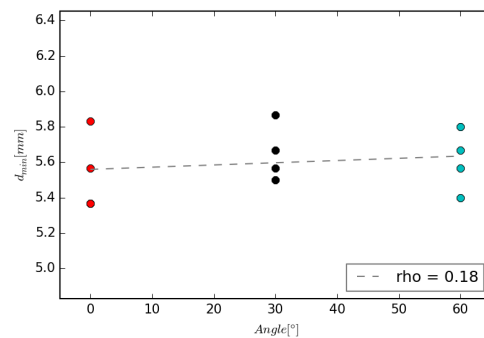
Different properties and parameters have been plotted against each other to investigate their relationships. For each plot, the Pearson product-moment correlation coefficient ρ has been presented. This value ranges from -1 to 1. The closer this value is to 1 or -1, the greater the correlation. Variables with a correlation coefficient that is (close to) 0 are not correlated.

Angle

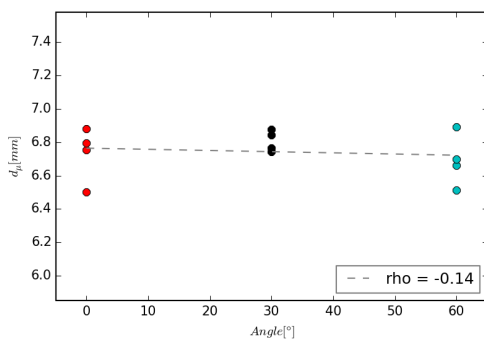
The plots in this subsection show how geometrical and mechanical properties vary with the angle at which the test pieces are produced.



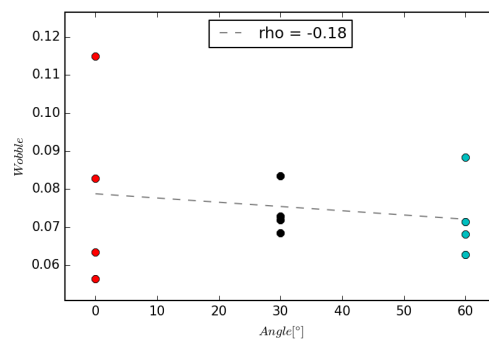
(a) Angle versus 5 percentile diameter



(b) Angle versus minimum diameter

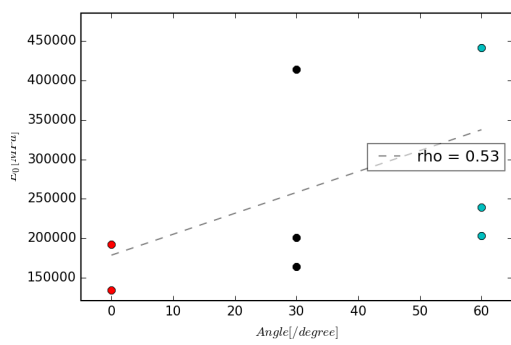


(c) Angle versus average diameter

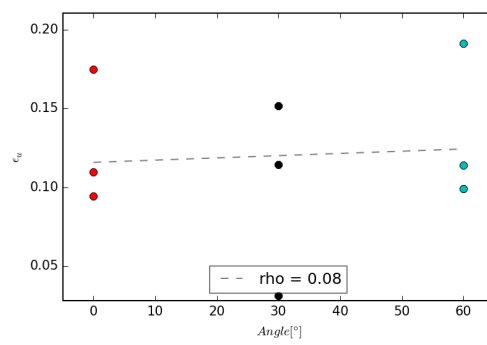


(d) Angle versus wobble factor

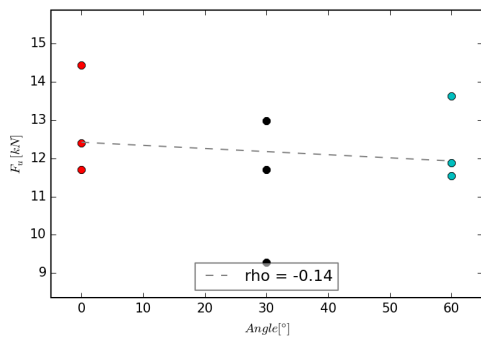
Figure C.75: Correlations between angle and geometry



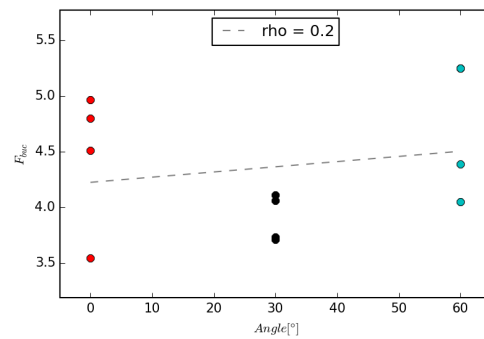
(a) Angle versus Young's modulus



(b) Angle versus ultimate strain



(c) Angle versus failure load

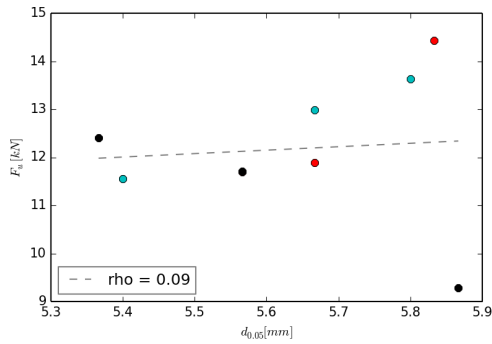


(d) Angle versus buckling load

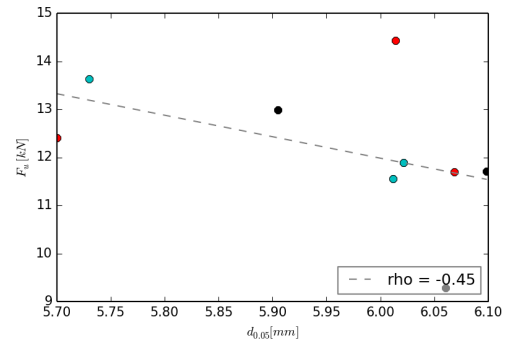
Figure C.76: Correlations between angle and mechanical properties

Geometry versus mechanical properties

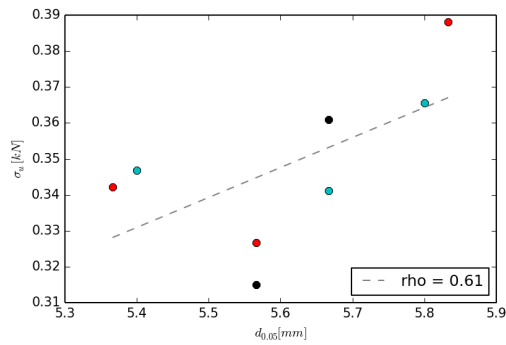
The plots in this subsection show correlations between geometrical and mechanical properties.



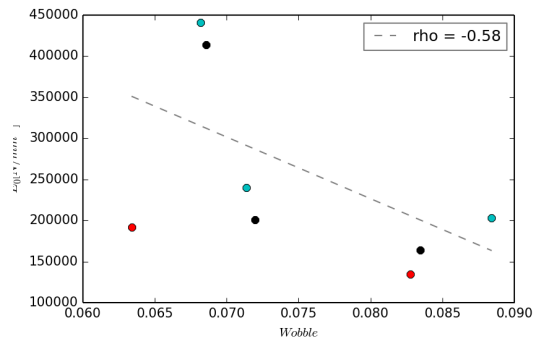
(a) Minimum diameter versus actual failure load



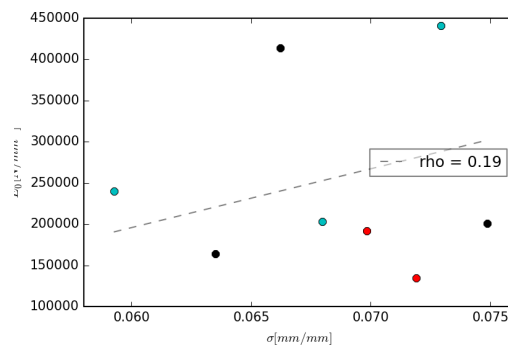
(b) 5 percentile diameter versus failure load



(c) Minim diameter versus ultimate stress



(d) Wobble factor versus Young's modulus



(e) Diameter standard deviation divided by mean cross section area versus Young's modulus

Figure C.77: Correlations between geometry and mechanical properties

C.5 Batch 4

C.5.1 Parameters

The process parameters in table C.7 have been used in the production of the third batch of tensile test specimens. The parameters were changed to increase strand diameter. The welding time was increased, increasing the amount of material deposited per layer. The waiting time, the minimum time between subsequent desposits is also increased. Note that, since this is a minimum value, this does not necessarily have an influence on the actual time between deposits at a certain rod. Let's say the printing robot is printing a batch of 9 specimens at the same. The welding time of each deposit at one of the specimens takes 1 second. From one specimen to the other, the robot has to move, which also takes time, for example another second. Then the entire run takes $9 \cdot (1 + 1) = 18$ seconds to complete. If the next round of deposits then starts all over in the same order, an actual waiting time of 18 seconds is realized.

Per request of MX3D, the process parameters have been excluded from this public version. Please contact MX3D at <http://www.MX3D.com> or gijs@MX3D.com.

Base material
CONFIDENTIAL
Robot
CONFIDENTIAL
Welding
CONFIDENTIAL

Table C.7: Process parameters tensile tests

C.5.2 Geometry

The histograms on the following pages show the distribution of the diameter of the different specimens. Per specimen, the data from four photos was taken and combined to get these results.

0 degrees

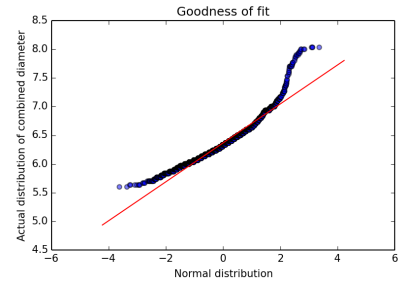
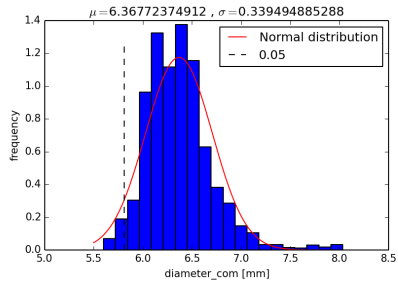


Figure C.78: 4-00-A geometry

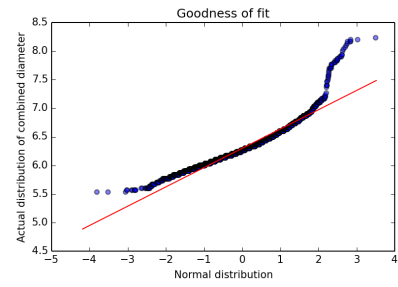
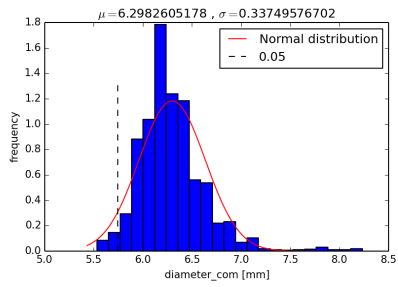


Figure C.79: 4-00-B geometry

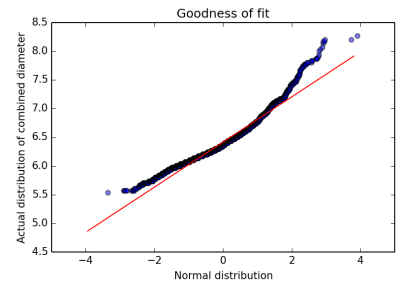
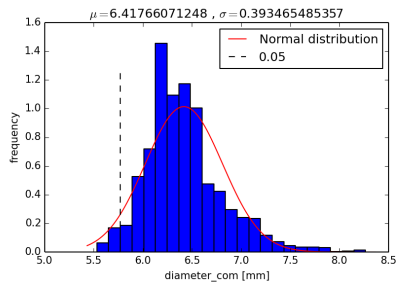


Figure C.80: 4-00-C geometry

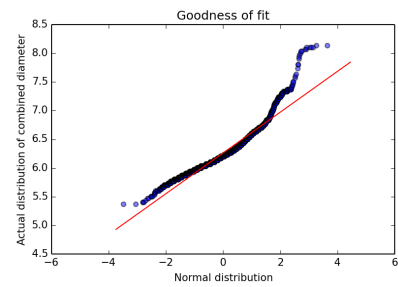
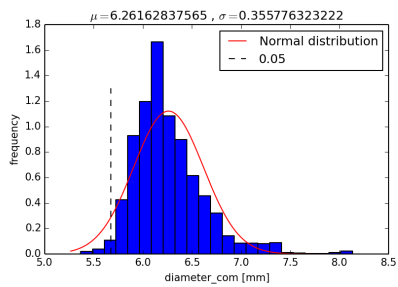


Figure C.81: 4-00-D geometry

30 degrees

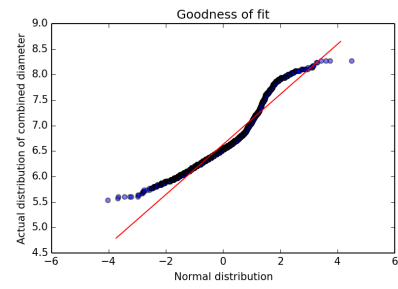
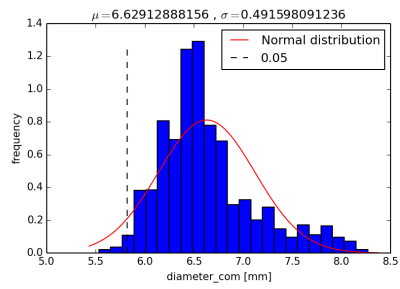


Figure C.82: 4-30-A geometry

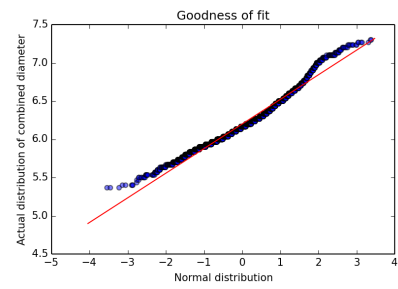
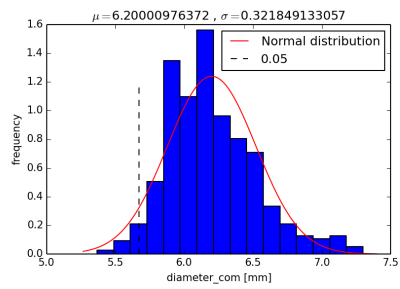


Figure C.83: 4-30-B geometry

60 degrees

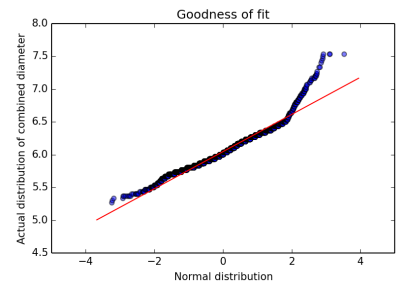
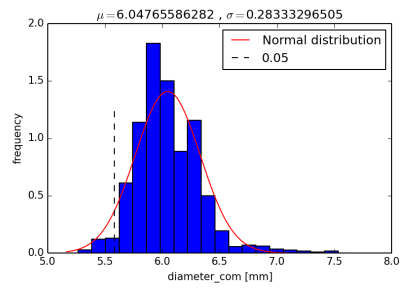


Figure C.84: 4-60-A geometry

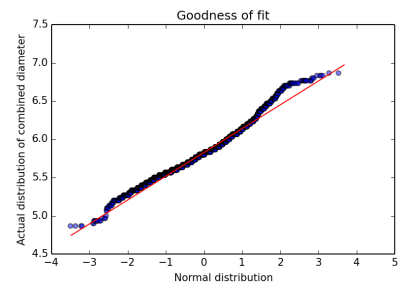
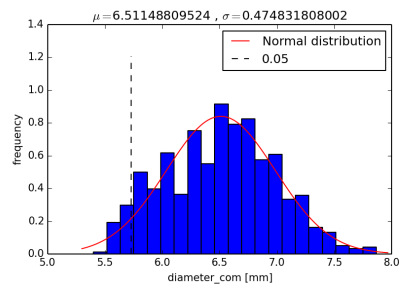
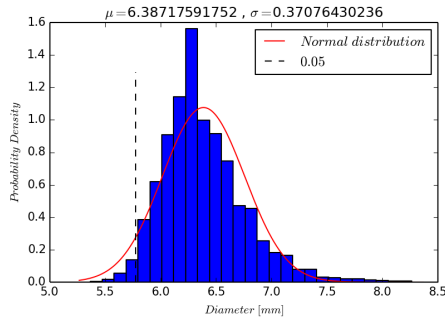


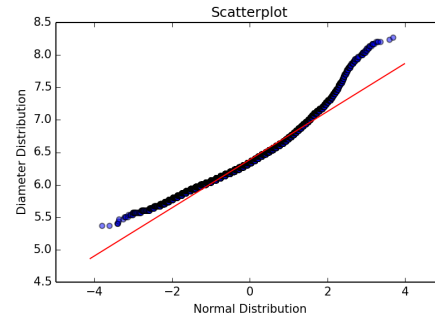
Figure C.85: 4-60-B geometry

Combined distributions per angle

Here, the distributions of each specimen are combined per angle, because they are produced in the exact same way, and should therefore be part of the same, larger total distribution. Again, normal distributions have been fitted to these combined distributions. Scatter plots are provided to study the goodness of fit.

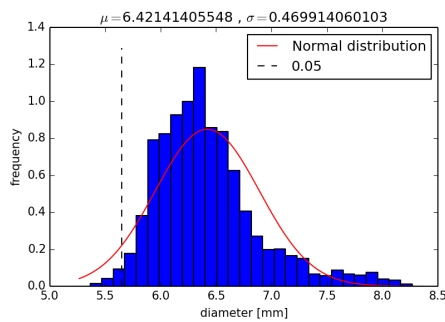


(a) Combined diameter distribution

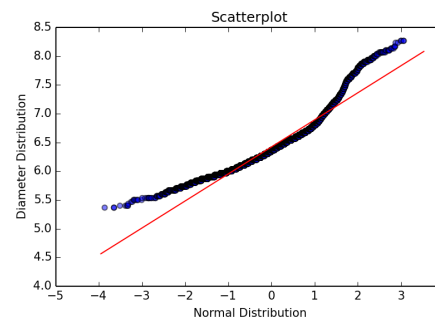


(b) Fit to normal distribution

Figure C.86: Combined geometry for specimen type 4-00

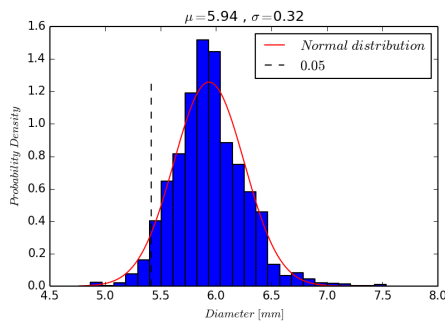


(a) Combined diameter distribution

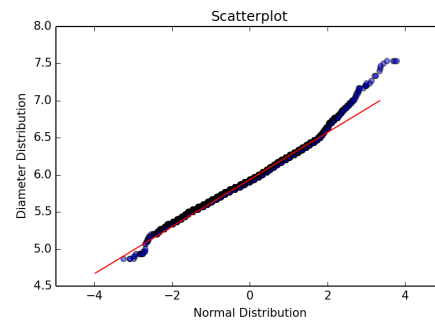


(b) Fit to normal distribution

Figure C.87: Combined geometry for specimen type 4-30



(a) Combined diameter distribution



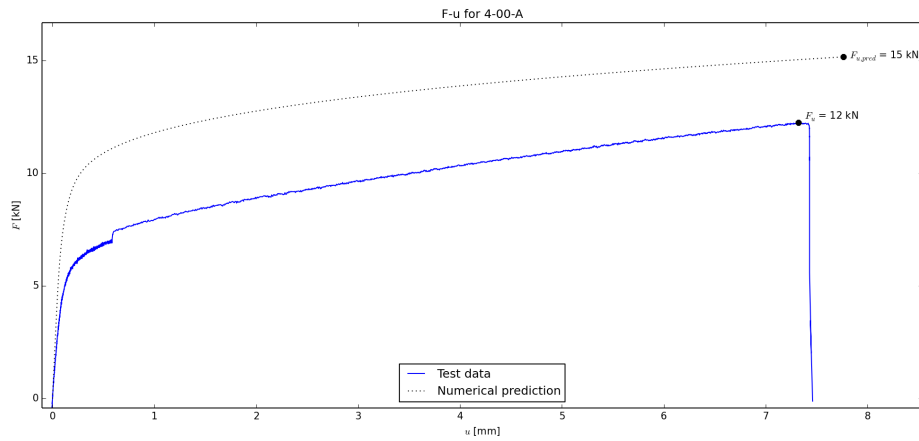
(b) Fit to normal distribution

Figure C.88: Combined geometry for specimen type 4-60

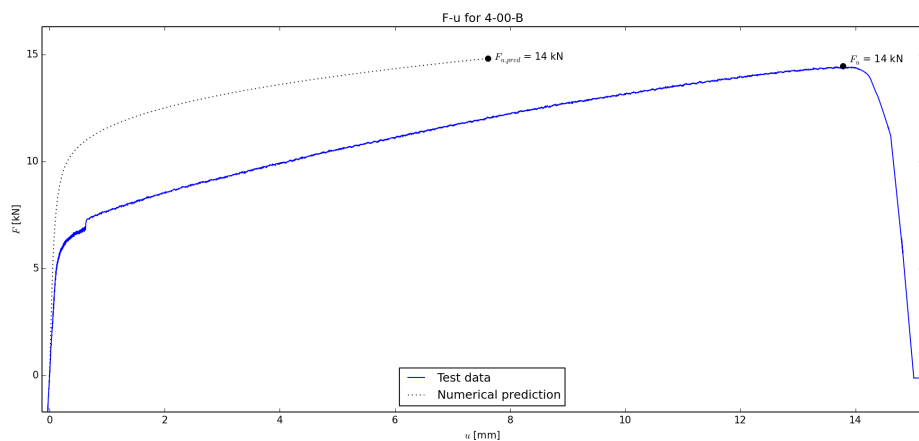
C.5.3 F-u curves

The following force-displacement curves show the raw results from the tensile tests that were performed.

0 degrees

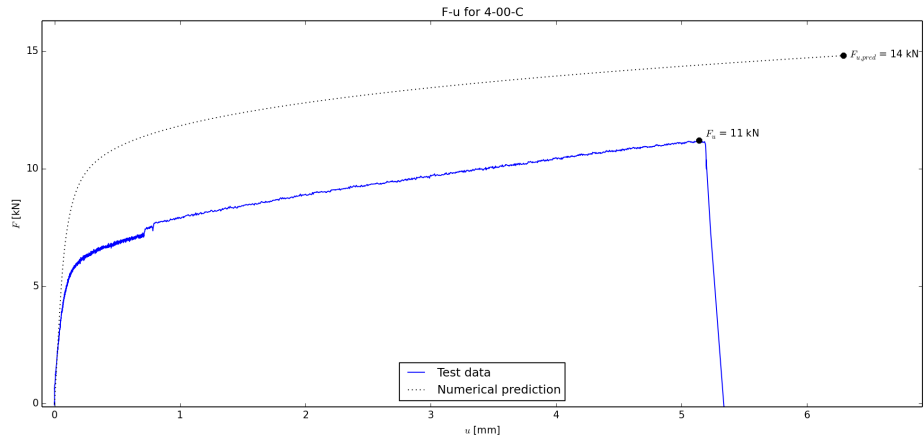


(a) 4-00-A

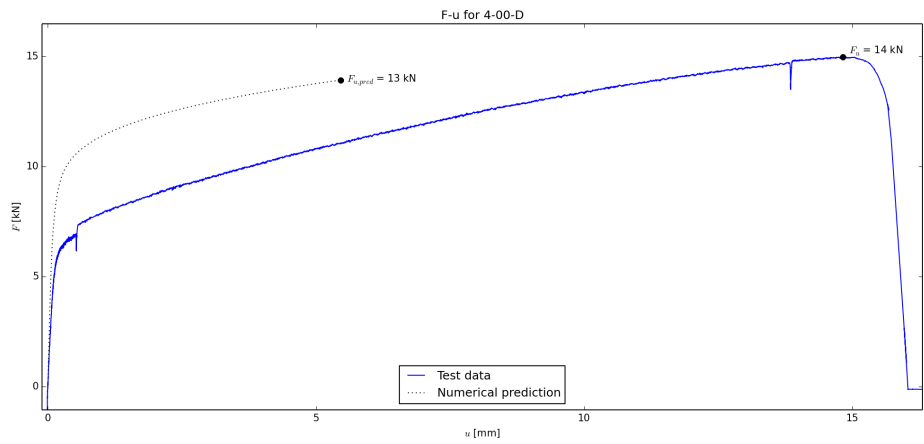


(b) 4-00-B

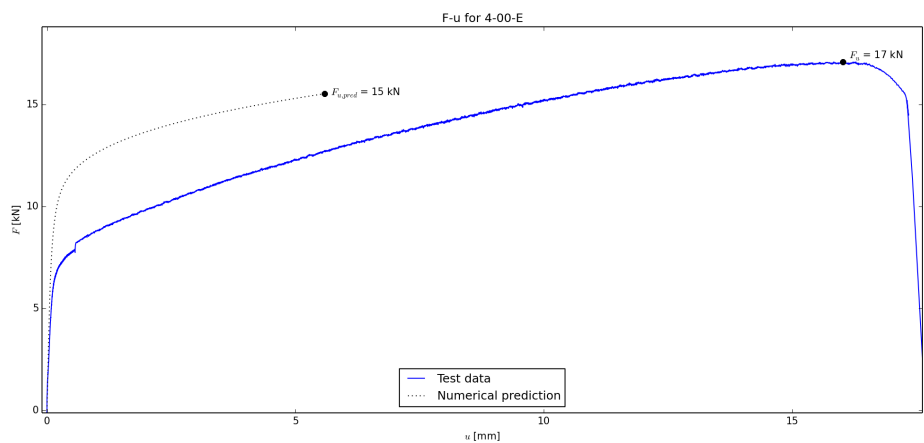
Figure C.89: F-u diagrams at 0 degrees



(a) 4-00-C



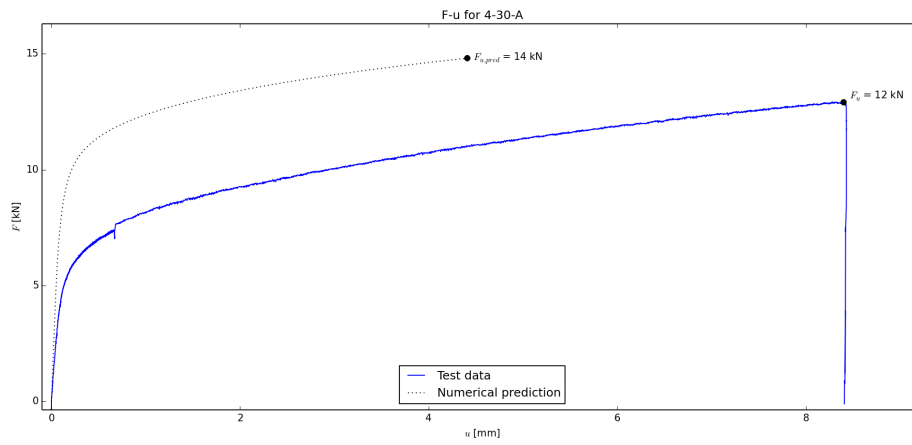
(b) 4-00-D



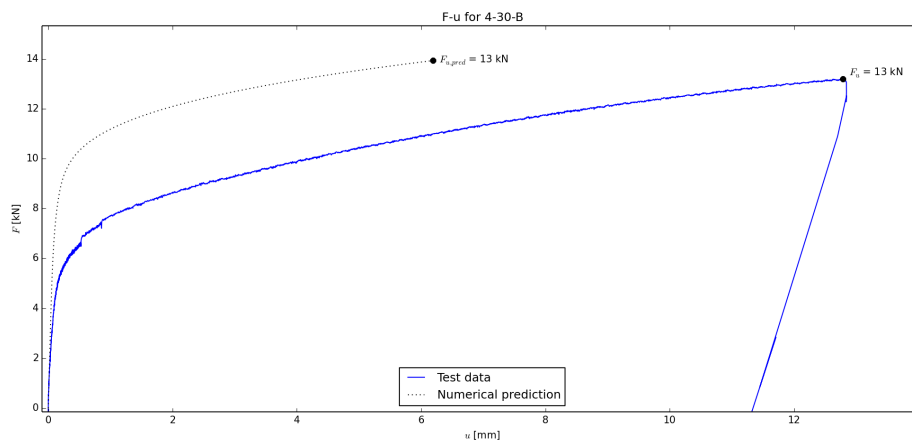
(c) 4-00-E

Figure C.90: F-u diagrams at 0 degrees

30 degrees



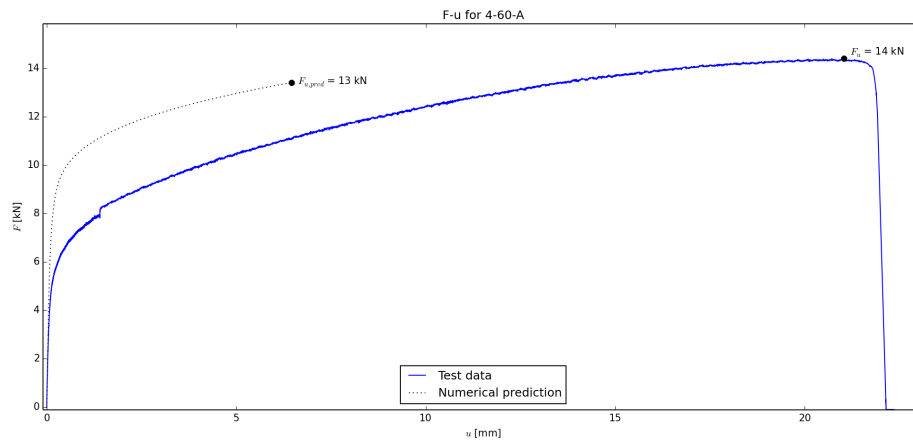
(a) 4-30-A



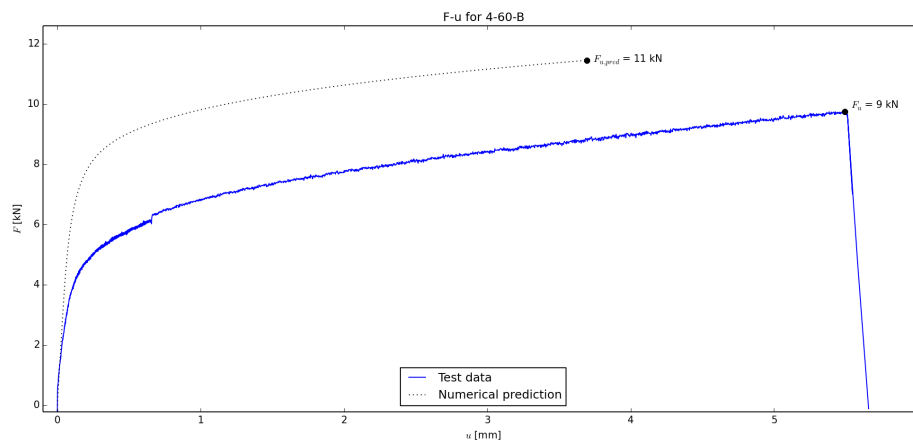
(b) 4-30-B

Figure C.91: F-u diagrams at 30 degrees

60 degrees



(a) 4-60-A



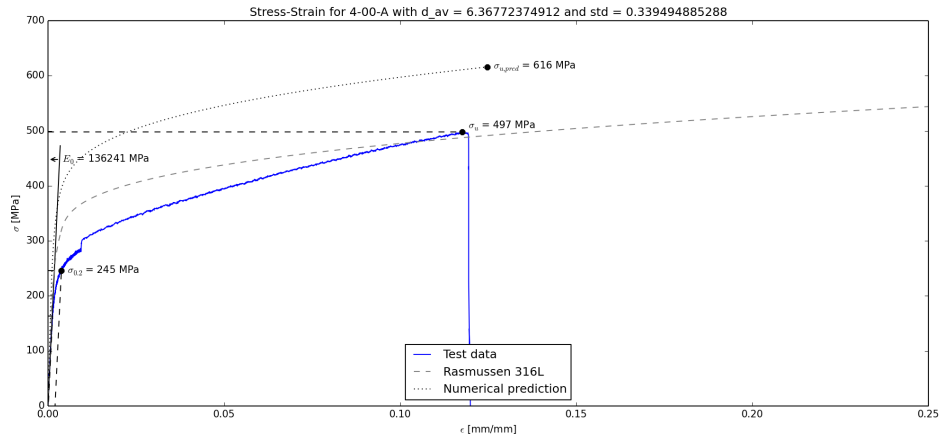
(b) 4-60-B

Figure C.92: F-u diagrams at 60 degrees

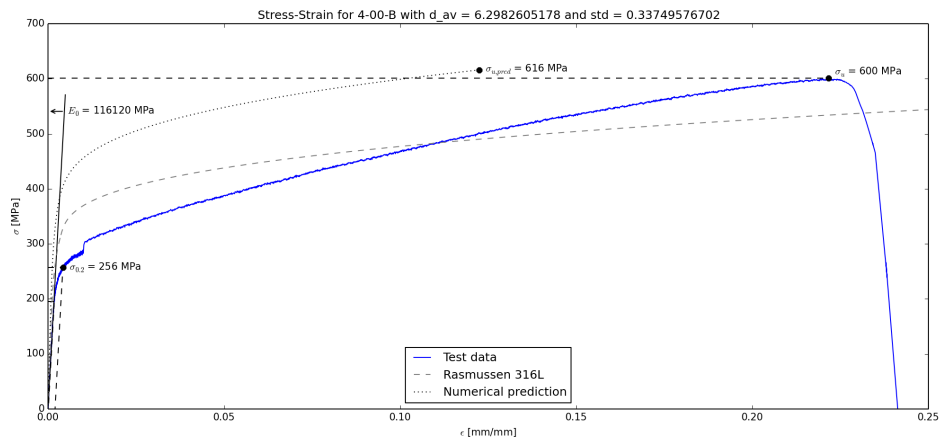
C.5.4 Stress-strain curves

The following stress-strain curves are based on the average diameters of the strands.

0 degrees

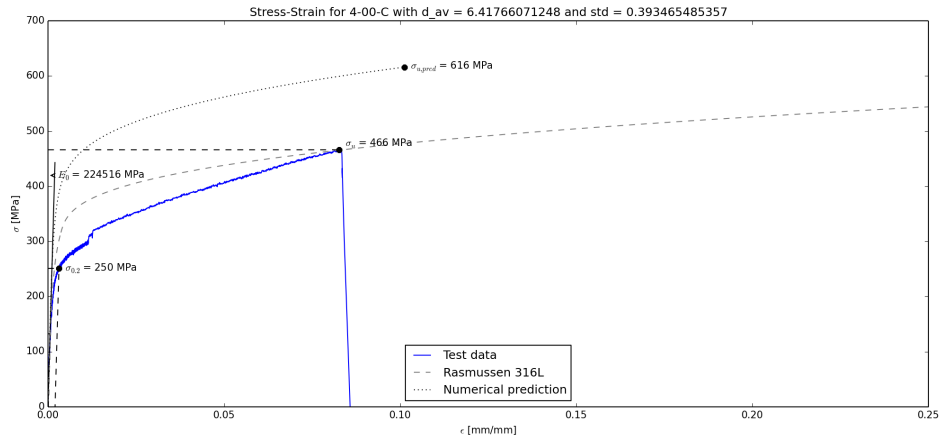


(a) 4-00-A

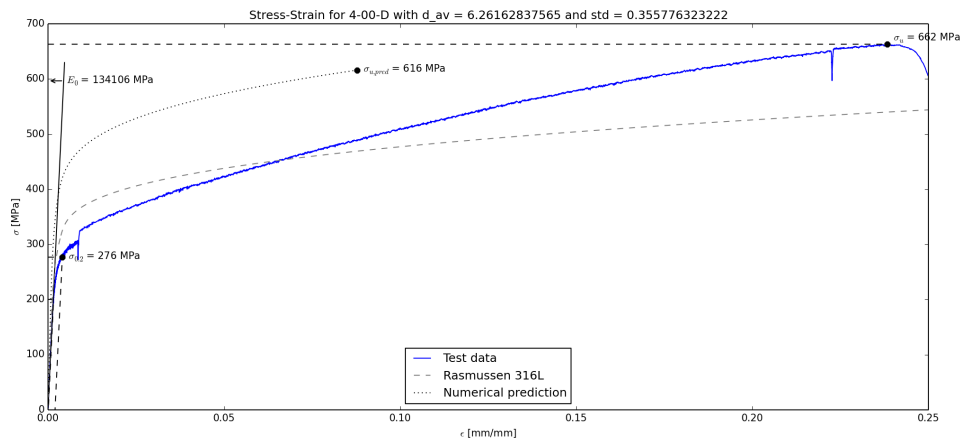


(b) 4-00-B

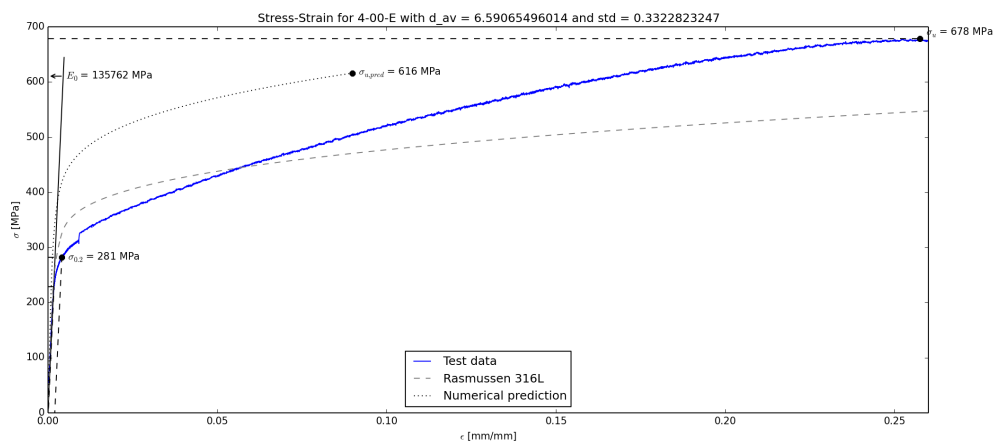
Figure C.93: Stress-strain diagrams at 0 degrees



(a) 4-00-C



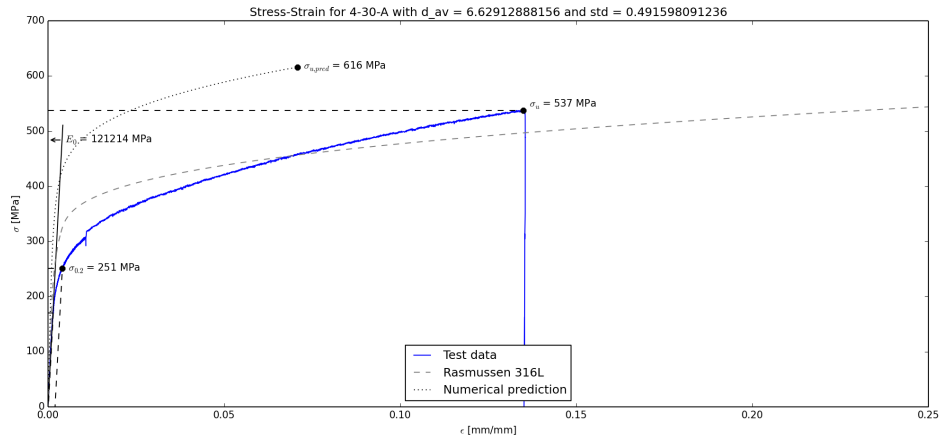
(b) 4-00-D



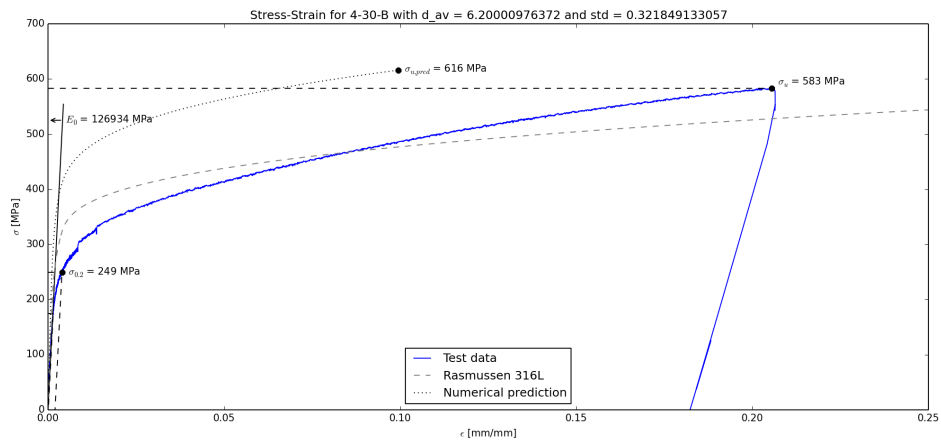
(c) 4-00-E

Figure C.94: Stress-strain diagrams at 0 degrees

30 degrees



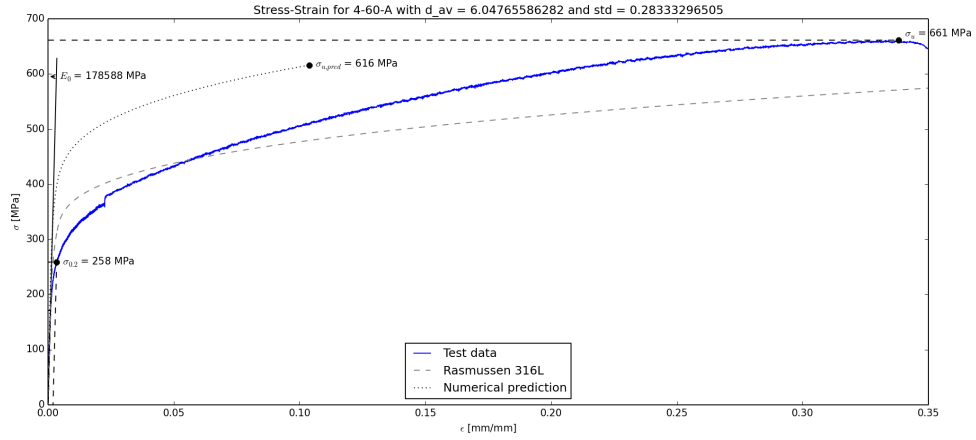
(a) 4-30-A



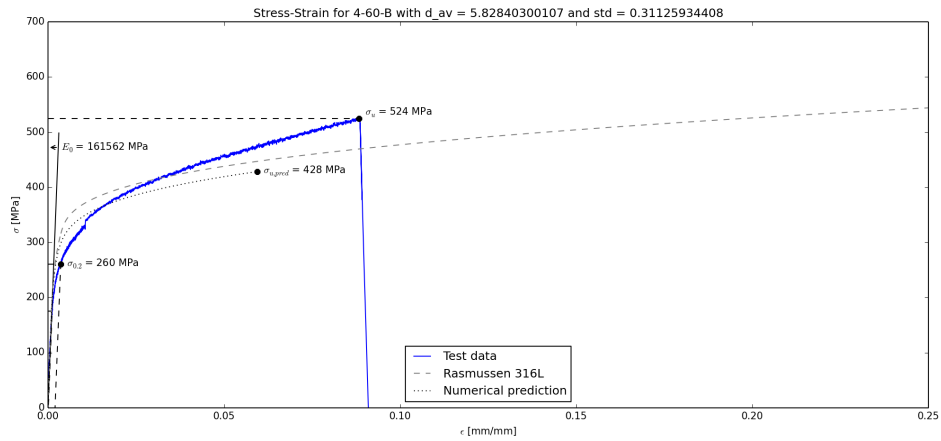
(b) 4-30-B

Figure C.95: Stress-strain diagrams at 30 degrees

60 degrees



(a) 4-60-A



(b) 4-60-B

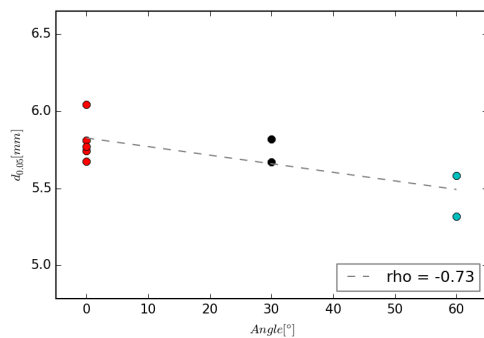
Figure C.96: Stress-strain diagrams at 60 degrees

C.5.5 Correlations

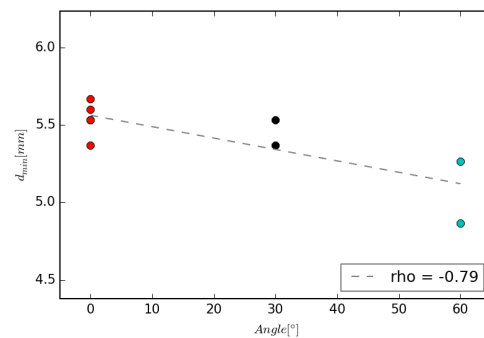
Different properties and parameters have been plotted against each other to investigate their relationships. For each plot, the Pearson product-moment correlation coefficient ρ has been presented. This value ranges from -1 to 1. The closer this value is to 1 or -1, the greater the correlation. Variables with a correlation coefficient that is (close to) 0 are not correlated.

Angle

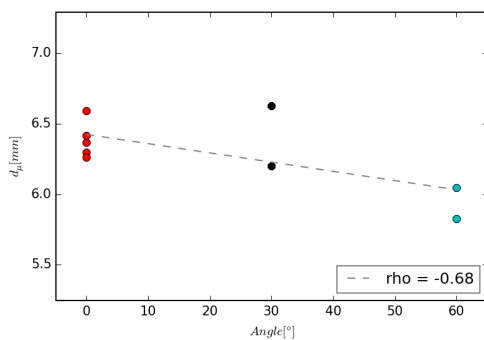
The plots in this subsection show how geometrical and mechanical properties vary with the angle at which the test pieces are produced.



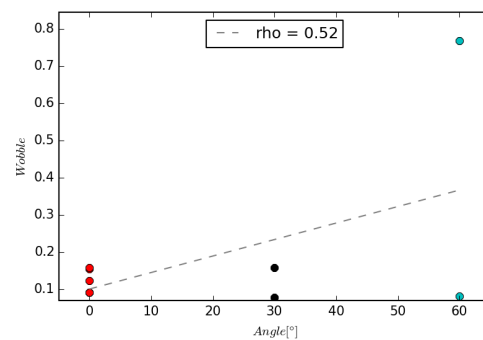
(a) Angle versus 5 percentile diameter



(b) Angle versus minimum diameter

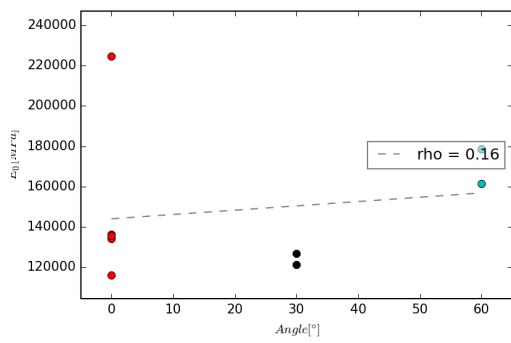


(c) Angle versus average diameter

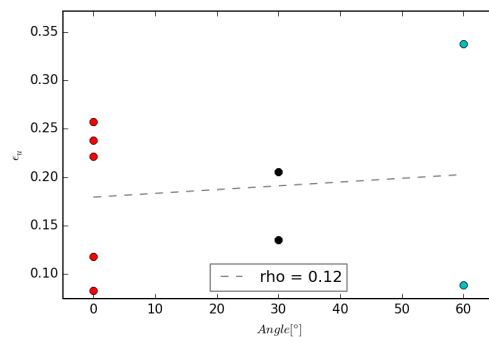


(d) Angle versus wobble factor

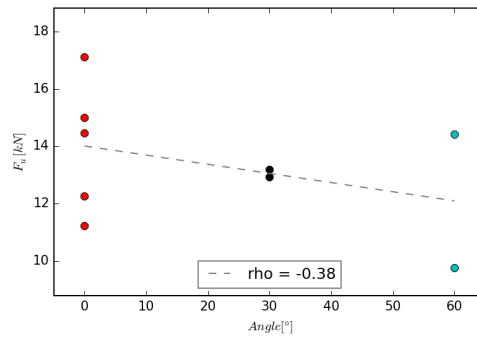
Figure C.97: Correlations between angle and geometry



(a) Angle versus Young's modulus



(b) Angle versus ultimate strain

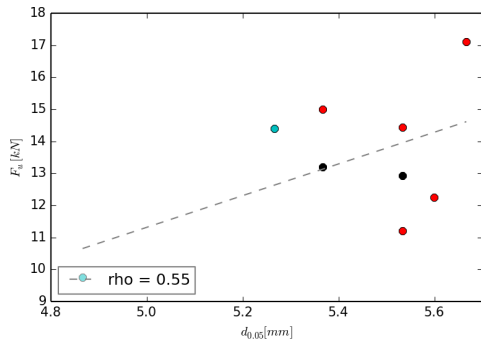


(c) Angle versus failure load

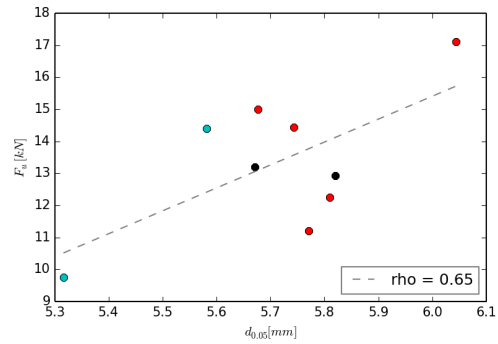
Figure C.98: Correlations between angle and mechanical properties

Geometry versus mechanical properties

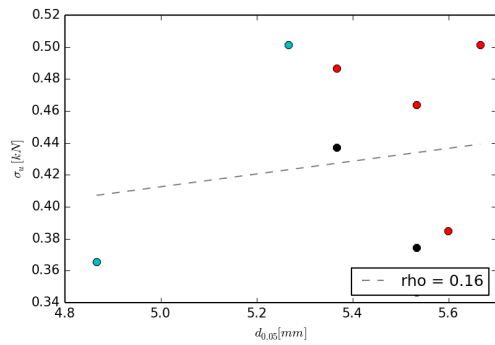
The plots in this subsection show correlations between geometrical and mechanical properties.



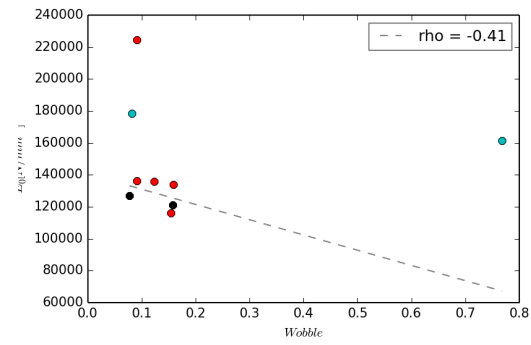
(a) Minimum diameter versus failure load



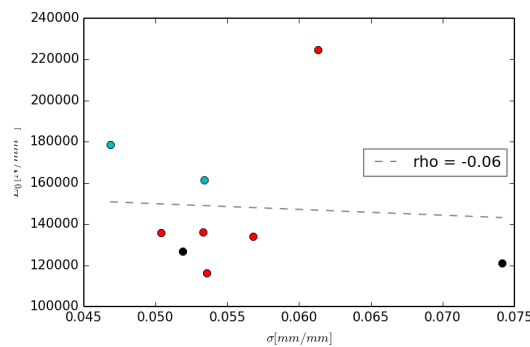
(b) 5 percentile diameter versus failure load



(c) Minimum diameter versus ultimate stress



(d) Wobble factor versus Young's modulus



(e) Diameter standard deviation divided by mean area versus Young's modulus

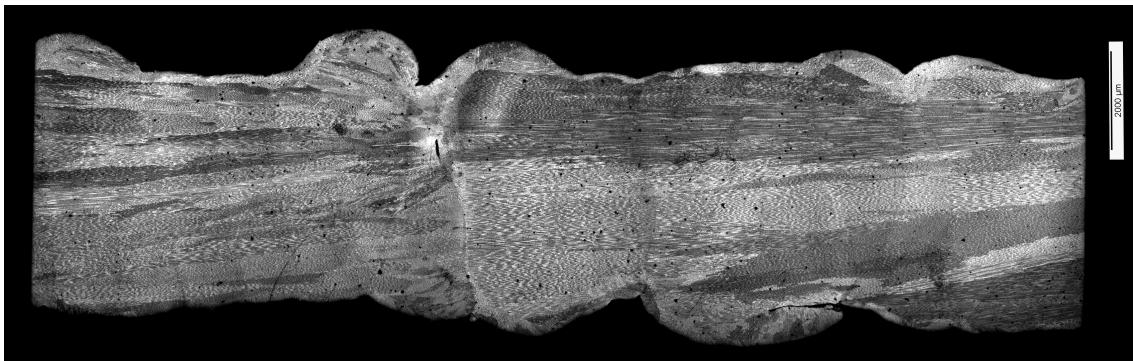
Figure C.99: Correlations between geometry and mechanical properties

C.5.6 Microstructure

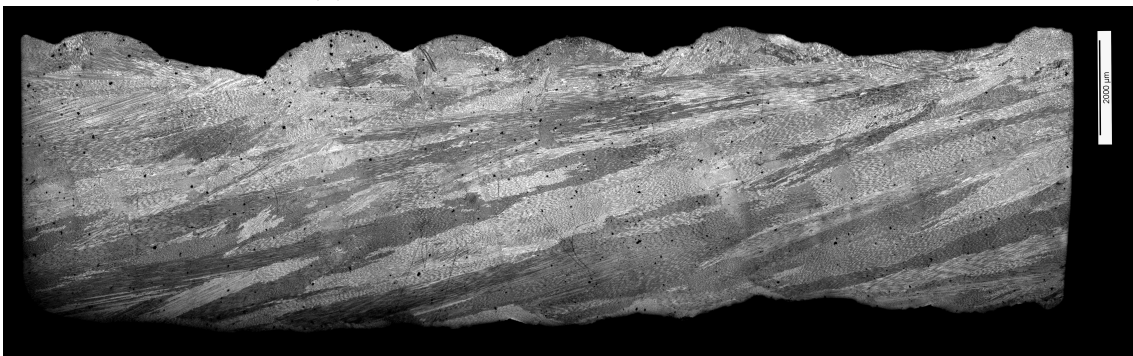
In this batch, only longitudinal sections were analysed. These specimens were only used for microstructural research, they were not cut from specimens that were structurally tested.



(a) Microstructure of specimen type 4-00



(b) Microstructure of specimen type 4-30



(c) Microstructure of specimen type 4-60

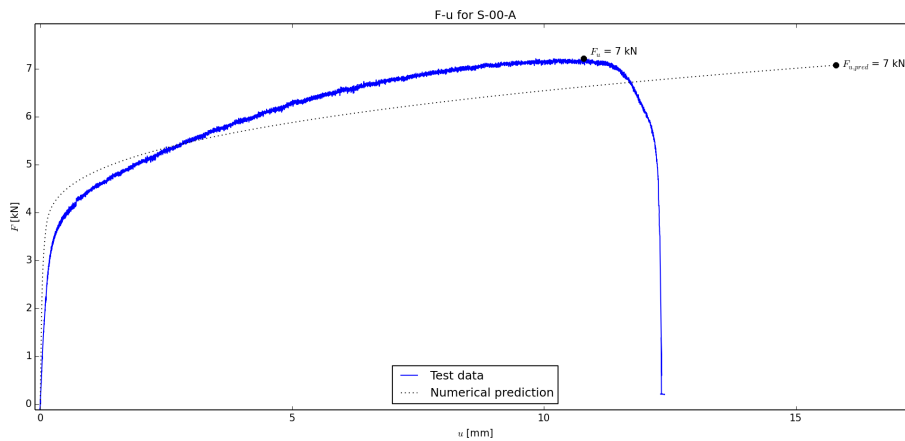
C.6 Milled specimens

These specimens were milled from rods from batch 4. The process parameters are given in appendix C.5.1.

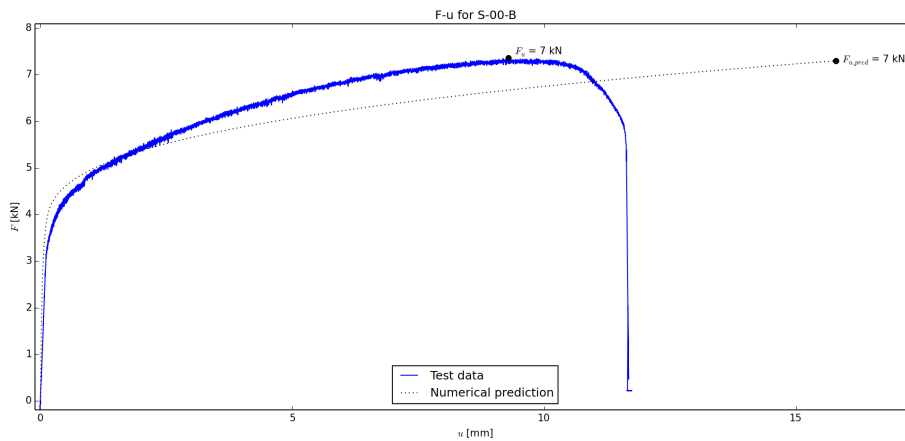
C.6.1 F-u curves

The following force-displacement curves show the raw results from the tensile tests that were performed.

0 degrees

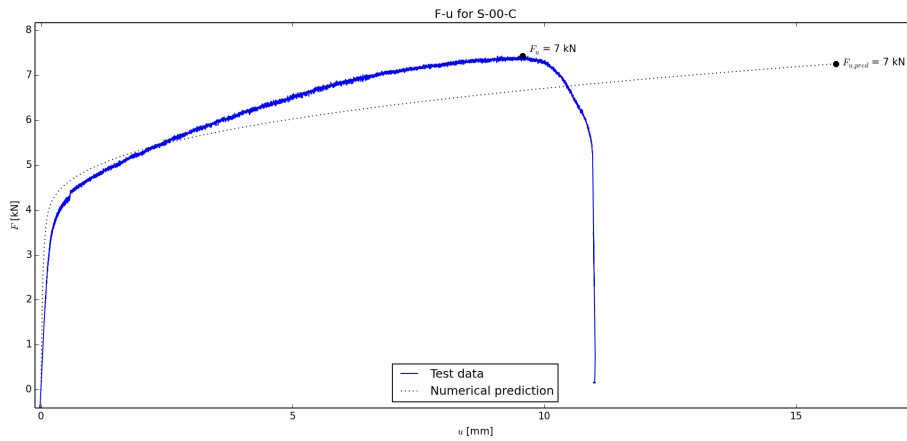


(a) S-00-A

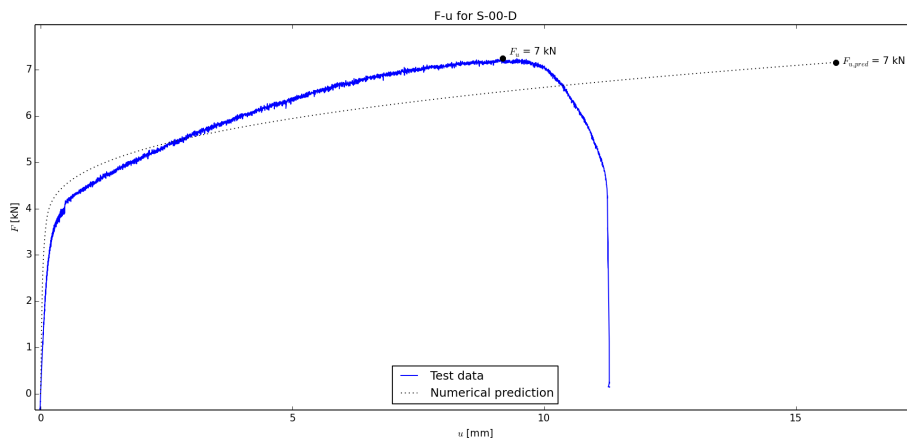


(b) S-00-B

Figure C.101: F-u diagrams at 0 degrees



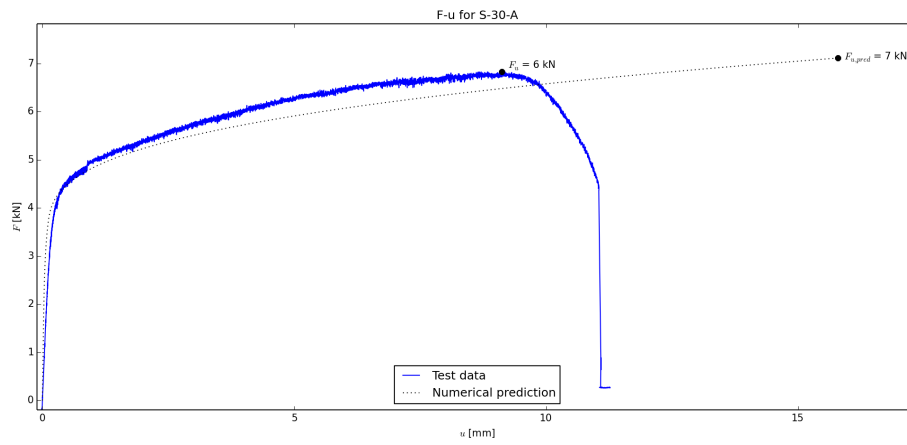
(a) S-00-C



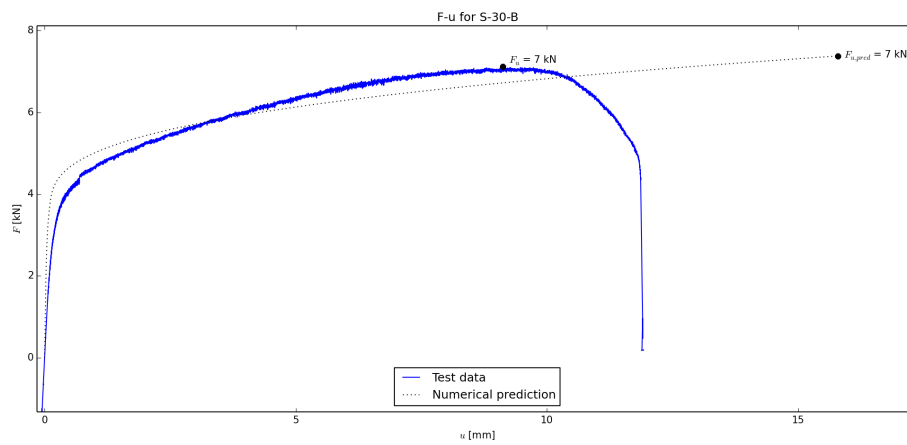
(b) S-00-D

Figure C.102: F-u diagrams at 0 degrees

30 degrees

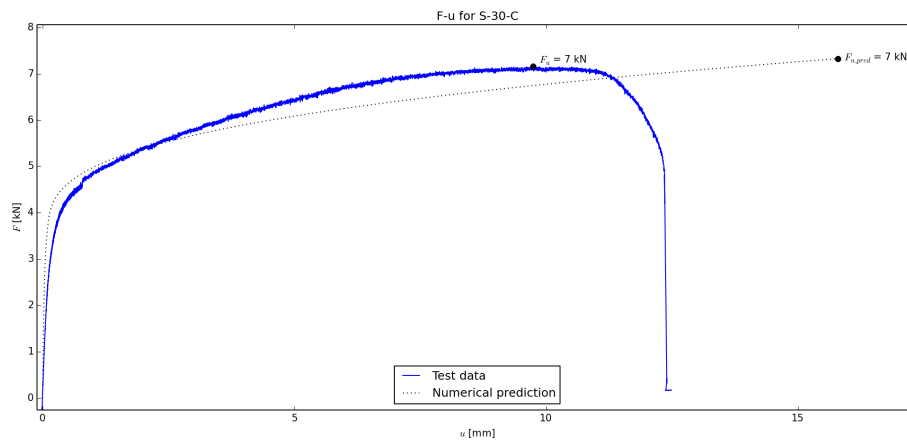


(a) S-30-A

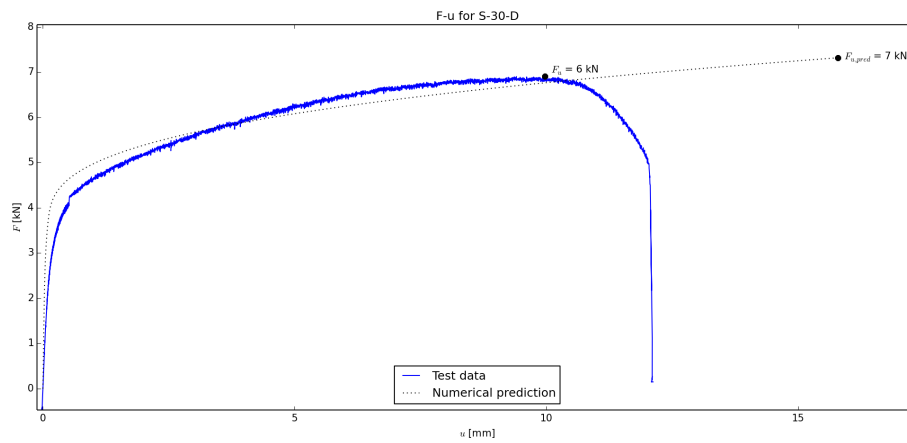


(b) S-30-B

Figure C.103: F-u diagrams at 30 degrees



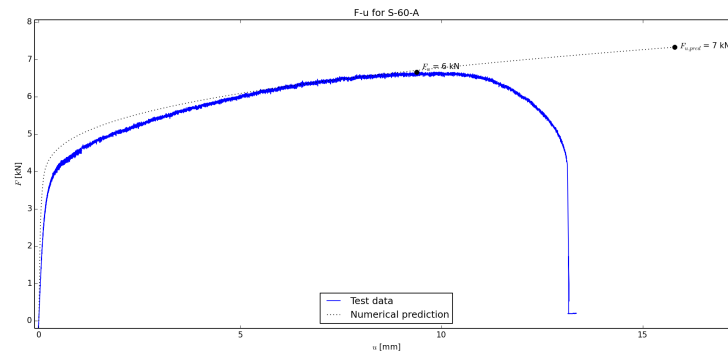
(a) S-30-C



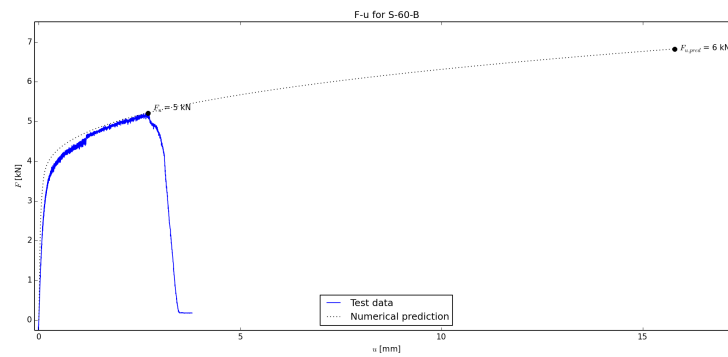
(b) S-30-D

Figure C.104: F-u diagrams at 30 degrees

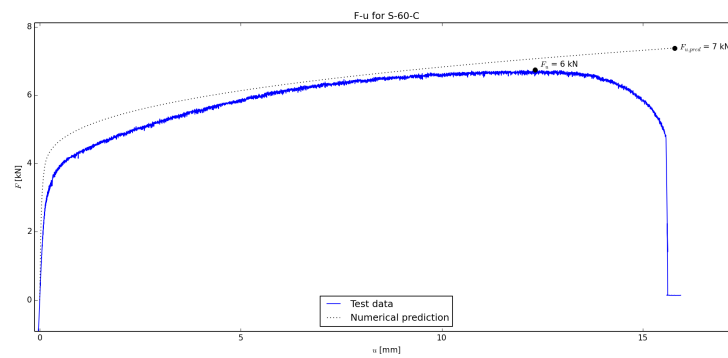
60 degrees



(a) S-60-A



(b) S-60-B



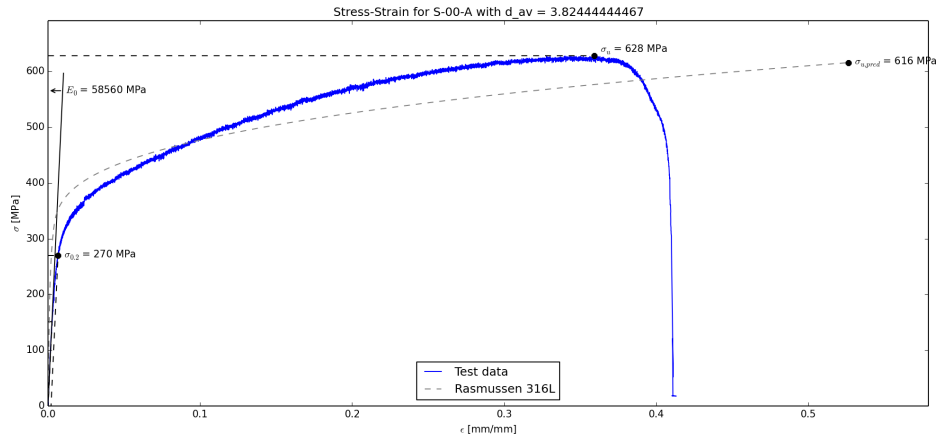
(c) S-60-C

Figure C.105: F-u diagrams at 60 degrees

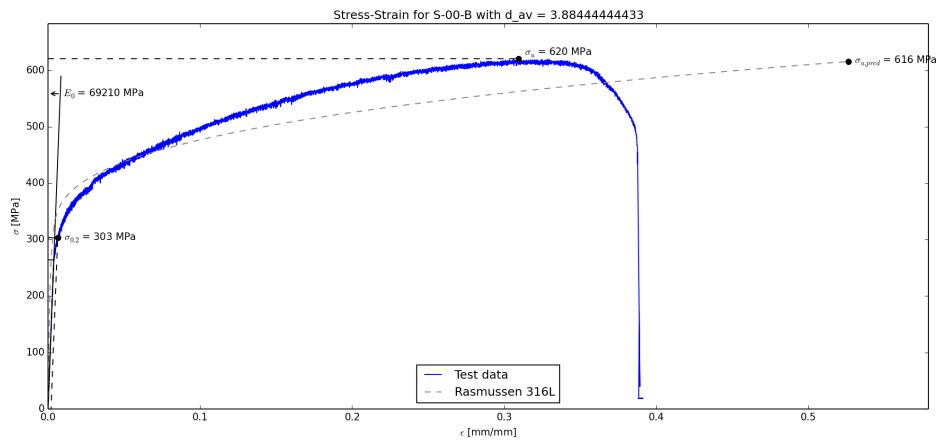
C.6.2 Stress-strain curves

The following stress-strain curves are based on the average diameters of the strands.

0 degrees

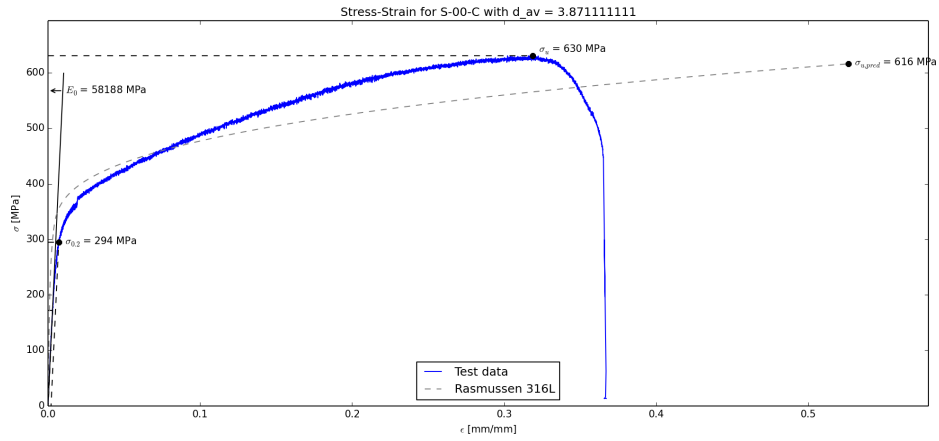


(a) S-00-A

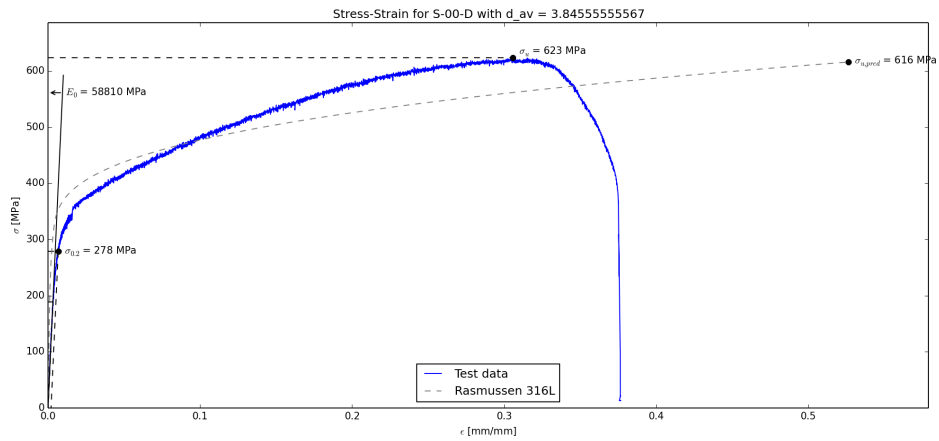


(b) S-00-B

Figure C.106: Stress-strain diagrams at 0 degrees



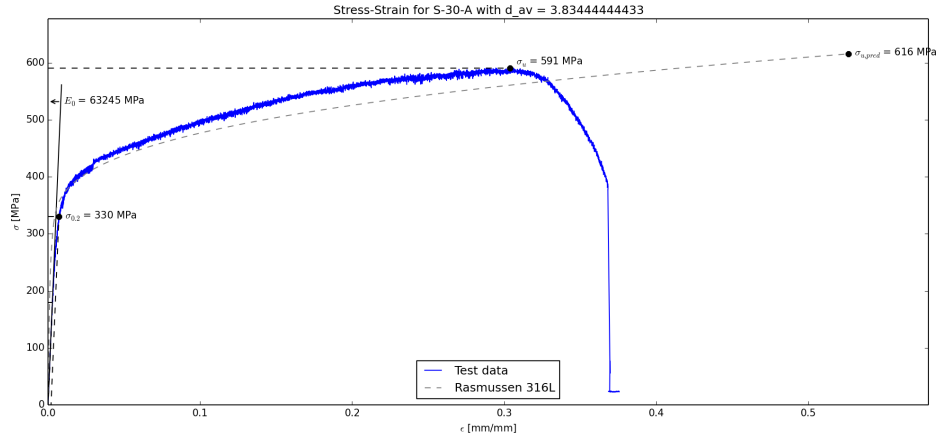
(a) S-00-C



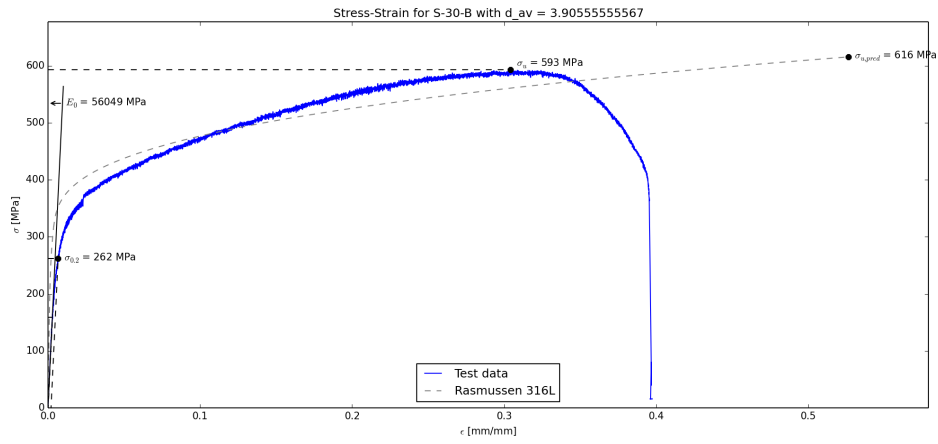
(b) S-00-D

Figure C.107: Stress-strain diagrams at 0 degrees

30 degrees

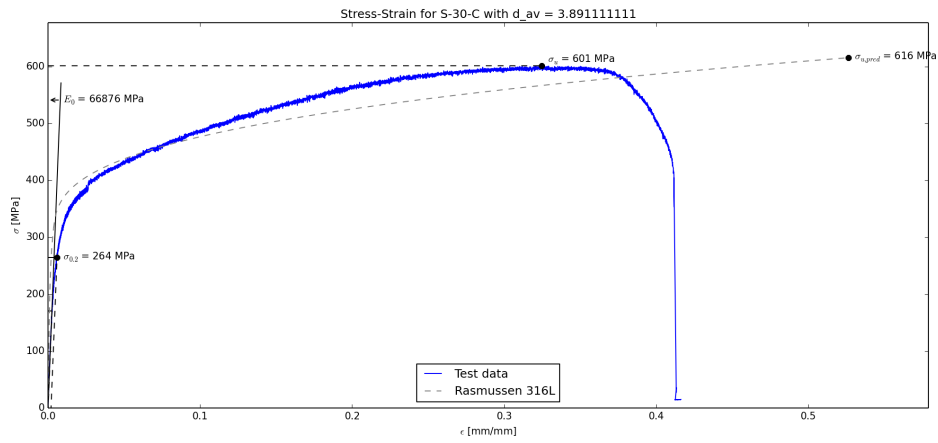


(a) S-30-A

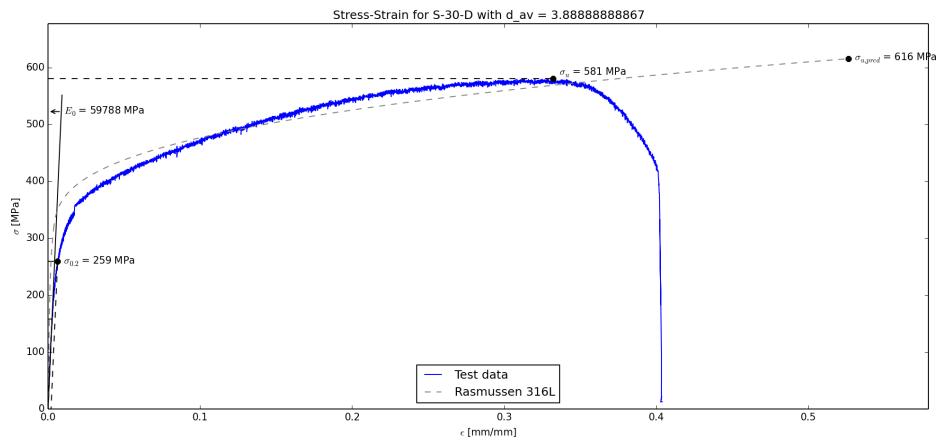


(b) S-30-B

Figure C.108: Stress-strain diagrams at 30 degrees



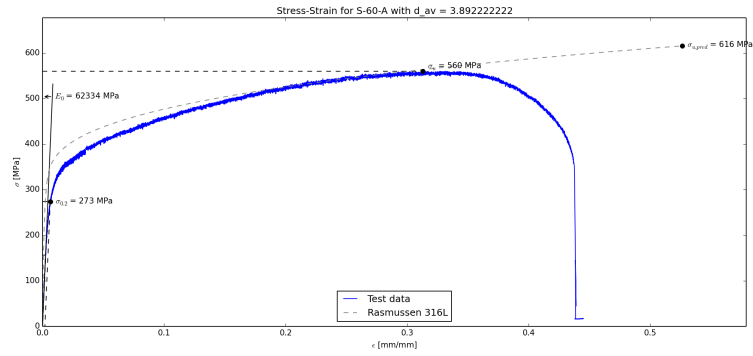
(a) S-30-C



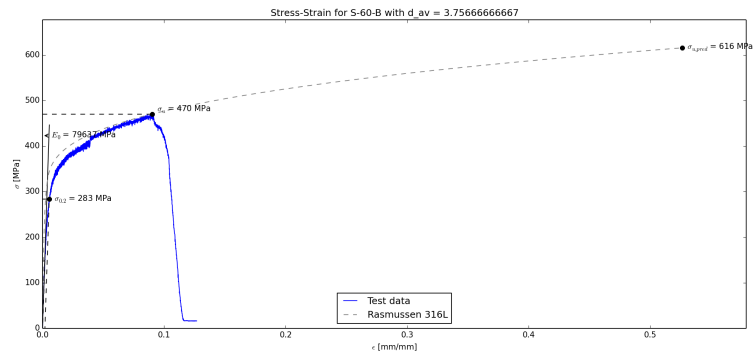
(b) S-30-D

Figure C.109: Stress-strain diagrams at 30 degrees

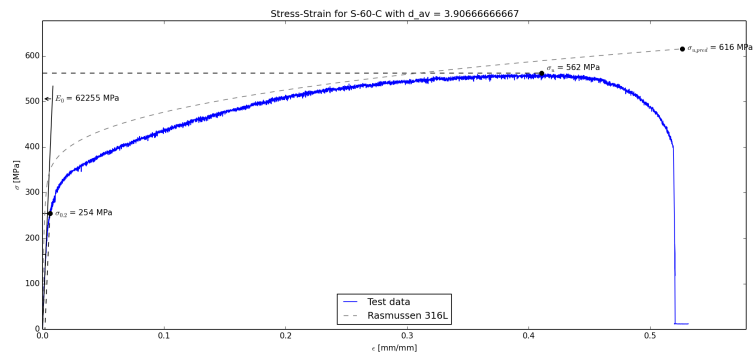
60 degrees



(a) S-60-A



(b) S-60-B



(c) S-60-C

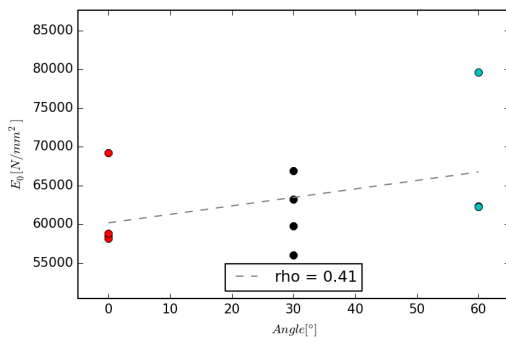
Figure C.110: Stress-strain diagrams at 60 degrees

C.6.3 Correlations

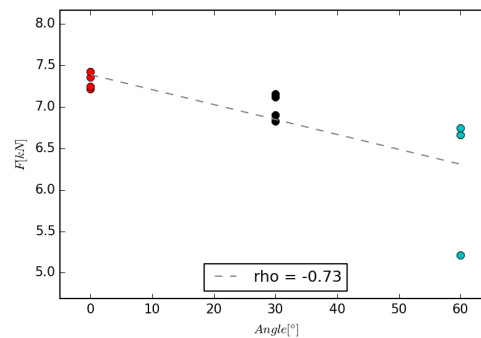
Different properties and parameters have been plotted against each other to investigate their relationships. For each plot, the Pearson product-moment correlation coefficient ρ has been presented. This value ranges from -1 to 1. The closer this value is to 1 or -1, the greater the correlation. Variables with a correlation coefficient that is (close to) 0 are not correlated.

Angle

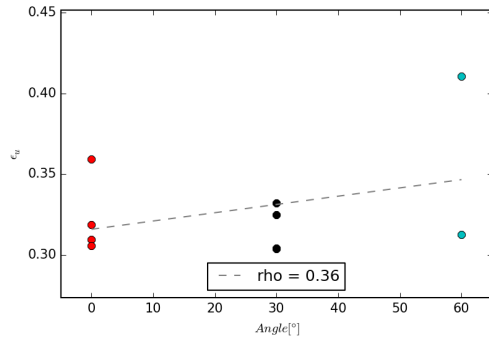
The plots in this subsection show how mechanical properties vary with the angle at which the test pieces are produced. Any bad results that were excluded in section 6.5.6 have been included here.



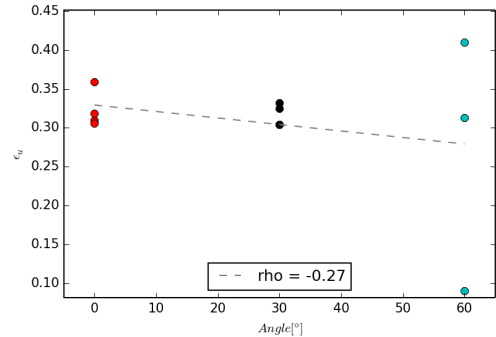
(a) Angle versus Young's modulus



(b) Angle versus failure load

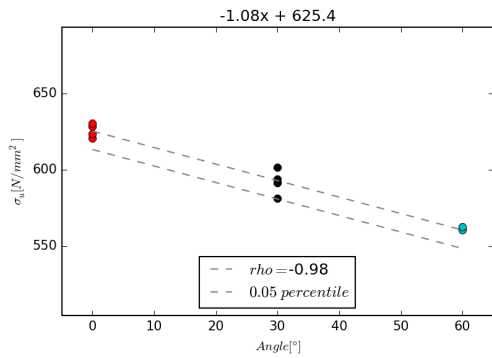


(c) Angle versus ultimate strain (bad result included)

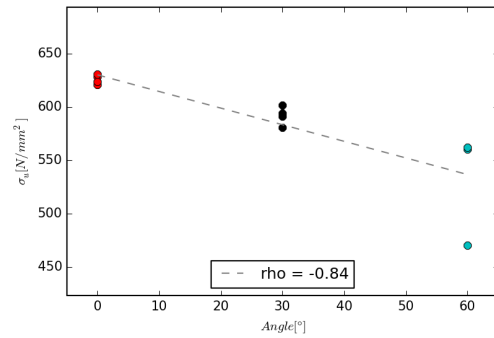


(d) Angle versus ultimate strain (bad result included)

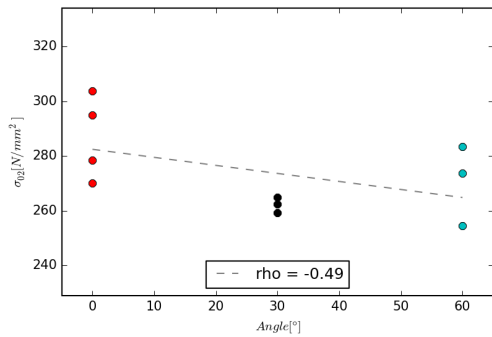
Figure C.111: Correlations between angle and mechanical properties



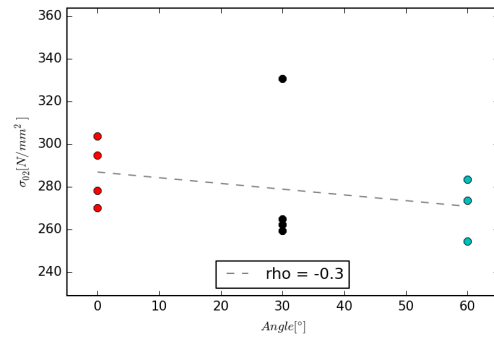
(a) Angle versus ultimate stress (bad result excluded)



(b) Angle versus ultimate stress (bad result included)



(c) Angle versus 0.2 % proof stress (bad result excluded)



(d) Angle versus 0.2 % proof stress (bad result included)

Figure C.112: Correlations between angle and mechanical properties

C.6.4 Microstructure

Since the milled specimens are produced from batch 4 specimens, the micrographs shown in appendix C.5.6 are representative of the microstructure of the milled specimens. It should be noted that that milled specimens have a diameter of about 3,9 mm. The outer edges of the material shown in the micrographs in in appendix C.5.6 have been milled away, so they are not present in the milled specimens.

C.7 Fatigue

The results from the fatigue tests are presented here.

C.7.1 Parameters

For the fatigue specimens, the material is the same as well as the welding parameters in comparison to the first two batches of tensile specimens. The robotic parameters, however, were slightly altered, see table C.8. The parameters ‘Road rad’, ‘Layer height - int’, ‘%lh’, and ‘Multiply’ are set to control the areas in which weld depositions are overlapping, i.e. at the wide clamped ends. They do not affect the tested parts that are being investigated.

Per request of MX3D, the process parameters have been excluded from this public version. Please contact MX3D at <http://www.MX3D.com> or gijs@MX3D.com.

Base material

CONFIDENTIAL

Robot

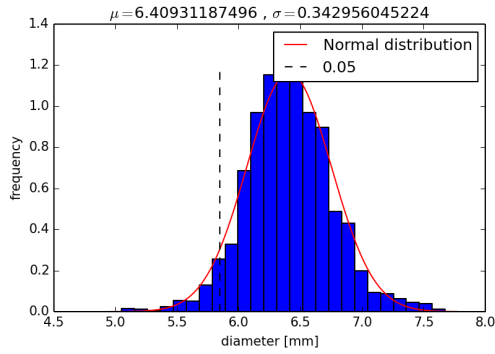
CONFIDENTIAL

Welding

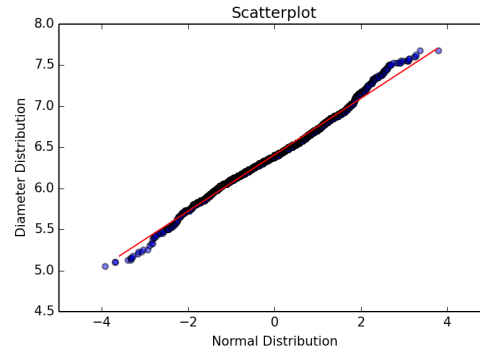
CONFIDENTIAL

Table C.8: Process parameters of fatigue specimens

C.7.2 Geometry

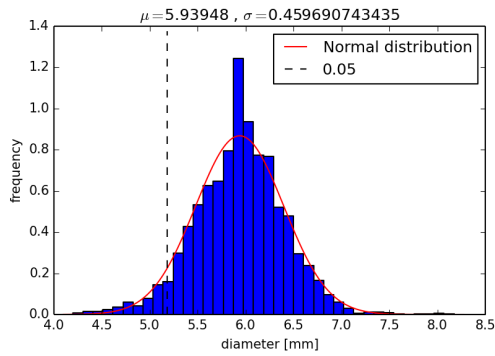


(a) Combined diameter distribution

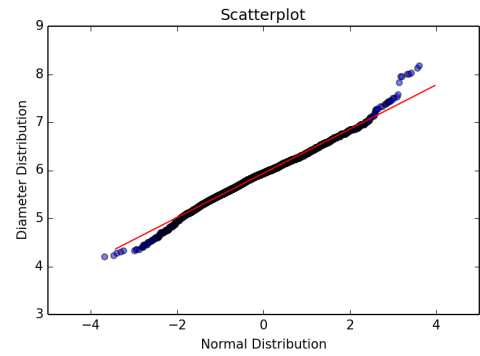


(b) Fit to normal distribution

Figure C.113: Geometrical properties of fatigue batch 1



(a) Combined diameter distribution



(b) Fit to normal distribution

Figure C.114: Geometrical properties of fatigue batch 2

C.7.3 S-N

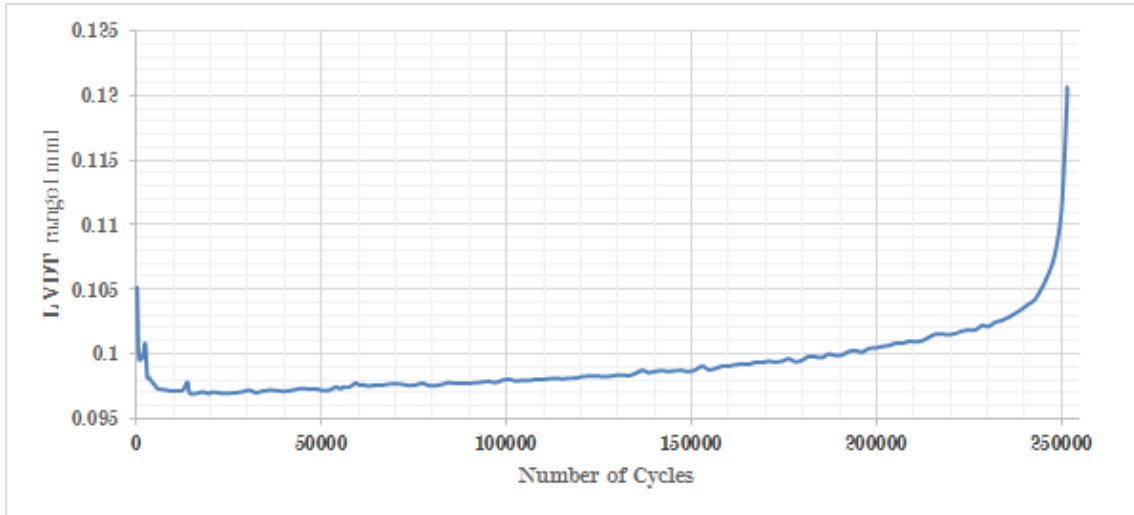


Figure C.115: Typical crack development in specimen 2F-D

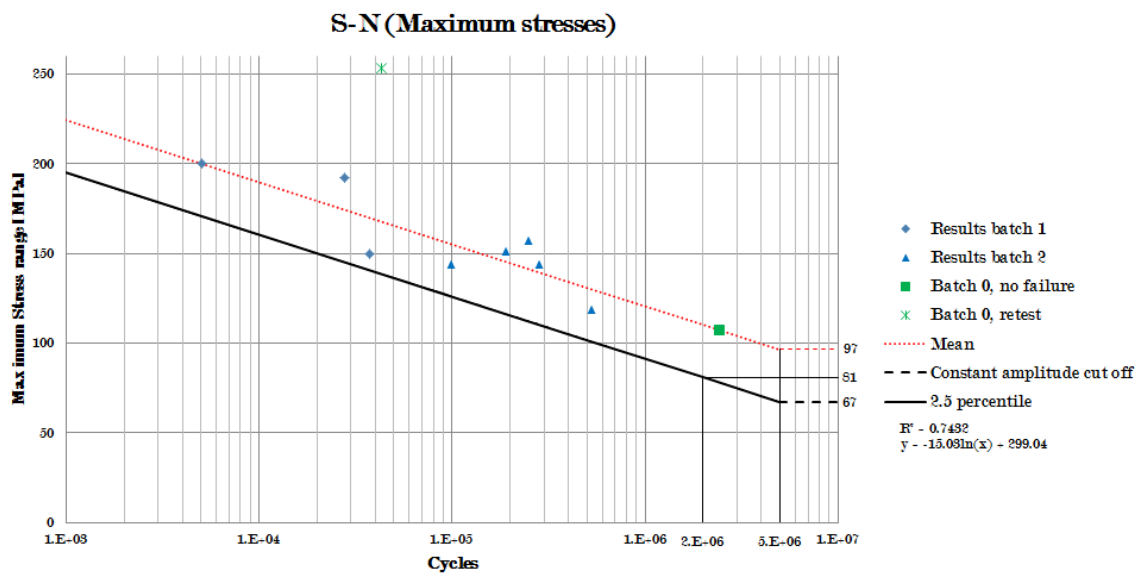


Figure C.116: S-N data

C.8 Buckling

In this section, some additional data from the buckling tests are presented. All buckling loads and average diameters can be seen in appendix C.1. Figure C.117 shows a typical result from a buckling test. Initially, the force increases linearly with the displacement. When a critical load is reached, the rod buckles and the deformations keep on increasing while the load remains constant.

F-u buckling diagram

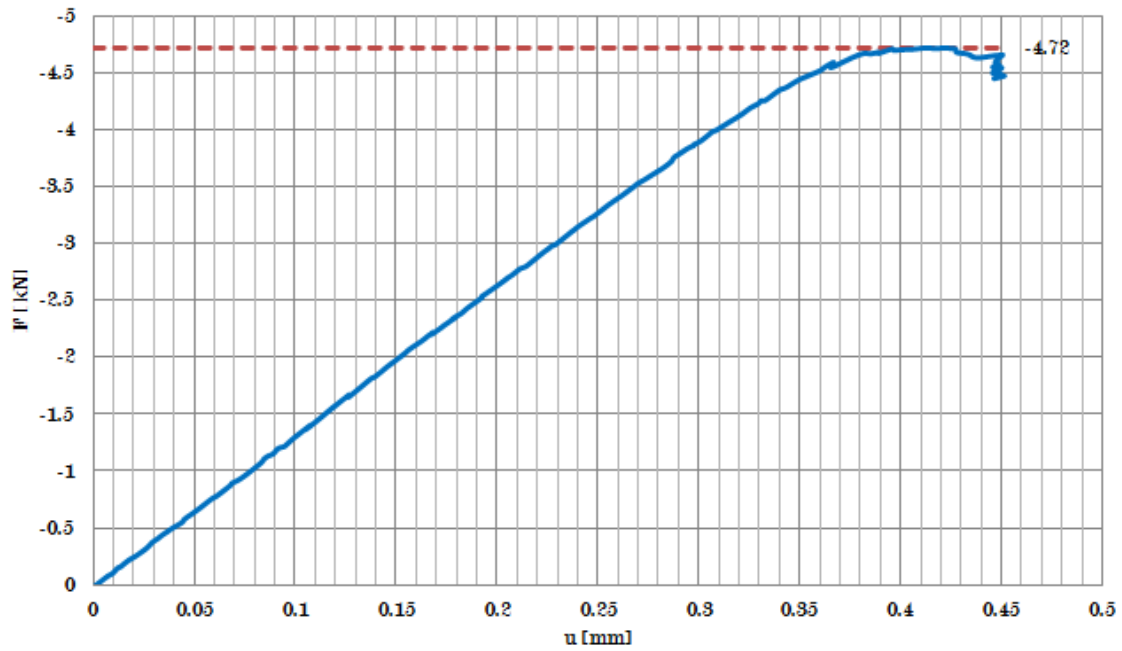
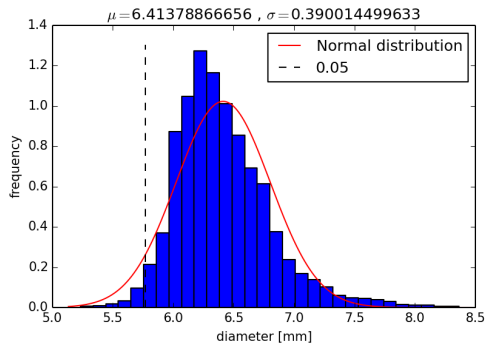
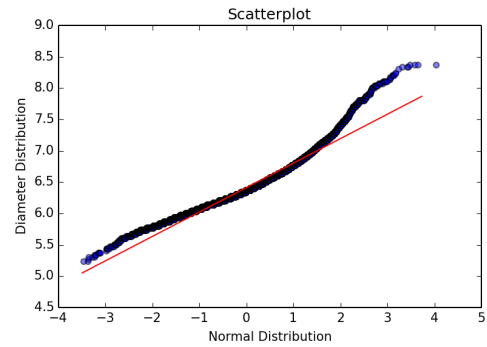


Figure C.117: Typical buckling behaviour in specimen 2-00-B

C.8.1 Geometry

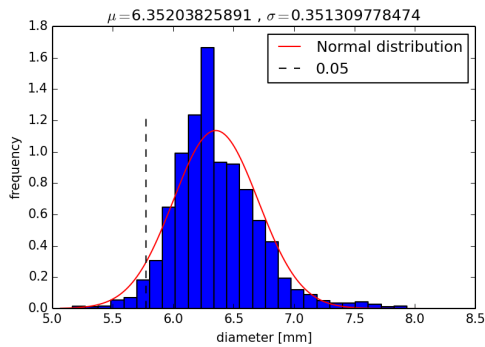


(a) Combined diameter distribution

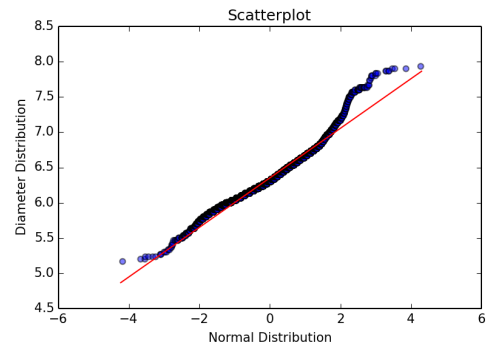


(b) Fit to normal distribution

Figure C.118: Combined geometry for specimen type 4B-00

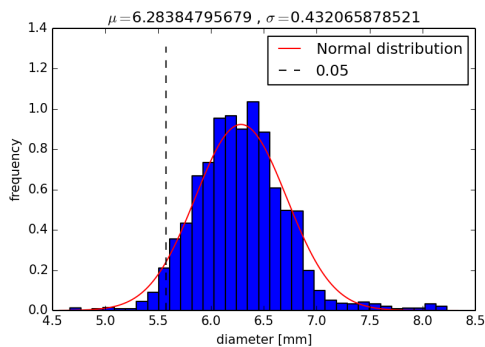


(a) Combined diameter distribution

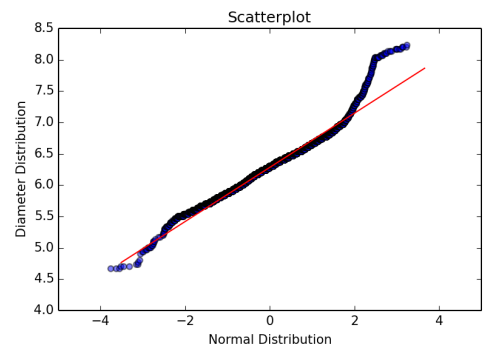


(b) Fit to normal distribution

Figure C.119: Combined geometry for specimen type 4B-30



(a) Combined diameter distribution

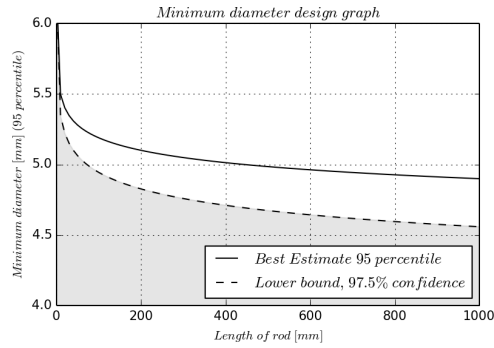


(b) Fit to normal distribution

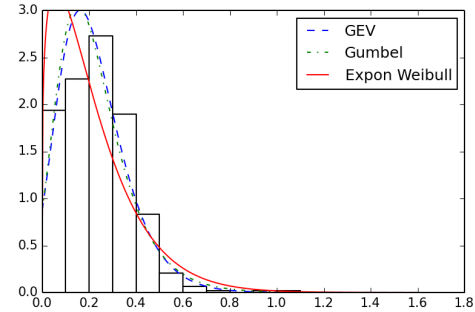
Figure C.120: Combined geometry for specimen type 4B-60

C.9 Geometry design graphs

On the following pages, the design graphs mentioned in section 6.2.7 are shown for the minimum diameter of different types of rods.

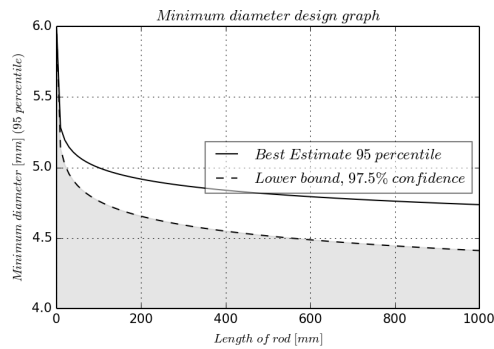


(a) Minimum diameter design

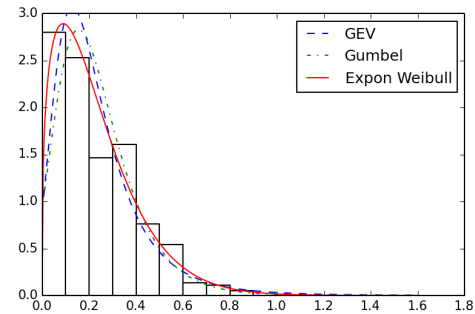


(b) Fit to weibull distribution

Figure C.121: Minimum diameter design for specimen type 1-00

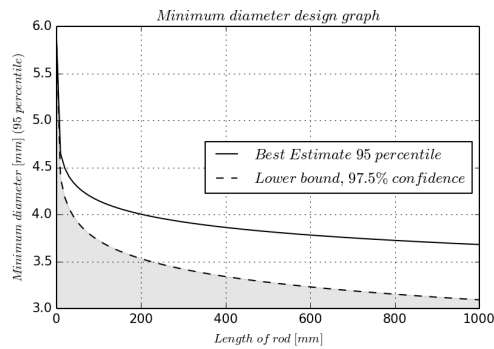


(a) Minimum diameter design

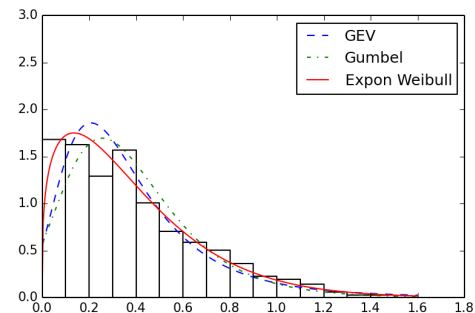


(b) Fit to weibull distribution

Figure C.122: Minimum diameter design for specimen type 1-30

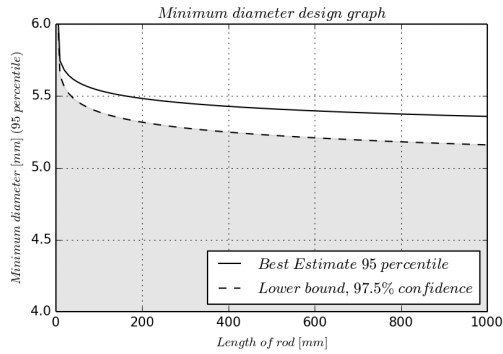


(a) Minimum diameter design

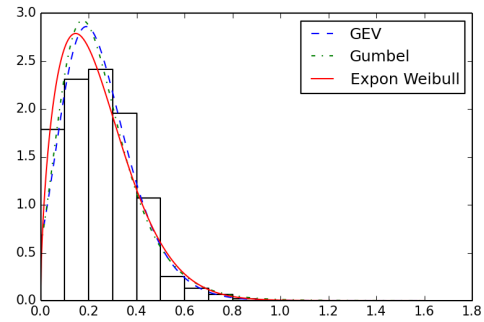


(b) Fit to weibull distribution

Figure C.123: Minimum diameter design for specimen type 1-60

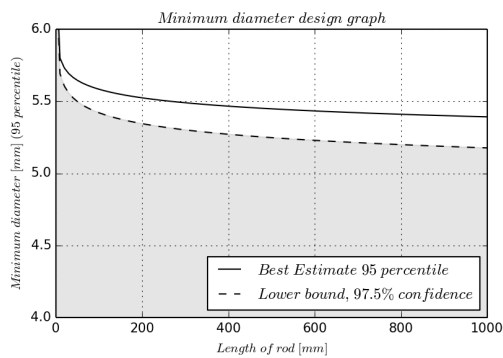


(a) Minimum diameter design

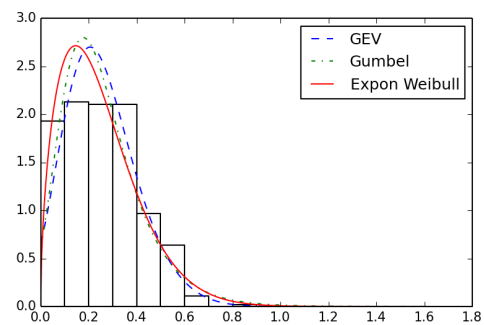


(b) Fit to weibull distribution

Figure C.124: Minimum diameter design for specimen type 2-00

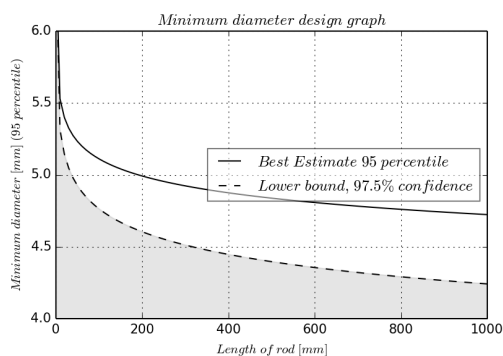


(a) Minimum diameter design

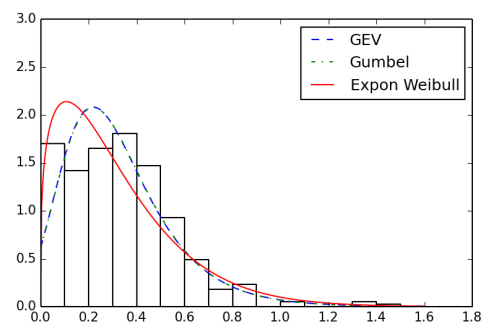


(b) Fit to weibull distribution

Figure C.125: Minimum diameter design for specimen type 2-30

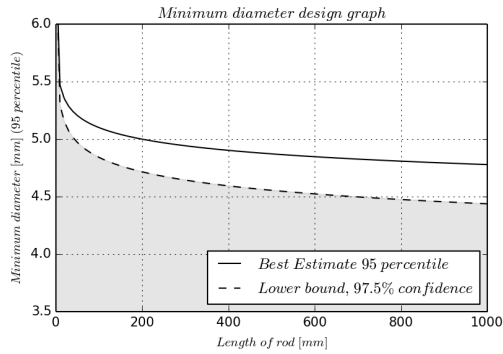


(a) Minimum diameter design

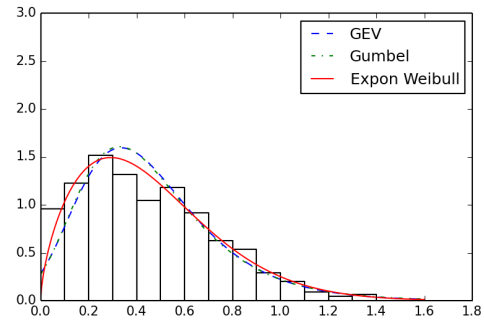


(b) Fit to weibull distribution

Figure C.126: Minimum diameter design for specimen type 2-60

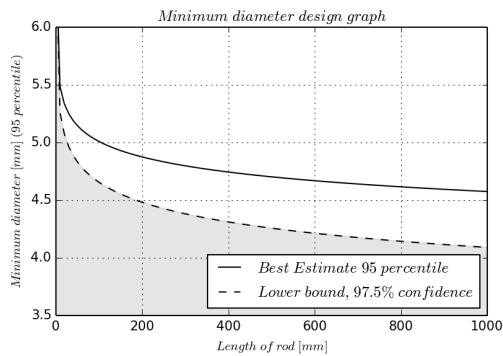


(a) Minimum diameter design

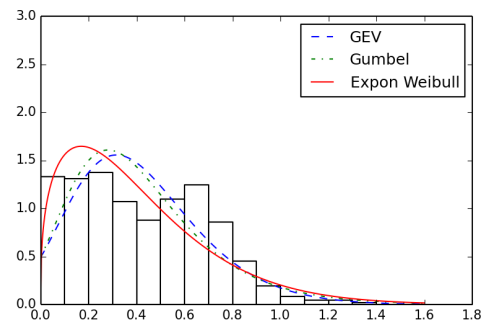


(b) Fit to weibull distribution

Figure C.127: Minimum diameter design for specimen type 3-00

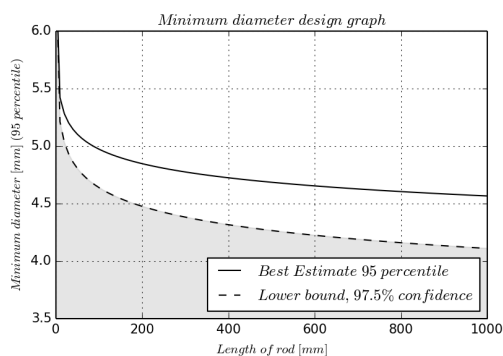


(a) Minimum diameter design

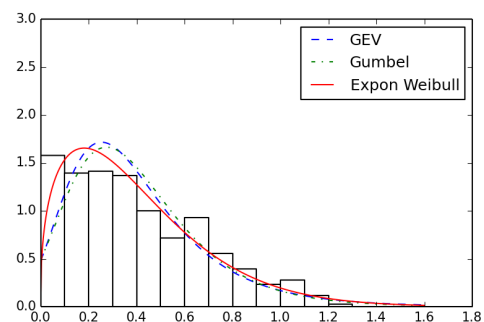


(b) Fit to weibull distribution

Figure C.128: Minimum diameter design for specimen type 3-30

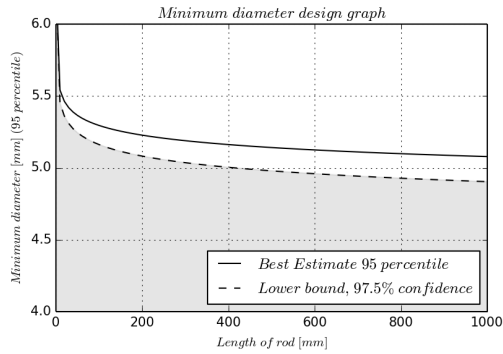


(a) Minimum diameter design

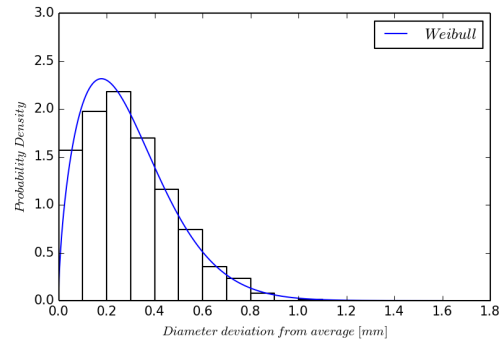


(b) Fit to weibull distribution

Figure C.129: Minimum diameter design for specimen type 3-60

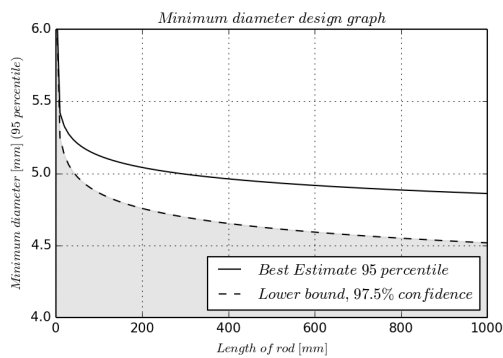


(a) Minimum diameter design

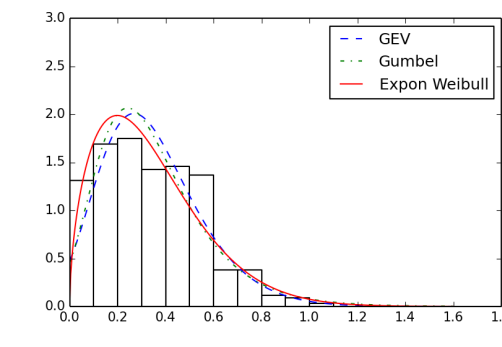


(b) Fit to weibull distribution

Figure C.130: Minimum diameter design for specimen type 4-00

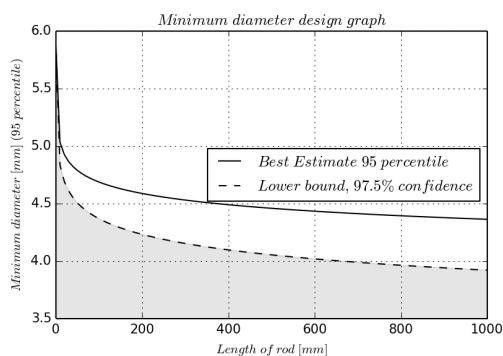


(a) Minimum diameter design

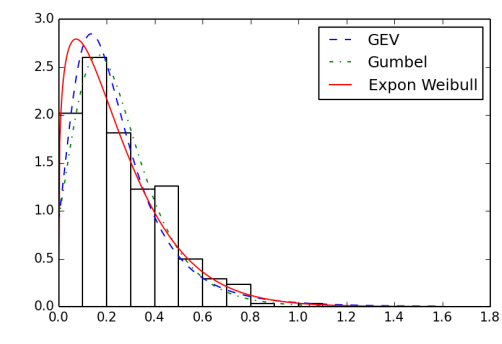


(b) Fit to weibull distribution

Figure C.131: Minimum diameter design for specimen type 4-30



(a) Minimum diameter design



(b) Fit to weibull distribution

Figure C.132: Minimum diameter design for specimen type 4-60

References

- ASTM (1963). *A guide for fatigue testing and the statistical analysis of fatigue data*. American Society for Testing and Materials. DOI: 10.1520/STP91A-EB.
- Baddoo, N.R. (2008). “Stainless steel in construction: a review of research, applications, challenges and opportunities”. In: *Journal of Constructional Steel Research* 64.11, pp. 1199–1206.
- BCSA, British Constructional Steelwork Association (2010). “Welding Procedure Specifications (WPSs)”. In: *Steel Industry Guidance Notes* 06. URL: www.steelconstruction.org/component/documents/?task=downloadDocument&doc=58963&file=65083&cd=1&hl=en&ct=clnk&gl=uk.
- Beardmore, R. (2014a). *Metal Costs*. URL: http://www.roymech.co.uk/Useful_Tables/Matter/Costs.html.
- (2014b). *Metal Fatigue*. URL: http://www.roymech.co.uk/Useful_Tables/Fatigue/Fatigue.html.
- Benyounis, K.Y. and A.G. Olabi (2008). “Optimization of different welding processes using statistical and numerical approaches - A reference guide”. In: *Advances in Engineering Software* 39, pp. 483–496.
- BSSA, British Stainless Steel Association (2014). *Comparison of structural design in stainless steel and carbon steel*. URL: <http://www.bssa.org.uk/topics.php?article=125> (visited on 08/19/2014).
- Cambridge, University of (2015). *Measurement of Texture 2*. URL: http://www.doitpoms.ac.uk/tlplib/crystallographic_texture/ebsd.php.
- Casagrande, A., G.P. Cammarota, and L. Micele (2011). “Relationship between fatigue limit and Vickers hardness in steels”. In: *Materials Science and Engineering: A* 528.9, pp. 3468–3473. ISSN: 0921-5093. DOI: <http://dx.doi.org/10.1016/j.msea.2011.01.040>. URL: <http://www.sciencedirect.com/science/article/pii/S0921509311000487>.
- Centre for Additive Layer Manufacturing, University of Exeter (2014). *What is additive layer manufacturing?* URL: <http://emps.exeter.ac.uk/engineering/research/calm/whatis/> (visited on 08/19/2014).
- Colegrove, P.I and S. Williams (2014). *High deposition rate high quality metal additive manufacture using wire + arc technology*. URL: <http://www.norsktitanium.no/en/News/~media/NorskTitanium/Titanidum%20day%20presentations/Paul%20Colegrove%20Cranfield%20Additive%20manufacturing.ashx> (visited on 11/11/2014).
- Cranfield, University (2013). *Revolutionary 3D metal production process developed at Cranfield*. URL: <http://www.cranfield.ac.uk/about/media-centre/news-archive/news-2013/revolutionary-3d-metal-production-process-developed-at-cranfield.html> (visited on 08/25/2014).
- Cruise, R.B. and L. Gardner (2008). “Residual stress analysis of structural stainless steel sections”. In: *Journal of Constructional Steel Research* 64, pp. 352–366.
- David, S.A. et al. (1987). *Effect of rapid solidification on stainless steel weld metal microstructures and its implications on the Schaeffler diagram*.
- Dekking, F.M. (2005). *A Modern Introduction to Probability and Statistics: Understanding why and how*. Springer.

- Elmer, J.W., S.M. Allen, and T.W. Eagar (1989). “Microstructural development during solidification of stainless steel alloys”. English. In: *Metallurgical Transactions A* 20.10, pp. 2117–2131. ISSN: 0360-2133. DOI: 10.1007/BF02650298. URL: <http://dx.doi.org/10.1007/BF02650298>.
- ESDEP, European Steel Design Educational Programme (2014a). *ESDEP LECTURE NOTE [WG18]*. URL: <http://www.fgg.uni-lj.si/~pmoze/ESDEP/master/wg18/10100.htm>.
- (2014b). *ESDEP LECTURE NOTE [WG2]*. URL: <http://www.fgg.uni-lj.si/~pmoze/ESDEP/master/wg02/10100.htm>.
- (2015). *Lecture 7.5.2: Columns II*. URL: <http://www.fgg.uni-lj.si/~pmoze/ESDEP/master/wg07/10520.htm>.
- EFW, European Welding Federation (2009). *Weldability of Corten Steels*. URL: http://www.efw.be/media/documentosdocs/doc_86_weldability_of_corten_steels.pdf.
- Funderburk, S.R. (1999). “Key concepts in welding engineering”. In: *Welding Innovation* 16.1.
- Hirano, A., M. Sakane, and N. Hamada (2005). “Relationship Between Vickers Hardness and Fatigue Strength”. In: *ICF XI-11th International Conference on Fracture, Turin*.
- Howe, A.A. (1991). *Segregation and phase distribution during solidification of carbon, alloy and stainless steels*. Luxembourg: EC. ISBN: 92-826-0518-3.
- Huang, Jiunn-Yuan et al. (2006). “High-cycle fatigue behavior of type 316L stainless steel”. In: *Materials transactions* 47.02, pp. 409–417.
- IMOA, International Molybdenum Association (2014). *Metallurgy of Mo in Stainless Steel*. URL: <http://www.imoa.info/molybdenum-uses/molybdenum-grade-stainless-steels/metallurgy-of-molybdenum-in-stainless-steel.php>.
- ISO (2009). “6892-1: 2009.(2009)”. In: *Metallic materials-Tensile testing-Part 1: Method of test at room temperature*.
- (2012). “Metallic materials - Fatigue testing - Statistical panning and analysis of data”. In:
- Kruth, J. et al. (2004). “Selective laser melting of iron-based powder”. In: *Journal of Materials Processing Technology* 149.1, pp. 616–622.
- Lampman, S. et al. (1997). *Weld Integrity and Performance: A Source Book Adapted from ASM International Handbooks, Conference Proceedings, and Technical Books*. ASM International.
- Lowry, R. (2014). *Concepts and applications of inferential statistics*. VassarStats. Chap. 4: A first Glance at the Question of Statistical Significance. URL: <http://vassarstats.net/textbook/ch4pt1.html>.
- Mathers, G. (2014). *Welding of austenitic stainless steel - Job knowledge 103*. TWI-Global. URL: <http://www.twi-global.com/technical-knowledge/job-knowledge/welding-of-austenitic-stainless-steel-103/> (visited on 08/25/2014).
- Mehnen, J. et al. (2011). “Design for wire and arc additive layer manufacture”. In: *Global Product Development*. Springer, pp. 721–727.
- Moysan, J et al. (2003). “Modelling the grain orientation of austenitic stainless steel multipass welds to improve ultrasonic assessment of structural integrity”. In: *International Journal of Pressure Vessels and Piping* 80.2, pp. 77–85.

- Murugan, N. and R.S. Parmar (1994). “Effects of {MIG} process parameters on the geometry of the bead in the automatic surfacing of stainless steel”. In: *Journal of Materials Processing Technology* 41.4, pp. 381–398. ISSN: 0924-0136. DOI: [http://dx.doi.org/10.1016/0924-0136\(94\)90003-5](http://dx.doi.org/10.1016/0924-0136(94)90003-5). URL: <http://www.sciencedirect.com/science/article/pii/0924013694900035>.
- Nagesh, D.S. and G.L. Datta (2002). “Prediction of weld bead geometry and penetration in shielded metal-arc welding using artificial neural networks”. In: *Journal of Materials Processing Technology* 123.2, pp. 303–312.
- NEN (2011a). *Eurocode 3: Ontwerp en berekening van staalconstructies - Deel 1-1: Algemene regels en regels voor gebouwen*. Delft, the Netherlands: Nederlands Normalisatie-Instituut.
- (2011b). *Eurocode 3: Ontwerp en berekening van staalconstructies - Deel 1-9: Vermoeding*. Delft, the Netherlands: Nederlands Normalisatie-Instituut.
- Niehe, P. (2014). *Construction steelwork makes its 3D printing premiere*. URL: http://www.arup.com/News/2014_06_June/05_June_Construction_steelwork_makes_3D_printing_premiere.aspx (visited on 08/25/2014).
- Oerlikon (2015a). *Inertfil 308LSi*. URL: http://www.oerlikon-online.de/Handbuch/pdf/MD/korrosionsbestaendig/Seite_179_INERTFIL_308LSi.pdf.
- (2015b). *Inertfil 316LSi*. URL: <http://www.oerlikonline.hu/files/230.pdf>.
- Olson, D.L. (1985). “Prediction of austenitic weld metal microstructure and properties”. In: *Welding journal* 64.10, 281s–295s.
- Rasmussen, K.J.R. (2003). “Full-range stress-strain curves for stainless steel alloys”. In: *Journal of Constructional Steel Research* 59.1, pp. 47–61. ISSN: 0143-974X. DOI: [http://dx.doi.org/10.1016/S0143-974X\(02\)00018-4](http://dx.doi.org/10.1016/S0143-974X(02)00018-4). URL: <http://www.sciencedirect.com/science/article/pii/S0143974X02000184>.
- Reardon, A. C. (2011). *Metallurgy for the Non-metallurgist*. ASM International.
- Sandmeyer (2015). *Specification Sheet: Alloy 316/316L*. URL: <http://www.sandmeyersteel.com/images/316-316L-317L-Spec-Sheet.pdf>.
- SCI, Steel Construction Institute (2006). *Design manual for structural stainless steel*. Brussels: Euro Inox and Steel Construction Institute. ISBN: 2-87997-204-3.
- Smallman, R. E. and A.H.W. Ngan (2013). *Modern Physical Metallurgy*. Butterworth-Heinemann. ISBN: 9780080982236.
- Smith, L. R. et al. (2006). *Springer handbook of materials measurement methods*. Springer. DOI: 10.1007/978-3-540-30300-8. URL: <http://dx.doi.org/10.1007/978-3-540-30300-8>.
- Spielman, J. (2013). *Open Source Photogrammetry*. URL: <http://wedidstuff.heavyimage.com/index.php/2013/07/12/open-source-photogrammetry-workflow/> (visited on 09/02/2014).
- Suryakumar, S. et al. (2011). “Weld bead modeling and process optimization in Hybrid Layered Manufacturing”. In: *Computer-Aided Design* 43.4, pp. 331–344.
- Takakuwa, O., Y. Kawaragi, H. Soyama, et al. (2013). “Estimation of the Yield Stress of Stainless Steel from the Vickers Hardness Taking Account of the Residual Stress”. In: *Journal of Surface Engineered Materials and Advanced Technology* 3.04, p. 262.
- TWI (2014a). *Effect of intermetallic content on pitting resistance of ferritic-austenitic stainless steels*. URL: <http://www.twi-global.com/technical-knowledge/>

- published - papers / effect - of - intermetallic - content - on - pitting - resistance - of - ferritic - austenitic - stainless - steels /.
- TWI (2014b). *Why is there no amperage control on a MIG welding power source?* TWI-Global. URL: <http://www.twi-global.com/technical-knowledge/faqs/process-faqs/faq-why-is-there-no-amperage-control-on-a-mig-welding-powersource/> (visited on 08/26/2014).
- (2015a). *Aluminium alloys: Weldability of materials*. URL: <http://www.twi-global.com/technical-knowledge/job-knowledge/weldability-of-materials-aluminium-alloys-021/>.
- (2015b). *What is Charpy Testing?* URL: <http://www.twi-global.com/technical-knowledge/faqs/material-faqs/faq-what-is-charpy-testing/>.
- Vander Voort, G.F. and G.M. Lucas (2015). *Microindentation hardness*. URL: <http://www.metallography.com/amp/micro.htm>.
- Vitek, J.M., A. Dasgupta, and S.A. David (1983). “Microstructural modification of austenitic stainless steels by rapid solidification”. English. In: *Metallurgical Transactions A* 14.9, pp. 1833–1841. ISSN: 0360-2133. DOI: 10.1007/BF02645553. URL: <http://dx.doi.org/10.1007/BF02645553>.
- Xiong, J., G. Zhang, H. Gao, et al. (2013). “Modeling of bead section profile and overlapping beads with experimental validation for robotic GMAW-based rapid manufacturing”. In: *Robotics and Computer-Integrated Manufacturing* 29.2, pp. 417–423.
- Xiong, J., G. Zhang, J. Hu, et al. (2014). “Bead geometry prediction for robotic GMAW-based rapid manufacturing through a neural network and a second-order regression analysis”. In: *Journal of Intelligent Manufacturing* 25.1, pp. 157–163. DOI: 10.1007/s10845-012-0682-1. URL: <http://dx.doi.org/10.1007/s10845-012-0682-1>.
- Zipperian, D. (2011). *Metallographic Handbook*. Tucson, Arizona USA: PACE Technologies.